Politecnico di Milano
Dept. of Aerospace Science and Technology
Doctoral Programme in Aerospace Engineering

Design of electric-powered aircraft for commercial transportation

Doctoral Dissertation of:
Francesco Salucci

Supervisor:
Prof. Lorenzo Trainelli

Co-supervisors:
Prof. Carlo E. D. Riboldi
Prof. Alberto Rolando

Coordinator:
Prof. Pierangelo Masarati

Academic year 2020/21 – Cycle XXXIII

ABSTRACT

ELECTRIC-powered aircraft introduce propulsion architectures so different from the old fuel-based ones that classic aeronautical design is deficient in terms of objectives and design methods. Thanks to these new technologies, parts of the air transport system can be rethought. This work proposes an exploration of new possible design objectives and related techniques, laying solid analytical foundations to design and analysis of aircraft with innovative electric propulsion and their integration into the air transport system. First, the development and validation of a new hybrid-electric aircraft conceptual design tool is shown. Second, a study on an innovative procedure for the optimal sizing of airport infrastructures in support to hybrid-electric transition is discussed. Third, models and tools for assessing the effect of hybrid-electric power-trains on the reduction of acoustic and chemical pollution are presented. Finally, the design of a zero-emission, liquid hydrogen-fuelled 19-seater aircraft for very short-haul air transportation is carried out, making use of the implemented methodologies and showing the benefits that such *miniliner* could bring to European citizens.

SOMMARIO

Gli aeroplani muniti di propulsione elettrica introducono delle differenze radicali nell'architettura propulsiva rispetto agli aeroplani convenzionali alimentati a combustibile. Tali differenze rendono impossibile l'utilizzo di metodi di progettazione classici e richiedono la definizione di nuovi obbiettivi di progetto. Grazie a queste nuove tecnologie, parte del sistema di trasporto aereo deve essere ripensato. Questa tesi descrive lo sviluppo di una serie di strumenti per la progettazione di aeroplani da trasporto commerciale muniti di propulsione elettrica. In primis, viene illustrato lo sviluppo e la validazione di un nuovo strumento per la progettazione concettuale di velivoli ibridi-elettrici. Poi, è proposta una originale procedura per il dimensionamento ottimo delle infrastrutture aeroportuali in supporto di una transizione verso la propulsione ibrido-elettrica. Infine sono mostrati dei modelli e degli strumenti per la stima degli effetti delle nuove architetture ibrido-elettriche sulle emissioni gassose e sul rumore. Queste procedure sono utilizzate per il dimensionamento di un rivoluzionario aeroplano da 19 posti per il trasporto a cortissima distanza, battezzato *miniliner*. Il miniliner è un aereo a zero emissioni da poter usare *come un autobus* per andare al lavoro o all'università. È propulso con delle celle a combustibile alimentate a idrogeno, presente a bordo in forma liquida. Questo velivolo potrebbe portare molti benefici al sistema di trasporto europeo, specialmente nelle aree dove il trasporto terrestre è poco sviluppato.

ACKNOWLEDGEMENTS

Special thanks go to the three pillars of my PhD path:

- Prof. Lorenzo Trainelli, *supervisor*
- Prof. Carlo E. D. Riboldi, *co-supervisor*
- Prof. Alberto Rolando, *co-supervisor*

I have been extremely lucky to have supervisors who cared so much about my work and I will be forever grateful for your invaluable contribution to my personal and professional growth. I hope to continue to work with you all.

I would like to thank also Prof. Fabrizio Oliviero for hosting me at TU Delft at the end of my 1st year. At TU Delft I've learnt more than I've given and I hope to come back one day.

As I said in the Introduction, this thesis is part of a huge team work and several wonderful thesis students have given their contribution. Namely: Federico Bigoni, Gabriele Poiana, Niccolò Rossi, Alejandro Moreno-Perez, Raouf Ibrahim, Andrea Marchionni, Davide Comincini, Luca Mariani, Violeta Álvarez Álvarez, Andrés F. Téllez, Andrea Matrone, Davide Gabrielli, Antonio Estrada Briz, Isacco Raimo, Germán García González, Gianluca Magni and Luis Miguel Chacha Guevara.

Finally, thanks and good luck to Yasir Mahmood Khan, the PhD candidate that will enhance and continue part of the work shown in this thesis.

TABLE OF CONTENTS

LIST OF FIGURES

LIST OF TABLES

LIST OF ACRONYMS

AC	Alternate Current
ACM	Aero Club Milano
AEO	All Engine Operating
ANCON	Aircraft Noise CONtour
ANP	Aircraft Noise and Performance
AHRES	Airport Hydrogen Refilling Equipment Sizing
ARES	Airport Recharging Equipment Sizing
ARGOS	AiRcraft GeOmetry Sizing
B2B	Battery to Battery
B2G	Battery to Grid
BP	Battery Pack
BPC	Battery Plug-in Charger
BMS	Battery Management System
BSS	Battery Swapping Station
BSFC	Brake Specific Fuel Consumption
BWB	Blended Wing Body
CAS	Calibrated Airspeed
CCH2	Cryo-compressed hydrogen
DC	Direct Current

DEP	Distributed Electric Propulsion
DOD	Depth of Discharge
ECAC	European Civil Aviation Conference
EM	Electric Motor
EV	Electric Vehicle
FC	Fuel Cell
FCHE	Fuel Cell Hybrid-Electric
FCM	Fuel Cell Module
GA	General Aviation
GH2	Gaseous Hydrogen
GHG	GreenHouse Gas
HE	Hybrid-Electric
HETA	Hybrid-Electric Transition Altitude
HYPERION	HYbrid PERformance SimulatION
ICE	Internal Combustion Engine
LH2	Liquid Hydrogen
LIB	Lithium-ion Battery
LSB	Lithium Sulfur Battery
LAB	Lithium Air Battery
MAB	Metal Air Battery
LTO	Lithium Titanate Oxide
LFP	Lithium Iron Phosphate
LCO	Lithium Cobalt Oxide
LMO	Lithium Manganese Oxide
NCA	Lithium Nickel Cobalt Aluminum Oxide
NMC	Lithium Nickel Manganese Cobalt Oxide
MXB	Metal-X Batteries
OEI	One Engine Inoperative
OD	Origin-Destination

PE	Pure-Electric
PGS	Power Generation System
PEM	Proton Exchange Membrane
PEMFC	Proton Exchange Membrane Fuel Cell
POH	Pilot Operating Handbook
PMCD	Power Management Control and Delivery
MAHEPA	Modular Approach to Hybrid Electric Propulsion Architecture
MILP	Mixed Integer Linear Programming
MDD	Most Demanding Day
MTOM	Maximum Take-off Mass
SHARONA	Short-Haul Air Route Optimal Network Assessment
SEL	Sound Exposure Level
SPL	Sound Pressure Level
SOC	State Of Charge
SOFC	Solid Oxide Fuel Cell
SMP	Sizing Matrix Plot
SA	Secondary Aerodrome
SB	Structural Battery
TE	Thermal Engine
THE	Thermal Hybrid-Electric
TOP	Take-Off Parameter
TLAR	Top Level Aircraft Requirements
TRL	Technology Readiness Level
TSFC	Thrust Specific Fuel Consumption
TGS	Thrust Generation System
UAM	Urban Air Mobility
UHC	Uncombusted Hydro-Carbon
UNIFIER19	commUNIty FrIendly minilinER 19
VFR	Visual Flight Rules

INTRODUCTION

In the aerospace and aviation industries, electric propulsion is trigging substantial shifts in several aspects of aircraft design, production and operations, leading to the biggest radical innovation since the introduction of jet engines.

A strong political push to dramatically cut gaseous emissions deriving from air transportation is currently undergoing [1]. Climate change poses increasingly severe risks to commercial aviation and the related economy. While flying is a fundamental capability for many aspects of human life and, in the author's opinion, a very cool thing to do, year 2019 has seen the rise of flight shaming: hashtags like *flightskam* became viral and people started discussing the environmental consequences of flying. Moreover, several countries implemented the so called green taxes: passengers have to pay a CO_2 tax on plane tickets in Switzerland, France and the Netherlands, in order to discourage them to fly [2].

Apart from the push of the *green wave*, there are several advantages and opportunities brought in by electric-powered aviation.

First of all, new aircraft equipped with pure-electric and hybrid-electric power-trains may have the most visible and audible effects in the vicinity of airports, where terminal manoeuvrers and circuit patterns may be flown in pure-or partially-electric mode. This new capability has the potential to cut the noise usually associated to airports and increase public acceptance of near-ground air operations well beyond today's limits.

The flexibility brought by the electrification of the power-train opens the

door to a new set of airframe configurations that can take advantage of distributing the thrust across several small electric motors. These configurational choices can change considerably from the traditional tube-and-wing, generating very different problems/design solutions.

Thanks to the reduction of noise, gaseous emissions and the increase in take-off and landing performance due to aero-propulsive interactions such as distributed electric propulsion, hybrid-electric aircraft may operate from secondary airports and smaller airfields, which may reveal as key nodes of a more connected continental transportation network through enhanced, environmentally sustainable regional air travel, especially in territories with inefficient ground transportation services. The use of this network can open new aviation markets, including urban air mobility and a new sub-regional market.

New propulsion architectures represent a good opportunity for the entrance of new companies in the aviation market, both as operators and manufacturers, subtracting the monopoly in the production of aircraft and engines from the usual players. This might have a disruptive effect on a market that has been impenetrable for decades and which for years has been stuck to configurations that are almost identical to themselves.

Finally, the use of batteries and innovative fuels, as alternative means of propulsion can finally relieve the burden of oil price on airplane tickets and disengage the air travel market from the dynamics of the oil market. In particular, the adoption of hydrogen can offer the very first chance of true energetic independence, being possibly produced from domestic energy sources.

On top of this, the sharp drop in demand for passenger air travel due to the COVID-19 pandemic and containment measures are jeopardizing the profitability of many companies in both the air transport market and the rest of the aviation industry, with many jobs at stake. The industry has proven many times its ability to bounce back from unanticipated shocks and the recent crisis looks like a good opportunity to get back on feet and introduce radical innovations.

This thesis aims at contributing to the research effort towards a more sustainable aviation and is framed in two European Commission's projects about hybrid-electric aircraft: Horizon 2020 MAHEPA and Clean Sky 2 UNIFIER19. MAHEPA has developed a thermal hybrid-electric and a hydrogen-driven fuel cell power-train for two 4-seater aircraft scheduled for flying in early 2021. UNIFIER19 is designing a zero-emission 19-seat miniliner for very short haul transportation featuring a hybrid fuel cell system with liquid hydrogen tanks. MAHEPA and UNIFIER19 are co-

ordinated by Pipistrel Vertical Solutions, a leading light aircraft manufacturer strategically committed to innovative technologies, and involve several universities (Politecnico di Milano, TU Delft, University of Ulm, University of Maribor), research centres (DLR) and SMEs. Both projects aim to build-up a technological know-how and study the possibility to scale the acquired technology to larger airplanes. Several activities were carried out in this sense during the PhD.

The present work addresses a broad variety of topics, which may appear somewhat disparate, but are mutually connected by the final goal of enabling an accurate and reliable conceptual design solution for an innovative electric-powered passenger aircraft. In order to present the material in an orderly fashion, the thesis in structured in two parts.

The first part is methodological and initially provides a technology review focusing on enabling technologies, without reporting about historical and current aeronautical realizations. An excellent discussion of concepts and prototypical development in the area of electric-powered aircraft can be found in [3, 4]. Further on, a set of original procedures and methodologies for the design of hybrid-electric airplanes and the study of their impact on the environment and the market is described. The following description details the chapters in Part I:

- **Chapter 1 – Setting the picture: opportunities and needs** introduces the reader to the main challenges and design space freedom brought by novel propulsion technologies.
- **Chapter 2 – Technology review** provides an extensive technological survey, discussing the main aspects and main performance indicators of several items present in hybrid-electric power-trains, such as batteries, electric motors, fuel cells, and hydrogen storage devices.
- **Chapter 3 – Innovative aircraft modelling for design and analysis** presents some design and performance modelling techniques for the main components of hybrid-electric architectures. In particular, focus is placed on the estimation of key parameters such as fuel cell and electric motor efficiency and on suggesting suitable procedures to size critical elements, as hydrogen storage devices. Secondly, an aero-propulsive interaction model is proposed and reframed for the adoption in the aircraft design process. The goal of this chapter is to build a knowledge-base for the preliminary sizing of hybrid-electric airplanes, discussed in Chapter 4.
- **Chapter 4 – Aircraft preliminary sizing** shows a general procedure for the preliminary sizing of innovative pure-electric and hybrid-

electric airplanes, with the ambition to provide a tool applicable to propeller-driven, fixed-wing vehicles of arbitrary size and mission requirements.

- **Chapter 5 – Airport infrastructures for innovative aircraft** describes an original methodology which provides the optimal solution to the sizing of airport battery recharging infrastructures for a future airports hosting hybrid-electric aircraft.
- **Chapter 6 – Environmental assessment of innovative aircraft** presents the development of an acoustic and gaseous pollution prediction model to quantitatively evaluate the advantages, in terms of emissions, of the application of modern electric power-trains to airplanes.

The second part focuses on the miniliner concept, an innovative 19-seat hybrid-electric aircraft designed to foster the intra-continental transport within Europe. This part introduces an original methodology for the prediction of the relevant market and goes on with the application of the design methodologies discussed in Part I. The following description details the chapters in Part II:

- **Chapter 7 – The miniliner concept** introduces the miniliner, illustrating the motivation and some example applications.
- **Chapter 8 – Market studies** illustrates some of the strategies adopted to set the top-level aircraft requirements for the miniliner. Application examples in different geographic contexts provide useful information for the definition of crucial design requirements such as payload, range, runway length, and cruising airspeed.
- **Chapter 9 – Top-level aircraft requirements for the miniliner** sums up the results obtained in the market study and states the top-level aircraft requirements for the design process.
- **Chapter 10 – Preliminary sizing of the miniliner** shows the application of our preliminary sizing tool introduced in Chapter 4 to the design of the miniliner, providing also sensitivity analysis.
- **Chapter 11 – Towards a conceptual design of the miniliner** proposes a first example of a Class I conceptual design of the miniliner, with geometric sizing and a first geometrical representation.

It is important to clearly state that this work is the fruit of a substantial team effort carried out in the FMSlab (Flight Mechanics and Flight Systems laboratory) at the Department of Aerospace Science and Technology, under the coordination of my supervisor Prof. Lorenzo Trainelli and co-

supervisors Prof. Carlo E. D. Riboldi and Prof. Alberto Rolando. An important part of the activities presented in this thesis have been carried out with the help of several MSc thesis students who graduated during the years of my PhD. Further information is provided at the beginning of each chapter and in the Conclusion.

Part I

A new framework for innovative aircraft design and analysis

CHAPTER 1

SETTING THE PICTURE: OPPORTUNITIES AND NEEDS

Aeronautics is a vital sector of European society and economy and is now directly concerned by new challenges regarding its competitiveness, performance and sustainability. European Commission invited key stakeholders of European aviation to come together in a high-level group to develop a vision for Europe's aviation system and industry: Flightpath 2050 [5]. This includes several ambitious goals, including:

- 90% of travellers within Europe will be able to complete their journey, door-to-door, within 4 hours;
- flights will arrive within 1 minute of the planned arrival time regardless of weather conditions;
- the number of accidents will be reduced by 80% compared to 2000 taking into account increasing traffic.

In this vision, protecting the environment and the energy supply is a key element: in 2050, technologies and procedures will allow a 75% re-

duction in CO_2 emissions per passenger kilometre and a 90% reduction in NO_x emissions. The perceived noise emission of flying aircraft will be also reduced by 65% with respect to the capabilities of typical new aircraft in 2000. The EU targets are considered as being on an equal footing with those announced by International Civil Aviation Organization (ICAO), International Air Transport Association (IATA), National Aeronautics and Space Administration (NASA) [6–8]. To fulfil these long-term emission goals, it is not possible to rely on conventional thermal propulsion: such technology has already been pushed to the edge. Indeed, a radical innovation is required.

Electric propulsion has recently emerged in the aerospace industry, buoyed by the pace of change in the automotive sector. Hybrid-Electric (HE) aerial vehicles promise several benefits: low- or zero-emission flight, the potential to open up new missions for aircraft, the possibility of safer flight, and - crucially - the design flexibility enabled by distributed propulsion and other innovative configuration elements. There are also drawbacks hindering the trend to HE propulsion: low technological maturity of energy storage devices, lack of regulation for future mobility concepts and uncertainty on future market demand.

1.1 Propulsion architectures

With the goal to explore the design space as much as possible, an initial identification of all the possible technological solutions for the propulsion systems is necessary.

First of all, when considering emissions (chemical and noise), as well as costs, the choice of the energy supply to be used to produce the required power is important. Today, a number of potential references exist to be used at least at a theoretical level for air-transport applications. In this thesis the following options will be considered for the qualitative trade off:

- Fossil Fuel: conventional AVGAS and Jet Fuel represent the benchmark when different energy sources are analysed.
- Batteries: batteries are used as electrical energy storage devices; currently, design and manufacture efforts have been focusing on boosting their weight and volume properties in order to be applied efficiently for air travel purposes.
- Hydrogen: hydrogen is in principle a very appealing energy source because of its very high specific (gravimetric) energy density together with the low emissions production when used in a thermal engine.

Hydrogen combustion in thermal engines, however, achieves very low burning efficiencies (around 25%). On the other hand, using hydrogen in a fuel cell system, where electrical energy is obtained by electrochemical reaction with an oxidizing agent, brings much higher efficiencies (50-70%) and only emits water vapour. This water vapour, being entirely free of soot particles cuts down the formation of contrails [9], which appear to be a significant portion of aviation-attributable climate warning. In principle, this technology allows to achieve a zero gaseous emission propulsion system, apart from water vapour.

Concerning the configuration of the propulsion system, many topological classifications exist. A tentative classification is based on the amount of sources of energy used that can be differentiated:

- Single energy source configuration: this group covers both traditional jet engines, turboprop/turboshaft and reciprocating engines used in aeronautical applications, as well as complete electrical systems featuring only batteries and fuel cells. In this case, energy is derived from a single source and transformed into mechanical power that can be connected to a thrust generation system (propeller or fan).
- Hybrid configuration: in this case, multiple sources of energy may be used (also simultaneously) to generate thrust. The use of a second source is generally meant to circumvent the shortcomings of a primary source in such a manner that the system's total output (for example, in terms of peak power or reliability) is somehow improved.

Various options of single energy source and hybrid configurations can be found in the scientific literature, mirroring and/or inspiring real aircraft prototypes and concepts under developments [10]. A number of representative schematics of these topologies are displayed in Fig 1.1. These architectures can be grouped in 4 categories:

1. Pure-electric (or all-electric, full-electric, fully electric, universally electric, electric propulsion): no thermal engine is included. The battery is the only source of energy and electric power, which is converted into mechanical power by an electric motor. The electric motor is then connected to the propeller or fan to produce thrust.
2. Serial (or series) hybrid-electric: electric motors are fed by batteries and/or electric energy coming from a PGS. This may be based on a thermal engine or a fuel cell system. A variation of this architecture is the turbo-electric one, where no battery is present.
3. Parallel hybrid-electric: both electric motors and thermal engines are

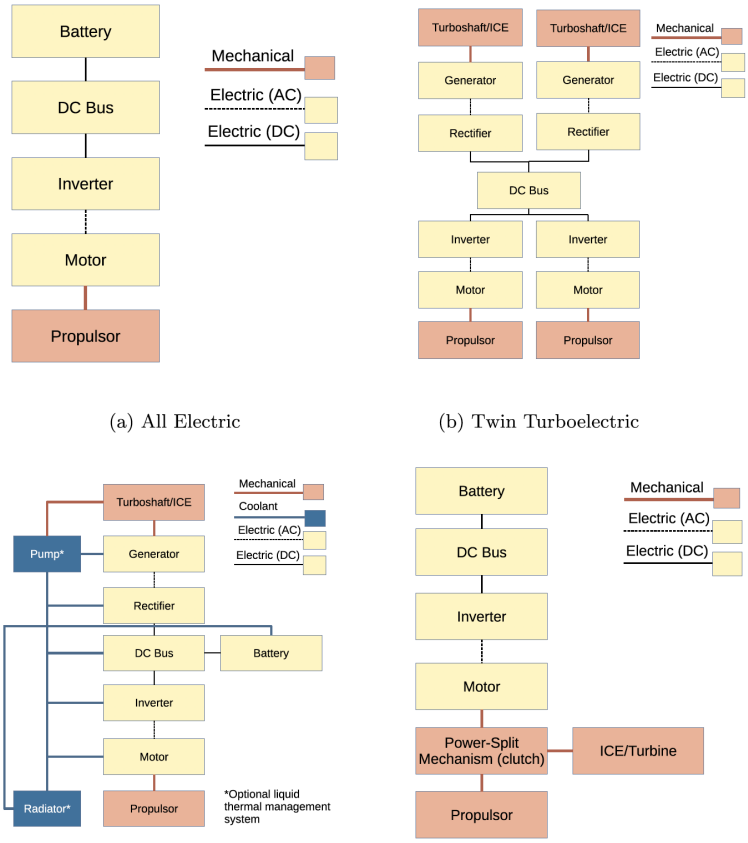

(a) All Electric

(b) Twin Turboelectric

(c) Series Hybrid (with Liquid Cooling)

(d) Parallel Hybrid

Figure 1.1: *Notional electric propulsion architecture [10].*

mechanically connected to propellers/fans. In this case, batteries are used to provide power boosts in high demand phases.

4. Conventional: the conventional power-train, with fuel burning thermal engines.

These configurations can be differentiated using quantitative indicators called degrees of hybridization or hybridization factors, trying to establish a connection among the various architectures. These were introduced in [11] and recalled by [10]:

$$H_P = \frac{P_m}{P_{tot}} \tag{1.1}$$

$$H_E = \frac{E_b}{E_{tot}} \tag{1.2}$$

where P_m and E_b are usually intended as the power and energy of the non-polluting source of energy, usually battery or hydrogen. It is noted that all the possible design choices cannot be completely defined by the schemes in Figures 1.1. Moreover, there is no clear understanding about which of these configurations can be the most sustainable for the environment or the cheapest. Few studies have been performed in this regard [12, 13] and cradle-to-grave environmental assessments concluded that there is a great difficulty in making an accurate prediction due to the dependence on many uncertain parameters, such as the energy sources employed to recharge the batteries, the usage of rare materials within the batteries and other factors. Notwithstanding these difficulties, a strong effort is currently being exerted in the investigation of these matters, especially in the frame of EU-funded research programs. The present work is indeed aimed at contributing to such effort, as it will be discussed in the following.

For this work, three types of architecture have been selected among the aforementioned ones:

1. Pure-Electric (PE).
2. Serial Thermal Hybrid-Electric (THE).
3. Fuel Cell Hybrid-Electric (FCHE).

PE and FCHE architectures can be called zero emission architectures at aircraft level, as they produce no harmful gaseous emissions. On the other hand, serial THE architectures can put together the advantages of thermal engines and electric motors, thus allowing to increase efficiency and reduce emissions without renouncing to good flight performance, as it happens for the PE case. Among the possible THE architectures, the serial option offers more possibilities in terms of innovation, as it does not need any

mechanical link between the thermal engine and the propeller/fan. This capability is crucial to exploit advantageous aero-propulsive interaction elements and the design freedom offered by the small size and weight of electric motors. For instance, the overall thrust can be distributed across multiple electric motors, placed along the wingspan and/or in other different locations, avoiding the use of wing pylons and reinforced wing ribs: this kind of arrangement is called DEP. The purpose of DEP is to optimize the vehicle's aero-propulsive efficiency by achieving advantageous interaction between the propulsion systems and the rest of the airframe. Distributed propulsion systems pledge aero-propulsive performance enhancements by, for example, decreased wing area and needing a smaller wing structure. Another example of a beneficial aero-propulsive interaction are wing-tip propellers. Wing-tip propellers are placed at the tips of the wing, counter-rotating with respect to tip vortices, with the consequence that the related induced drag may be reduced. From a design perspective, this solution entails a higher apparent wing aspect ratio with improved flight performance in most mission conditions. The installation of this technology was not possible in the past, because of the heavy weight of thermal engines to be mounted at the wing tip arising substantial aero-elastic concerns. With the advent of light electric motors, this solution seems now feasible and potentially advantageous.

As depicted in Figure 1.2, the following macro-elements are common to the selected PE, serial THE and FCHE architectures:

- Energy storage: fuel, batteries and/or supercapacitors.
- Power Generation System (PGS): all the elements capable of generating electrical energy to feed the motors. Usually the PGS involves either a fuel cell system or a thermal engine coupled with an electric generator.
- Power Management Control and Delivery (PMCD): the PMCD is a complex module, made up by multiple elements (regulators, buck-boost converters, power electronic devices, high-power and low-power bus, fault current limiters, etc.) necessary for the correct operation of the various power-train electrical system. Particularly, the PMCD has the ability to allocate the energy flows from the systems for energy storage and power generation. The PMCD has access to the state parameters of all the modules, in order to apply predefined logics for the control of power flows on the basis of such measurements.
- Electric drive: the combination of electric motors and controllers necessary for their use.

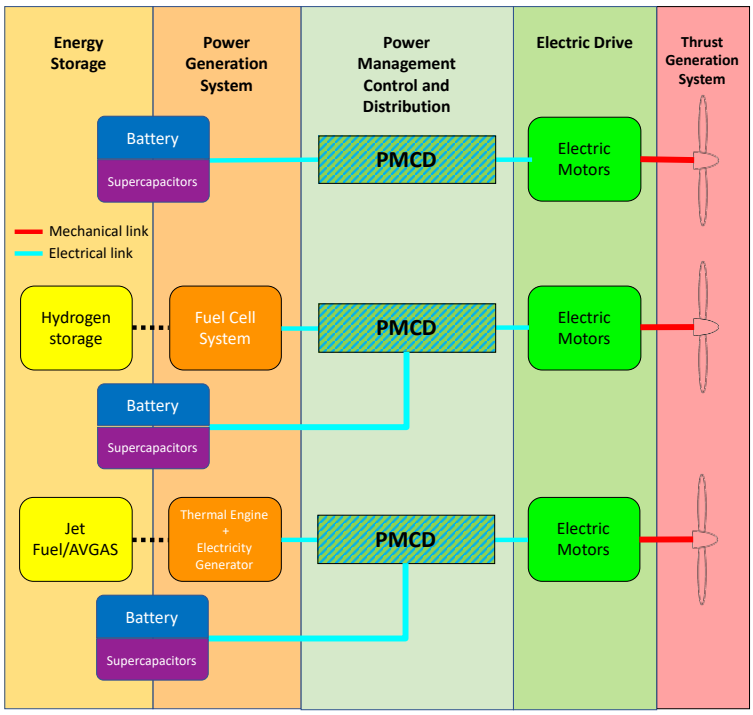

Figure 1.2: *Schematics of selected power-trains (top: pure-electric, middle: fuel cell hybrid-electric, bottom: serial thermal hybrid-electric).*

- Thrust Generation System (TGS): this includes devices used to produce thrust, that are mechanically moved by the electric motors, i.e. propellers and/or ducted fans.

Chapter 2 provides a detailed description of the state of the art of many building blocks of these power-train macro-elements, namely: battery, supercapacitors, hydrogen storage systems, fuel cells and electric motors.

1.2 Scenario studies

Towards the understanding, applicability and profitability of novel electric-powered aircraft, it is crucial to perform a quantitative analysis of the air transport network they can support and assess the main changes that are required to the existing airport infrastructure.

Indeed, the existing airport framework was not designed for supporting the operations of this new type of aircraft. Therefore, setting up an adequate ground infrastructure is necessary in view of a massive penetration of HE-based regional transportation. Particularly, battery charging infrastructures will play a paramount role, given the need to support the timely recharge of large aircraft battery packs. This entails a need for an increased electric power supply in the reconfiguration of an existing airport. Therefore, the price of electric energy, or the ability to produce it on site, will represent a major cost to be taken into account, in addition to the acquisition and maintenance costs of the chargers and possible adaptations to the airport grid.

The airport infrastructure will be impacted also by the transition towards hydrogen-fuelled flights [14]. The entire hydrogen supply chain, from the production to storage and distribution, should be adapted to the existing and future airport network, exploiting what is already in place for other transport modes. There are many ways of producing hydrogen which bring to very different cost schemes and environmental impact. The steam methane reforming of natural gas is the most widely used and cheapest in the industry, but it has a net negative impact in terms of CO_2. The sustainable way of producing hydrogen (the so-called *green hydrogen*) is through electrolysis, but this process is the most expensive, both monetarily and energetically. On the other hand, *green hydrogen* can be produced locally and sustainably near airports, resorting to renewable energy sources, such as solar or wind power. If not produced locally, hydrogen must be transported to airports in gaseous or liquefied form by road (trailers), rail, and water or by pipelines. . Once at the airport, hydrogen must be stored in one of the following ways:

- as gas inside storage pressure vessels,
- as a compressed supercritical fluid,
- as a liquid in cryogenic tanks,
- in materials based H_2 storage systems, or
- as slush hydrogen (solid state) [15].

Hydrogen refuelling points should be put in place together with safety and monitoring equipment.

Finally, the interest in serial THE propulsion for future airplane lies also in the ability of this architecture to allow a PE flight mode, for example during terminal manoeuvrers, thus greatly reducing the chemical and acoustic footprint of departure and arrival operations. In general, HE aircraft allow reducing the power of the fuel-burning component, which does not need to support the total power requirement for the flight. Despite these evident advantages, a methodology to quantify the noise and gaseous emissions of this novel type of power-train has not been identified yet. Therefore, a contribution in this direction would represent a fundamental step towards the assessment of the potential contribution of HE aircraft to a greener aviation global scenario.

1.3 Research framework: the MAHEPA and UNIFIER19 projects

As anticipated in the Introduction, this thesis is framed within the MAHEPA project. The MAHEPA project is a four-year research effort funded in the EU's Horizon 2020 programme, ending in mid-2021. Within the project, HE technologies have been brought to a high Technology Readiness Level (TRL) by developing a thermal hybrid-electric power-train and a hydrogen-driven fuel cell power-train for two 4-seater aircraft, from initial design to flight testing [16].

The first aircraft is the HE version of the conventionally-powered Panthera, featuring a cutting edge serial THE power-train: the Panthera Hybrid. The propeller of the Panthera Hybrid is driven by an electric motor powered by a traditional turbocharged internal combustion engine (Rotax 915 with a power output of 104 kW) and a battery system consisting of two parallel battery packs fitted in the wing. A picture of this beautiful airplane is shown in Figure 1.3. The Panthera Hybrid is currently in an advanced state of development, with the maiden flight expected in early 2021.

Figure 1.3: *Picture of the Pipistrel Panthera Hybrid.*

The second aircraft is an hydrogen-driven double-fuselage aircraft, built starting from the airframe of Pipistrel Taurus motor glider: the HY4. The FCHE system composed by fuel cell stacks and batteries supplies the maximum power of 90 kW required during the flight to the electric motor. Hydrogen tanks and batteries are positioned in the fuselages behind the occupant seats, while the fuel cell system is located right behind the electric motor, inside the pot at the center of the mid-wing section. The HY4 has successfully flown at the end of 2020. Figure 1.4 portrays the peculiar shape of this airplane.

In addition to the design, development and testing of the new modular HE power-trains, the MAHEPA project involves a substantial research effort towards the possibility to extend the developed technologies to commercial aviation and the effects of a future fleet switching from conventionally-powered to HE regional airliners. The Department of Aerospace Science and Technology at Politecnico di Milano is strongly involved in two work packages of the MAHEPA project related to such research activities:

- Scalability studies (WP9): among HE configurations, a need arises for the availability of methods capable to support the conceptual/preliminary design and analysis of HE vehicles, departing from traditional procedures for conventionally-driven aircraft that cannot be immediately extended to electric-powered realizations. A thorough assessment of numerical predictions will be performed, based also on flight data coming from the Panthera Hybrid and HY4 flight test campaign. When a validated, reliable framework is established, a fundamental step forward is the extension of the technology from the

Figure 1.4: *Picture of the HY4.*

current light aircraft application to the conceptual design of a 19-seat commuter aircraft and a 70-seat regional liner, both specifically designed for a HE propulsion system. In this regard, the determination of scalability relations and parameters is crucial.

- Scenario studies (WP10): strategies for maximizing the impact of hybrid-electric aircraft on near-term, medium-term and long-term scenarios. The analysis performed in the HE aircraft design field, will enable to gather, analyse and compare in-flight performance and emission data to build prediction models and quantify the advantages and limitations of HE propulsion for the environment and for the market. Indeed, the MAHEPA project aims at defining the regulatory implications, airport infrastructure requirements and airspace procedural practices necessary with the introduction of HE aircraft and to give estimates on fleet switching and operating costs. There is a remarkable lack of information about this topic in the literature, little data being only available for terrestrial hybrid-electric applications.

On top of the knowledge acquired in project MAHEPA, another Clean Sky 2 funded project, UNIFIER19, guided the development of the present thesis.

The ultimate goal of UNIFIER19 (commUNIty FrIendly minilinER 19) is perform the conceptual design for a 19-passenger commuter with freight and passenger cabin configurations powered by a modular hybrid-electric power-train. This 19-passenger aircraft has been named the *miniliner*. The modular architecture of the propulsion system should allow the pro-

Figure 1.5: *MAHEPA logo.*

duction of a single airframe capable of handling several configurations of propellers, batteries and range-extending technologies, each customized to commercially effective zero emission operations on specific markets.

The design criteria for the miniliner will be gathered considering the European demand for mobility in at least two types of service [17, 18]:

- the *microfeeder* service: for the transfer of passengers to a major hub from scattered small aerodromes in the area surrounding it, to avoid longer and less comfortable car traveling
- the *intercity* service: *as easy as a bus*, aimed at linking small airports to each other through scheduled or on-demand services

Ultimately, the miniliner goal is creating an innovative environmentally sustainable zero emission air mobility solution for European communities, specially aimed at those that lack of adequate ground-based transport infrastructures.

Figure 1.6: *UNIFIER19 logo.*

The UNIFIER19 initiative not only focuses on the design of the miniliner, but is a detailed and creative plan that focuses on multiple aspects of the overall transportation system. Apart from aircraft design, this includes market studies, sustainability analysis and cost analysis, not only from the operating point of view, but also by considering in detail the underlying technological issues.

CHAPTER 2

TECHNOLOGY REVIEW

In this chapter, a technology review of the main PE and HE power-train components is reported. This review has the purpose of identifying the most important performance indicators of each component and what are the current and future predicted values of such indicators. Once assessed, the performance indicators will be used in the design exercises discussed in the next chapters, in reference to the current and future technological scenarios.

2.1 Battery

For PE or HE aircraft, batteries represent the source of all or part of the propulsive power. They are typically separated from the airframe load-bearing elements, being installed in dedicated bays or conformal to structural elements, in order to provide mass distribution advantages. Another, very advance type currently undergoing development is that of Structural Batteries (SBs), i.e. multifunctional composite materials that can store electric energy while contributing to withstanding loads. As such, they can be conceived as a part of the aircraft structure itself [19–21]. In the

following, we shall refer to non-structural batteries, given the low TRL value associated to SB technology. Battery research and development has surged in recent times, mainly due to the spread of electric vehicles [22–24]. The most common battery types on the market and/or in development today are:

- Lithium-ion Battery (LIB).
- Lithium Sulfur Batteries (LSBs).
- Lithium Air Batteries (LABs).

Batteries are usually compared and contrasted considering several parameters. Some of the most important are:

1. Specific energy: energy stored per mass unit (Wh/kg or J/kg), usually expressed in the charged state.
2. Specific power: available power output per mass unit (W/kg). Sometimes can be expressed in terms of C-Rate or rated power.
3. Energy density: the amount of energy stored per volume unit (Wh/l or J/l).
4. Cycle life: no. of full charge/discharge cycles that a battery can withstand before losing 20% of its original capacity.

Other important parameters are operating temperature range, maximum and optimal charging rate, calendar life, safety and cost. It is interesting to note that battery technology developments are not following trends such as Moore's law which postulates that the capacity of computers doubles every 18 months [25]: indeed, from 1950 to 1990 the specific energy of batteries has increased by 3 % per year. Since then the growing rate was about 5-8% per year [26].

2.1.1 Lithium-ion technology

The state of the art of modern electrochemistry for electric mobility applications is represented by LIBs [27–29]. LIBs are near an optimal performance and might reach their full potential on a shorter term than other battery types still in early development [30]. Many different kinds of LIBs exist, based on the cathode option, as shown in Table 2.1. The most common types are: Lithium Titanate Oxide (LTO) Lithium Iron Phosphate (LFP), Lithium Cobalt Oxide (LCO), Lithium Manganese Oxide (LMO), Lithium Nickel Cobalt Aluminum Oxide (NCA) and Lithium Nickel Manganese Cobalt Oxide (NMC).

Table 2.1: *Common cathode options for Li-ion batteries. Data from [4, 31, 32].*

Li-ion type	Specific energy [Wh/kg]		C-Rate [1/h]		Voltage [V]	Energy density [Wh/l]
	Actual	Theo.	Chg	Dhg	Nom.	
LTO	80	420	5	10-30(peak)	2.4	177
LFP	120	580	1	25	3.4	292
LCO	140	600	1	1	3.8	380
LMO	200	470	1	10-30(peak)	4.1	560
NCA	200	800	1	1	3.7	380
NMC	350	700	1	2	3.7	390

Currently, commercially available batteries with the highest specific energy use NCA or NMC, such as the Panasonic NCR18650A or 2170 cells in current Tesla battery packs [33]. One of the biggest drawbacks of some LIBs is the intensive use of cobalt and nickel, which are at a premium and usually come from countries with disputable mining ethics [34]. Commercially widespread LIBs, show a specific energy of about 250 Wh/kg at cell level, see Figure 2.1. In 2020, the LIB specific energy was around 300 Wh/kg, at a cell level. Values of 400 Wh/kg and 500 Wh/kg are considered attainable by 2025 and 2030 according to [26]. However, due to physical and chemical limitations, LIBs will soon reach their ceiling in specific energy values. Considering a packing efficiency between 65-80 % [4], a specific energy density of 350 Wh/kg is the expected full potential for this type of batteries at battery level [12], which is still two orders of magnitude lower than kerosene or jet fuel.

On the other hand, according to BloombergNEF results[1], lithium-ion battery packs cost plummeted from 650 $/kWh in 2013 to 176 $/kWh in 2018, following an exponential trend as reported in Figure 2.2.

For what concerns battery life (usually intended as the number of cycles before battery gets to 80% of its rated capacity), values ranging between 1,500-2,500 cycles are common [33], but recent tests showed that LIBs can get up to 5,000 cycles, claiming life ranges for cars in the order of millions of kilometres (Figure 2.3) [36].

2.1.2 Lithium sulfur technology

Lithium Sulfur Batteries feature lithium at the anode coupled with sulfur at the cathode to generate high energy density. LSBs are the most

[1] https://about.bnef.com/blog/behind-scenes-take-lithium-ion-battery-prices/

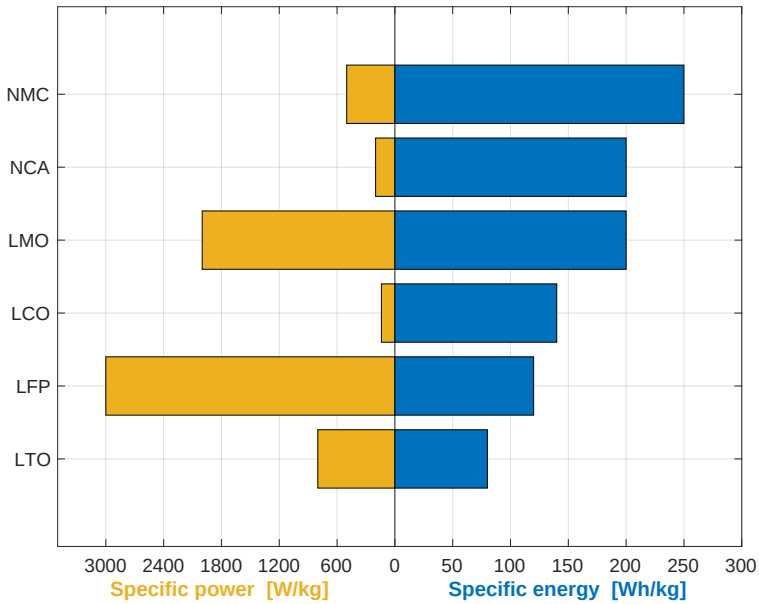

Figure 2.1: *Typical specific energy and specific power of lithium-ion batteries.*

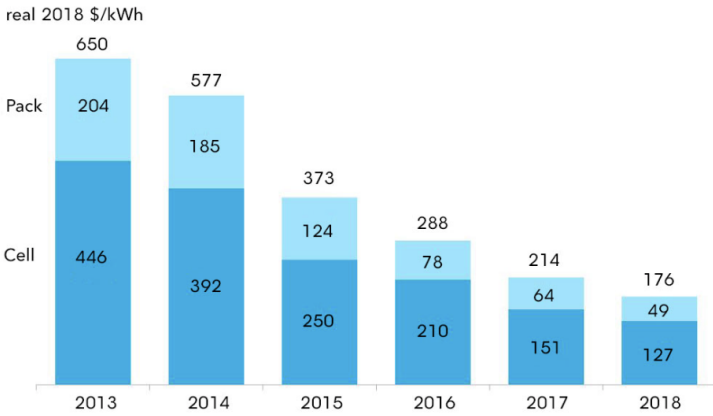

Figure 2.2: *LIB price survey [35]*

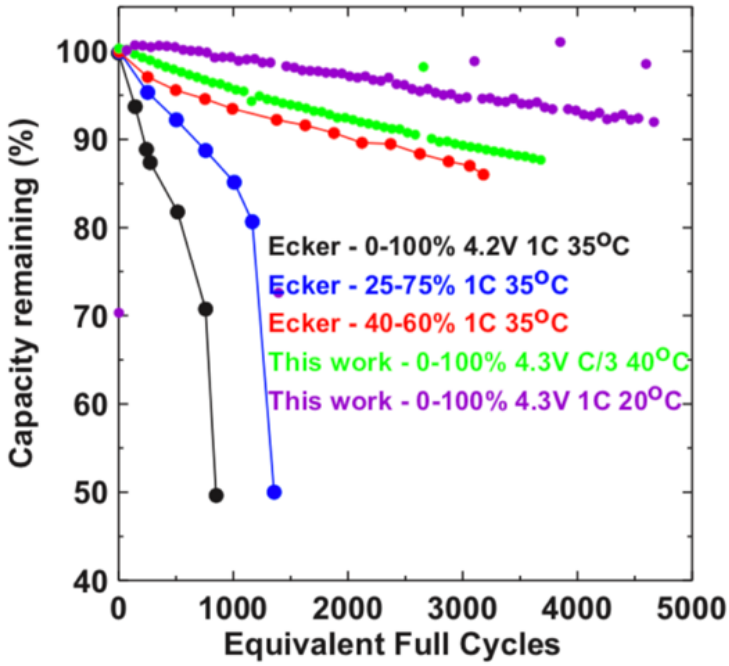

Figure 2.3: *Residual capacity with discharge cycles for LIBs [36].*

promising low-cost, high-capacity energy storage device available due to their high charge-storage capacity, and the wide availability of low cost sulfur. Sulfur is naturally abundant and therefore cheap, but the use of lithium-metal anode may soon be a problem due to the limited availability of lithium sources. An extensive review tailored for aeronautical applications of this technology can be found in [4, 12, 37–39]. The theoretical specific energy of LSBs is 2,567 Wh/kg but they have a low open circuit voltage of 2.1 V, compared to 4.1 of Li-ion. LSBs have also lower power rate when compared to LIBs [4]. A number of companies have the manufacturing capability to produce large capacity LSB cells featuring more than 300 Wh/kg in specific energy. Examples could be the American SionPower (500 Wh/kg [40]), OxisEnergy [41] and works on developing batteries with 1,000 Wh/kg from Innolith [42] that is predicted to be available for industrial use between 2025 and 2030. The Global Lithium-Sulfur Battery Market [43] says that the global LSB market could grow of 71% during the period 2018-2022. High performance cannot be maintained over long periods of time as the cycle lives and stability of current LSB cells are not competitive with the current-day lithium-ion technology (500-1,000 cycles vs 2,500 cycles, respectively). LSBs also have a lower energy density than LIBs due to the use of sulfur cathode (700Wh/l vs

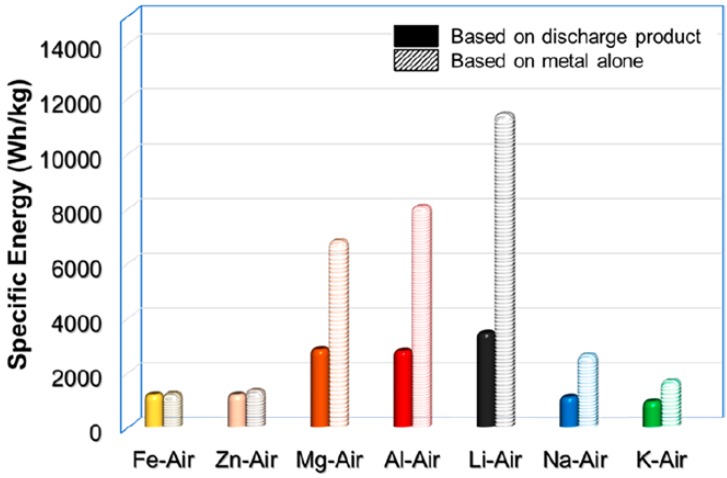

Figure 2.4: *Theoretical specific energy of metal air batteries [27].*

450 Wh/l), which naturally has a low density compared to LIB materials. In [37] it is pointed out that LSB cells may be most appropriate for applications where minimizing the mass is more important than the volume, and therefore powering electric heavy-duty vehicles, aerial vehicles, high altitude aeronautical vehicles, and energy-storage plants.

2.1.3 Lithium air technology

Lithium Air Batteries fall into the wider class of Metal Air Batteries (MABs). Several MABs using alkali metals (Li, Na, and K), alkaline earth metal (Mg), and first-row transition metals (Fe, Zn) or Al as the anode have been investigated and their theoretical specific energies are presented in Figure 2.4 [27]. LAB is composed of metallic lithium as the anode, and oxygen as the cathode. The theoretical specific energy is around 115,000 Wh/kg or 3,500 Wh/kg depending on the inclusion of the oxygen in the calculation. LABs might deliver the required step-change in the battery market. Initial LAB systems required an air feed system with a compressor, as well as air filters and dehumidifiers to get rid of moisture on the oxygen side [44]. Additionally, capacity fading was present, strongly dependent on the purity of oxygen. However, LAB has been transformed over the last six years with the introduction of redox mediators and Li anode protections. Now, significant quantities of water can be tolerated, alleviating the need for heavy, complex and bulky air handling. Considering these recent advances, [27] predicts the specific energy and the energy (volumetric) density of a full air battery, including the balance of plant, to be 610 Wh/kg and 680 Wh/l respectively, without specifying a pre-

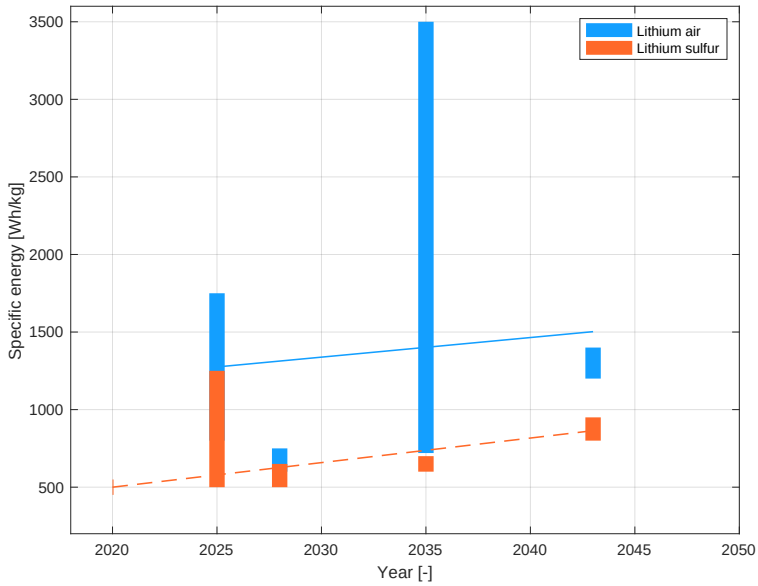

Figure 2.5: *Specific energy of future battery technologies at cell level.*

cise time frame. Other authors speculated differently as reported in [12]. Figure 2.5 tries to summarise in a graphical way all the speculations on future battery specific energy with a bar plot, and the level of uncertainty is very high also for a short time horizon. The LAB depicted in Figure 2.6 by Samsung [45] proved a performance of 1,214 Wh/kg and 896 Wh/l at cell level.

2.1.4 Metal-S, Metal-ion and Metal-air

Based on the development and progress achieved with LSBs, and due to the rising price and scarcity of lithium on the planet, researchers have explored a broad range of metal-sulfur batteries, metal-air batteries and metal-ion batteries. In general, these are referred to as Metal-X Batteries (MXBs). Metallic anodes examples are sodium, potassium, magnesium. MXBs have all high theoretical capacity and low material cost. However, MXBs also face similar challenges as LSBs and LABs with regard to stability, number of cycles, and corrosion of the metallic anodes. MXBs are actively being researched in [28, 37, 44–48].

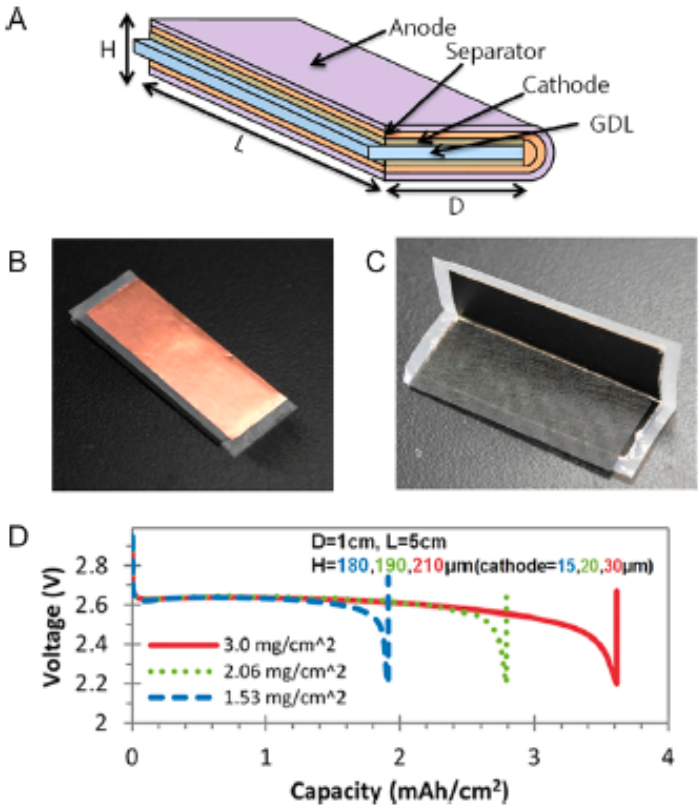

Figure 2.6: *(A) Schematic, (B,C) images, and (D) discharge curves of a single folded cell [45].*

2.2 Supercapacitors

Supercapacitors are electronic devices which derive from conventional capacitors. They are called supercapacitors as they are able to store a large amount of electric energy. A supercapacitor consists of two electrodes with a solid or liquid electrolyte in the middle. The thickness of the electric double layer is around 1 nm. Usual materials employed for the manufacturing of the electrodes are nano-structured carbon applied on an aluminium foil as a current collector. Analogously to battery cells, supercapacitor cases are usually cylindrical or prismatic (pouch) [49]. Much attention is being payed to supercapacitors as they are very efficient and can be rapidly charged and discharged at extremely high power. Moreover, they feature a high cycle life and are considered safe. As for batteries, the main performance parameters for supercapacitors is represented by

- Specific energy (Wh/kg).
- Energy density (Wh/l).

Supercapacitors have higher specific energy than conventional capacitors, but less than batteries (e.g. 10 Wh/kg, compared to 200-250 Wh/kg for LIBs). On the other hand, they can deliver energy much faster. For instance, current specific power values are 5 to 10 times bigger than the batteries (10 kW/kg vs 1-2 kW/kg). This enables rapid charge and discharge, which is ideal if a sudden burst of power is required. The calendar life of supercapacitors can be over 15 years, compared to approximately five years for batteries. Research is currently under way worldwide to improve the specific energy of supercapacitors without losing their high specific power [50, 51]. Yunasko [52], an energy storage company based in Ukraine, has reported working towards marketing a 30-40 Wh/kg hybrid battery-supercapacitor while retaining the power density at 3-5 kW/kg with an efficiency of 80%. Research at universities aims to increase the specific energy of supercapacitors on a laboratory scale as well. Reported numbers for specific energy range from 50 to 150 Wh/kg. Such result is based on studies on a laboratory scale and must be proven on a manufacturing scale. Graphene and carbon nanotubes seem to lie at the root of these improvements [47]. A recent supercapacitor breakthrough was reported by start-up company Superdielectrics, Ltd., which has developed a novel polymeric material [53]. The new polymer delivers largely higher capacitance than usual supercapacitor materials and could potentially actualize energy densities of up to 180 Wh/kg. Rolls-Royce is working together with Superdielectrics on these topics [54]. A supercapacitor with high specific power and reasonable specific energy (50–100 Wh/kg), could

be employed during power intense flight phases, possibly helping in the use of smaller batteries

2.3 Fuel cells

Fuel Cells are similar to batteries, but the reactants are stored outside the cell. FC operation is based on a redox reaction that takes place in two separate, but electrically connected, anode and cathode. As usual, oxidation happens in the anode and reduction in the cathode. When operating with pure hydrogen, H_2 molecules are oxidized at the anode and lose two electrons which feed the electric load. At the same time, hydrogen ions (H^+) travel through the electrolyte, closing the circuit. O_2 is reduced at the cathode producing, in this case, just water. FCs can be fed also with compounds containing hydrogen, such methane, methanol or ethanol. In this case emissions are not only water, but also carbon compounds (i.e. CO and CO_2) [55].

It should be noted that FCs are not energy storage devices, but electric power generation devices. Energy is stored in the hydrogen fuel contained in an external tank, while the oxygen is normally present in the ambient air. This differs from batteries, where the device operates at the same time as an energy storage system and a power generation device.

Two types of FCs are mostly used: the Solid Oxide Fuel Cell (SOFC) and the Proton Exchange Membrane Fuel Cell (PEMFC) [56–58]. The former uses solid ceramic oxide as electrolyte and works at high temperatures (800-1000°C). SOFCs are usually used for stationary applications, due to their heavy weight, slow start up time (in the order of hours) and fragile nature of the ceramic materials. PEMFCs have proven to be the most successful commercially, especially for mobility applications. [59–61]. The PEMFC runs at relatively low temperatures (70-80°C). The performance of the PEMFC is highly sensitive to impurities, such as carbon monoxide and sulphur, which are produced during the reforming of hydrocarbon-based fuel to hydrogen. Therefore, pure hydrogen is the preferred fuel choice for the PEMFC [47]. Single FCs are connected in series in order to reach the desired voltage value, creating a subsystem called stack. Different stacks can be connected in parallel and the resulting current is the sum of each stack current. A complete FC system includes one or multiple stacks, as well as balance of plant equipment, such as heat exchangers, pressure regulators, water management systems and possibly air compressors to eventually pressurize oxygen. Further details about FCs can be found in the textbooks [55, 62] where it is outlined that performance of

aFCsystem can be evaluated trough some key figures of merits:

- Specific power (kW/kg).
- Cost per power unit ($/kW or €/kW).
- Lifetime: usually given as the loss of the cell voltage per 1000 h, as electrodes and the electrolyte gradually deteriorate. The FC life is declared over when it can no longer deliver the rated power.
- Efficiency: electrical energy delivered by the system compared with the energy supplied as fuel.

PEMFC efficiency ranges between 50% and 60%, as discussed in Chapter 3. For what concerns specific power, DOE Technical Targets for Fuel Cell Systems and Stacks for Transportation Applications [63] specifies that the specific power of current state of the art FC system (including balance of plant: compressor, stack modules, cooling system) ranges between 0.6 and 1 kW/kg. Developmental PEMFC systems have specific power in the order of 1.6 kW/kg at system level. However, increasing the power density of the PEMFC is not the current focus of development efforts for automotive and ground power applications. Instead, the emphasis today is on reducing costs, decreasing platinum loading, and increasing life [47]. It is estimated that specific power may be improved up to 8 kW/kg only by optimizing current FCs for aviation applications [60]. The power density of existing PEMFC systems oscillates around 0.6 - 1 kW/l. Current costs at system level are around 45 $/kW. However, this figure is expected to drop as production of PEMFCs for middle to heavy ground transport application will ramp up. For what concerns lifetime, US DOE found that service life of FCs for automotive applications was around 2,500 hours (corresponding to about 120,700 km) in 2015 [63]. In 2018, [62] claimed that the service life had increased to more than 20,000 or even 100,000 h in stationary energy storage applications. The lifetime improvement has occurred since the mechanisms of cell depletion have become more known and can be safeguarded.

2.4 Hydrogen storage

Hydrogen is present on Earth only in the form of compounds with other elements, unlike oxygen or nitrogen that are commonly present in the atmosphere at a molecular level. When separated from these compounds, being the lightest element of the periodic table, it naturally rises and dissipates. Hydrogen is indeed a very light element and is gaseous at ambient temperature, which implies some difficulties in storing it efficiently. The

storage of hydrogen is the most difficult challenge associated with hydrogen economy [64, 65]. According to [56], the main quantities to assess the goodness of a storage device are:

- Gravimetric density or gravimetric index: usually the ratio between the fuel mass and the total storage + fuel mass.
- Volumetric density: same as gravimetric density, but for volumes, (Wh/l).
- Operating temperature.
- Operating pressure.
- Cost.

Hydrogen storage methods can be divided in physical and chemical methods as illustrated in Figure 2.8

As testified by the rise in the number of technical reports and regulation guidelines, hydrogen usage on airplane is moving from successful isolated experiments on small aircraft, to larger applications [66, 67]. Types of hydrogen storage system exist which involve chemical absorption of hydrogen in other materials [68, 69]. Although many of them might seem appealing, they are at a very early development stage and not suited for application with PEMFC. Therefore, only physical storage systems are illustrated hereafter.

2.4.1 Gaseous hydrogen

Gaseous Hydrogen (GH2) tanks are the current industry standard for mobility applications. Several engineering and regulation standards are already in place, to detail the production and testing of this type of storage. An extensive review of these Regulations, Codes and Standards is reported in [70]. GH2 pressure for mobility applications typically ranges between 20 and 70 MPa. The trend in the transportation field is to use a pressure storage value of 70 MPa [69]. There are four main types of hydrogen pressure vessels Figure 2.7 Most of FC-driven cars use GH2 carbon-fibre Type IV tanks that are pressurized at a global standard of 70 MPa. Some public transport applications use 35 MPa composite tanks since gravimetric density is less important in larger vehicles. Composite fibres are usually assembled using filament winding. However, a public concern exists because of such high pressure (70MPa). Moreover, the hydrogen compression can use up to 20% of the energy content. Future outlook of compressed hydrogen storage in terms of gravimetric density is still unclear. More attention is being payed to safety, cost reduction and

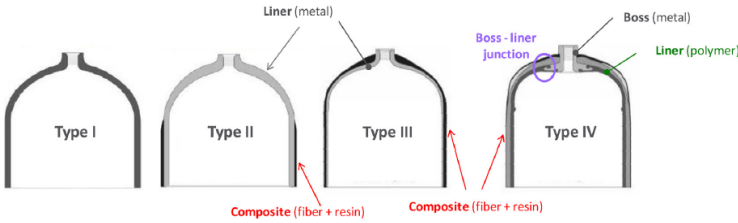

Figure 2.7: *Hydrogen pressure vessel types [71].*

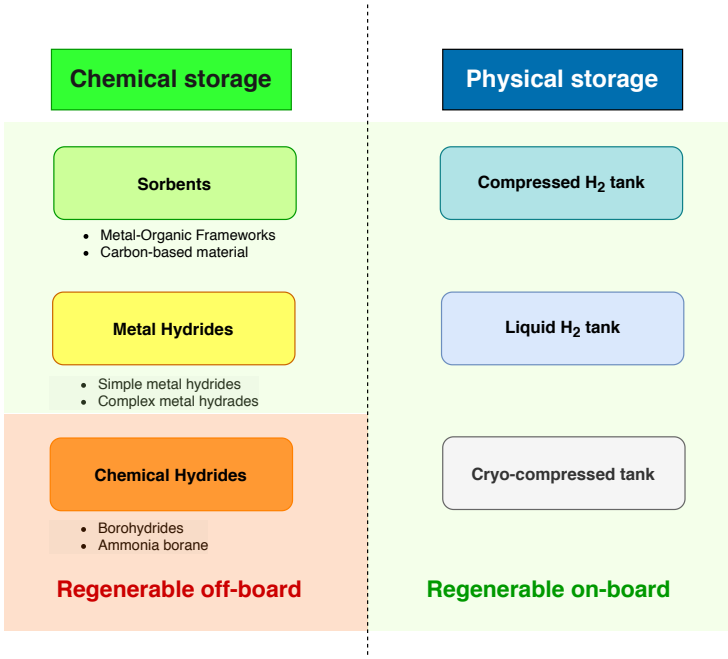

Figure 2.8: *Overview of possible hydrogen storage methods.*

operation optimization. Refuelling current compressed gaseous hydrogen tanks takes no more than 5 min, which is comparable to gasoline [65, 69, 72–75].

2.4.2 Liquid hydrogen

Hydrogen liquefies at -253°C or 20 K at atmospheric pressure, therefore, a LH2 tank must be designed to minimize heat transfer through its walls. However, zero heat transfer is not possible, so, in order to avoid pressure increase inside the tank, a relief valve is added, usually called the boil-off valve. This valve lets expanded hydrogen escape. The best shape for a LH2 tank is the one that maximises volume to surface area ratio, i.e. a sphere. This shape minimizes the heat transfer, main responsible for the boil-off effect. Of course, this shape is not particularly suitable for aeronautical application. LH2 storage has been extensively used for industrial and space applications and has improved significantly in the last years, achieving the best gravimetric density (15%) among other hydrogen storage systems [65, 66, 76, 77]. The cost of hydrogen liquefaction is significant, both in terms of energy and equipment, resulting in a 40 % energy loss. However, LH2 storage is strongly temperature-dependent and implies the addition of a heat management system which adds cost, complexity, and mass. Liquid hydrogen tanks do not have to withstand high pressure, but they must be heavily insulated, which results in reservoirs with thick walls. The costs associated with hydrogen liquefaction can reach 1.00 $/kg [68].

Apart from some historical experimental campaigns ([78–81]) and one practical application on an experimental UAV [82], some recent works are found, at a conceptual design level, on LH2 tanks for transport aircraft in [83–86]. These studies focus on the entire design process of the LH2 tank, including the effect of heat leakage during the flight mission and the boil-off losses. The sizing is specifically tailored for transport aircraft and is done taking into account the outgoing mass flow rate of hydrogen that has to feed the FCs/thermal engine and optimizing the tank design for the flight profile. The resulting gravimetric index of the cryogenic tank can range between 60 and 75 % with very small boil-off losses. This result seems very promising for future aircraft applications. One example of the peculiar cabin layout featuring LH2 integral tanks fitted in the semi-monocoque fuselage structure is shown in Figure 2.9.

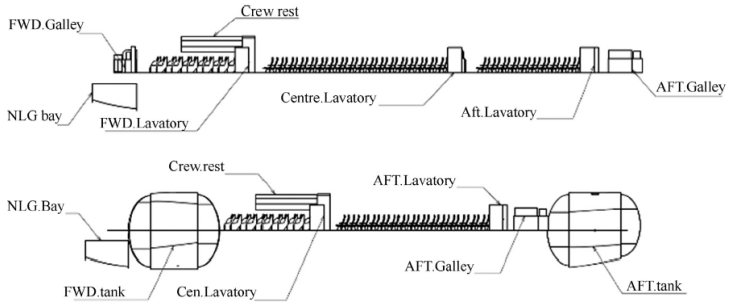

Figure 2.9: *Changes in cabin layout due to integration of LH2 tanks [83].*

2.4.3 Cryo-compressed hydrogen

Since LH2 storage requires a certain level of complexity and a careful heat management system to handle very low temperatures, it might be impractical for small-scale use in mobility applications. A possible workaround is to store hydrogen in liquid form, but under pressure. This process is commonly called cryo-compression. Smaller internal pressure than GH2 allows for lesser strength material, less expensive composites and cheaper metals. The boil-off problem is extremely limited, with a record of 0% losses within a week duration [56]. References [87, 88] report that Cryo-compressed hydrogen (CCH2) turned out to be the most attractive hydrogen storage method for what concerns overall energy efficiency and global well-to-wheel cost, even though this system had the highest energy use, hydrogen cost and GreenHouse Gas (GHG) emissions.GHG emissions are particularly high, mainly due to the significant amount of energy to convert gaseous hydrogen into a liquid state. This drawback affects also LH2 storage. However, GHG emissions are largely dictated by the method used to produce the hydrogen. Currently, limited development has been made for onboard liquid hydrogen fuel tanks for automotive use [56, 89].

2.5 Electric drive system

Regardless of the chosen power-train architecture, another key component is represented by Electric Motors and their controllers. There are several types of Electric Motor (EM). A good summary of the most used types in aeronautical applications is reported in [10]. Usually EMs are coupled with a controller or converter. For instance, brushless DC motors need a converter to provide electricity to the windings with the correct phase.

Aeronautical propulsive applications of EMs are found in some general

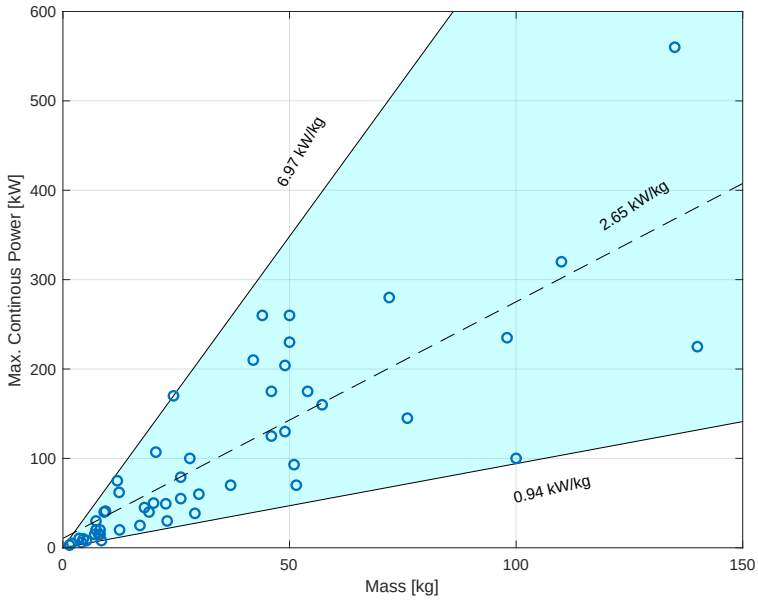

Figure 2.10: *Maximum continuous power vs. mass of existing EMs for aeronautical applications. The full database is in Appendix A.*

aviation and ultralight aircraft [10]. The main motor manufacturers today are Siemens (whose electric aircraft division has been sold to Rolls Royce), Compact Dynamics, EMRAX and YUNEEC International. EMs are usually much simpler and durable than thermal engines, allowing for scalability, working well for both small and big applications. Aircraft EMs must be designed with a special focus on safety and redundancy. Apart from this, three quantities are usually named as performance indicators when comparing different EMs:

- Specific power [kW/kg].
- Overrating: the amount of extra power, with respect to maximum continous power, that can be drawn for limited period of time.
- Efficiency.

Current values of specific power for aeronautical applications have been obtained from a survey on existing EMs, illustrated in Figure 2.10. The vast majority of EMs feature very small power ratings, and are not used for propulsive applications. However, there are examples of EMs with specific power up to 7 kW/kg. NASA [90] claims that EMs with specific power of 13.2 kW/kg and efficiency greater than 96% as well as power converters with 19 kW/kg and efficiency greater than 98% will be attainable by 2030.

Several research programmes have addressed both cryogenic and ambient

temperature conducting electric technologies for EMs [91]. Superconducting systems can achieve superior performance with lower heat waste and are conceived for the megawatt class. A superconducting system features peculiar zero-resistance conductors, but this property vanishes at ambient temperature. Therefore, liquid nitrogen is usually employed to control the temperature. It is immediate to reckon the possibility of using LH2 instead. In fact, hydrogen must be heated up before entering the FCs and the EMs must be cooled down. This would be a win-win solution. However, in [92] NASA envisages that cryogenic systems would not be ready for the operation on an aircraft in the mid-term due to the lower development of cryogenic superconductors. Furthermore, the National Academies of Sciences, Engineering and Medicine is even more cautious, hypothesizing a shy value of 9 kW/kg for the specific power of MW-order EMs in the next 20 years [93]. Predictions in [94] lay in the middle, considering specific power in the range of 13-16 kW/kg for the electrical machine and 10-19 kW/kg for the power converters of a turbo electric 150-seat aircraft.

CHAPTER 3

INNOVATIVE AIRCRAFT MODELLING FOR DESIGN AND ANALYSIS

This chapter illustrates modelling techniques for the performance evaluation and sizing of some of the most important and innovative power-train components, namely:

- Battery.
- Fuel cell.
- Hydrogen tank.
- Electric motor.
- Thermal engine.

The purpose is to detail some of the modelling techniques that will be applied in the following chapters for aircraft preliminary sizing and conceptual design. For some of these components, such as the battery and electric motors, multiple modelling approaches with different level of detail are illustrated and compared, in order to understand the applicability

to design applications. Secondly, an aero-propulsive interaction model is adopted from literature in order to simulate the effect that DEP has on the wing aerodynamics. This model is reframed for the sake of aircraft design and is included in the assessment of the SMP for the determination of the wing and power loading.

A part of the work presented was developed with the contribution of the following MSc students in the frame of their thesis project: Gabriele Poiana (ICE-hybrid power-train modelling), Davide Comincini (fuel cell modelling), Luis Miguel Chacha Guevara (hydrogen tank modelling), Andrea Matrone (DEP modelling).

3.1 Battery

The battery is one of the most critical component to be sized and modelled as it must safely feed EMs and store energy for the full flight mission or important parts of it. Its inherent weight inevitably implies a significant effect on the overall aircraft sizing. A BP is usually formed by battery cells connected in series and/or parallel to achieve desired current and voltage levels. A Battery Management System (BMS) must be added, as it provides control of battery parameters to prevent any possible over/under voltage, over temperature, over current and other possible dangerous events. Good BMS design is critical to get a fail safe battery.

Multiple ways of modelling battery performance are found in the literature, at various levels of detail. Examples are:

1. Electrochemical-thermal models.
2. Electric-circuit based models
3. Energy-in-the-box models.

Electrochemical-thermal models Electrochemical-thermal modelling implies the specification of mass and charge conservation equations in various regions of the battery cell. This requires a detailed knowledge of battery chemistry and is useful when a special focus on internal battery elements is necessary [95]. Therefore, a detailed electrochemical-thermal model is outside the scope of this work.

Electric-circuit based models Electric-circuit based models are the most commonly employed in engineering applications. Part of the power produced during the electrochemical reaction within a battery is lost in the

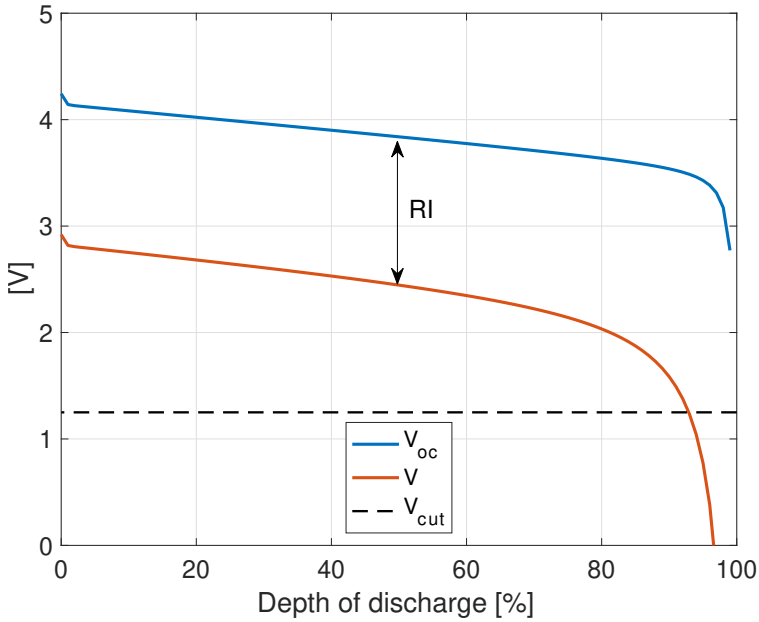

Figure 3.1: *Discharge curve of LIB cell.*

process. A common way to model this behaviour is representing the battery as a lumped resistance and voltage source [96]. The battery output voltage V is

$$V = V_{oc}(c) - R(c)I \tag{3.1}$$

whereas the battery output power P_b is

$$P_b = VI. \tag{3.2}$$

In the previous equations, V_{oc} is the open-circuit voltage, i.e. the voltage that the battery would provide in the absence of current, R, the internal resistance of the battery, I the current and V the output voltage. Both V_{oc} and R depend heavily on the battery chemistry and on the battery State Of Charge (SOC) c. Power is mainly lost due to ohmic, activation and concentration losses. Figure 3.1 plots the voltage curve of an LIB cell [4]. The blue line represents the open circuit voltage, while the orange line is the resulting battery output voltage V including the voltage drop RI in the resistance. However, the battery voltage V cannot drop below a certain cutoff voltage V_{cut}, (dashed line) as it would damage the battery chemistry. This poses a clear limit to the maximum current I_{max} (and therefore maximum C-Rate, defined as the ratio I_{max}/C, where C is the battery capacity in Ah) that can be drained from a battery:

$$I_{max}(c) = \frac{V_{oc}(c) - V_{cut}(c)}{R(c)}. \tag{3.3}$$

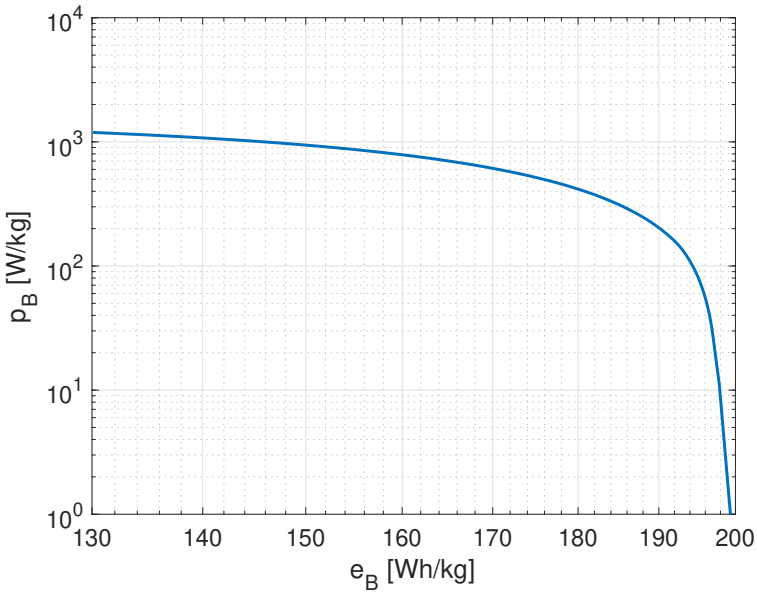

Figure 3.2: *Ragone plot of LIB cell with* $p_b = 1200$ *W/kg and* $e_b = 200$ *Wh/kg*

This effect is reversed when charging the battery: there is a limit charging current, so as the battery peak voltage V_{peak} is not exceeded. Unfortunately, the maximum discharging/charging C-Rate depends on the battery SOC. There is no notional value of the SOC to be used in defining the nominal C-rate. The most common choices are 50% or 80% state of charge [97].

As a consequence of the internal resistance, battery capacity decreases depending on the current it is presently providing. This effect can be shown by time integrating a range of power values to find the amount of available energy, using the battery discharge curve. This leads to the well-known Ragone plot [98], shown in Figure 3.2. The battery specific power p_b, on the y axis, is plotted against the specific energy e_b. The Ragone plot graphically illustrates that is not possible to use the entire stored energy of the battery at full power.

In [4, 99, 100] it is shown that it is possible to use a simplified electric-circuit model (where R and V_{oc} depend only on SOC) for aircraft conceptual design, simply knowing specific points of the open circuit discharge curve or using experimentally derived functions for the open circuit voltage and internal resistance.

Energy in the box models An *energy-in-the-box* approach simplifies the dependency of open-circuit voltage on SOC, assuming a constant nominal

value. Losses are accounted for with charging (η_B^c) and discharging efficiencies (η_B^d) and maximum charging/discharging C-Rates can be set. In this case, the total amount of battery energy is

$$E_B \geq \int_0^{t_f} \dot{E}_B(t)dt \tag{3.4}$$

where

$$\dot{E}_B = \frac{P_B^{out}(t)}{\eta_B^d} - \eta_B^c P_B^{in}(t). \tag{3.5}$$

The term P_B^{out} is the discharging battery power and P_B^{in} is the charging battery power. Although very simplistic, this method is particularly suitable for aircraft preliminary sizing exercises where battery technology is often not yet defined and assumptions on the battery discharge curve cannot be made.

For what concerns mass sizing, battery mass is sized by two parameters: the maximum battery power and the battery stored energy. To represent this interaction, the battery mass is given by

$$M_B \geq \max\left(\frac{P_{BMax}}{p_B}, \frac{E_B}{e_B}\right) \tag{3.6}$$

where P_{BMax} is the maximum battery power.

3.2 Fuel Cell

The considered FC type is the Proton Exchange Membrane (PEM), which is the most suited for transport application. Hydrogen enters the FCs in gaseous form, and the air flow necessary for the redox reaction may be compressed using a compressor, which acts as an auxiliary system. The proposed modelling of the FC system is based on its inner physics and specifically on the polarization curve that relates current density input i to the voltage output V [101]. The current density of the cell, is defined as the ratio between the current I_{cell} and the cell area A_{cell}.

3.2.1 Polarization curve

The polarization curve $V(i)$ is described as

$$V(i) = V^- - \underbrace{\frac{R\,T_{FC}}{\alpha\,F}\,\ln\left(\frac{i}{i_0}\right)}_{\text{activation loss}} - \underbrace{\frac{R\,T_{FC}}{\alpha\,F}\ln\left(A_{O2}\left(1-\frac{i}{i_{lim}}\right)\right)}_{\text{concentration loss}} - \underbrace{\frac{\delta_m}{\sigma_m}\,i}_{\text{ohmic loss}} \tag{3.7}$$

where three types of losses decrease the anode voltage of the FC, V:

- activation loss,
- concentration loss,
- ohmic loss.

In Equation (3.7), the symbols R and F recur multiple times and indicate the universal gas constant and the Faraday constant respectively

$$R = 8.314 \, \frac{\mathrm{J}}{\mathrm{mol\,K}}, \qquad F = 96\,485 \, \frac{\mathrm{C}}{\mathrm{mol}}. \tag{3.8}$$

Also, $\alpha = 0.8$ is the charge transfer coefficient of hydrogen and T_{FC} is the operating temperature of the cell.

The anode voltage V^- is given by

$$V^- = \frac{R\,T_{FC}}{2\,F} \, \ln\left(A_{H_2}\right) \tag{3.9}$$

where

$$A_{H_2} = \frac{\mathcal{P}_{FC}}{R\,T_{FC}} \, \frac{y_{H_2}}{C_{ref}} \tag{3.10}$$

is the hydrogen activity. For ideal-like gases, the activity is the ratio between the operating pressure $\mathcal{P}_{FC}$ and a reference pressure $\mathcal{P}_{ref}$. Note that in case of unpressurized FCM, $\mathcal{P}_{FC}$, is not constant but changes according to the outside pressure. The term

$$C_{ref} = \frac{\mathcal{P}_{ref}}{R\;T_{ref}} \tag{3.11}$$

is the reference constant C_{ref}, estimated with a reference temperature $T_{ref} = 80\ ^\circ\mathrm{C} = 353\,\mathrm{K}$ and a reference pressure $\mathcal{P}_{ref} = 1\ \mathrm{atm} = 101\,325\,\mathrm{Pa}$. The hydrogen molar fraction y_{H_2} is (considering 100% relative humidity and 80°C)

$$y_{H_2} = 1 - \frac{0.47 \cdot 10^5}{\mathcal{P}_{FC}}. \tag{3.12}$$

The term i_o in the activation loss indicates the reaction exchange current density, which represents the reaction rate,

$$i_0 = 2 \cdot 10^{13} \, \frac{\mathrm{A}}{\mathrm{m}^2}. \tag{3.13}$$

In the concentration loss, A_{O_2} expresses the oxygen activity,

$$A_{O_2} = \frac{\mathcal{P}_{FC}}{R\,T_{FC}} \, \frac{y_{O_2}}{C_{ref}} \tag{3.14}$$

where y_{O_2} is the air oxygen molar fraction

$$y_{O_2} = 0.209. \tag{3.15}$$

To evaluate the limit current density in the cell i_{lim}, two parameters are defined with regard to the gas diffusion layer: the gas diffusion layer diffusivity

$$D_{GDL} = 0.05 \cdot 10^{-4} \frac{\mathcal{P}_{ref}}{2\,\mathcal{P}_{FC}} \frac{\mathrm{m}^2}{\mathrm{s}} \tag{3.16}$$

and the gas diffusion layer thickness

$$d_{GDL} = 200 \cdot 10^{-6} \cdot 2.5 \text{ m}. \tag{3.17}$$

Hence, limit current density i_{lim} is

$$i_{lim} = \frac{\mathcal{P}_{FC}}{R\,T_{FC}}\, y_{O_2}\, 4\,F\, \frac{D_{GDL}}{d_{GDL}}. \tag{3.18}$$

Finally, to evaluate the ohmic loss, the membrane thickness δ_m and ion conductivity σ_m are set as

$$\delta_m = 30 \cdot 10^{-6} \text{ m}, \tag{3.19}$$

$$\sigma_m = 4.39 \frac{\mathrm{S}}{\mathrm{m}}. \tag{3.20}$$

Another important curve used to evaluate FC performance, is the polarization power curve. It is obtained by multiplying the current density i by the voltage V

$$P(i) = i\ V(i). \tag{3.21}$$

An example of the polarization curve is reported in Figure 3.3.

3.2.2 Fuel cell sizing

A Fuel Cell Module (FCM) is composed by several elementary cells connected in order to achieve the required power, through the product of output current and voltage. These two parameters can be varied by connecting the total number of cells in different ways. Specifically, by connecting cells in series, the total voltage is the sum of the voltage of each cell, and a new sub-system, called stack, is obtained. Connecting multiple stacks in parallel, the total current is the sum of the current flowing in each stack:

$$I = \sum_{i=1}^{N_{stack}} i_{cell_i}\ A_{cell_i} \qquad V = \sum_{k=1}^{N_s} v_{cell}. \tag{3.22}$$

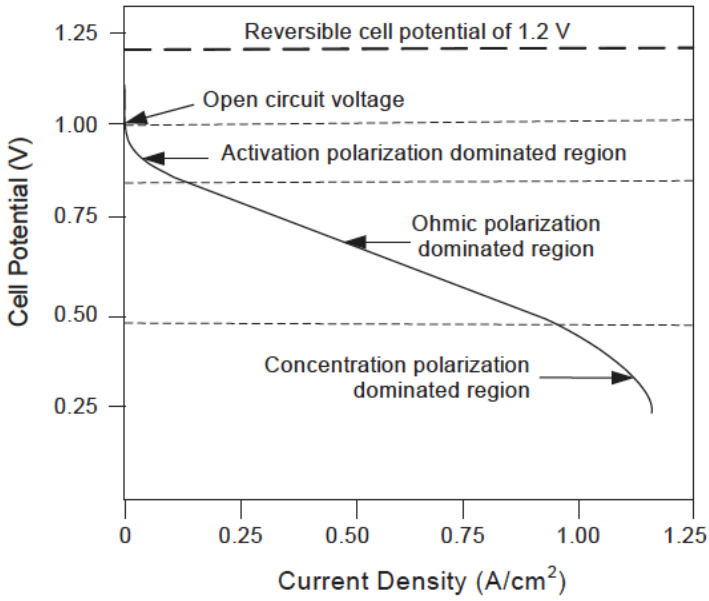

Figure 3.3: *Example of voltage polarization curve [101].*

The polarization curve, and especially the cell power curve, are used for the FCM sizing. N_s is the number of cells in series and N_p the number of stacks in parallel. The total number of cells in the module N_{FCM} is

$$N_{FCM} = N_p \, N_s. \tag{3.23}$$

Multiple design choices arise when it comes to sizing the FCM, as depicted in Figure 3.4. The red curve represents the efficiency of the single FC, the blue curve the efficiency of the FC including auxiliary systems (compressor, humidifier, pumps) and the yellow curve is the polarization power curve, obtained multiplying the polarization voltage curve by the respective current density. The two dotted vertical lines represent two possible sizing solutions:

- **Sizing for power**: the maximum point polarization power curve is chosen in order to size the FCM for maximum power. However, this working point could be a source of instability, due to the tendency of the polarization curve to have an increasing slope, typically in the region above $i = 1.2$ A/cm^2. This slope is the effect of the concentration loss in the cell, see Figure 3.3. A workaround is to use a current density $i_{size} \leq i_{max}$ using a scale factor ν ($\nu < 1$).
- **Sizing for efficiency**: efficiency changes with i as shown in Figure 3.4. Therefore, designing the FCM such that the most recurrent

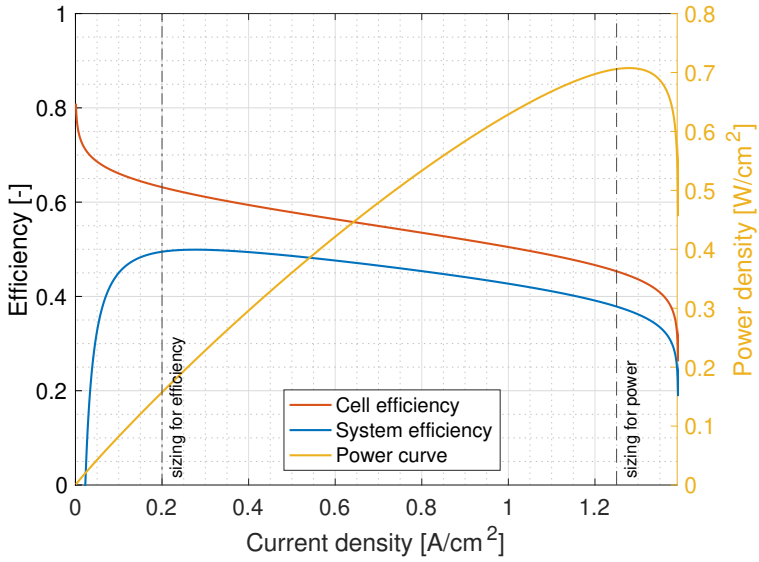

Figure 3.4: *Example of FC efficiency and power polarization curve with the sizing points for power and efficiency.*

working condition is the one with the maximum efficiency could be a valuable option to reduce fuel consumption. However, this condition does not occur at the maximum power point. Hence, the fuel cell ends up being oversized.

.

The mass of the FCM can be estimated resorting to the specific power p_{FC}, so that

$$M_{FC} = \frac{P_{FC}}{p_{FC}}. \tag{3.24}$$

For what concerns the volume of the fuel cell system, a similar approach is followed:

$$V_{FC} = \frac{P_{FC}}{\rho_{FC}}. \tag{3.25}$$

The term ρ_{FC} represents the power density of the fuel cells, i.e. power per unit volume. In order to relate the power density to the specific power, an analysis on existing FC systems led to the regression depicted in Figure 3.5 (the complete database is found in Appendix A).

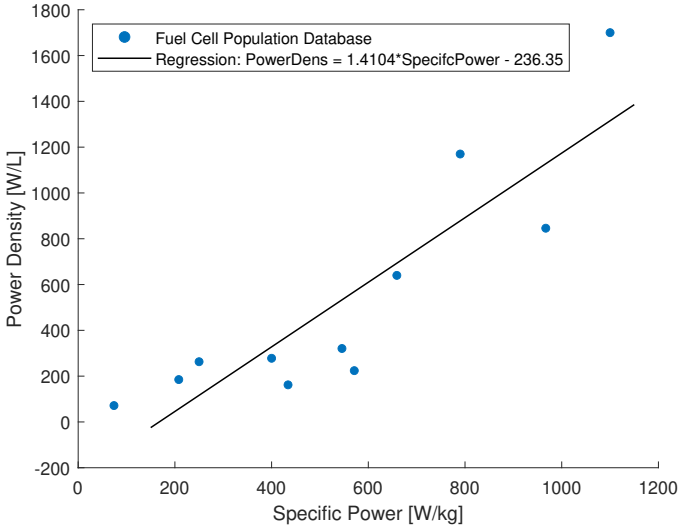

Figure 3.5: *Fuel cell power density regression vs. specific power. Full database is in Appendix A.*

3.2.3 Fuel cell performance

The FCM performance during operation can be evaluated using the FC efficiency η_{FC}, defined as

$$\eta_{FC} = \frac{P_e - P_{aux}}{\dot{m}_{H_2} e_{H_2}} \tag{3.26}$$

where $P_e = VI$ is the electrical power of the FCM, P_{aux} is the power of the auxiliary systems, $\dot{m}_{H_2}$ the hydrogen mass flow rate and e_{H_2} the hydrogen lower heat value

$$e_{H_2} = 119.96 \cdot 10^6 \, \frac{\mathrm{J}}{\mathrm{kg}}. \tag{3.27}$$

The hydrogen mass flow rate is given by

$$\dot{m}_{H_2} = w_{H_2} \, \dot{\mu}_{H_2} \tag{3.28}$$

where

$$\dot{\mu}_{H_2} = \frac{\Lambda_{H_2} \, I \, N_{FC}}{2 \, F} \tag{3.29}$$

is the molar flow rate of hydrogen, that is a function of the current I in the stack. The parameter Λ represents the excess of reactant with respect to stoichiometric value:

$$\Lambda_{H_2} = 1.05. \tag{3.30}$$

The term

$$w_{H_2} = 2.02 \cdot 10^{-3} \, \frac{\text{kg}}{\text{mol}}. \tag{3.31}$$

is the molar mass of hydrogen.

The power of the auxiliary systems considers the power required by a compressor, which guarantees a constant air operating pressure to the FCM. The power consumed by the compressor, called P_{aux} (auxiliary power), is function of the ambient pressure (altitude) and of the air mass flow rate required by the FCM. The compressor work l_c is evaluated using the adiabatic compression equation and considering a compressor efficiency η_c. $\mathcal{P}$ and T are the local values of pressure and temperature, in a specified flight condition:

$$l_c = \frac{1}{\eta_c} \, c_P \, T \, (1 - \beta^{\frac{1-\kappa}{\kappa}}) \tag{3.32}$$

in which β is the compression ratio, κ is the air heat capacity ratio and c_P is the air specific heat at constant pressure

$$\kappa = \frac{c_P}{c_V} = 1.4, \tag{3.33}$$

$$\beta = \frac{\mathcal{P}_{FC}}{\mathcal{P}}, \tag{3.34}$$

$$c_P = 1\,005 \, \frac{\text{J}}{\text{kg K}}. \tag{3.35}$$

Hence the total power of the compressor is

$$P_{aux} = \dot{m}_{air} \; l_c \tag{3.36}$$

where the air mass flow rate $\dot{m}_{air}$ is

$$\dot{m}_{air} = w_{air} \; \dot{\mu}_{air}. \tag{3.37}$$

As usual, the terms s $\dot{\mu}_{air}$ and w_{air} are the molar flow rate and the molar mass of the air

$$\dot{\mu}_{air} = \frac{\Lambda_{air} \; I \; N_{FC}}{4 \; F} \tag{3.38}$$

$$w_{air} = 28.96 \cdot 10^{-3} \, \frac{\text{kg}}{\text{mol}}. \tag{3.39}$$

The excess of reactant with respect to stoichiometric value for air is

$$\Lambda_{air} = 1.7. \tag{3.40}$$

3.3 Hydrogen tanks

3.3.1 Gaseous hydrogen tank

In reference to the discussion in Chapter 2, Type III and Type IV vessels are commonly used for the storage of hydrogen gas. Type III tanks are composite pressure vessels with metallic liners and usually compress the hydrogen at 35 MPa. The metallic liner has many advantages, such as elevated anti-collision performance, good impermeability and distinct plasticity, which enhance the overall performance of composite vessels by applying autofrettage pressure. Type IV tanks manage to halve the overall volume of the tank by increasing the pressure to 70 MPa. These vessels are made of a composite wound around a polymer liner. Type IV pressure vessels are the considered tank type for GH2 in aeronautical applications.

The mass M_t of GH2 tanks can be retrieved using the tank gravimetric index μ_g and knowing the mass of hydrogen M_{H_2} that has to be stored. The gravimetric index is defined as

$$\mu_g = \frac{M_{H_2}}{M_{H_2} + M_t}. \tag{3.41}$$

For what concerns the volume, assumed a certain mass of hydrogen M_{H2}, and knowing the operating pressure $\mathcal{P} = 70\ MPa$ and temperature $T = 357\ K$ (maximum operating pressure of the hydrogen pressure vessel), it is possible to estimate volume of hydrogen within the tank V_{H2}.

$$V_{H_2} = \frac{M_{H_2}}{\rho_{H_2}} \tag{3.42}$$

where $\rho_{H_2} = \frac{\mathcal{P}}{R_{H_2} T}$ is the density of the compressed hydrogen. At this point, the volume of the tank+hydrogen assembly (i.e. the filled tank) can be found using a corrective coefficient χ:

$$V_t = V_{H_2}(1 + \chi) \tag{3.43}$$

A value of $\chi = 0.1$ is found from the analysis on state of the art GH2 tanks in Appendix A.

3.3.2 Liquid hydrogen tank

Liquid hydrogen is better, in terms of energy per unit volume, when compared to gaseous hydrogen (2.3 kWh/L vs 0.003 kWh/L). Moreover, LH2 tanks display higher gravimetric indexes than their gaseous counterpart.

However, the main drawback of LH2 systems is the very low temperatures required to keep the hydrogen in the liquid state (about -253°C). In addition to this, PEM FCs must be fed with hydrogen in a gaseous form and with at a minimum pressure ($\mathcal{P}_{min}$), hence LH2 must evaporate before being sent to the FCs. In order to do this, it is necessary to allow some heat flux to enter the LH2 tank and control the LH2 evaporation flow rate so that it matches the GH2 flow rate necessary for the FCs. In this manner, it is possible to keep the boil-off losses to a minimum. On the other hand, it would be possible to size the tank to avoid the boil-off completely, but ending up with a heavier tank, with a thicker insulation layer. In both cases, the presence of the boil-off and the need to control the evaporation rate requires a more detailed approach for the sizing of LH2 tanks with respect to the simple assumption of a predetermined gravimetric index, as for GH2 tanks.

3.3.2.1 Liquid hydrogen tank design

The design of cryogenic tanks for aeronautical applications has been studied in many works in the literature, as shown in Section 2.4.2. Verstraete's design process [102] sizes the tank so that the venting pressure $\mathcal{P}_{max}$, the pressure at which the boil-off valve opens, letting GH2 in excess be exhausted, is never reached during the flight. In this case, boil-off losses are not present by design and no hydrogen is lost. In contrast, Winnefeld's approach [86] allows for some boil-off and sizes the tank so that the dimensionless storage density or corrected gravimetric index

$$\mu_{req} = \frac{M_{req}}{M_{H_2} + M_t} \tag{3.44}$$

is maximised. In Equation 3.44 the term M_{req} is the hydrogen mass, required throughout the flight for propulsion. Additional hydrogen is stored, if some mass has to be vented, M_{vent}. Hence, $M_{H_2} = M_{req} + M_{vent}$.

A schematic of the LH2 tank sizing procedure that will be applied for preliminary sizing is sketched in Figure 3.6.

The main inputs of the procedure are

- The three non-dimensional parameters (Figure 3.7) that can be used to univocally describe the shape of tank (λ, ϕ, ψ), generically featuring elliptical shell and ellipsoidal heads.
- The feeding pressure and tank venting pressure $\mathcal{P}_{min}$ and $\mathcal{P}_{max}$.
- The requested fuel flow from the FCs $\dot{m}_{req}(t)$ at every time step of the flight mission.

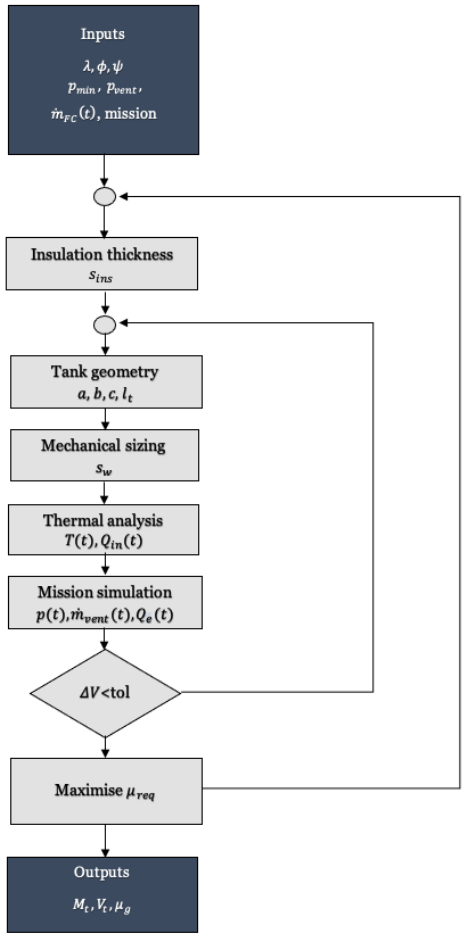

Figure 3.6: *Procedure for the design of LH2 tanks for aeronautical applications.*

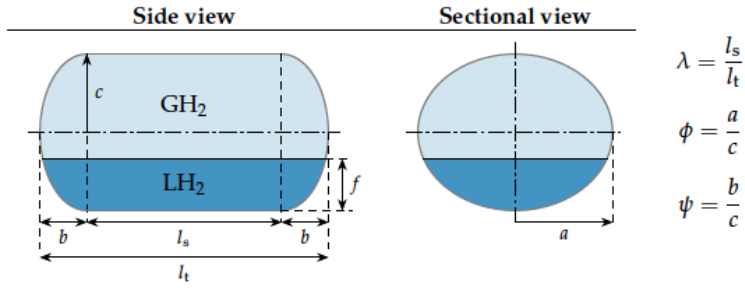

Figure 3.7: *Geometry of LH2 tanks for aeronautical applications [86]*

- Other mission parameters, such as airspeed, altitude, external temperature and pressure.

Then, the outer loop of the procedure stems from guessing a value for the insulation thickness s_{ins}. A set of values for s_{ins} will be tested and the value that maximises the dimensionless storage density μ_{req} resulting from the design procedure will be selected.

For what concerns the inner loop of the tank design process, the tank volume V_t is estimated and also its dimensions (a, b, c, l_t) are found integrating $\dot{m}_{req}$.

After this, the thickness s_w of the tank necessary to bear the mechanical loads is found and, following a thermal analysis, the heat $Q(t)$ leaking into the tank and the tank temperature distribution across the insulation layers are calculated for the entire flight mission.

Finally, the tank internal pressure $\mathcal{P}(t)$ as well as the mass flow rate of vented hydrogen $\dot{m}_{vent}(t)$ and the extra heat $Q_e(t)$ necessary to evaporate the LH2 requested from the FCs can be computed at every time step.

By time integrating $\dot{m}_{vent}(t)$ along the mission, it is possible to estimate the mass of vented hydrogen M_{vent} and use this value to correct the volume of the tank V_t. The inner loop goes on until the tank size keeps changing and ΔV is greater than a prescribed tolerance.

This methodology differs from [86] only in what concerns the internal convection of the tank that is not considered in the thermal analysis. The proposed methodology has been validated in [103].

3.4 Thermal engines

Thermal engines are mostly employed as part of the PGS within THE airplanes. Thermal Engines (TEs) are complex machines and, despite incremental improvements, constitute a well-known technology. The study of TEs is beyond the scope of the present thesis. However, for the sake of aircraft preliminary sizing, it is necessary to derive appropriate and reliable surrogate models to estimate the Brake Specific Fuel Consumption (BSFC) of TEs in order to accurately estimate fuel needs. Another important aspect of TEs is the decrease of maximum power with altitude that inevitably impacts the correct sizing of the engine. For the present purposes, two types of TEs were considered:

- Turboshaft engine.
- Reciprocating engine.

3.4.1 Effect of altitude in the engine rated power

Some simple models are used to estimate the effect of altitude on the power performance of an engine.

The first one can be applied to turboshaft engines. In such model, the power P_z at an altitude z is given by

$$P_z = P_r \left(\frac{\rho}{\rho_c} \right)^{\xi}. \tag{3.45}$$

The terms ρ and ρ_c indicate the air density at the desired altitude at the engine critical altitude. The exponent ξ is an engine-dependent constant that ranges between 0.7 and 0.9 [104, 105]. In this case, is was assumed equal to 0.8. The critical altitude z_c, is the altitude up to which the engine can provide full rated power P_r.

A similar model is used for reciprocating engines, the Gagg and Ferrar model [106]. For turbocharged engines

$$P_z = \begin{cases} P_r, & \text{for } z \leq z_c \\ P_r \left(a\sqrt{\frac{\rho}{\rho_c}} + b \right), & \text{for } z \geq z_c \end{cases} \tag{3.46}$$

where $a = 1.132$ and $b = -0.132$. For normally aspirated engines, z_c corresponds to sea level.

3.4.2 Brake Specific Fuel Consumption

3.4.2.1 Turboshaft engine

For the turboshaft model, a reference BSFC map as a function of the flight Mach number M, altitude z and throttle δ was derived from Thrust Specific Fuel Consumption (TSFC) maps in the appendices of [107]. This map for the BSFC c_P were normalized by c_{P_0}, that represents the BSFC at sea level and $\delta = 1$:

$$\hat{c}_P = \frac{c_P}{c_{P_0}}. \tag{3.47}$$

The map for $z = 8000$ ft is reported in Figure 3.8. Other maps for different altitudes are reported in Appendix A.

3.4.2.2 Reciprocating engines

Reciprocating engines for aeronautical applications have usually featured a large displacement and very low RPM, as a way to increase reliability and

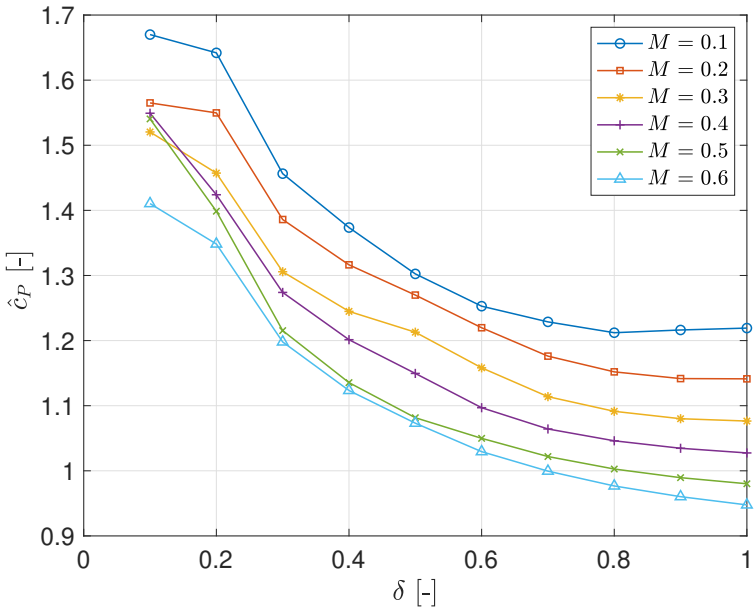

Figure 3.8: *Map of normalised BSFC $\hat{c}_P$ as a function of Mach number M and throttle δ for a representative turboshaft engine at 8,000 ft.*

reduce mechanical stress on the engine. However, greater manufacturing precision and new materials are pushing the usage of more efficient *high-RPM* reciprocating engines (such as the Rotax 91x family). *Low-RPM* reciprocating engines and *high-RPM* reciprocating engines show very different behaviours in terms of BSFC with respect to throttle. Hence, two different efficiency maps are employed for each type of reciprocating engine.

Low-RPM reciprocating engine Three fuel flow maps were extracted from three models in the Lycoming engine series: IO360-A,-C,-D,-J,-K, IO540-A,-B,-E,-G,-P and IO720-A. Whenever present, a *Best Power Mixture* setting was selected to obtain a function that depends only on the throttle. Three curves were thus derived. These curves were averaged and fitted using an exponential curve. The result is shown in Figure 3.9 in terms of normalised reference BSFC $\hat{c}_P$ as a function of $\hat{P}$, that is a fraction of the rated power:

$$\hat{P} = \frac{P}{P_r}. \tag{3.48}$$

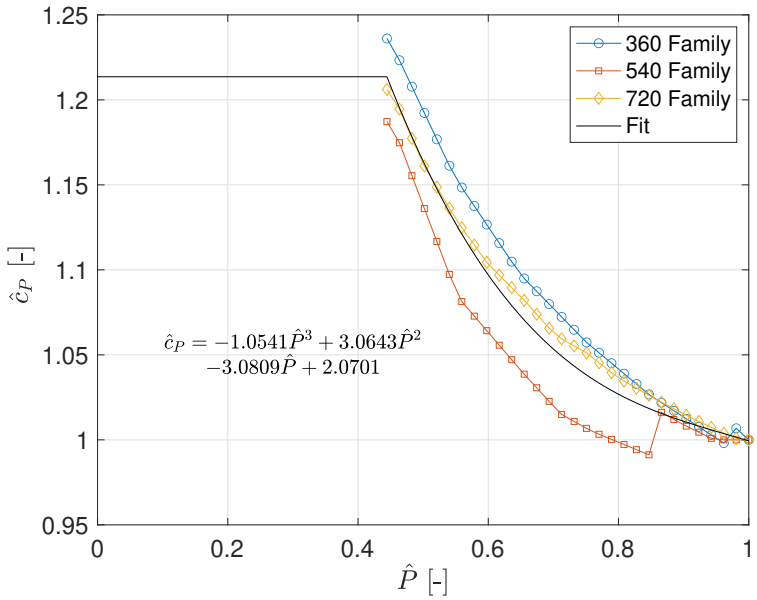

Figure 3.9: *Map of normalised BSFC as a function of fraction of rated power for low-RPM reciprocating engines.*

High-RPM alternative engine The Rotax 915 BSFC map was used as a reference map for High-RPM reciprocating engine as a function of $\hat{P}$. The map is displayed in Figure 3.10.

3.5 Electric motor and generator

Electric Motors are easier to operate and maintain thanks to the lower number of moving parts, and are less exposed to component failures than TEs. EMs normally work within a lower temperature range, and a warm-up process is not needed for this purpose. By design, an electric motor can serve as an electric generator receiving external mechanical power. As mentioned in Chapter 2 brushless Direct Current (DC) and Alternate Current (AC) induction motors are extensively used in hybrid vehicle applications. Brushless DC motors have several apparent advantages including higher efficiency and reliability, longer lifetimes, reduced noise, the elimination of sparks from the commutator, and less electromagnetic interference. However, due to higher costs, brushless DC motors are generally used in higher-end applications. On the other hand, AC induction motors are less expensive and are thus suitable for cost-sensitive applications. No matter what type of motor is used, the model for system performance analysis and simulation is the same and is used primarily

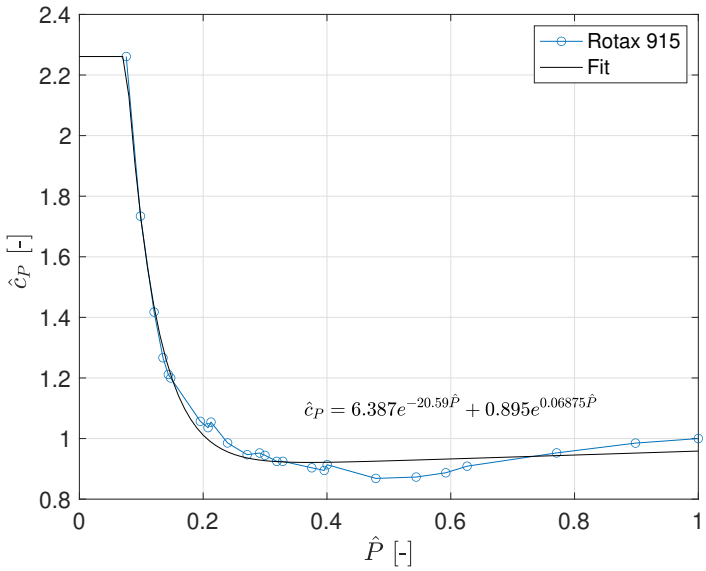

Figure 3.10: *Map of normalised BSFC as a function of fraction of rated power for high-RPM reciprocating engines.*

to describe the external electrical and mechanical behaviours. Electric

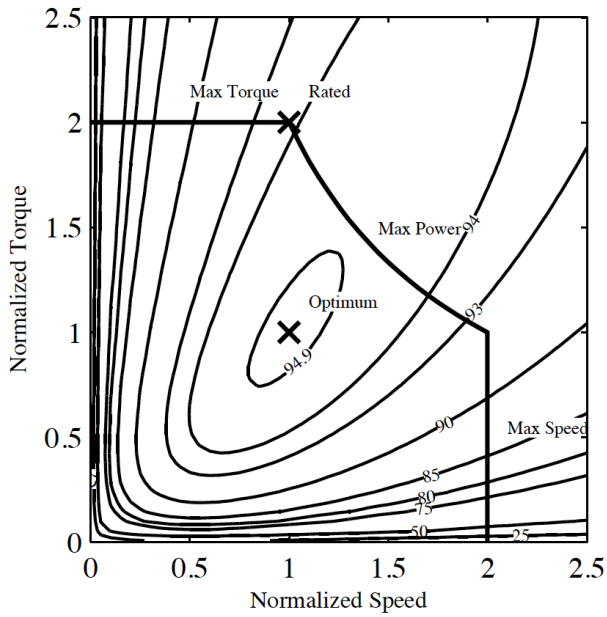

Figure 3.11: *Map of EM efficiency as a function of normalized torque and normalized rotational speed [108].*

motors are usually rated in terms of efficiency η_m

$$\eta_m = \frac{P_{shaft}}{P_{in}}. \tag{3.49}$$

P_{shaft} is the mechanical shaft power, provided by the EM fed with an input electric power P_{in}. By definition

$$P_{shaft} = T\omega \tag{3.50}$$

T is the motor torque and ω is the rotational speed. The EM efficiency can also be written as

$$\eta = \frac{P_{shaft}}{P_{shaft} + P_L} \tag{3.51}$$

where the term P_{in} was written as $P_{shaft} + P_L$, in which P_L is the total power loss. A simple efficiency model developed by [97] shows that the main sources of losses are

- Iron losses: eddy currents and hysteresis, mainly in the rotor. They depend on the change of the magnetic field, i.e. on the rotational speed.
- Copper losses: or ohmic losses, they are caused as electric current flows through the "copper" windings.
- Friction losses: mechanical friction in the bearings and air-drag.
- Constant losses: losses due to motor drives, and electronics.

A possible way to estimate the efficiency of EMs is the rubber motor technique introduced in [108]. This starts from the map of a real EM and a loss model. By selecting the desired optimal efficiency, torque and rotational speed the model can be customised to any specific application. This model results in the plot shown in Figure 3.11 where the EM efficiency η_m is plotted against the normalized torque T and normalized rotational speed ω. From the plot it is clear that in 75% of the working conditions η_m is greater or equal to 90% of the maximum efficiency. Therefore, a constant efficiency model can be adopted if a complete EM map is not easily applicable to the design process. A safety factor can be applied for the sake of conservativeness.

The mass of electric machines is estimated using the specific power p_m. Usage of this assumption is encouraged by the scalability of EMs as seen in Chapter 2. However, there is a maximum power rating at which the expectation of constantly increasing power for an increasing size of the motor is no longer true. This happens when heat control criteria become important in the sizing of the motor after a certain power threshold. In

this analysis, this effect is not modelled as the values for p_m are taken from regressions that take into account the technological scenario in which the EM will be used.

3.6 Distributed electric propulsion

Distributed Electric Propulsion (DEP) is currently seen as one of the main innovations brought by aeronautical power-train electrification. A boosting interest in the possible advantages that may be secured through DEP is easily witnessed by looking at the scientific literature and the concepts under development across all segments from Urban Air Mobility (UAM) applications to airliners [109, 110]. Notwithstanding the investigations carried out in the modelling of the related aero-propulsive interactions [111–114] and the experimental assessment, such as with wind tunnel testing [115] as with respect to other innovations, there is a lack in general conceptual design methodologies capable to introduce DEP effects from the performance point of view, as well as other important aspects (such as the inherited changes in the wing structure).

A contribution in this direction is presented here, starting from basic considerations about the changes that DEP may induce in the preliminary sizing of the aircraft, and particularly, the transformation of the Sizing Matrix Plot (SMP) and the feasibility design area that it defines. The SMP, also known as performance matching plot, is a peculiar graph that can be used in the determination of the design power loading W_{TO}/P_s and wing loading W_{TO}/S, being W_{TO} the design gross weight, P_s the shaft brake-power and S the wing surface. This design point guarantees a number of point and terminal (take-off and landing) performance requirements derived from mission analysis, certification standards, and other design specifications. Figure 3.12 shows a typical SMP for a single-engine GA aircraft complying with the CS-23 regulations. Each curve in the diagram corresponds to a specific performance requirement, including flight and field characteristics. These include

1. Stall speed in landing configuration (red).
2. Take-off distance (blue).
3. High-speed cruise or maximum cruising speed (green).
4. Maximum rate of climb (purple).
5. Climb gradient (yellow).
6. Absolute ceiling (black).

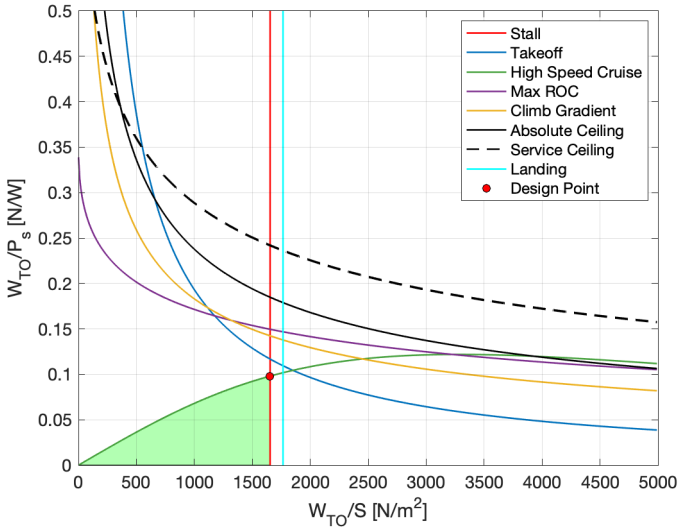

Figure 3.12: *Example of SMP for a GA aircraft.*

7. Service ceiling (dashed black).

8. Landing distance (cyan).

Let us remark that some of these required performance items are part of the regulation requests, mainly inspired to safety of operations, while others represent design desiderata, derived from market studies and other considerations. As the curves represent feasibility boundaries, admissible values for the design power loading/wing loading pair lie under each curve or on the left in the case of vertical lines, and the admissible area is found as the region which satisfies all performance constraints. In the case of Figure 3.12, the feasibility region is bounded, from increasing values of the design wing loading, by the maximum cruising speed and the stalling speed in the landing configuration. Any point in this region, painted in green, may be chosen for the design solution. However, a typical choice is to stay close to the corner where the vertical line of the stalling speed crosses the nearest constraint curve, yielding an aircraft with minimum wing size at given design gross weight. In the case of Figure 3.12, this design point is chosen exactly at the intersection of the high-speed cruise constraint and the stall speed constraints.

The classical SMP is radically changed in the case of DEP implementation. In this case, the distributed array of high-lift propellers on the wing leading edge is able to increase the local dynamic pressure on the wing section laying behind, thus augmenting the corresponding lift coefficient. This

aero-propulsive interaction couples the power loading and wing loading in a more complicated way than that shown in Figure 3.12 for the traditional "concentrated" propulsion case. This section has the purpose of showing how the constraints in the SMP are affected by DEP. Particularly, new analytical expressions are derived for each curve and these expressions include the *extra* lift and drag coefficients deriving from the high-lift DEP propellers. For the sake of brevity, and also because of their paramount importance in the sizing of aircraft in the category of interest in Part II of this work, only three constraints will be analysed in detail:

1. Stall speed in landing configuration.
2. Take-off distance.
3. Maximum cruising speed.

A wider array of constraints is discussed in [116].

3.6.1 Aerodynamic model

In order to model the aero-propulsive interaction effects deriving from DEP, extra *delta* terms for the lift coefficient, ΔC_L, and the drag coefficient, ΔC_D are calculated.

The model adopted for the estimation of these *delta* terms is based on the modelling by Patterson and German [111] and de Vries et al. [117, 118]. The model by De Vries et al. stems from [111] for the estimation of the lift coefficient C_L but adds the drag coefficient estimation from Biber's research [119] and makes the model suitable for preliminary design applications.

The model represents the propellers as actuator disks and the wing as a flat plate, incorporating Patterson's semi-empirical correction for finite slipstream height. The model includes several assumptions worth highlighting:

- The velocity increase at the actuator disk is computed assuming uniform axial inflow.
- Variations in lift due to swirl are neglected (actuator disk assumption).
- The flow over the wing is attached.
- The effect of each propeller on the adjacent ones is neglected.
- The effect of the propeller on the wing is limited to the interval defined by the contracted diameter's slipstream of the single propeller.

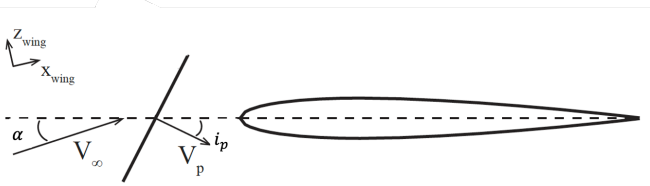

Figure 3.13: *Representation of the airfoil and propeller angle of attack [111].*

- Within this span-wise interval, the effect on the wing is considered uniform in span-wise direction.
- The wing is supposed to be fully immersed in the slipstream, that is, half of the slipstream flows under the wing and half over the wing.
- The stall behaviour of the wing is not taken into account.

3.6.1.1 Lift coefficient

From [118], the sectional lift coefficient increase depends on the axial induction factor at the wing leading edge a_w and on the finite-slipstream correction factor β as

$$\Delta C_l = 2(\left[(\sin\alpha - a_w\beta\sin i_p)\sqrt{(a_w\beta)^2 + 2a_w\beta\cos(\alpha + i_p) + 1} - \sin\alpha\right] \tag{3.52}$$

where α is the geometric angle of attack of the wing and i_p is the propeller setting angle, as depicted in Figure 3.13. Since in the sizing process the angle of attack of the wing is unknown, it has to be estimated using the three-dimensional lift coefficient. For this purpose, the expression presented by Roskam [120] can be used:

$$\alpha = \left(\frac{C_{Lu}}{2\pi AR}\right)\left[2 + \sqrt{AR^2(1-M^2)\left(1 + \frac{\tan^2\Lambda_{c/2}}{1-M^2}\right) + 4}\right]. \tag{3.53}$$

In the above equation C_{Lu} is the unblown lift coefficient, M is the free-stream Mach number, AR the wing aspect ratio and $\Lambda_{c/2}$ the wing half-chord sweep angle.

The finite-slipstream correction factor β can be estimated from a surrogate model in Patterson and German's work [111] as a function of R/c, the ratio between the propeller disk radius R and the airfoil chord c, the velocity of the contracted slipstream far downstream of the disk and the distance x upstream of the leading edge where the disk is placed. According to Patterson's theory, $\beta = 1$ is imposed as an effective upper limit.

In order to derive the axial induction factor at wing leading edge a_w, we must compute the axial induction factor at the propeller disk a_P, which is a function of the propeller thrust coefficient T_c and derived from the actuator disk theory

$$a_P = \frac{1}{2}\left(\sqrt{1+\frac{8T_c}{\pi}}-1\right) \tag{3.54}$$

The thrust coefficient of each propeller is defined as

$$T_c = \frac{T_{DP}}{2q_d N D^2} \tag{3.55}$$

where $q_d = \frac{1}{2}\rho V^2$ is the dynamic pressure, N the number of high-lift propellers, D the diameter of the high-lift propellers and, T_{DP} is the thrust of the DEP system. Hence, a_w is given by

$$a_w = \frac{a_P+1}{\left(\frac{R_w}{R}\right)^2}-1 \tag{3.56}$$

where the contraction ratio of the slipstream at the wing leading edge $\frac{R_w}{R}$ is, from momentum theory principles

$$\frac{R_w}{R} = \sqrt{\frac{1+a_P}{1+a_P\left(1+\frac{\frac{x}{R}}{\sqrt{\left(\frac{x}{R}\right)^2+1}}\right)}}. \tag{3.57}$$

The axial position of the propeller x, the radius of the propeller R and the chord can be expressed using the three non-dimensional parameters $x_c = x/c$, $x_R = x/R$ and $r_c = R/c$.

Finally, the ΔC_l can be extended to three dimensions, as shown by Patterson

$$\Delta C_L = \sum_{i=1}^{N} (\Delta C_l)_i \left(\frac{b_{blown}}{b}\right)_i \tag{3.58}$$

where b_{blown} is the span of the contracted slipstream upon which the propeller is acting. This term too can be derived from momentum theory principles, resulting in:

$$b_{blown} = D\sqrt{\frac{1+a_p}{1+a_p\left(1+\frac{\frac{x}{R}}{\sqrt{\left(\frac{x}{R}\right)^2+1}}\right)}}. \tag{3.59}$$

3.6.1.2 Drag coefficient

The increased dynamic pressure due to high-lift propellers increases the friction drag on the wing. This contribution can be calculated as indicated by [118] as

$$\Delta C_{D0} = \sum_{i=1}^{N} a_w^2 c_f \left(\frac{b_{blown}}{b}\right)_i = N\ a_w^2 c_f \left(\frac{b_{blown}}{b}\right) \tag{3.60}$$

where c_f is the sectional skin friction coefficient, for which a typical value of 0.009 is used in [111]. Let us remark that this equation does not include the contribution to friction drag due to pylons and nacelles.

The increase in induced drag is instead estimated from ΔC_L and the unblown lift coefficient C_{Lu} as

$$\Delta C_{Di} = K\left(2C_{Lu}\Delta C_L + \Delta C_L^2\right) \tag{3.61}$$

The terms K is the quadratic coefficient of the drag polar, defined as

$$K = \frac{1}{\pi A R e} \tag{3.62}$$

where e is the Oswald factor. The total increase in drag coefficient is therefore obtained as

$$\Delta C_D = \Delta C_{D0} + \Delta C_{Di}. \tag{3.63}$$

3.6.2 Adaptation to sizing matrix plot formulation

The delta terms introduced in Equations (3.58) and (3.63) must be elaborated to highlight their dependence on the wing loading and power loading and include them in the SMP analysis. Starting from the DEP model described above, the first step is to express the non-dimensional thrust coefficient of single propeller T_c as a function of the total thrust T and, ultimately, as a function of the total power P_s. In this section, we shall apply a simplified modelling assuming that all the DEP thrust units (propellers and motors) are the same and that they are uniformly distributed along the wing span. A special condition will be included in case of the presence of a thrust unit at the wing tip.

Geometrical parameters Some geometrical parameters must be introduced, in order to rewrite Equations (3.58) and (3.63) and explicit their dependence on W_{TO}/S and W_{TO}/P_s First of all, the effective wingspan b_e is expressed as the difference between the wing span b and the fuselage width

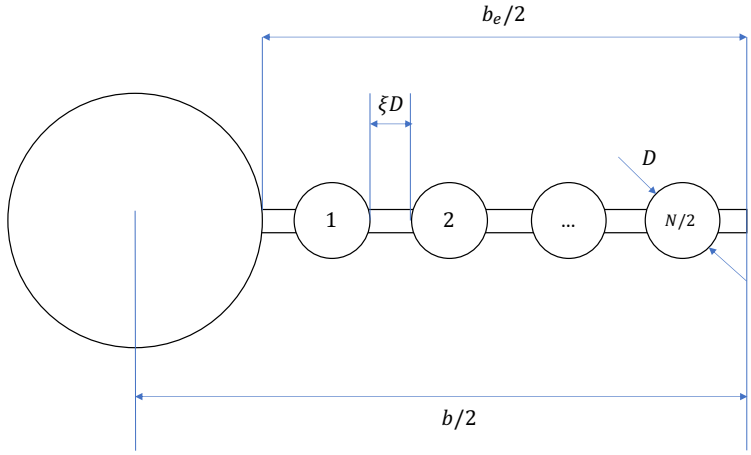

Figure 3.14: *Frontal view of the DEP array.*

b_f as

$$b_e = b - b_f \tag{3.64}$$

Then, we introduce two geometric parameters:

- ζ takes into account the position of the propellers along the wing

$$\zeta = \begin{cases} \frac{1}{2} & \text{if the propeller is located at the wing tip} \\ 1 & \text{otherwise} \end{cases}. \tag{3.65}$$

- ξ represents the span-wise separation between each propeller along the DEP array as a fraction of the propeller diameter D.

Figure 3.14 depicts a situation in which both the distance between the fuselage and the first propeller disk and that between the last propeller disk and the wing tip are $\xi D/2$. The definition of b_e, ζ and ξ allows to express the propeller diameter D as a function of the effective wingspan

$$D = \frac{1}{1+\xi}\frac{b_e}{N + 2(\zeta - 1)}. \tag{3.66}$$

Then, the geometric parameter δ is defined as

$$\delta = \frac{D}{b} \tag{3.67}$$

and can be elaborated into

$$\delta = \frac{D}{b} = \frac{1}{1+\xi}\left(\frac{b_e}{b}\right)\frac{1}{N + 2(\zeta - 1)}. \tag{3.68}$$

As an example, when $\zeta = 1$ (no wing-tip propellers) and $\xi = 0$ (no spacing between propellers), δ becomes

$$\delta = \frac{D}{b} = \left(\frac{b_e}{b}\right)\frac{1}{N}. \tag{3.69}$$

Let us remark that the non-dimensional ratio b_e/b is introduced in the equations in order to remove the dependence on the wingspan b. During the preliminary sizing phase, b_e/b can be gathered from historical regressions or can be guessed from *back-of-the-envelope* sketches of the aircraft, especially for classic "tube and wing" configurations.

Thrust coefficient and axial induction factor With some manipulation, the non-dimensional thrust coefficient of single propeller T_c is rewritten as function of total thrust:

$$T_c = \frac{T_{DP}}{N\rho V^2 D^2} = \frac{T\chi}{N\rho V^2 D^2} = \frac{\chi}{N\rho V^2}\frac{T}{W_{TO}}\frac{W_{TO}}{S}\frac{S}{D^2} \tag{3.70}$$

and therefore of shaft power as

$$\begin{aligned} T_c =& \frac{\chi\eta_P}{N\rho V^3}\frac{P_s}{W_{TO}}\frac{W_{TO}}{S}\frac{b^2}{AR\ D^2} \\ =& \frac{\chi\eta_P}{N\rho V^3}\left(\frac{W_{TO}}{P_s}\right)^{-1}\left(\frac{W_{TO}}{S}\right)\frac{1}{AR\ \delta^2} \end{aligned} \tag{3.71}$$

where T_{DP} is the thrust of the DEP system and χ is

$$\chi = \frac{T_{DP}}{T}. \tag{3.72}$$

Taking advantage of the geometrical quantities introduced in the previous paragraph, T_c can be evaluated as a function of the two variables of the SMP, W_{TO}/P_s and W_{TO}/S:

$$T_c = \frac{\chi\eta_P}{N\rho V^3}\left(\frac{W_{TO}}{P_s}\right)^{-1}\left(\frac{W_{TO}}{S}\right)\frac{1}{AR}\frac{(1+\xi)^2\left(N+2\left(\zeta-1\right)\right)^2}{\left(b_e/b\right)^2} \tag{3.73}$$

Plugging this expression of T_c into the expression for the axial induction factor at the propeller disk a_P we obtain

$$a_P = \tfrac{1}{2}\left(\sqrt{1+\tfrac{8}{\pi}\left[\tfrac{\chi\eta_P}{N\rho V^3}\left(\tfrac{W_{TO}}{P_s}\right)^{-1}\left(\tfrac{W_{TO}}{S}\right)\tfrac{1}{AR}\tfrac{(1+\xi)^2(N+2(\zeta-1))^2}{(b_e/b)^2}\right]}-1\right) \tag{3.74}$$

Finally, the axial induction factor at wing leading edge a_w is rearranged as

$$a_w = \frac{1}{2}\left(\sqrt{1+\frac{8}{\pi}\left[\frac{\chi\,\eta_P}{N\rho V^3}\left(\frac{W_{TO}}{P_s}\right)^{-1}\left(\frac{W_{TO}}{S}\right)\frac{1}{AR}\frac{(1+\xi)^2\left(N+2\left(\zeta-1\right)\right)^2}{\left(b_e/b\right)^2}\right]}-1\right) \left(1+\frac{\frac{x}{R}}{\sqrt{\left(\frac{x}{R}\right)^2+1}}\right) \tag{3.75}$$

It is worth pointing out that, at certain altitude (ρ fixed), once the geometric parameters $(\xi, \zeta, \delta, x/R)$, the wing wing aspect ratio AR, and the propeller efficiency η_P are known T_c, a_P and a_w become functions of only four variables:

$$T_c = T_c\left(\frac{W_{TO}}{S}, \frac{W_{TO}}{P_s}, V, N\right) \tag{3.76}$$

$$a_P = a_P\left(\frac{W_{TO}}{S}, \frac{W_{TO}}{P_s}, V, N\right) \tag{3.77}$$

$$a_w = a_w\left(\frac{W_{TO}}{S}, \frac{W_{TO}}{P_s}, V, N\right) \tag{3.78}$$

Replacing these relationships in Equation 3.52, the sectional lift coefficient is

$$\Delta C_l = \Delta C_l\left(\frac{W_{TO}}{S}, \frac{W_{TO}}{P_s}, V, N, C_{Lu}\right). \tag{3.79}$$

Moving to the 3D lift coefficient, we get

$$\begin{aligned}\Delta C_L &= \sum_{i=1}^{N}\left(\Delta C_l\right)_i\left(\frac{b_{blown}}{b}\right)_i = \\ &= N\Delta C_l\left(\frac{W_{TO}}{S}, \frac{W_{TO}}{P_s}, V, N, C_{Lu}\right)\left(\frac{b_{blown}}{b}\right)\end{aligned} \tag{3.80}$$

that can be rewritten more explicitly as

$$\begin{aligned}\Delta C_L =& N\Delta C_l\left(\frac{W_{TO}}{S}, \frac{W_{TO}}{P_s}, V, N, C_{Lu}\right)\left(\frac{D}{b}\right)\cdot \\ &\cdot\sqrt{\frac{1+a_P\left(\frac{W_{TO}}{S}, \frac{W_{TO}}{P_s}, V, N\right)}{1+a_P\left(\frac{W_{TO}}{S}, \frac{W_{TO}}{P_s}, V, N\right)\left(1+\frac{\frac{x}{R}}{\sqrt{\left(\frac{x}{R}\right)^2+1}}\right)}}.\end{aligned} \tag{3.81}$$

Making use of Equation 3.68, the last expression becomes

$$\Delta C_L = \left(\frac{b_e}{b}\right) \Delta C_l \left(\frac{W_{TO}}{S}, \frac{W_{TO}}{P_s}, V, N, C_{Lu}\right) \cdot \cdot \sqrt{\frac{1 + a_P\left(\frac{W_{TO}}{S}, \frac{W_{TO}}{P_s}, V, N\right)}{1 + a_P\left(\frac{W_{TO}}{S}, \frac{W_{TO}}{P_s}, V, N\right)\left(1 + \frac{\frac{x}{R}}{\sqrt{\left(\frac{x}{R}\right)^2 + 1}}\right)}}. \tag{3.82}$$

Considering the term b_e/b a constant for tube and wing airplanes, we eventually can concisely state that

$$\Delta C_L = \Delta C_L \left(\frac{W_{TO}}{S}, \frac{W_{TO}}{P_s}, V, N, C_{Lu}\right). \tag{3.83}$$

The same line of reasoning can be applied to the ΔC_D terms. In particular, the parasite ΔC_{D0} is

$$\begin{aligned} \Delta C_{D0} &= \sum_{i=1}^{N} a_w^2 c_f \left(\frac{b_{blown}}{b}\right)_i = N a_w^2 c_f \left(\frac{b_{blown}}{b}\right) = \\ &= \Delta C_{D0}\left(\frac{W_{TO}}{S}, \frac{W_{TO}}{P_s}, V, N\right) \end{aligned} \tag{3.84}$$

while the induced term ΔC_{Di} is

$$\Delta C_{Di} = \frac{\left[2 C_{Lu} \Delta C_L \left(\frac{W_{TO}}{S}, \frac{W_{TO}}{P_s}, V, N, C_{Lu}\right) + \Delta C_L \left(\frac{W_{TO}}{S}, \frac{W_{TO}}{P_s}, V, N, C_{Lu}\right)^2\right]}{\pi AR\, e}. \tag{3.85}$$

Ultimately,

$$\begin{aligned} \Delta C_D &= \Delta C_{D0}\left(\frac{W_{TO}}{S}, \frac{W_{TO}}{P_s}, V, N\right) + \\ &+ \Delta C_{Di}\left(\frac{W_{TO}}{S}, \frac{W_{TO}}{P_s}, V, N, C_{Lu}\right) = \\ &= \Delta C_D \left(\frac{W_{TO}}{S}, \frac{W_{TO}}{P_s}, V, N, C_{Lu}\right). \end{aligned} \tag{3.86}$$

In order to illustrate what actually results from Equations (3.83) and (3.86), Figure 3.15 shows the application to a wing layout inspired by that of NASA X-57 aircraft, a remarkable example of a DEP concept in advanced state of development. The selected airspeed is the NASA X-57 stall speed at sea level (29.8 m/s). The full list of values for the parameters in Equations (3.83) and (3.86) are summarised in Table 3.1. Particularly, Figure 3.15a depicts the variation of ΔC_L with the number of propellers N, while Figure 3.15b that of the ΔC_{D0}.

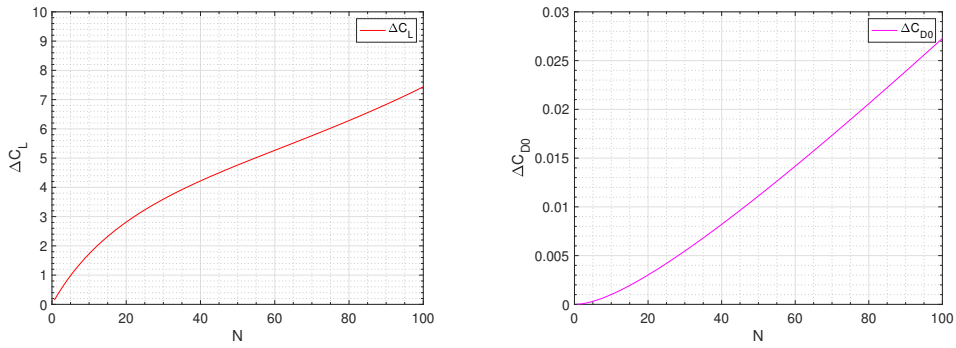

(a) (b)

Figure 3.15: *Increase in lift coefficient (a) and zero-lift drag coefficient (b) with respect to the number of propellers considered for the DEP system in Table 3.1*

Table 3.1: *Input data for evaluation of ΔC_L and ΔC_D on NASA X-57*

Input data	Numeric values	Units
W_{TO}/S	2154.6	N/m^2
W_{TO}/P_s	0.0542	N/W
V	29.8	m/s
C_{Lu}	2.8	-
C_{D0u}	0.022	-
ξ	0	-
ζ	1	-
N	12	-
AR	15	-
b_e/b	0.873	-
x/c	0.310	-
x/R	0.691	-
$\Lambda_{c/2}$	1.9	deg
i_p	0.0	deg
e	0.8	-
c_f	0.009	-

3.6.2.1 Stall speed

The stall speed V_S requirement is a limit on the minimum allowable operating speed in a specific configuration, usually landing. In general, a low stall speed is desirable, since this results in a safer aircraft. This requirement is classically represented by the equation

$$\left(\frac{W_{TO}}{S}\right) - \frac{1}{2}\rho_0 V_S^2 \; C_{L\ MAX} = 0. \tag{3.87}$$

In the conventional case, there would be no dependence on the power loading W_{TO}/P_s since Equation 3.87 derives from the (simplified) vertical equilibrium at stall, with the stall lift coefficient $C_{L\ MAX}$. However, adapting the stall speed requirement to the DEP model, the lift coefficient must be expressed as the sum of the stall lift coefficient of the unblown wing $C_{Lu\ MAX}$ and the delta lift coefficient derived by Equation 3.58. Hence,

$$\left(\tfrac{W_{TO}}{S}\right) - \tfrac{1}{2}\rho_0 V_S^2 \left[C_{Lu\ MAX} + \Delta C_L \left(\tfrac{W_{TO}}{S}, \tfrac{W_{TO}}{P_s}, V_S, N, C_{Lu\ MAX}\right)\right] = 0 \tag{3.88}$$

Graphically, Equation 3.88 is represented by the blue solid line of Figure 3.16, as opposed to the constraint relative to the conventional case represented by the vertical red solid line. The graph has been derived using the same data of Table 3.1 and sea level air density. In Figure 3.17, it is possible to observe the behaviour of the stall speed constraint with an increasing number of blowing propellers N along the DEP array. Since the stall speed V_S represents an upper limit, the area of the graph on the left side of the curve is the region where the stall requirement is met, while on the right side the stall requirement is not. The stall speed curve in the DEP case tends to increase the acceptable design region for the determination of the design point within the SMP as N increases. Particularly, the wing loading that satisfies the stall speed requirement becomes a function of power loading, as opposite to the conventional case where the stall wing loading is totally independent from W_{TO}/P_s. Furthermore, comparing the conventional case and the DEP case, it can be observed that the stall speed requirement derived with the DEP model degenerates into the vertical line of the conventional unblown case when $N = 0$ (no DEP system).

3.6.2.2 Take-off distance

The take-off distance constraint represents the limit on the minimum ground distance required to safely take-off, from sea level or any different altitude.

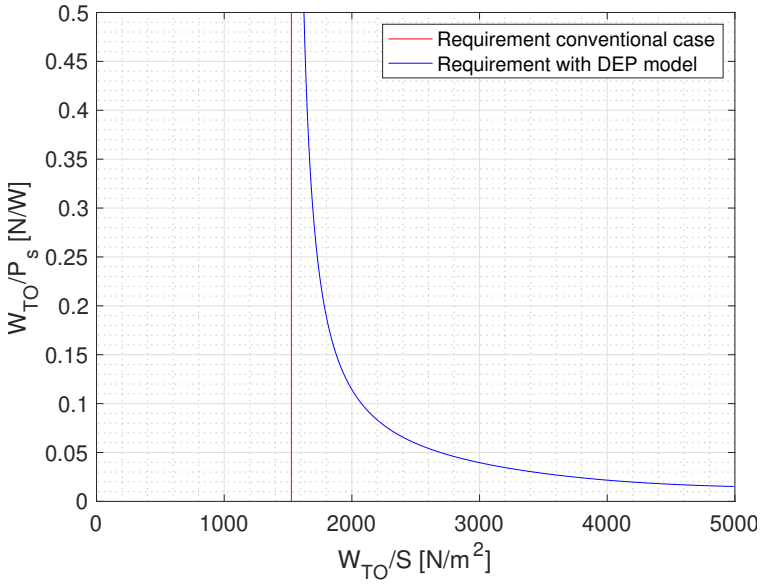

Figure 3.16: *Change in the SMP stall constraint with the DEP model*

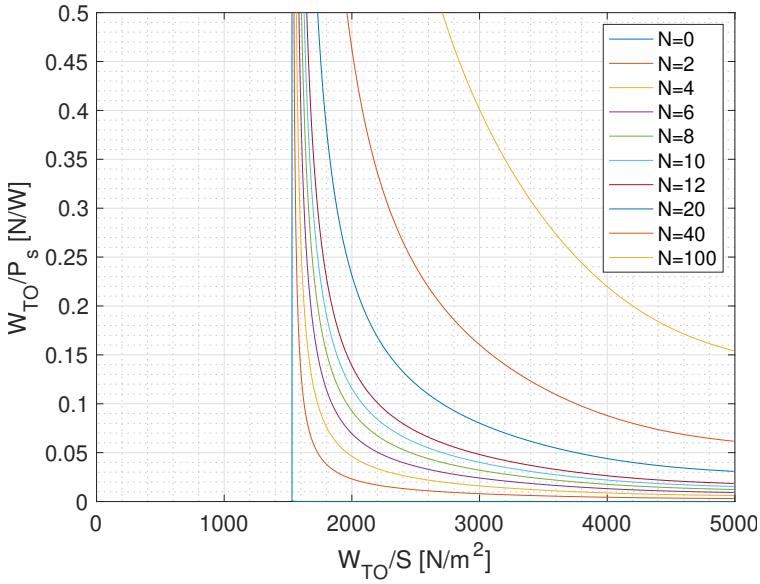

Figure 3.17: *Sensitivity of stall constraint with the DEP model to the number of high-lift propellers*

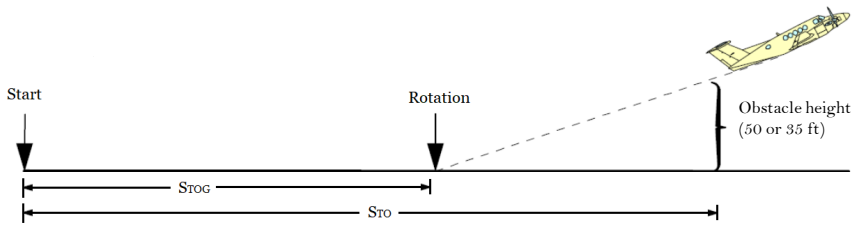

Figure 3.18: *Take-off run breakdown in the ground run and airborne phase [122].*

The take-off constraint is classically formulated making use of the Take-Off Parameter (TOP) [107, 121]. The TOP for a FAR-23/CS-23 propeller-driven airplane is defined as

$$TOP_{23} = \frac{\left(\frac{W_{TO}}{P_s}\right)\left(\frac{W_{TO}}{S}\right)}{\frac{\rho_{TO}}{\rho_0} C_{L\ MAX}^{TO}} \tag{3.89}$$

where ρ_{TO}/ρ_0 is the air density ratio at the airport level, and $C_{L\ MAX}^{TO}$ is the stall lift coefficient in take-off configuration. The values of the TOP have been historically derived using statistics on different categories of airplanes, from GA to two-, three- and four-engine certified airplanes. Once the TOP is known, the resulting constraint on the SMP is

$$\left(\frac{W_{TO}}{P_s}\right) = \frac{TOP \frac{\rho_{TO}}{\rho_0} C_{L\ MAX}^{TO}}{\left(\frac{W_{TO}}{S}\right)}. \tag{3.90}$$

Unfortunately, DEP systems are fairly new and there is not enough historical data to set up a TOP estimation. Therefore, the use of Equation 3.90 is not advisable. However, it is possible to evaluate the SMP requirement for DEP fixed-wing aircraft following the equations suggested by [104, 122]. Sadraey models the take-off run as an accelerated motion. The take-off distance S_{TO} is split into the ground run S_{TOG} and airborne phase that ends when a reference obstacle (35 or 50 ft) is crossed, as portrayed by Figure 3.18. The aircraft speed varies from standstill to rotation speed V_R and then to take-off speed V_{TO} at the lift-off. The take-off speed is assumed slightly greater than the stall speed in take-off configuration V_S^{TO} and is set to $V_{TO} = 1.2V_S^{TO}$ while $V_R = 1.15V_S^{TO}$. The resulting expression for the take-off run is

$$\begin{aligned} S_{TO} = & \frac{1.65\left(\frac{W_{TO}}{S}\right)}{g\rho_0\left(C_D^{TO} - \mu C_L^{TO}\right)} \cdot \\ & \cdot \ln\left[\frac{\frac{\eta_P}{V_{TO}}\left(\frac{P_s}{W_{TO}}\right) - \mu}{\frac{\eta_P}{V_{TO}}\left(\frac{P_s}{W_{TO}}\right) - \mu - g\rho_0 \frac{\left(C_D^{TO} - \mu C_{L\ TO}\right)}{1.19 C_L^{TO}}}\right]. \end{aligned} \tag{3.91}$$

As a general warning, it is important to remark that Equation 3.91 is derived by [122] as the result of an integration process on the accelerating airspeed. This integration process should be repeated entirely and the equation should involve an integral function. After some manipulations with the goal of highlighting the dependencies on W_{TO}/S and W_{TO}/P_s, Equation (3.91) becomes

$$\left(\frac{W_{TO}}{P_s}\right)\frac{V_{TO}}{\eta_P}+ \\ -\frac{1-\exp\left(0.6\rho_{TO}g\ (C_D^{TO}-\mu C_L^{TO})S_{TO}\left(\frac{W_{TO}}{S}\right)^{-1}\right)}{\mu-\left(\mu+\frac{(C_D^{TO}-\mu C_L^{TO})}{1.19C_L^{TO}}\right)\left[\exp\left(0.6\rho_{TO}g\ (C_D^{TO}-\mu C_L^{TO})S_{TO}\left(\frac{W_{TO}}{S}\right)^{-1}\right)\right]}=0 \tag{3.92}$$

where g is the gravity acceleration and μ is the static rolling friction coefficient (considered through standard value for dry concrete/asphalt surfaces). The terms C_L^{TO} and C_D^{TO} are the aircraft lift and drag coefficients at lift-off and, due to the effect of DEP, they are expressed as

$$\begin{cases} C_L^{TO}=C_{Lu}^{TO}+\Delta C_L^{TO}\left(\frac{W_{TO}}{S},\frac{W_{TO}}{P_b},V_{TO},N,C_{Lu}^{TO}\right) \\ C_D^{TO}=C_{D0u}^{TO}+\Delta C_{D0}^{TO}+\Delta C_{Di}^{TO}\left(\frac{W_{TO}}{S},\frac{W_{TO}}{P_b},V_{TO},N,C_{Lu}^{TO}\right) \end{cases} \tag{3.93}$$

The term C_{D0u}^{TO} is usually derived from the airplane *clean* C_{D0} by adding the contribution of flaps and the landing gear. The term C_{Lu}^{TO} was assumed, as $C_{Lu}^{TO}=C_{Lu\ MAX}^{TO}/(1.2)^2$ while the take-off speed V_{TO} is unknown and can be derived from the vertical equilibrium. Hence, the full system of equations is

$$\begin{cases} \left(\frac{W_{TO}}{P_s}\right)\frac{V_{TO}}{\eta_P}-\frac{1-\exp\left(0.6\rho_{TO}g\ (C_D^{TO}-\mu C_L^{TO})S_{TO}\left(\frac{W_{TO}}{S}\right)^{-1}\right)}{\mu-\left(\mu+\frac{(C_D^{TO}-\mu C_L^{TO})}{1.19C_L^{TO}}\right)\left[\exp\left(0.6\rho_{TO}g\ (C_D^{TO}-\mu C_L^{TO})S_{TO}\left(\frac{W_{TO}}{S}\right)^{-1}\right)\right]}=0 \\ \left(\frac{W_{TO}}{S}\right)-\frac{1}{2}\rho_0 V_{TO}^2\ C_L^{TO}=0 \end{cases} \tag{3.94}$$

and, for a fixed value of W_{TO}/S, the unknowns are W_{TO}/P_s and V_{TO}.

The curve deriving from Equation 3.94 is represented by the blue solid line in Figure 3.19 and is compared to the constraints derived for the conventional case represented by the solid red line (Sadraey's formulation [122]) and dashed red line (using Roskam's TOP [121]). Figure 3.20 shows the behaviour of the take-off requirement with DEP when the number of blowing propellers N is increased. This plot depicts clearly that the take-off distance requirement curve tends to move north-east thus enlarging the feasibility region for the determination of the design point. This displacement is higher as N grows, allowing for a higher value of W_{TO}/P_s at fixed W_{TO}/S (a higher value of W_{TO}/P_s means less power). Once again, if $N=0$, the DEP take-off distance requirement matches the curve of the conventional unblown case.

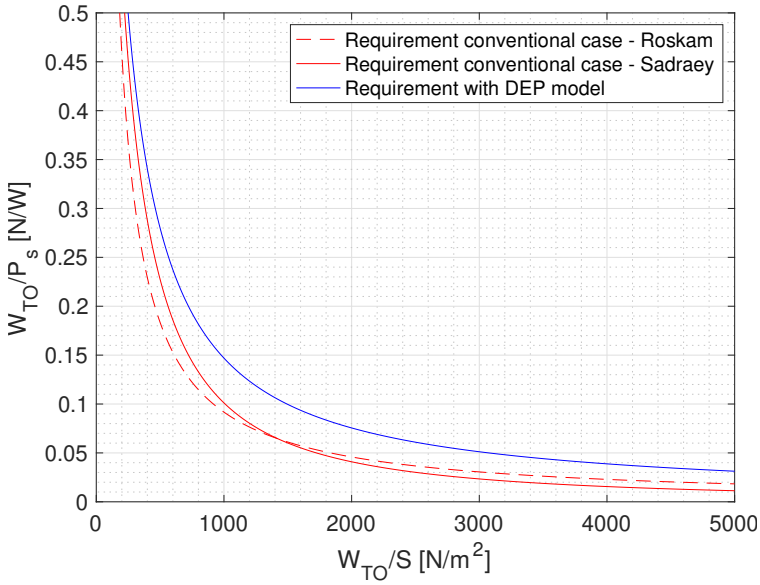

Figure 3.19: *Change in the SMP take-off constraint with the DEP model.*

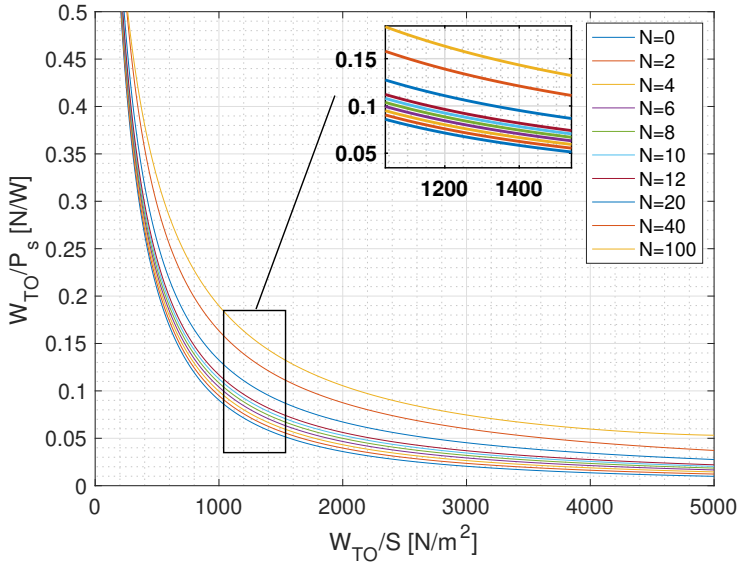

Figure 3.20: *Sensitivity of take-off constraint with the DEP model to the number of high-lift propellers.*

3.6.2.3 Maximum cruising speed

The next SMP requirement is the maximum cruising speed. This requirement is evaluated following the description presented in Sadraey [122] for a propeller-driven aircraft which is flying with the maximum constant speed at a specified altitude. The aircraft is in longitudinal trim, hence the maximum available engine power must be equal to the maximum required power, which is thrust multiplied by maximum speed. This holds true also for DEP aircraft:

$$\left(\frac{W_{TO}}{S}\right)\left(\frac{W_{TO}}{P_s}\right)^{-1}\frac{\eta_P}{V_{CR\ MAX}} = \frac{1}{2}\rho_{CR}V_{CR\ MAX}^2 C_D^{CR} \tag{3.95}$$

Expressing the drag coefficient using the parabolic drag polar

$$C_D^{CR} = C_{D0}^{CR} + \frac{\left(C_L^{CR}\right)^2}{\pi\ AR\ e} \tag{3.96}$$

and exploiting the vertical equilibrium

$$C_L^{CR} = \frac{\left(\frac{W_{TO}}{S}\right)}{\frac{1}{2}\rho_{CR}V_{CR\ MAX}^2} \tag{3.97}$$

it is possible to derive the expression

$$\begin{aligned}&\left(\frac{W_{TO}}{S}\right) - \left(\frac{W_{TO}}{P_s}\right)\frac{1}{2}\rho_{CR}\frac{V_{CR\ MAX}^3}{\eta_P}C_{D0}^{CR} + \\ &- \left(\frac{W_{TO}}{S}\right)^2\left(\frac{W_{TO}}{P_s}\right)\frac{2}{\rho_{CR}V_{CR\ MAX}\ \pi\ AR\ e\ \eta_P} = 0\end{aligned} \tag{3.98}$$

where the parameter C_{D0}^{CR} represents the total aircraft drag coefficient due to friction and dynamic pressure in cruise configuration, computed with the DEP model as

$$C_{D0}^{CR} = C_{D0u}^{CR} + \Delta C_{D0}\left(\frac{W_{TO}}{S}, \frac{W_{TO}}{P_s}, V_{CR\ MAX}, N\right) \tag{3.99}$$

The constraint coming from Equation 3.98 is depicted in Figure 3.21 as the blue curve and is compared to the constraint relative to the conventional case represented by the red curve. The maximum cruising speed requirement with DEP tends to slightly shrink the acceptable design region with respect to the traditional constraint without DEP. This reduction of the design space increases with N, as depicted in Figure 3.22. This behaviour is opposite to that of the stall speed and take-off run constraints, where the DEP had a beneficial effect in the expansion of the feasibility region.

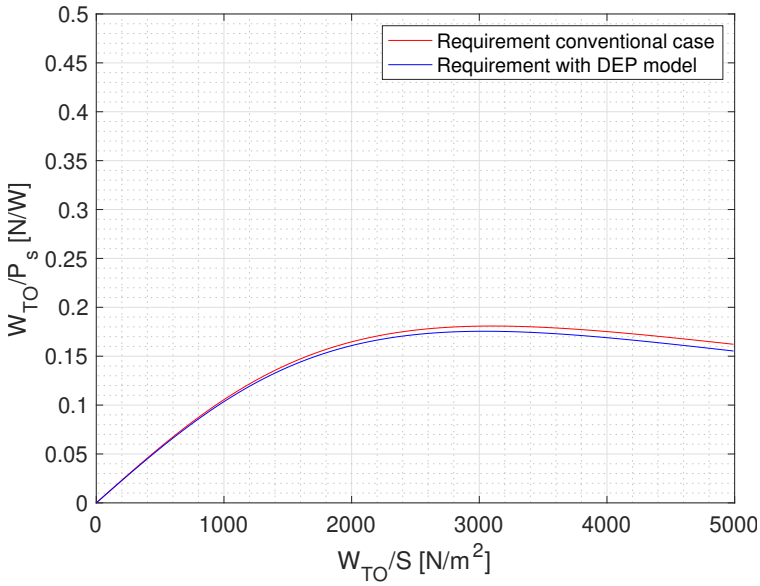

Figure 3.21: *Change in the SMP maximum cruising speed constraint with the DEP model.*

On the contrary, here the extra drag that derives from Equation (3.99) as an effect of the rise in friction on the blown wing, increases the required power for level flight and reduces slightly the design space in terms of W_{TO}/P_s and W_{TO}/S.

3.6.3 Application example

The DEP model introduced in the previous sections is here applied to derive a complete SMP. The reference aircraft is the NASA X-57 Maxwell Mod IV. The data for this airplane is taken from NASA's documentation and the technical papers [112, 123–127]. The fuselage of NASA X-57 is that of Tecnam P2006T, which allowed to gather geometrical data on the fuselage from the P2006T Pilot Operating Handbook (POH) [128].

The NASA X-57 Maxwell is an experimental aircraft being developed by NASA, intended to demonstrate DEP technology. The X-57 development started from a pure-electric version of the Tecnam P2006T. Then, the wing was changed and provided with 12 small high-lift electric motors with their propellers mounted on the wing leading edges and two larger tip-mounted electric motors with their propellers. All motors are used during take-off and landing, with only the tip motors used during cruise. The 12 high-lift thrust units use special folding fixed-pitch propellers designed to sustain an augmented airflow over the wings and increase the local dynamic pressure.

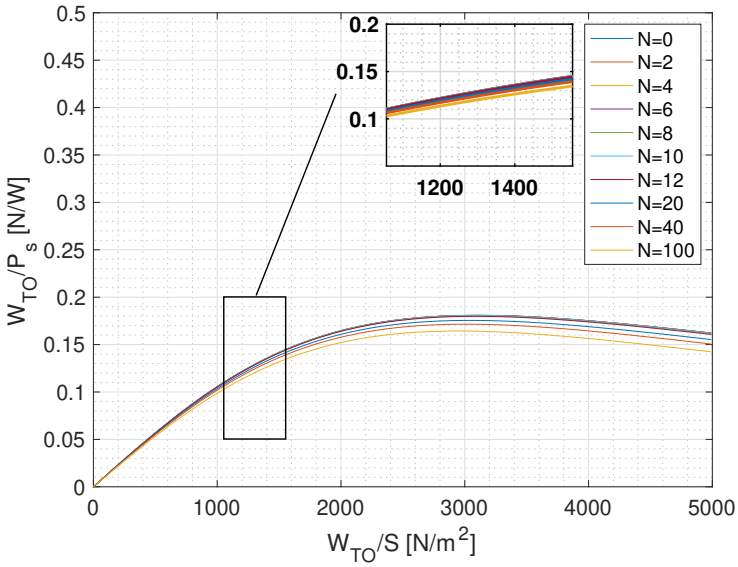

Figure 3.22: *Sensitivity of maximum cruising speed constraint with the DEP model to the number of high-lift propellers.*

The result is a larger lift coefficient, despite the very small wing.

The SMP for the X-57 was derived both without and with DEP. The necessary input data of the model is summarized in Table 3.2. Apart from the stall, take-off run and maximum cruising speed constraint, also the minimum rate of climb on the ground, All Engine Operating (AEO) climb gradient requirements coming from CS-23 and absolute ceiling, service ceiling and cruise ceiling are shown in the following graphs. The full list of equations employed to plot these constraints can be found in [116].

The SMP of the non-DEP version is shown in Figure 3.23 and has been derived using Roskam [121], except for the landing and take-off constraints which are taken from Sadraey [122]. The SMP featuring the DEP system is, instead, represented in Figure 3.24. Comparing the SMP with DEP model and without it, it is interesting to note how the feasibility region, painted in green in both figures, is enlarged when high-lift propellers are present. The design point of the X57, marked with a red dot, falls inside the acceptable region, lying at the intersection between the take-off and the landing curves in both cases. An interesting aspect of the wider feasibility region is the virtually unlimited extension towards larger values of wing loading. This extension is mainly due to the change in shape of the stall speed requirement and the landing distance requirement. Since the expression of the lift coefficient with the DEP is also a function of the

Table 3.2: *Data employed for the SMPs constraints of Figures 3.24 and 3.23.*

Symbol	Value	Unit
Stall Speed		
h_s	0	m
V_s	29.83	m/s
η_P	0.7	-
Take-off run		
h_{TO}	0	m
η_P	0.7	-
S_{TO}	394	m
μ	0.04	-
Maximum cruising speed		
h_{CR}	2438	m
$V_{CR\ MAX}$	92.6	m/s
η_P	0.8	-

power loading, the traditionally vertical cyan and red lines of Figure 3.23 become curves with an asymptote on the horizontal axis and drastically change the appearance of the SMP. As a result, the maximum wing loading of Figure 3.23 is increased by 40%. On the other hand, this higher wing loading can be sustained only lowering the power loading (0.060 N/W in the non-DEP case and 0.054 N/W in the DEP case) and thus increasing the necessary shaft power.

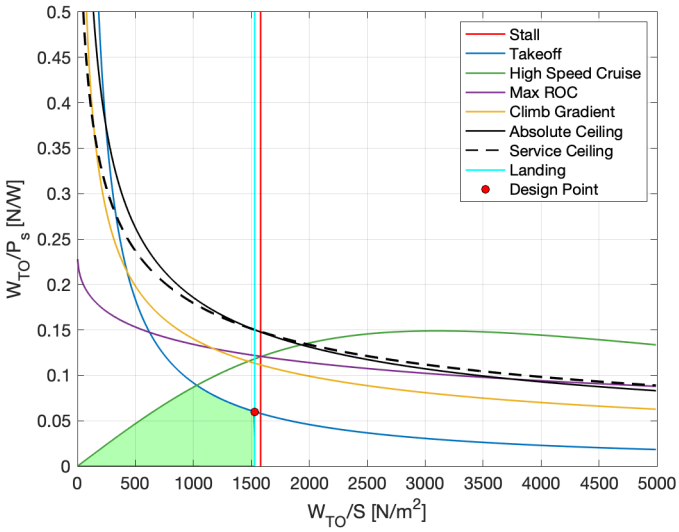

Figure 3.23: *SMP for NASA X-57 without DEP model.*

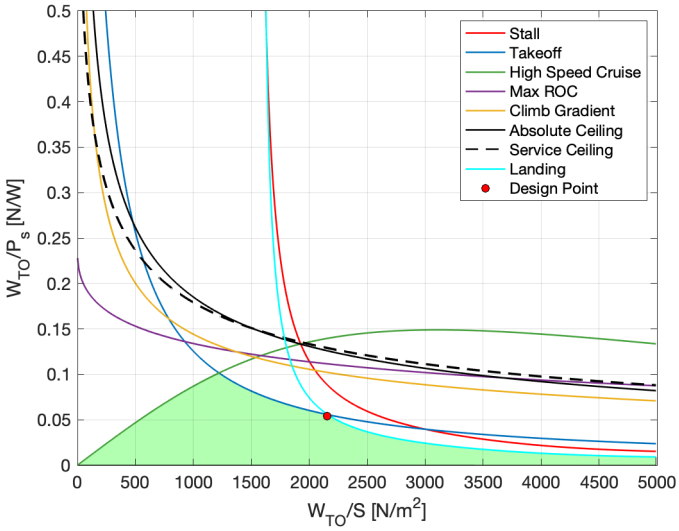

Figure 3.24: *SMP for NASA X-57 with DEP model.*

CHAPTER 4

AIRCRAFT PRELIMINARY SIZING

This chapter introduces a general procedure for the preliminary sizing of PE, THE and FCHE aircraft with the ambition to provide a tool applicable to propeller-driven, fixed-wing vehicles of arbitrary size and mission requirements. This fills up a need that is keenly felt nowadays. In fact, when looking at the blossoming literature about electric aircraft, the typical situation is either that of a retrofit of an existing airframe, or of design considerations more or less specific to a single application. The present approach to the determination of the design weights, the sizing of power-train components, and the global dimensions of the aircraft, is pursued by an integrated performance evaluation procedure, with specific provisions for electrically-driven aircraft and even for conventionally-powered ones. Hybrid-electric power-trains and their onboard integration are of primary interest in the prototypal developments of the MAHEPA project as well as in the preliminary design activities within the UNIFIER19 project, which shall soon provide measured laboratory and flight test data to make the proposed sizing methodology further accurate and reliable.

Power and energy mission requirements lead to the sizing of electric motors

and batteries, as well as the PGS and its fuel system. Other specifications peculiar to electrically-driven aircraft, such as PE-mode operations below a given altitude or energy recuperation through propeller wind-milling during descent, are considered, providing predictions related to future realistic operational uses.

A part of the work presented was developed with the contribution of the following MSc students in the frame of their thesis project: Niccolò Rossi (initial implementation of the preliminary sizing of thermal hybrid-electric aircraft), Antonio Estrada Briz and Isacco Raimo (Class I design procedures). Results related to this activity have been published in [129–132].

4.1 Methodology

The proposed sizing methodology is able to generate optimal PE and HE preliminary sizing solutions to specified mission, technology, certification, and other applicable requirements. This amounts to determining the aircraft design gross mass (Maximum Take-off Mass (MTOM)), the top-level mass breakdown specifying the mass of each of the main aircraft subsystems, the power rating of all the power-generating components, and the reference wing area. Optimality involves the minimization of MTOM, but may also be extended to other elements in the design, such as the sizing of single power-train components or the in-flight energy and power management strategies. In fact, the presented method also provides the complete time histories of numerous variables along the sizing mission. The method applies to propeller-driven airplanes with a general serial HE power-train architecture. This implies an EM driving each propeller, fed by electric energy derived from the combination of a BP and an electric PGS. The latter is included here in two fashions: in the THE case, the PGS is an engine-generator combining an electrical generator and a hydrocarbon-burning, Internal Combustion Engine (ICE) (possibly a reciprocating or turboshaft engine), supplying energy to the EM and/or the BP. In the FCHE case, the PGS is a hydrogen driven fuel cell system. Hydrogen can be stored in the gaseous or liquid form. A general serial HE architecture is outlined in Figure 4.1. The yellow box on the left represents the fuel tank, connected to the big orange box in the middle that represents the PGS. Then, the PGS is electrically linked (light blue line) to the EM (green box) which, in turn, is mechanically connected (red line) to the propeller. The blue box on top represents the BP, electrically linked to the PGS and to the EM.

Conveniently, the formulation can be implemented so that PE (battery-

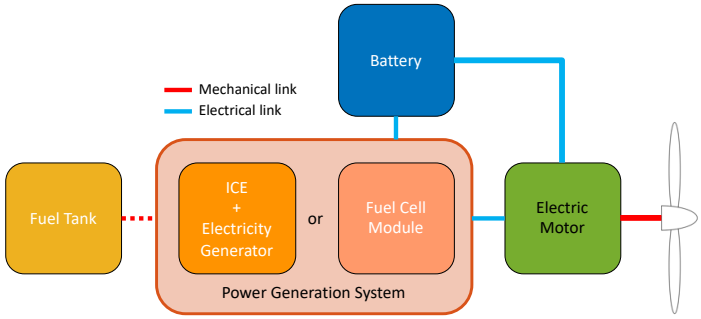

Figure 4.1: *Serial hybrid-electric power-train scheme.*

only) and conventional aircraft are easily obtained as extreme cases in the serial HE spectrum: the former by eliminating the PGS and the latter by eliminating the electric components of the power-train, i. e., BP, EMs and generators, and by 'plugging in' directly the ICE included in the PGS to the propellers.

The methodology combines the ability to resort to historical-statistical estimations and the direct modelling of aircraft main subsystems, in a modular fashion. The following discussion details the mass breakdown strategy and the sizing approach to the various power-train components, which permit to close the loop and find a reliable initial solution. Further on, it will be shown how this initial result is fine-tuned through time-marching simulations and iterations thereof. Both phases necessarily start with the consideration of a specific sizing mission.

4.1.1 Mission profile

Power and energy requirements to be applied in the mass estimation are obtained through the analysis of the flight profile of the sizing mission. When considering a typical transfer mission for a civil passenger or freight airplane, the flight profile is composed by take-off, climb, cruise at constant altitude, descent, loiter at constant altitude, approach, and landing. A diversion to an alternate destination can be considered as well. Loiter, diversion and possibly other elements may be constrained by specific applicable regulations. Apart from terminal ones, all phases are typically flown at constant Calibrated Airspeed (CAS).

Specific requirements can be imposed to each phase in relation to power and energy management. For THE, one of the most important elements is the capability to fly trajectories below a given altitude in pure-electric mode, i. e., with the PGS shut off. We shall term this altitude the Hybrid-

Electric Transition Altitude (HETA). This possibility enables a serial THE aircraft to fly as a PE one in the lower phases of flight, when both chemical and acoustic pollution is perceived the most. These include take-off, initial climb, final descent, landing, and possibly loiter as well. The capability to operate in PE mode is a crucial advantage granted by the serial architecture (in contrast to the parallel one, where a mechanical mixing of motive power from both EMs and ICEs occurs), allowing zero-emission and a considerable degree of noise abatement in the vicinity of airports as it will be discussed in Chapter 6.

Another interesting feature that can be considered is the possibility to achieve energy recuperation in descent. This means to derive battery recharging power from wind-milling propellers in gliding flight, with the PGS shut off. The importance of such feature in the design and operation of aircraft clearly depends on the flight profile characteristics and cannot be assessed *a priori*.

Above the HETA, and also below for FCHE airplanes, the PGS can be switched on according to various programmes, relative to diverse options for in-flight energy management. These may be inspired by various alternative criteria (such as minimizing the number of battery discharge/recharge cycles per flight, or minimizing the fuel burned per flight) and are clearly allowed by the possibility to draw power for flight from two independent power sources, i. e., the BP and PGS. A study illustrating the differences in the sizing of the aircraft, and consequently in the fuel consumption for a given sizing mission, when different energy management strategies are applied has been discussed in [133].

Finally, minimum values for BP SOC and fuel remaining at mission completion can be specified, to provide a reserve of energy for emergency manoeuvres and other contingencies.

4.1.2 Mass breakdown

In the present approach, the starting point for PE and HE aircraft modelling for preliminary sizing purposes lies in an appropriate formulation for the design all-up mass, i. e., the MTOM M_{TO}. This is needed to go beyond the traditional formulation of the design mass breakdown used for conventional aircraft, as found in widely-known reference textbooks [107, 121, 122] This generally provides a very convenient framework for the weight sizing of aircraft provided with a hydrocarbon fuel-burning propulsion system and reads

$$M_{TO} = M_l + M_c + M_e + M_f, \tag{4.1}$$

where M_l represents the payload mass, M_c the crew mass, M_e the empty mass, and M_f the fuel mass. While the first two terms are typically set at the beginning of the design process as a mission requirement, the latter two need appropriate estimation procedures, which typically rely on historical data and, for fuel mass, on relatively simplified performance fomulæ. Indeed, the empty mass is determined by resorting to statistical regressions based on data available for similar existing aircraft, leading to a relationship of the form $M_e/M_{TO} = f(M_{TO})$. Furthermore, the fuel mass can be determined by the 'fuel fraction method' in which each phase of a given mission profile is assigned a ratio between initial and final fuel quantities, retrieved either by statistical data or by application of range and endurance formulæ for cruise and loiter flight phases, respectively, such as Breguet equations. This also ends up with a relationship of the form $M_f/M_{TO} = f(M_{TO})$, relating mission fuel to MTOM, one a few basic parameters are assumed. Using Equation 4.1, the above relations allow to solve for M_{TO} without further difficulties. The accuracy of this procedure clearly relies on the availability of a coherent set of data related to similar existing aircraft.

When tackling the problem of PE and HE aircraft weight sizing, the procedure just sketched cannot be applied, due to the lack of consolidated data for these new airplane types, as well as to the inherent characteristics of the new power-train architectures. Therefore, a more fine-grained mass breakdown formulation is proposed for serial HE aircraft, irrespective of their category based on weight, performance, or other specifications.

$$M_{TO} = M_l + M_c + M_a + M_m + M_b + M_g + M_f + M_t, \tag{4.2}$$

where, in addition to the mass components introduced previously, M_a represents the non-propulsive airframe mass, M_m the mass of electric motors, M_b the mass of the BP, M_g the mass of the PGS and M_t the mass of the fuel tank to be considered in the case of FCHE.

The term 'non-propulsive airframe' mass is introduced here to indicate the component that takes into account of all airframe masses except those related to the power-train, encompassing structure and non-propulsive systems. This element plays an important role in matching statistical estimations from different sources. In fact, in the present case, the sum $(M_a + M_m + M_b + M_g + M_t)$ may be thought as corresponding to the empty mass but differently from the conventional approach where M_e is found as a single entity, here its estimation must be achieved term by term, by appropriate usage of statistical regressions at subsystem level, or other applicable models, such as physics-based analytic ones.

Models of either kind pertaining to EMs , BP, and PGS involve their

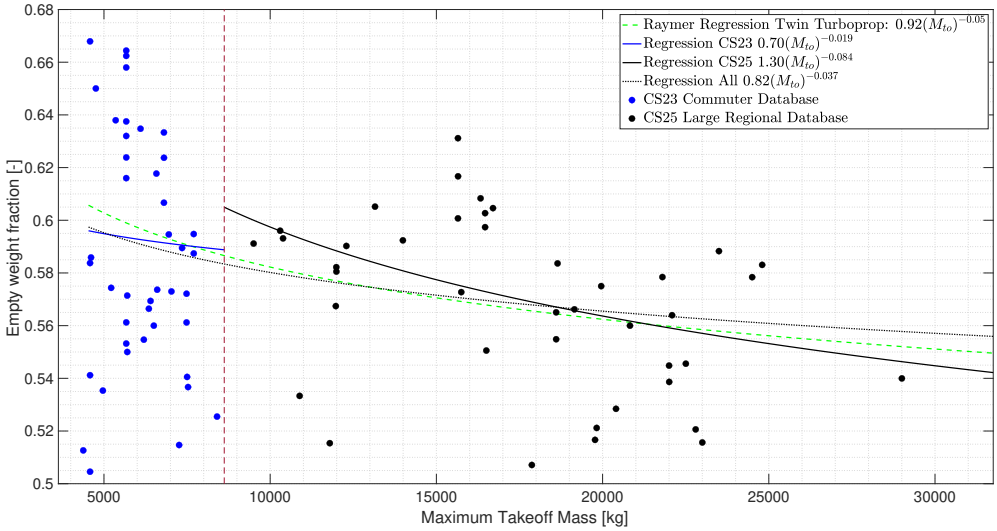

Figure 4.2: *Empty weight fraction against Maximum Take-off Mass for CS-23 Commuter and CS-25 Large regional airplanes*

power output characteristics, making the process of weight sizing inherently coupled with that performance-based sizing, which involves the determination of power loading (or its reciprocal, power-to-weight ratio) and wing loading. This is contrary to the case encountered in conventionally-powered aircraft, where weight sizing and performance-based sizing are independent of each other in principle. In addition, the integration of power required along the sizing mission provides energy storage requirements, which enter the sizing of BP and fuel tank. The following details the specific considerations adopted for the weight sizing of the components in Equation 4.2.

4.1.3 Non-propulsive airframe mass

As anticipated, the empty mass fraction M_e/M_{TO} is a typical datum retrieved by historical statistical regressions for conventionally-powered aircraft. Figure 4.2 shows examples of these regressions twin turboprop airplanes, such as the one from [107] (dashed green line) and customised ones based on airplanes data gathered from literature. The M_e term comprises the load-bearing structure, on-board systems unrelated to the power-train, including the landing gear, and the engines with their ancillary systems. This element represents a strong point in the effectiveness of the conventional preliminary sizing procedure, as suitable historical statistical regressions can be produced for the aircraft category at hand, taking into account the technology level applicable to the airframe structure and other

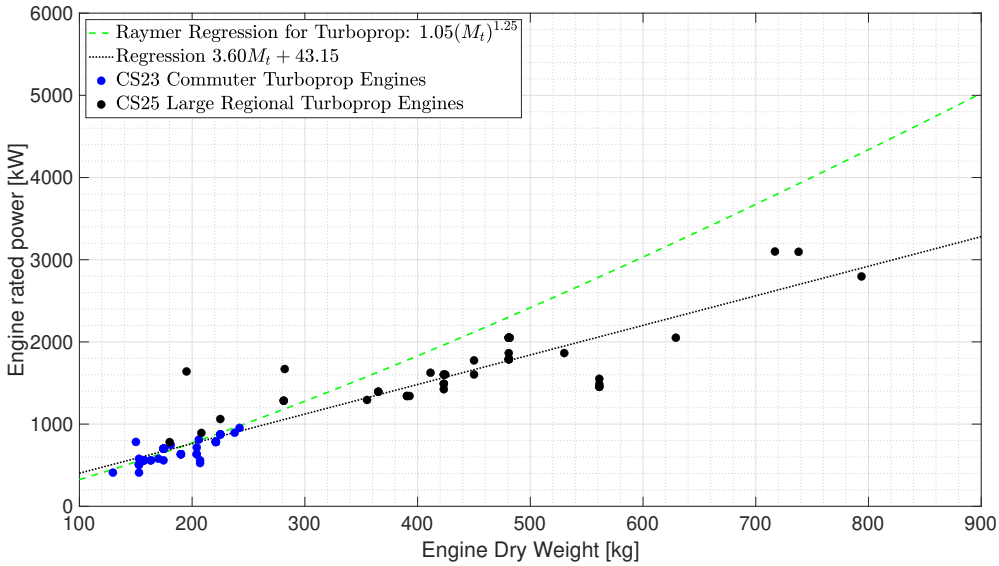

Figure 4.3: *Thermal rated power against engine dry weight for CS-23 Commuter and CS-25 Large regional airplanes*

systems.

However, this cannot be translated to the case of electrically-driven aircraft, given the scarcity of available data and the wider range of applicable general configurations. Therefore, in order to derive a suitable estimation of the non-propulsive airframe mass M_a for preliminary sizing purposes, a dedicated procedure has been deployed, leveraging on the wide availability of data for conventionally-powered aircraft.

This simple idea consists in depriving the empty mass values retrieved for conventional aircraft of the share pertaining to their engines, obtaining

$$M_a = M_e - M_{ICE}, \tag{4.3}$$

where M_{ICE} represents the mass of the thermal engines. The latter can be estimated by a historical statistical regression, based on their power such as that in Figure 4.3. The data points in the figure represent the power of the turboprop engines of the same twin turboprop airplanes in Figure 4.2, plotted against the respective engine dry weight. Two regressions are plotted on top of these points: the green dashed line is the power regression from [107] and the dotted black line is a linear regression derived from the data points.

Alternatively, M_a may directly be computed from known data pertaining to existing aircraft and then generalized by a regression. Upon validation of this approach, with regard to existing aircraft spanning multiple weight

categories, the difference between operational empty mass and engine mass is assumed as the quantity of interest M_a.

4.1.4 Batteries

Batteries are considered through their specific energy (ratio of stored energy on mass) e_b and specific power (ratio of output power on mass, this terminology is also used in the following for other components) p_b. These parameters are characteristic of a given battery cell technology and are further modified to provide for the inefficiencies related to cell stacking into packs. The mass of the battery pack M_b is then obtained as

$$M_b = \max(M_b^E, M_b^P), \tag{4.4}$$

the terms on the right-hand side being defined as $M_b^E := E_b e_b$ and $M_b^P := P_b p_b$, where E_b represents the energy to be provided by the BP according to the mission needs and P_b its required maximum power output.

For PEs and THE aircraft this corresponds to maximum power conditions, which typically occur at take-off and initial climb. Indeed, in both cases, it is the EM fed by the BP that drives the propeller, so the entirety of the motive power comes from the batteries. In the THE case this is necessary in order to allow flying terminal manoeuvres and, more generally, trajectories below the HETA in PE mode, i. e., with the PGS shut off. Therefore, the BP is sized to fulfill maximum mission power first (sizing to power), and then increased, if needed, to provide energy for the flight phases below the hybrid transition altitude (sizing to energy). Upper and lower threshold values of the BP SOC different from full charge and null charge are considered, motivated by the need to preserve battery capacity and health upon a number of discharging/recharging cycles. Also, BP charge/discharge rates can be considered, on the same bases.

In the FCHE case instead, the batteries need to help FCs to provide power during the most demanding phases of the mission (usually take-off and climb), while FCs are sized for maximum continuous power as will be discussed in the next sections. In this case the BP power is given by the difference between the maximum peak power and the FC power.

4.1.5 Electric motors

Electric motors are considered mainly through their specific power p_m, so that $M_m = P_m p_m$, where P_m is the required shaft power output. The parameter p_m is an input of the method and can retrieved from statistical

regressions based on known data of suitable existing products or be set according to predictions on future technology. An example of the current values is given in Section 2.5. Among other important parameters for the sizing lies the motor's extra power capability. This is the possibility to draw substantially higher power values for limited period of time, often in much greater amounts than with thermal engines. This extra power, Θ_m may cover take-off and initial climb requirements, thus lowering the rated power reference value, and consequently the EM mass.

4.1.6 Power generation system

4.1.6.1 Internal combustion engine

The PGS for THE power-trains combines an ICE (either reciprocating or turboshaft) of mass M_{tg} and an electrical generator of mass M_{eg}, to provide electric energy for the BP and EM needs, so that $M_g = M_{tg} + M_{eg}$, providing an output power P_g. The ICE component is sized according to its specific power p_{tg}, so that $M_{tg} = P_{tg} p_{tg}$, where P_{tg} is the required shaft power output. The parameter p_{tg} can be retrieved from statistical regressions based on known data of suitable existing products, such those in [107] or can be derived from the analysis of a selection of ICEs. As opposed to electric motors, ICEs mass is not scalable with power and the p_{tg} must be selected carefully.

For the electrical generator, as this can be considered a reversible EM, the same considerations seen above apply, with $M_{eg} = P_{eg} p_{eg}$, where $P_{eg} \equiv P_g$ is the electric power output and p_{eg} the specific power. The electrical generator power sizing is based on the power required for cruising. A basic condition may be to size the PGS so that it sustains cruise with no need of contribution by the BP, while a wider flexibility is obtained when more power is delivered by the PGSs, allowing for BP recharge in flight. Therefore, an important design parameter is represented by the ratio of P_g and the value needed to balance the power required for flight in a given cruise condition (for PEs aircraft the latter value applies to the full cruise phase, as weight is constant, while for HE aircraft the power required for cruise changes with weight along the mission).

4.1.6.2 Fuel cells

In the case of FCHE, the PGS is represented by the fuel cell system. The fuel cell system is based on a set of elementary FCs connected in series and in parallel and is directly capable of producing electricity without the

need for an electric generator. So $M_g = M_{fc}$ where $M_{fc} = P_{fc}p_{fc}$ is the mass of the overall fuel cell system. The term p_{fc} is the specific power while P_{fc} is the rated power. Opposite to the the PGS in the THE case, the fuel cell system is sized with the maximum continous power.

4.1.7 Fuel

The fuel quantity for the design sizing mission is clearly related to the energy delivered through the PGS according to the various phases of the mission profile (including adequate reserves). Fuel energy density e_f (ratio of stored chemical energy on mass) is the primary parameter used in the sizing as well as the efficiency of the thermal engine/fuel cell (η_{tg} or η_{FC} respectively) so that $M_f = E_f e_f \eta_{tg}$ for the thermal engine or $M_f = E_f e_f \eta_{FC}$ for fuel cell systems. The efficiency of the TE and FC is not constant and usually varies with altitude, airspeed and, most importantly, power rating. For η_{tg} the maps introduced in Section 3.4.2 to retrieve the BSFC can be used. The BSFC c_P is, in fact, linked to η_{tg} as

$$\eta_{tg} = \frac{1}{c_P e_F}. \tag{4.5}$$

The FC efficiency η_{FC} instead, is calculated recurring to the polarization curve and the definition of efficiency in Equation (3.26).

4.1.8 Fuel tank

The mass of the fuel tank is neglected for conventional ICE driven airplanes, as tanks are usually part of the airframe. However, as outlined in Chapter 2, hydrogen tanks are usually both heavy and bulky and their mass cannot be neglected in the sizing process. Therefore

$$M_t = \frac{M_f(1-\mu_g)}{\mu_g} \tag{4.6}$$

being μ_g the gravimetric index of the tank. For GH2 tanks the gravimetric index is taken as a given input, while for LH2 tanks, the gravimetric index is estimated with a tank design process that minimizes the boil-off losses while maximizing the corrected gravimetric index in Equation (3.44).

4.1.9 Matching performance requirements

As previously mentioned, the classical separation that exists – at least at conceptual level – between design gross mass estimation and the power

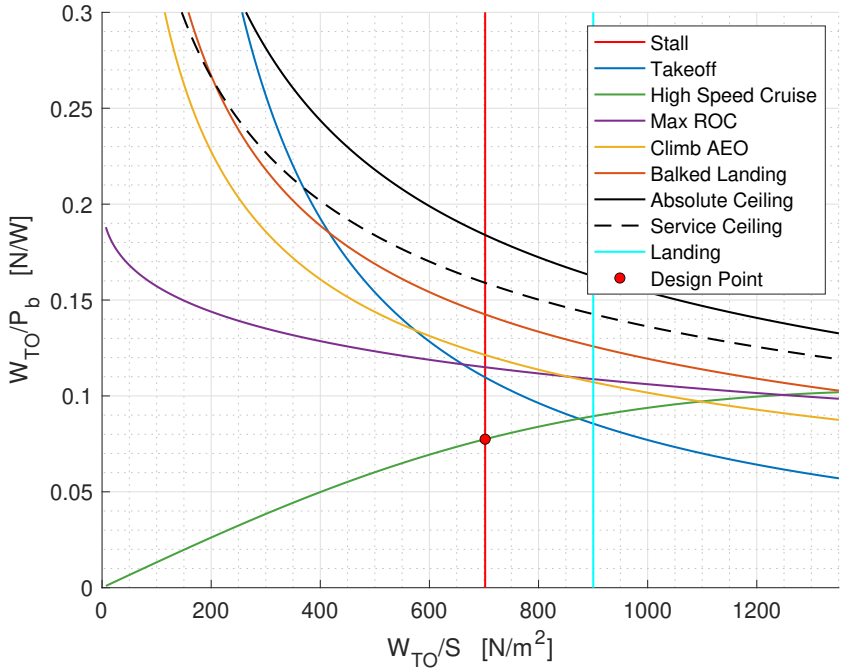

Figure 4.4: *Sizing matrix plot for the Cessna 172.*

loading/wing loading pair for conventionally-powered aircraft does not hold with PE and HE aircraft [133–135]. This separation basically amounts to the fact that power needs determine the engine sizing, while mission energy is independently taken into account by the fuel fraction method [107, 121]

Here, point performance and mission profile requirements are inherently coupled when it comes to the sizing of the energy sources and power supply devices, as seen from the above considerations. Therefore, all power and energy mission requirements must be considered in order to solve Equation 4.2 simultaneously with the choice of an appropriate design point on the SMP as discussed in Section 3.6. This consists in the determination of the design power loading W_{TO}/P_s and wing loading W_{TO}/S, being $W_{TO} = M_{TO}g$ the design gross weight, P_s the shaft brake-power and S the wing surface, which guarantees a number of point and terminal performance requirements derived from mission analysis, certification standards, and other design specifications.

As an example, Figure 4.4 shows the SMP for Cessna 172 four-seater, that will be later used as a reference GA aircraft for the validation of the sizing methodology. Let us remark that the curves represent feasibility boundaries and admissible values for the design values of the power loading/wing

loading pair lie under each curve or on the left in the case of vertical lines. In the case of Figure 4.4, the feasibility region is bounded, from increasing values of the design wing loading, by the maximum cruising speed and the stalling speed in the landing configuration.

4.1.10 Mission simulation

Once a solution is found for Equation 4.2, the resulting airplane model can be used to simulate the sizing mission and assess the results obtained in a situation where further details that may have an impact on the preliminary sizing are considered. The basic equations of motion used in Flight Mechanics for trajectory analysis and performance evaluation are invoked in simulating the mission with a time-marching algorithm, to derive the time histories of various quantities of interest, such as power ratings, BP SOC, fuel level, etc.

A critical element in the simulation is the in-flight energy and power management strategy. Given the plurality of energy sources on board, the designer has the possibility to define diverse strategies in employing energy from the BP and/or the PGS, as well as recharging the BP by using excess power from the PGS or even by recuperating energy in gliding phases. A first strategy could be "cyclic" operation for the BP. Indeed, in this case, the battery is discharged in the beginning of the mission, up to the lower threshold and then recharged. As soon as the upper threshold is reached, the BP is again discharged, and so on. The activation of the PGS follows accordingly to the current power requirement, so that it is kept off if the BP power is sufficient, and then turned on when the BP cannot sustain the power required for flight. A second strategy could be operating the BP in a quasi “steady” SOC for most of the time. In this case, after the completion of the initial portion of the flight performed in PE mode, the BP is recharged and kept as close to full charge as possible during the remaining part of the mission. Consequently, the PGS is kept running until the HETA is reached during descent. It can be demonstrated that neither of the previous strategies is energy-optimal, under the considered conditions [133]. Indeed, both of them cannot guarantee to complete the sizing mission with the minimum amount of energy stored on board, nor to fly each segment at the best possible efficiency, given that the aircraft mass changes in different ways. A study in optimization reveals that the optimal strategy is very similar to the “steady” strategy. This has the advantage of burning fuel, so reducing aircraft mass, as soon as possible, except for the fact that towards the end of the mission, the PGS is switched off before reaching the transition altitude and PE mode is estab-

lished so that the residual energy on board at landing exactly matches the requirements.

Depending on the mission characteristics and the other design requirements, the energy and power management strategy may have an impact on the preliminary sizing, so that a correction of the initial sizing solution may be in order. This fine tuning is obtained by iterating between the process providing the initial guess and the simulation of the sizing mission, until convergence.

Furthermore, the mission simulation capability may be used to analyze off-design performance and perform parametric studies of a given design solution.

4.2 Implementation

The methodology consists in a two-step procedure. First, the requirements from mission analysis are imposed together with certification standards, and other design specifications, a first-guess design point is chosen on the SMP, and an iterative calculation gathering all elements discussed above is carried out for the weight sizing until Equation (4.2) converges. This provides an initial solution in terms of mass breakdown, power sizing and wing sizing, together with the estimation of some basic quantities of geometric and aerodynamic nature (such as the wing aspect ratio and the aircraft drag polar curve). The initial solution is used to start another iterative computation in which the full sizing mission is simulated by a time-marching algorithm. This procedure allows to take into account the time evolution of the dynamics of the power-train in a finer manner, typically leading to adjustments on the initial estimations.

This process was implemented in a computational tool named HYbrid PERformance SimulatION (HYPERION). Its schematics is depicted in Figure 4.5, where *AircraftSizing* stands for the core of the operations leading to the initial solution, while *FMS* (Flight Mission Simulation) represents the time-marching computation block. The process starts by solving Equation (4.2) through an initial MTOM guess and looping until convergence, while accommodating all mission requirements and performance specifications derived by the applicable certification basis or other design considerations and bringing into play a number of parameters yielded by the market analysis and technology survey that are normally carried out prior to the start of conceptual design.

Within *AircraftSizing*, all components of Equation (4.2) are adjusted in a fully coupled manner, taking into account changes in power and en-

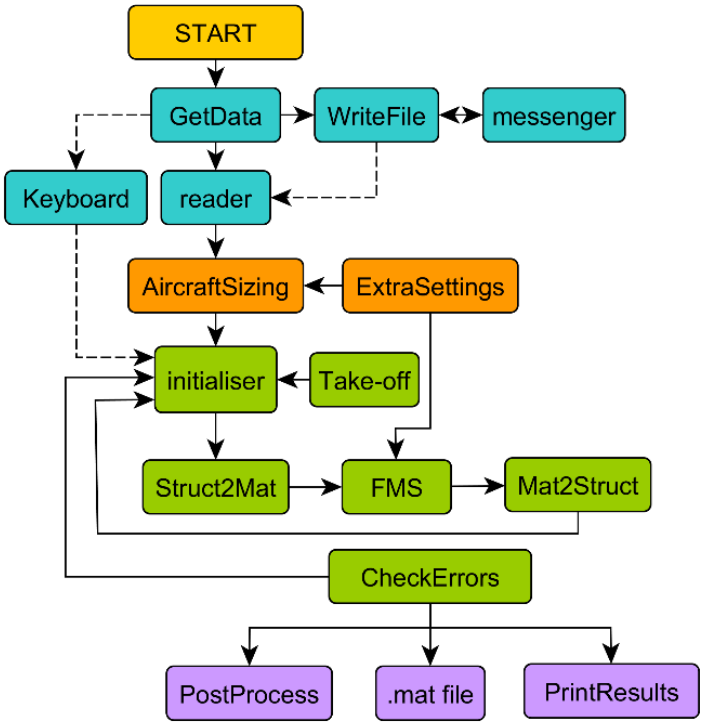

Figure 4.5: *Flowchart of the HYPERION preliminary sizing tool.*

ergy needs arising from changes in mass of the various components, and viceversa, and seeking minimum gross design weight. Once convergence is achieved, the time simulation in *FMS* is deployed, and the masses of energy storage components, i. e., BP and fuel tank, are corrected in order to satisfy mission requirements punctually. This typically leads to small adjustments that do not require adaption of the masses of the other variable components, i. e., EMs , PGS, and non-propulsive airframe. In case adjustments are more substantial, the process can be repeated feeding *AircraftSizing* with the *FMS* solution as the initial guess.

4.3 Validation

Since the methodology is aimed to the maximum generality in the field of propeller-driven airplanes, an extensive validation effort has been deployed to check its ability in supporting design exercises across the various aircraft classes. To this end, numerous application exercises dealing with aircraft types certified under both FAR23/CS-23 and FAR25/CS-25, ranging from the lighter GA models to large regional turboprops have been considered. The aim is the comparison of the preliminary sizing results MTOM and mass breakdown, wing area, and power installed from a HYPERION simulation obtained by imposing the Top Level Aircraft Requirements (TLAR) corresponding to an existing airplane model and the corresponding data of such model.

As HE aircraft are not yet in the market, the few examples being essentially prototypes that cannot represent a statistically meaningful population, a first task involves the comparison of results obtained for conventionally-powered aircraft for which sufficient data are available. In the following, four examples are reported: a four-seat GA airplane; a 11-seat small commuter ; a 19-passenger large commuter; and a 70-passenger airliner. The possibility to retrieve a conventional, ICE-powered design solution without changing anything in the implementation of the method is especially convenient in permitting such a validation against existing aircraft types. Secondly, in order to provide at least an example concerning an existing HE aircraft, a case study has been carried out by taking reference on the Pipistrel Panthera Hybrid, one of the two innovative prototypes currently being developed in the MAHEPA project [16].

This "validation" is to be considered as a mean to assess the proximity of an original design solution obtained by the present approach and an existing aircraft, for which a number of other factors, out of the scope of the present methodology, may have come into play when it comes to

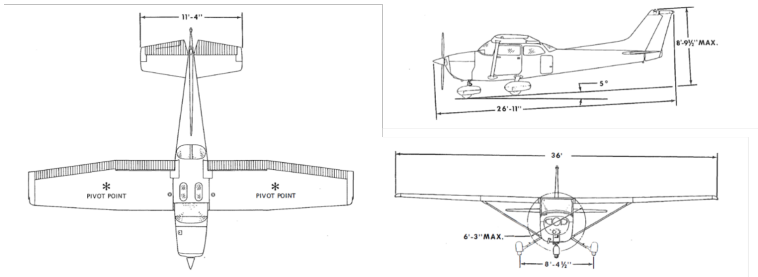

Figure 4.6: *Cessna Model 172 Skyhawk (from the aircraft Pilot's Operating Handbook).*

its final sizing. This process is a "blind" comparison, as no tuning of parameters on a case-by-case basis was enforced, nor any other action aimed at providing a better match. Therefore, a perfect superposition is largely unlikely to occur and a reasonable criterion to assess the quality of the results must be adopted. Presently, we shall consider a difference up to 5% for all items in the preliminary sizing data to be a measure of high reliability of the design solution, with discrepancies occurring in some items up to 10% to be still acceptable.

As the two major sources of uncertainty in the sizing of a conventional airplane are related to the statistical estimation of the empty mass and the modelling of the propulsion system, namely with respect to specific engine power and fuel consumption, a pre-validation was carried out before deriving a completely original design solution. This pre-validation consisted in running the HYPERION tool by substituting the empty mass estimation with the actual value for the aircraft at hand, thus eliminating one of the sources of possible uncertainty. This operation allows thus to appreciate possible discrepancies in the propulsive model.

4.3.1 General aviation validation

The first case study involves a well-known airplane, the Cessna 172, shown in Figure 4.6. This high-wing aircraft, powered by a Continental O-300 piston engine providing 145 hp, is a mainstay in GA worldwide and provides the capability of hosting four occupants for leisure and flying school missions.

The HYPERION design solution was obtained by imposing a sizing mission characterized by the official data for this type, as reported in Table 4.1 and applying the FAR23/CS-23 regulations. The mass of the occupants corresponds to four persons on board.

Table 4.1: *Main design requirements for the Cessna 172.*

Crew+payload mass	258 kg	17.7 slug
Range	960 km	518 NM
Stalling EAS	24.7 m/s	48 kn
Cruising EAS	56.1 m/s	110 kn
Cruising altitude	2,500 m	8,202 ft
Take-off distance	497 m	1,630 ft
Landing distance	407 m	1,335 ft
Max maximum rate of climb at sea level	3.71 m/s	730 ft/min

Table 4.2: *Pre-validation for the Cessna 172 design solution.*

	M_{TO} [kg]	M_f [kg]	S [m^2]	P_s [kW]
Real	1,157	147	16.2	134
Simulated	1,165	153	16.2	147
Error [%]	+0.6	+3.7	0.0	+9.6

In the pre-validation, by forcing the airplane empty mass value, the sizing results in Table 4.2 were obtained. Here and in the following, "Real" stands for official data, "Simulated" for the HYPERION results, and "Error" for the percentage difference, i. e., the latter minus the former, divided by the former. The tabulated values show a very accurate solution, with the exception of installed power, for which a discrepancy of nearly 10% is observed, suggesting the degree of uncertainty in the statistical estimation of the specific power of the ICE.

The unconstrained design solution was then considered, by restoring the empty mass estimation based on statistic data for single-engine GA airplanes, obtaining the sizing results in Table 4.3, Case I. As seen, the simulated aircraft is surprisingly much lighter and smaller than the real one, with differences in all mass items ranging from 15% to 25%, that in wing reference surface over 18%, while the discrepancy in the installed power is close to the value obtained in the pre-validation.

This seems at odds with the pre-validation results, hinting at possible problems in estimating the empty mass, which is the item achieving the maximum variance. Indeed, by changing the empty mass fraction regression from the one representing single-engine GA airplanes to that of agricultural airplanes, the sizing results in Table 4.3, Case II, are retrieved. In this case the simulated aircraft is extremely close to the real one: the difference in all mass items is below 2.3%, that in wing reference surface is 1.7%. Again, the installed power shows a discrepancy of the same order of the previous cases.

We conclude that a likely reason for this behaviour lies in the old age of

Table 4.3: *Validation for the Cessna 172 design solution.*

	M_{TO} [kg]	M_e [kg]	M_f [kg]	S [m^2]	P_s [kW]
Real	1,157	754	147	16.2	134
Simulated I	950	568	124	13.2	120
Error I [%]	-17.9	-24.7	-15.3	-18.4	-10.5
Simulated II	1,145	737	150	15.9	144
Error II [%]	-1.1	-2.3	+2.0	-1.7	+7.7

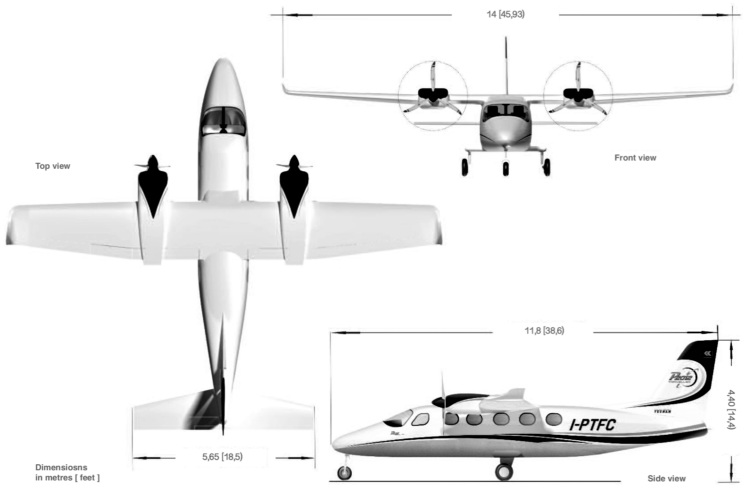

Figure 4.7: *Tecnam P2012 Traveller (adapted from a company publication in the public domain).*

the Cessna 172 design, which implies a higher weight of its airframe when compared to other, more recent models. Therefore, rugged airplanes in the agricultural category, characterized by higher empty mass fractions, seem to better fit this case.

4.3.2 Small commuter validation

The second case study involves an utility airplane, the P2012 Traveller, a FAR23/CS-23 commuter designed and manufactured by the Italian Tecnam, shown in Figure 4.7. This high-wing aircraft, powered by a pair of Lycoming TEO-540-C1A piston engines, each providing 375 hp, is included here as a recent example in the smaller commuter category, carrying up to nine passengers.

The HYPERION design solution was obtained by imposing a sizing mission characterized by the official data for this type, as reported in Table 4.4, where a single-pilot operation with eight passengers is assumed,

Table 4.4: *Main design requirements for the Tecnam P2012.*

Crew mass	100 kg	6.9 slug
Payload mass	810 kg	55.5 slug
Range	825 km	445 NM
Stalling EAS	30.9 m/s	60 kn
Cruising EAS	76.2 m/s	148 kn
Cruising altitude	1,830 m	6,000 ft
Take-off distance	570 m	1,870 ft
Landing distance	506 m	1,660 ft
Max maximum rate of climb at sea level	8.13 m/s	1600 ft/min

Table 4.5: *Pre-validation for the Tecnam P2012 design solution.*

	M_{TO} [kg]	M_f [kg]	S [m^2]	P_s [kW]
Real	3,600	440	25.4	560
Simulated	3,617	458	25.4	553
Error [%]	+0.5	+4.0	+0.0	-1.3

and applying the FAR23/CS-23 regulations. Again, a pre-validation was carried out, obtaining the sizing results shown in Table 4.5. The matching is clearly very accurate, even better that in the case of the Cessna 172.

The unconstrained design solution led to the sizing results shown in Table 4.6. In contrast to the pre-validation, in this case the results are less satisfactory. The difference in MTOM amounts to 14.6%, with the HYPERION solution being the lighter, and again this is the effect of the discrepancy in the empty mass, amounting to 21.1%. We are led to suppose a problem related to the capability of the empty mass fraction statistical regression used in this case to capture this specific case. Indeed, by considering a population of similar aircraft, such as in Figure 4.2, a significant scattering (much higher than for other categories, such as FAR25/CS-25 aircraft) is observed and the value for the P2012 looks higher than "average". The lighter overall weight induces a lower need for installed power, with almost 10% difference, which in turn implies a lower weight for the engines.

Although the validation results do not guarantee a sufficient reliability in this specific case, the *outlier* character of this airplane seems to explain the discordant results, while the pre-validation plainly confirms the overall validity of the method.

Table 4.6: *Validation for the Tecnam P2012 design solution.*

	M_{TO} [kg]	M_{oe} [kg]	M_f [kg]	S [m^2]	P_s [kW]
Real	3,600	2,250	440	25.4	560
Simulated	3,074	1,775	389	21.6	503
Error [%]	-14.6	-21.1	-11.6	-15.0	-10.1

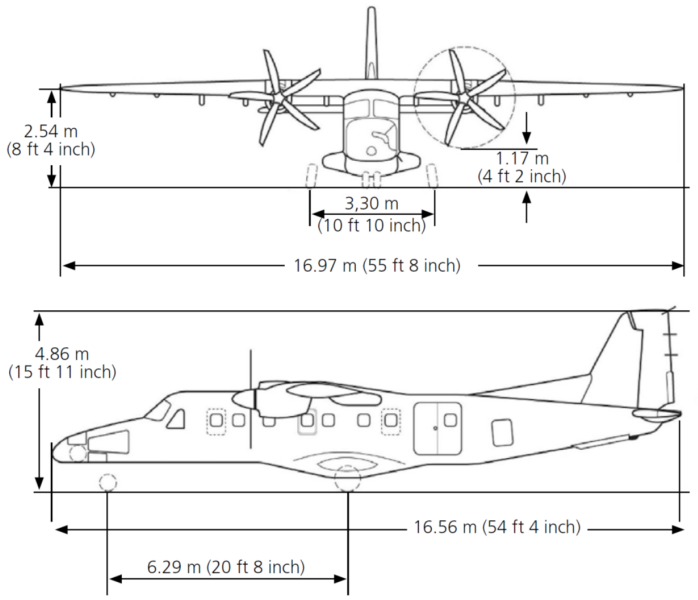

Figure 4.8: *Dornier Do228NG (adapted from a company publication in the public domain).*

4.3.3 Large commuter validation

The third case study involves a larger airplane, the 19-passenger Dornier Do228NG, which lies at the upper end of the FAR23/CS-23 commuter category, shown in Figure 4.8. This high-wing, pressurized STOL aircraft, powered by a pair of Pratt & Whitney Canada PT6A turboprop engines, each providing 776 shp, is now produced by RUAG.

The HYPERION design solution was obtained by imposing a sizing mission characterized by the official data for this type, as reported in Table 4.7, relative to a crew of two and a full load of 19 passengers, and applying the FAR23/CS-23 regulations.

The pre-validation provided the sizing results shown in Table 4.8. The agreement is generally very good, again with a larger variance in the fuel mass, which is attributed to a discrepancy in the assumed equivalent specific fuel consumption (ESFC) of the turboprop engines.

Table 4.7: *Main design requirements for the Dornier Do228NG.*

Crew mass	206 kg	14.1 slug
Payload mass	1,960 kg	134.3 slug
Range	398 km	215 NM
Stalling EAS	35.0 m/s	68 kn
Cruising EAS	105.1 m/s	204 kn
Cruising altitude	2,438 m	8,000 ft
Take-off distance	792 m	2,598 ft
Landing distance	900 m	2,953 ft
Max maximum rate of climb at sea level	7.98 m/s	1,571 ft/min

Table 4.8: *Pre-validation for the Dornier Do228NG design solution.*

	M_{TO} [kg]	M_f [kg]	S [m^2]	P_s [kW]
Real	6,400	540	32.0	1,402
Simulated	6,330	470	31.4	1,382
Error [%]	-1.1	-13.0	-1.8	-1.5

The unconstrained design solution led to the sizing results shown in Table 4.9. As it can be noticed, the simulated aircraft is extremely close to the real one. The differences are all reduced with respect to the previous case, as the slight overestimation of M_{oe}, balances out the variance in M_f. The agreement appears extremely good for all other items.

4.3.4 Large regional validation

The fourth case study involves a much larger aircraft in the CS-25 category, the ATR72-600, shown in Figure 4.9. This is a high-wing, pressurized airplane powered by a pair of Pratt & Whitney Canada PW127 turboprop engines, each providing 2,475 shp, that can carry up to 78 passengers. This aircraft is one of the most common regional airliners worldwide and may typify the upper end of mid-future HE applications in air transportation.

The HYPERION design solution was obtained by imposing a sizing mission characterized by the official data for this type, as reported in Table 4.10, assuming a crew of two pilots and two flight attendants, and a payload of 72 passengers, and applying the FAR25/CS-25 regulations.

Table 4.9: *Validation for the Dornier Do228NG design solution.*

	M_{TO} [kg]	M_{oe} [kg]	M_f [kg]	S [m^2]	P_s [kW]
Real	6,400	3,694	540	32.0	1,402
Simulated	6,441	3,796	478	32.0	1,406
Error [%]	+0.6	+2.8	-11.5	0.0	-0.3

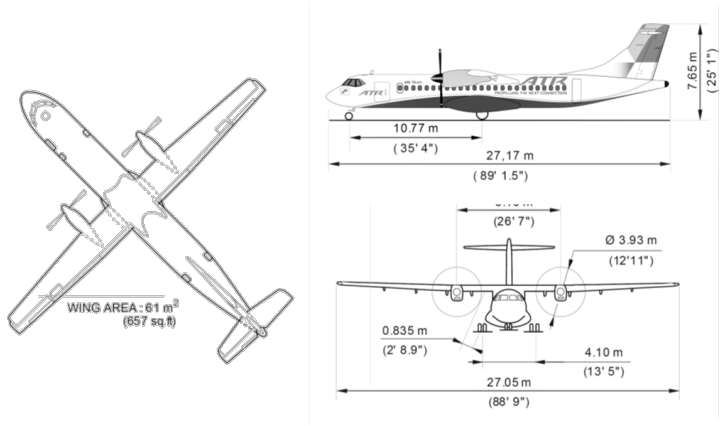

Figure 4.9: *ATR72-600 (adapted from a company publication in the public domain).*

Table 4.10: *Main design requirements for the ATR72-600.*

Crew mass	380 kg	26.0 slug
Payload mass	7,500 kg	514.0 slug
Range	1,297 km	700 NM
Stalling EAS	47.8 m/s	93 kn
Cruising EAS	87.5 m/s	170 kn
Cruising altitude	7,010 m	23,000 ft
Take-off distance	1,367 m	4,485 ft
Landing distance	900 m	2,953 ft
Max maximum rate of climb at sea level	6.09 m/s	1,200 ft/min

Table 4.11: *Pre-validation for the ATR72-600 design solution.*

	M_{TO} [kg]	M_f [kg]	S [m^2]	P_s [kW]
Real	23,000	2,000	61.0	3,728
Simulated	22,937	1,936	60.5	3,945
Error [%]	-0.3	-3.1	-0.9	+5.8

Table 4.12: *Validation for the ATR72-600 design solution.*

	M_{TO} [kg]	M_{oe} [kg]	M_f [kg]	S [m^2]	P_s [kW]
Real	23,000	13,120	2,000	61.0	3,728
Simulated	23,233	13,389	1,963	61.2	3,996
Error [%]	+1.0	+2.1	-1.9	+0.4	+7.2

The pre-validation provided the sizing results shown in Table 4.11. The agreement is very good, the larger variance being again found in the fuel mass, hinting to a discrepancy in the ESFC estimation.

The unconstrained design solution led to the sizing results shown in Table 4.12. Also in this case, the simulated aircraft represents almost a copy of the real one, from the point of view of preliminary sizing, with differences below 2.1% for the masses, 0.4% for the wing surface and 7.2% for the shaft power.

4.3.5 Hybrid-electric aircraft validation

The Panthera Hybrid is a serial HE aircraft derived by the piston-engine powered Panthera, a FAR23/CS-23 category aircraft designed and manufactured by Slovenian Pipistrel, shown in Figure 4.10. The original Panthera is an all-composite, four-seat GA aircraft powered by a Lycoming IO-540, providing 260 hp. It has been chosen as the candidate for a high-technology retrofit based on a serial HE power-train based on a new 200 kW EM and a 110 kW PGSs, developed within the MAHEPA project. This aircraft is expected to achieve its maiden flight by the end of 2020.

The HYPERION design solution was obtained by imposing a sizing mission according to company data. Table 4.13 reports data that is not restricted by confidentiality. The mission assumes two occupants.

The pre-validation provided the sizing results shown in Table 4.14. In this case, the fixed quantity is not the empty mass but the non propulsive mass M_a. Clearly, in the present case the output of the sizing include not only MTOM, fuel mass, wing area, and installed power, but battery mass and PGSs-ICE power as well. The agreement is very good, and the larger error is found in the fuel mass, as before with a difference of 11%, the

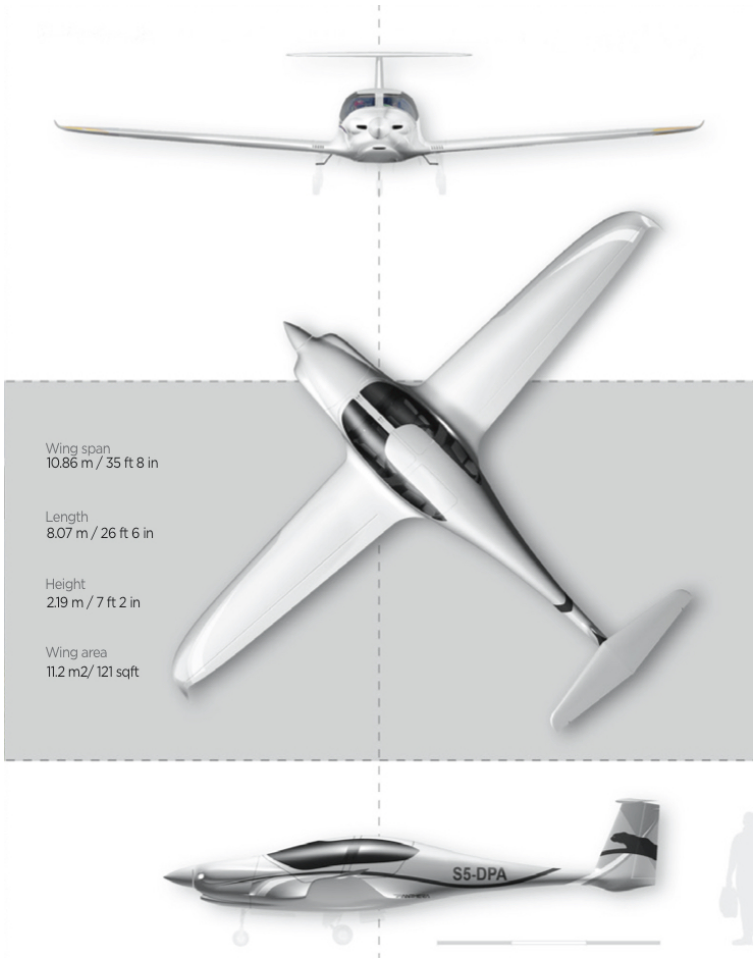

Figure 4.10: *Pipistrel Panthera (from a company publication in the public domain).*

Table 4.13: *Design requirements for the Panthera Hybrid*

Crew + payload mass	312 kg	21.4 slug
Range	650 km	350 NM
Stalling EAS	30.9 m/s	60 kn
Cruising EAS	75.0 m/s	145.7 kn
Cruising altitude	3700 m	12000 ft
Take-off distance	530 m	1,740 ft
Landing distance	570 m	1,870 ft
Max maximum rate of climb at sea level	5.9 m/s	1150 ft/min

Table 4.14: *Pre-validation for the Panthera Hybrid design solution.*

	M_{TO} [kg]	M_b [kg]	M_f [kg]	S [m^2]	P_m[kW]	P_{tg} [kW]
Real	1,315	150	53	11.2	150	99
Simulated	1,333	157	59	11.4	147	107
Error [%]	+1.4	+5	+11	+1.6	-2.4	+7.7

Table 4.15: *Validation for the Panthera Hybrid design solution.*

	M_{TO} [kg]	M_a [kg]	M_b [kg]	M_f [kg]	S [m^2]	P_m[kW]	P_{tg} [kW]
Real	1,315	691.4	150	53	11.2	150	99
Simulated	1,241	621.0	146	54.8	10.6	136	99
Error [%]	-5.7	-10.0	-2.7	+3.4	-5.5	-9.3	-9.5

simulated being heavier.

The unconstrained design solution led to the sizing results shown in Table 4.15. Also in this case, results are quite satisfactory with the biggest error being 10% for the M_a term. The error on the battery mass is very contained, only -2.7%, while the error on EM installed power and PGS power is less than 10%.

4.3.6 Distributed electric propulsion aircraft validation

A final validation exercise is shown for an airplane equipped with a DEP system. The selected reference aircraft is the PE NASA X-57 Maxwell Mod IV, already introduced in Section 3.6 and shown in Figure 4.11. In the case of DEP, HYPERION performs the sizing using the new SMP formulation introduced in Section 3.6 for the definition of the wing loading and power loading design point. The SMP employed for the sizing is that of Figure 3.24. The HYPERION design solution was obtained by imposing a sizing mission characterized by the data retrieved in literature for this airplane, as reported in Table 4.16, assuming a crew/payload of 209 kg, and applying the FAR23/CS-23 regulations, apart for One Engine Inoperative (OEI) requirements, that are still in discussion for DEP systems. A residual 20% battery SOC is assumed as energy reserve at the end of the mission with no provision for loiter [124]. The battery is sized with a specific energy of 120 Wh/kg and a specific power of 700 W/kg, estimated from dissemination material on X57. The efficiency of all the EMs, is set to 0.875 while the specific power is 2737 W/kg for the tip motors and 4487 W/kg for EMs that drive the high-lift propellers [136].

The pre-validation provided the sizing results shown in Table 4.17. The agreement is generally very good, with a larger variance in the battery

Figure 4.11: *Rendering of NASA-X57 (from NASA's website).*

Table 4.16: *Main design requirements for the NASA X57*

Payload mass	209	14.3 slug
Range	106 km	57 NM
Stalling EAS	29.8 m/s	58 kn
Cruising EAS	61.7 m/s	120 kn
Cruising altitude	1,829 m	6000 ft
Take-off distance	394 m	1,293 ft
Landing distance	350 m	1,148 ft
Max maximum rate of climb at sea level	3.20 m/s	630 ft/min

Table 4.17: *Pre-validation for the NASA X-57 design solution.*

	M_{TO} [kg]	M_b [kg]	S [m^2]	P_m [kW]
Real	1,360	390	6.2	246
Simulated	1,381	413	6.4	253
Error [%]	1.5	5.9	3.2	2.8

Table 4.18: *Validation for the NASA X57 design solution.*

	M_{TO} [kg]	M_a [kg]	M_b [kg]	S [m^2]	P_m [kW]
Real	1,360	688	390	6.2	246
Simulated	1,336	659	399	6.2	245
Error [%]	-1.8	-4.2	2.3	0.0	-0.4

mass, which is slightly overestimated. The unconstrained design solution led to the sizing results shown in Table 4.18. As it can be noticed, the simulated aircraft is extremely close to the real one. Except for the MTOM, the differences are all reduced with respect to the pre-validation. In this case, the biggest error is -4.2% on the airframe mass estimation and, while still observing a slight overestimation of the battery mass, the agreement appears extremely good for all other items.

4.4 Thermal hybrid-electric solutions

First, we are concerned with a THE solution for a small GA aircraft, inspired by the model already considered in the validation, the Cessna 172. This implies the consideration of the same requirements shown in Table 4.1, together with the applicable FAR23/CS-23 regulations and other applicable rules, including energy reserves for a 45-minute loiter at 1,500 ft.

A first THE design solution, named A4THE, was investigated by considering the same sizing mission specifications of the Cessna 172. The corresponding SMP is shown in Figure 4.12, where the same array of limiting curves is depicted with the same color coding as in Figure 4.4. It must be remarked that the two figures do not coincide, some curves being different, in spite of them representing exactly the same performance constraints. In fact, some special features of HE aircraft have an influence on the drawing of the SMP curves, essentially for two main reasons, related to the adoption of the nominal power P_s in the evaluation of the power loading:

a. In performance at altitude items, the reference power value does not depend on altitude, being P_s coincident with P_m; this is particularly

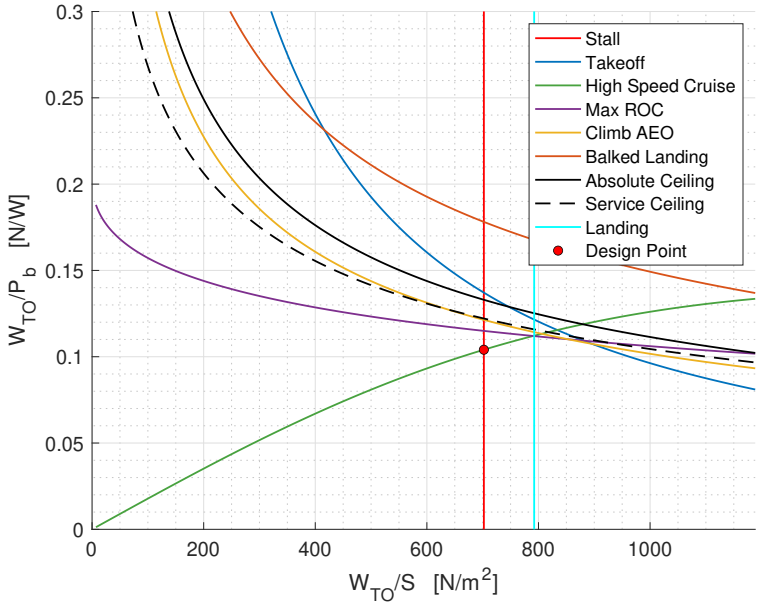

Figure 4.12: *Sizing matrix plot for the A4H.*

visible in the rising of the maximum cruising speed curve.

b. In time-limited maximum performance items, the reference power is higher than P_s, i. e., maximum continuous shaft power, whenever significant extra power can be supplied by the EMs; this is particularly visible in the rising of the take-off distance curve, as we assumed a 25% extra power.

The net effect is a remarkable enlargement of the admissible design area, leading to a choice of the design point at $(704.7\,\mathrm{N/m^2}, 104.4\,\mathrm{N/W})$ instead of the Cessna 172 case at $(704.7\,\mathrm{N/m^2}, 77.7\,\mathrm{N/W})$. The resulting 18.5% increase in power loading allows a design that needs less power installed (and therefore a lighter EM) at the same MTOM, which is definitely a favourable circumstance when dealing with the generalized weight penalties of electric propulsion systems.

The HETA was set to 1,400 ft ($\approx$ 425 m), in both climb and descent. The selected battery technology involves $p_b = 1.365$ kW/kg and $e_b = 0.210$ kWh/kg. These values are representative of 2020 LIB technology. This allows the BP to be sized according to power needs (thus, extra energy is available). The maximum and minimum allowed BP SOC values are set at 85% and 20%, respectively. In addition, end-of-flight stored energy requirements are imposed, calling for minimum BP SOC and 5% fuel remaining at landing.

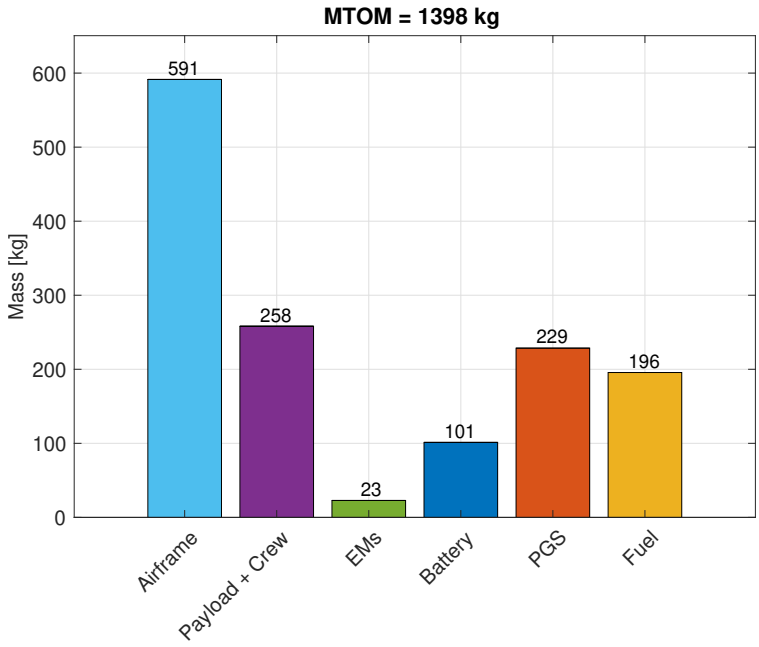

Figure 4.13: *Mass breakdown for the A4H design solution.*

The value for the A4H MTOM is found as 1,392 kg, which represents a 21% increase compared to the original Cessna 172 value. It must be noted, however, that the empty mass fraction regression for single-engine GA airplanes was employed in computing the non-propulsive airframe mass, therefore a fairer comparison should be made with respect to the values obtained in the validation for the Cessna 172, Case I.

The value for the wing reference surface is 19.5 m^2, representing a 20% increase with respect to the Cessna 172 Case I design solution. The installed EM power is 131.3 kW, which is lower by 2.3% than the installed power of the original Cessna, in spite of the larger dimensions of the airplane, mainly thanks to the high available extra power (25%).

Figure 4.13 shows the mass breakdown for the A4H: it is seen that the non-propulsive airframe mass M_a amounts to 44.1% of M_{TO}, while M_m, M_b, M_g, M_f represent the 1.6%, 7.2%, 16.4%, 14.0%, respectively. The payload mass ratio is $M_l/M_{TO} = 18.4\%$ (including the crew).

Figures 4.14a and 4.14b depict the time evolution of the energy stored on board, obtained by applying an optimized energy management strategy [133]. In Figure 4.14a, the BP SOC (blue), fuel quantity (yellow), and PGS throttle level (red) are shown together with the altitude profile (dashed black). The PGS throttle level represents how much power is

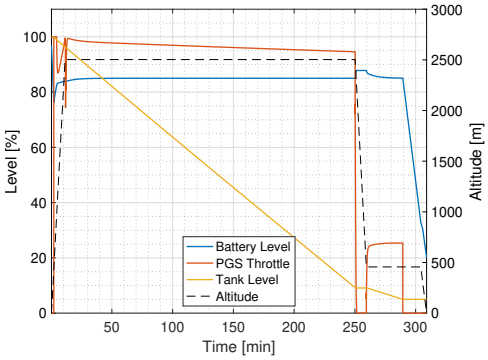

(a) *Time histories of battery state of charge (blue), PGS throttle (red), fuel quantity (yellow), and altitude (black) for the A4H.*

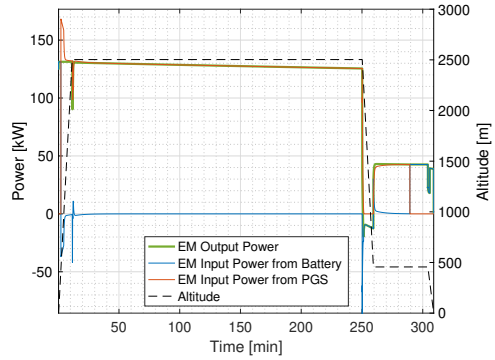

(b) *Time histories of shaft power (green), BP power (blue), PGS power (red), and altitude (black) for the A4H.*

Figure 4.14: *Time histories of A4H.*

used from the PGS to sustain the flight and/or to recharge the batteries. In Figure 4.14b, the corresponding values for shaft power (green), power supplied to the EM by the BP (blue), and power supplied to the EM by the PGS (red) are shown, again together with the altitude profile (dashed black). It can be seen that the battery is discharged during the PE phases (which indeed last only a few minutes), while it is charged throughout the rest of the flight and discharged again towards the end of the loiter and in the final descent. The PGS is kept running during the BP charging phases (close to maximum rating) to provide the recharge. Negative values of BP power in Figure 4.14b correspond to charging phases. Once the BP SOC is sufficient to carry out the final part of the mission, insuring the required residual energy at flight completion, the PGS is shut down permanently, even before reaching the HETA. The complete set of time histories pertaining A4THE in terms of true airspeed, vertical speed, range and more is reported in Appendix B

A second serial HE solution, named B4H, was sought, by looking at the range allowed by limiting the MTOM to the original Cessna 127 value, i. e., 1,157 kg. Keeping the same battery technology and all other applicable performance constraints, as well as the same limitations for battery SOC, end-of-flight stored energy, and EM extra power, a maximum range of 495 km was found (48% less than the original Cessna 172) for the B4H. The corresponding values for installed power and wing reference surface are 108.7 kW and 16.1 m^2, or 17.2% and 17.4% lower than the A4THE case, respectively.

Figure 4.15 shows the mass breakdown for this lighter solution, which

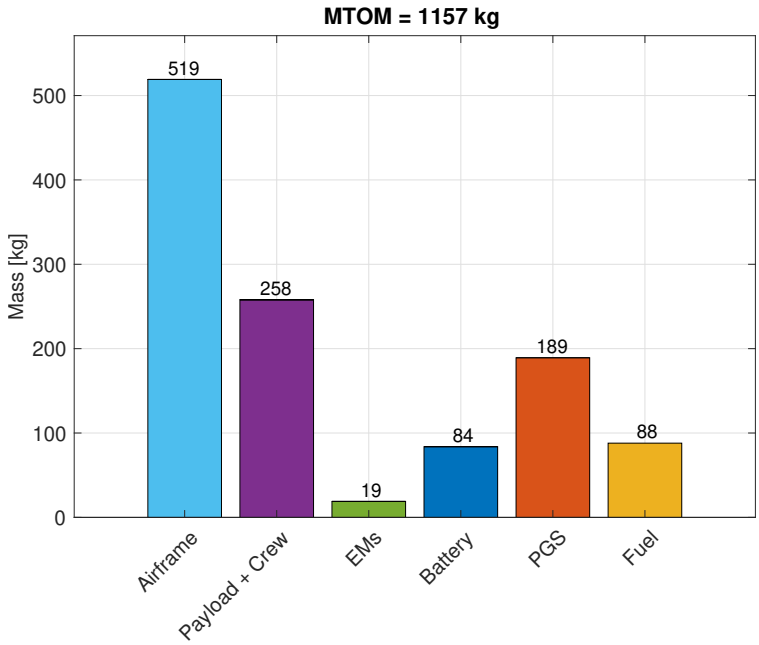

Figure 4.15: *Mass breakdown for the B4H design solution.*

requires 81 kg (or 48%) less fuel, while asking for only slightly lower masses for BP, EM and PGS. This is clearly an effect of the sizing to power, which induces only slight changes in all mass components except fuel, even when a significant change in range is imposed. The payload mass ratio amounts to the original Cessna 172 value, i. e., $M_l/M_{TO} = 22\%$.

The time evolution of the energy stored on board is shown in Figure 4.16a, depicting BP SOC, fuel quantity, and PGS throttle level, together with the altitude profile. It is noted that the only significant difference with the A4H case lies in the shorter activation of the PGS during loiter, as a result of the abundant energy stored in the BP. This allows to fly most of the loiter in PE mode, even if above the HETA Figure 4.16b is very similar to Figure 4.16a with battery power (blu line) being zero for almost the entirety of the cruise phase.

4.5 Pure-electric solution

A third variant, this time a PE one was considered. This, named B4PE, was sized by keeping the same performance and loiter provisions of the A4THE apart for the range, which was lowered to match the original Cessna 172 MTOM (as done for B4THE case). The same battery technology and limitations for battery SOC and end-of-flight battery stored

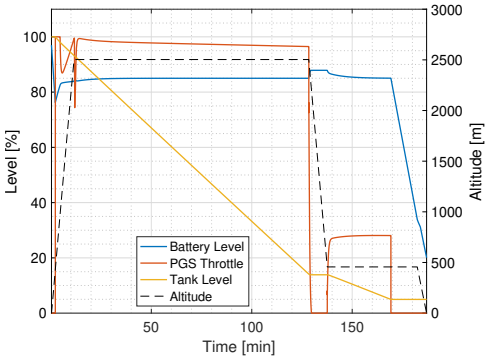

(a) *Time histories of battery state of charge (blue), PGS throttle (red), fuel quantity (yellow), and altitude (black) for the B4H.*

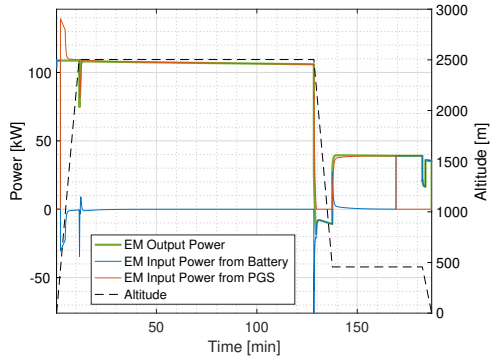

(b) *Time histories of shaft power (green), BP power (blue), PGS power (red), and altitude (black) for the B4H.*

Figure 4.16: *Time histories of B4H*

energy, as well as EM extra power are applied.

The value for the B4PE range is found as 56 km, which is 11.2% compared to the B4THE case or 5.6% of the original airplane. The mass breakdown for M_a, M_b and M_m is of 512 kg (44.2%), 369 kg (31.9%) and 19 kg (1.6%) respectively. Without considering the loiter phase, but still considering a minimum SOC of 25% the full range of the B4PE becomes 126 km. However, while the first flight lasted 71.8 min, the second mission only lasts a total of 45.1 min (-37.2 %). The time evolution of the energy stored on board, contrasting the BP SOC with the altitude profile for the two missions is shown in Figure 4.18. In particular, in the mission with the loiter phase, (Figure 4.18a) the cruise phase is extremely short, 2 min, against 20 min in Figure 4.18b. The comparison of the power profiles in the missions with and without loiter (Figure 4.19) shows that the most demanding phases of the flight, in terms of power, are climb and cruise, whit loiter being flown at the airspeed for minimum required power. The condition for minimum required power, for propeller-driven airplanes, usually corresponds to the best endurance airspeed, and this the reason why the same battery can carry out two, very different, missions.

4.6 Fuel cell hybrid-electric solution

FCHE solutions are found for the large regional case, considering both GH2 and LH2 tanks: A70GH2 and A70LH2. These solutions are inspired by the regional aircraft model already considered in the validation phase, the ATR72. The same performance of the original aircraft, as in Table 4.10

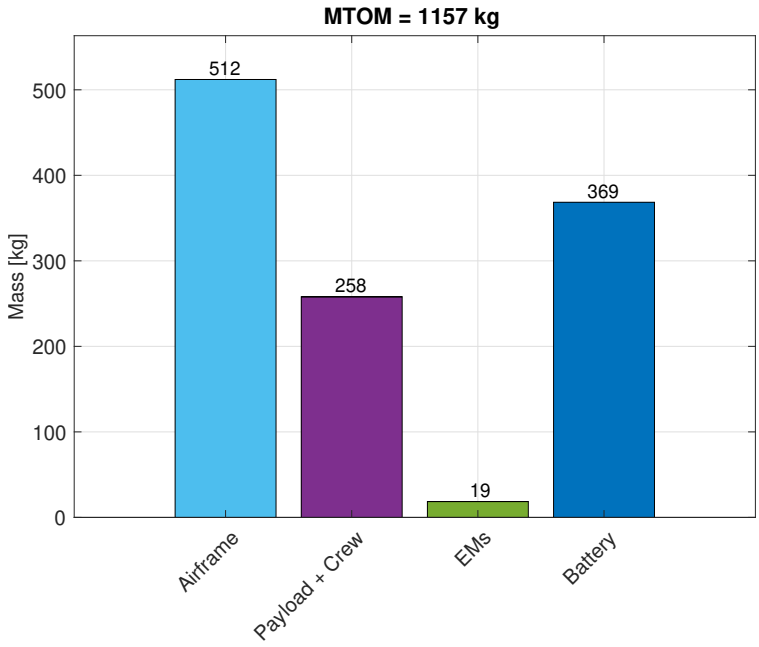

Figure 4.17: *Mass breakdown for the B4E design solution.*

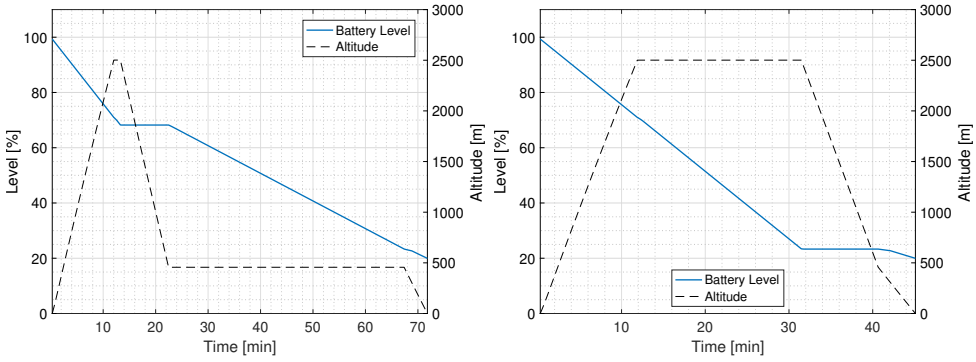

(a) *Mission with loiter* **(b)** *Mission without loiter*

Figure 4.18: *Time histories of battery state of charge (blue) and altitude (black) for the B4PE.*

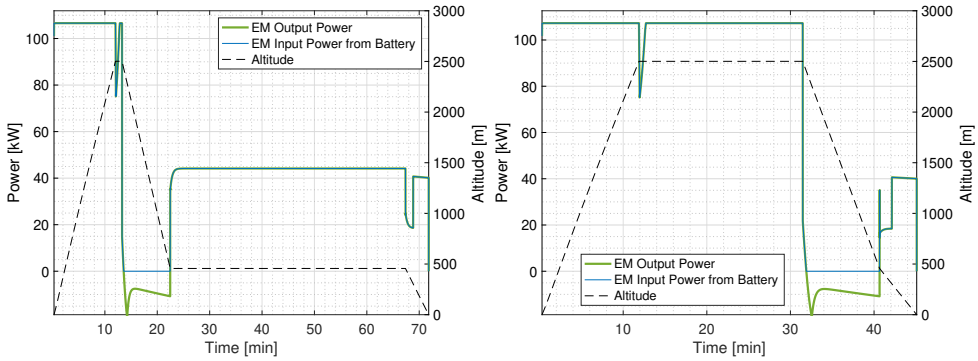

(a) *Mission with loiter* **(b)** *Mission without loiter*

Figure 4.19: *Time histories of shaft power (green), BP power (blue) and altitude (black) for the B4PE.*

is enforced to the solutions, including energy reserves (370 km diversion to alternate airport plus 30 min loiter at 1,500 ft) and FAR25/CS-25 regulations. The sizing matrix plot corresponding to such power requirements is shown in Figure 4.20, including the improvements brought in by the EM extra power. The sizing matrix plot of A70GH2 and A70LH2 solutions looks much more crammed than the one of the A4THE in Figure 4.12. There are, in fact, many more performance requirements for CS-25 airplanes as, for example, the 5 constraints related to OEI conditions. OEI constraints usually impose specific climb gradients in specific phases of the take-off/initial climb, in different aircraft configurations [122]. The results are 5 additional lines in the plot. Please note that, for the A70 solutions, the sizing constraint in terms of power turns out to be the OEI balked landing climb gradient (dashed orange line). The second most important constraint is the OEI en route climb gradient (dot-dashed brown line) and the third is the take-off (blue line).

Three technological scenarios are assumed for the FCHE study cases. These scenarios drive the choice for the values of p_g and μ_g (fuel cell specific power and gravimetric index of GH2 tank), as well as BP specific energy e_b, power p_b and EM specific power p_m. The reference years are 2020 and 2035. In particular, two types of battery chemistries (LIB and LSB/LAB) are expected to be competing in 2035, leading to two scenarios, christened 2035i and 2035ii (35i and 35ii for short). Table 4.19 summarises the values for all the aforementioned quantities.

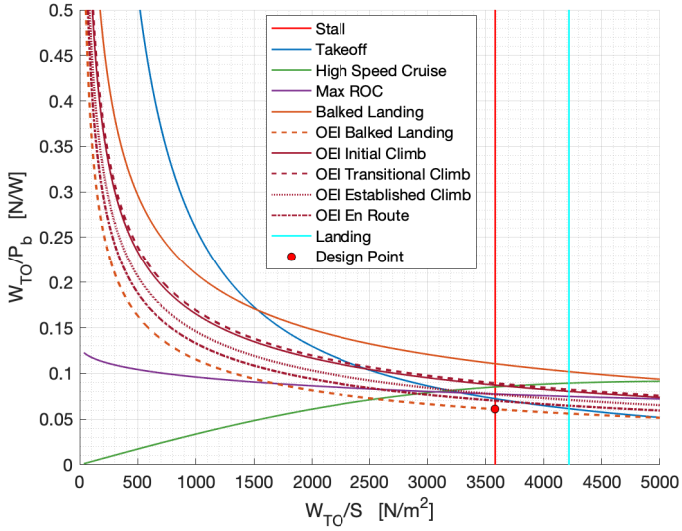

Figure 4.20: *Sizing matrix plot for the A70GH2 and A70LH2 FCHE solutions.*

Table 4.19: *Technology parameters*

	Symbol	2020	2035i	2035ii
Battery type		Li-ion	Li-ion	Li-S/Li-air
Battery specific energy [Wh/kg]	e_b	210	350	1,150
Battery specific power [W/kg]	p_b	1,365	2,275	3,450
EM specific power [W/kg]	p_m	5,750	11100	
ICE specific power [W/kg]	p_g	2,359	4,122	
FC specific power [W/kg]	p_g	800	4,800	
GH2 tank gravimetric index [%]	μ_g	5.7	17.4	

4.6.1 Gaseous hydrogen

Bar plots in Figure 4.21 show design solutions obtained for FCHE aircraft with GH2 tanks. In the same graphs, the blue lines represent the relative error between the bars, using the first bar as a reference. In particular, Figure 4.21a shows the resulting MTOM from the technological scenarios 2035i and 2035ii. The bar for the 2020 result is missing because HYPERION could not converge to a feasible solution. On the other hand, in 2035i and 2035ii cases, a solution is found: M_{TO} amounts to 29.0 and 28.1 tonnes respectively. On the same plot, the value for M_a is visible both in kg and as a fraction of the MTOM, here corresponding to 54.3% in both cases. Figure 4.21b displays the values for the wing surface while Figure 4.21c those of PGS, EM and BP power (orange, green and blue bar respectively). In particular, this graph shows that the PGS power amounts, net of efficiencies, to the EM maximum continuous power. On the other hand, the battery is sized for the difference between the maximum peak power of the EM and the FCs power. This value is greater than $P_m - P_g$, as the temporary extra power of the EM must be accounted for together with the EM efficiency η_m. Figure 4.21d, depicts the overall mass of EMs and FCs that amount to 1,543 kg for 2035i case and 1,495 kg for the 2035ii case. The mass of the battery is instead illustrated in Figure 4.21e. The reduction of M_b between the 35i and 35ii cases is remarkable: -36%. Such difference shows also the potential advantages of LSB as an energy source for large applications, such as a large regional aircraft. Finally the bars in Figure 4.21f represent the overall mass of hydrogen and tank, $(M_t + M_f)$. The promising gravimetric index expected in 2035 (17.4%), still leads to extremely high values of M_t in both 35i and 35ii cases. Focusing on the mass of hydrogen, there is a reduction of 4.7% in the 35ii case with respect to 35i, that results in an equivalently smaller mass of the tank.

The full mission simulation in terms of on board energy for the 2035i case is reported in Figure 4.22 (the graphs for the 2035ii case are in Appendix B). In particular, the battery is used during take-off together with the FCs, which run at full power. The battery is slightly recharged during cruise and descent and is used, once again, during the go around phase. Finally, the battery is depleted up to 25% SOC towards the end of the mission, at the end of the loiter. The power profile in Figure 4.23 shows the share of power at the EM from the FCs and the BP. The BP has positive spikes corresponding to take-off and go around phases and negative spikes at the beginning of cruise and descent, when the PGS needs some time to adjust to the new power level and some power is recuperated in the batteries. Figure 4.24 shows the efficiency of the FC system, that is

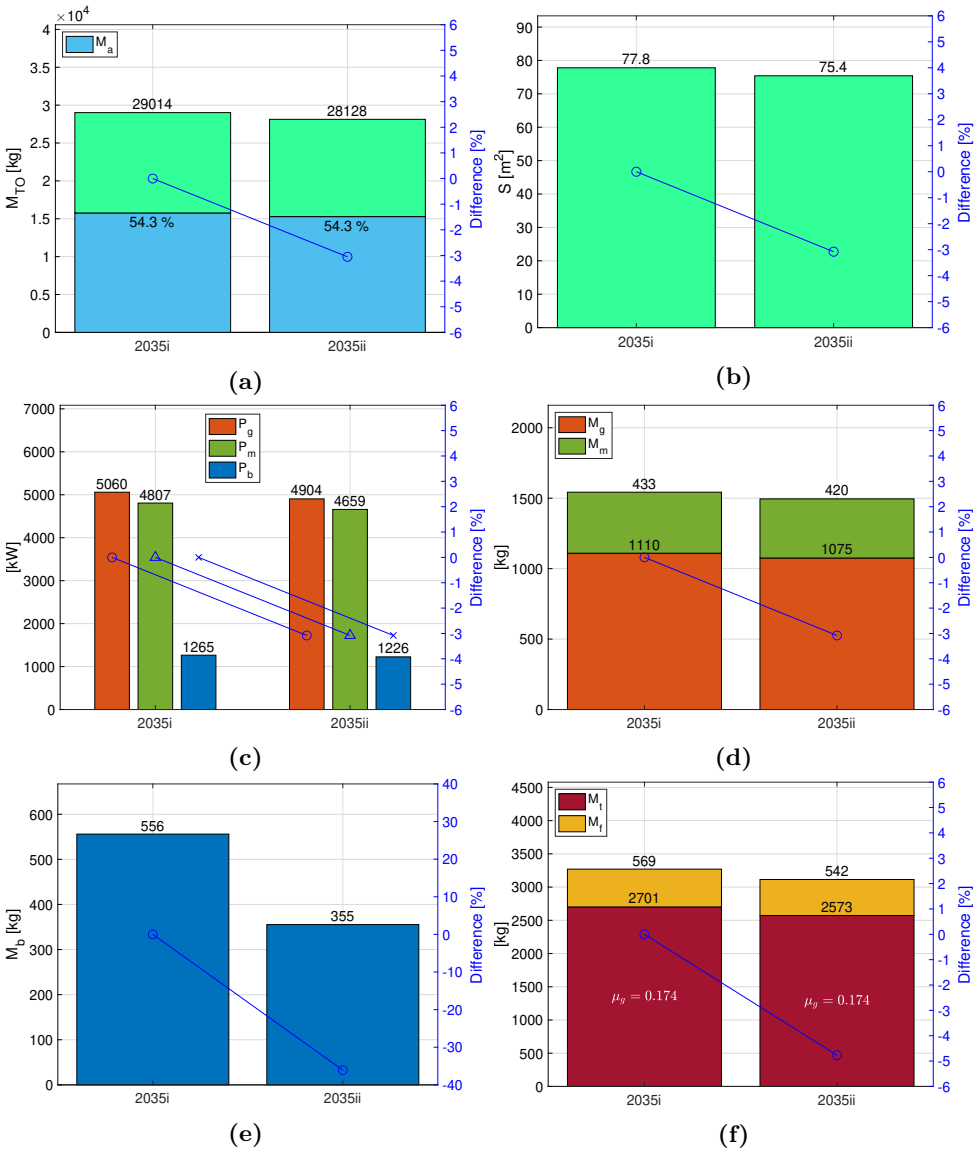

Figure 4.21: *A70GH2 results.*

higher during cruise and loiter. FCs are, in fact, sized for the maximum continuous power but the efficiency is higher at lower power ratings (see Section 3.2.2). This effect of having a higher efficiency during cruise, could be particularly beneficial for commercial aviation flights, where cruise is usually the longest part of the flight.

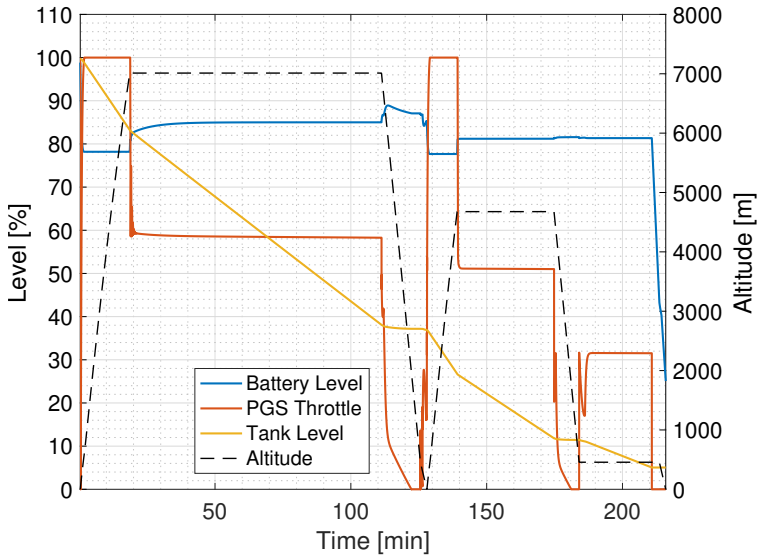

Figure 4.22: *Time histories of battery state of charge (blue), PGS throttle (red), fuel quantity (yellow), and altitude (black) for the A70GH2-2035i*

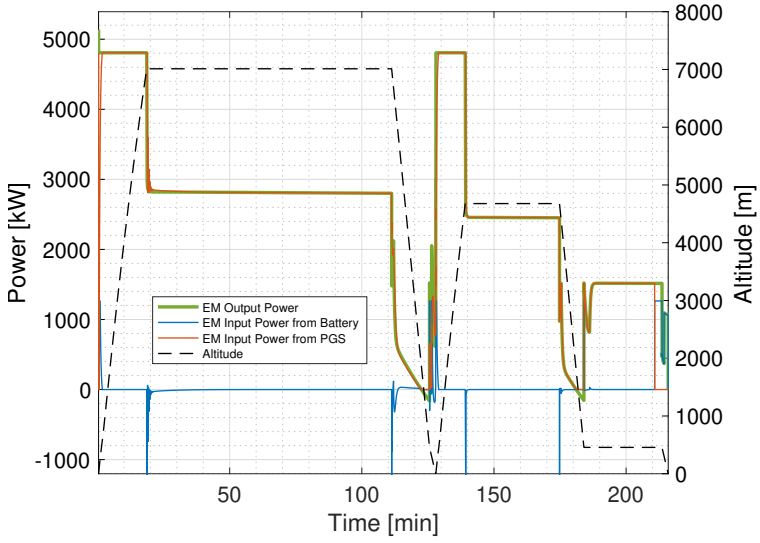

Figure 4.23: *Time histories of shaft power (green), BP power (blue), PGS power (red), and altitude (black) for the A70GH2-2035i.*

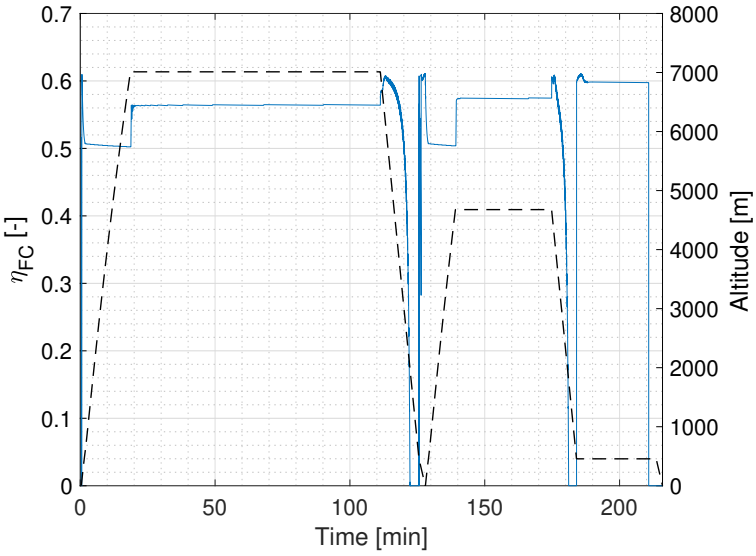

Figure 4.24: *Time histories of the fuel cell efficiency(blue) and altitude (black) for the A70GH2-2035i.*

4.6.2 Liquid hydrogen

The values for the MTOM using LH2 tanks (Figure 4.25a) are definitely more promising than those with GH2 tanks, especially when compared to the original ATR72 MTOM: the 35i M_{TO} is actually 4.8% lower and 35ii case is 6.5% lower. This is possibly linked to the very much higher value of the gravimetric index for the LH2 tank as shown in Figure 4.25f. It is remarked that, opposed to the GH2 case, the LH2 tank is actually designed as illustrated in Section 3.3.2.1, considering the entire flight mission and estimating the incoming heat flow trough the tank wall. The tank design process finds the best insulation thickness to minimise the overall tank weight and hydrogen losses. In particular, for 35i and 35ii cases, the resulting gravimetric index is 64.4% and 64.0% respectively. Although these values are almost one order of magnitude bigger than those in the GH2 cases, a solution for 2020 could not be found. The variation of the overall tank and fuel mass is -3.0% between 35i and 35ii as shown by the blue line in Figure 4.25f. The difference in the battery chemistry is once again leading to a very different battery mass in the two cases. The battery of 35ii is, in fact, 35.3% lighter than that of the 35i. The corresponding values for installed power and wing reference surface are reported in Figures 4.25c and 4.25b. The values of M_g and M_m are instead shown in Figure 4.25d. Figures 4.26 and 4.27 depict the time evolution of the energy stored on board, again obtained through an optimal energy management and the

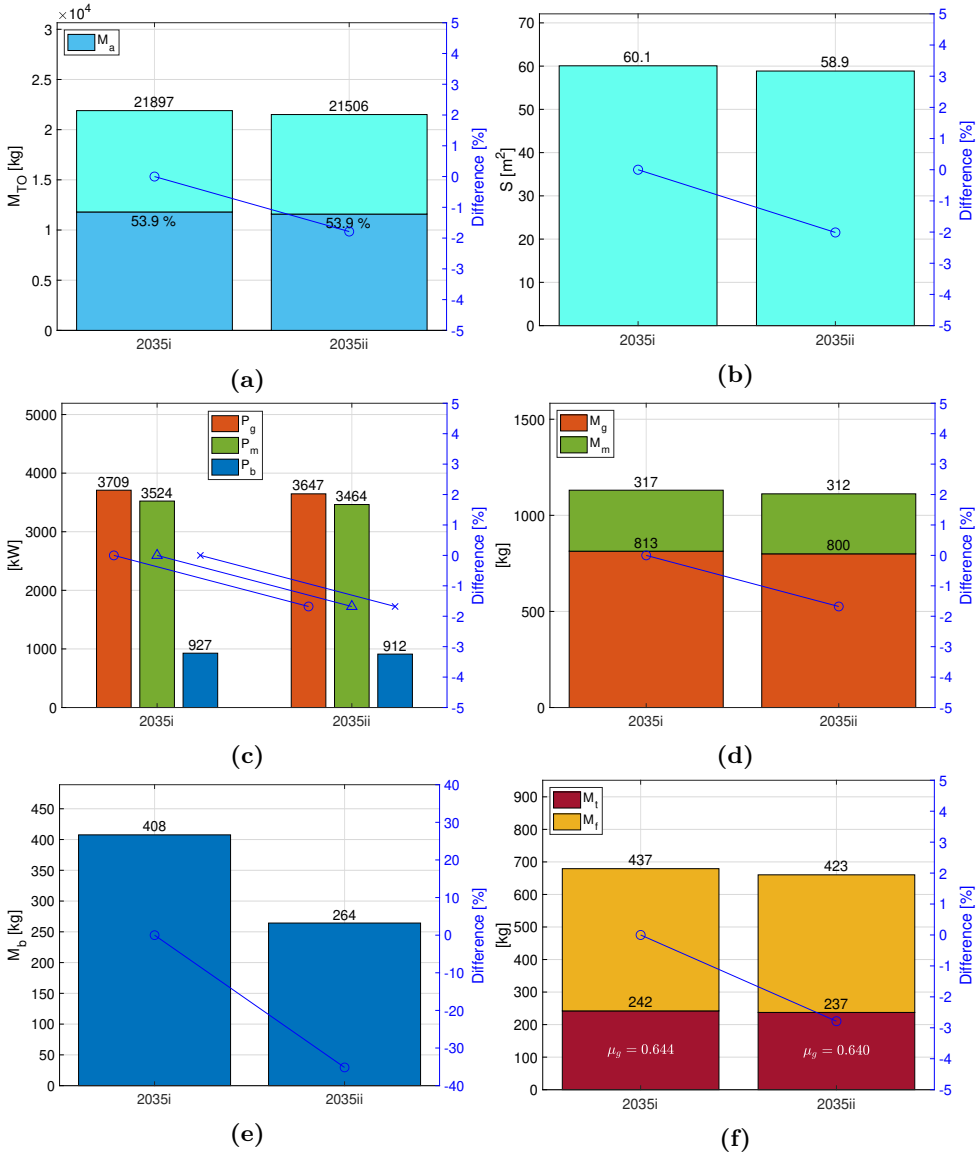

Figure 4.25: *A70LH2 results.*

time evolution of the EM output power for A70LH2-2035i solution. The graphs for the 2035ii case are in Appendix B. In Figure 4.26 it is readily seen that, PGS and BP SOC globally follows a similar trend as in the Figures 4.22. Apart from small-duration boosts, during take-off and go around, BP recharge only occurs at the beginning of cruise and descent, when FCs need some time to respond to the different requested power between the climb and the cruise phase of between cruise and descent. The corresponding EM input power coming from the battery is visible in

Figure 4.27, looking at the blue line, while the red line represents the EM input power coming from the FCs which grossly matches the total EM output power (green line). Figure 4.28 shows the efficiency of the FCs

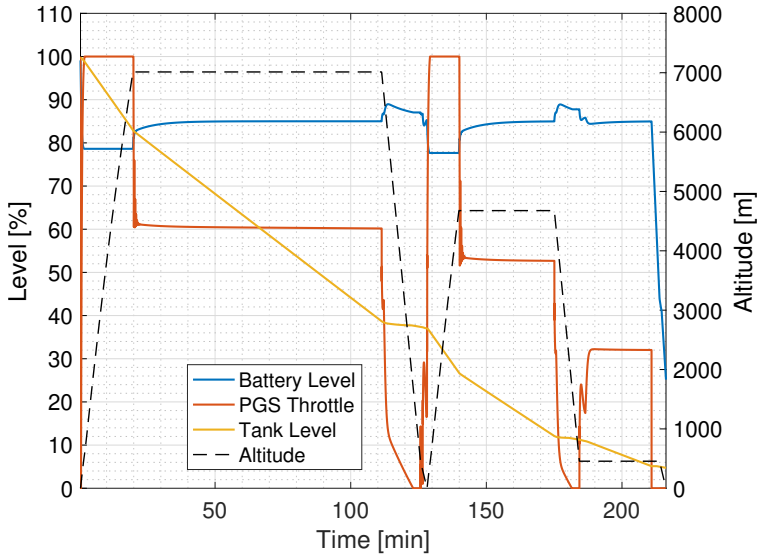

Figure 4.26: *Time histories of battery state of charge (blue), PGS throttle (red), fuel quantity (yellow), and altitude (black) for the A70LH2-2035i.*

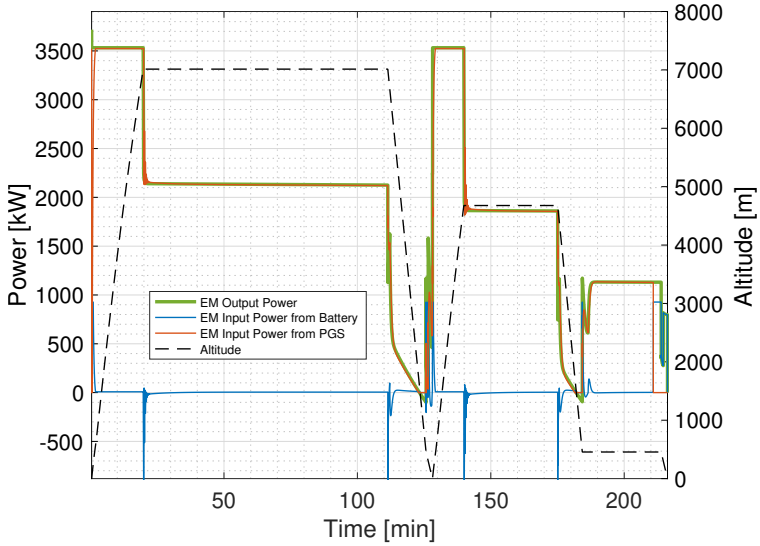

Figure 4.27: *Time histories of shaft power (green), BP power (blue), PGS power (red), and altitude (black) for the A70LH2-2035i.*

that ranges between 50% in climb, where the power setting is higher and 60% in loiter, where the power setting is at a minimum. During cruise,

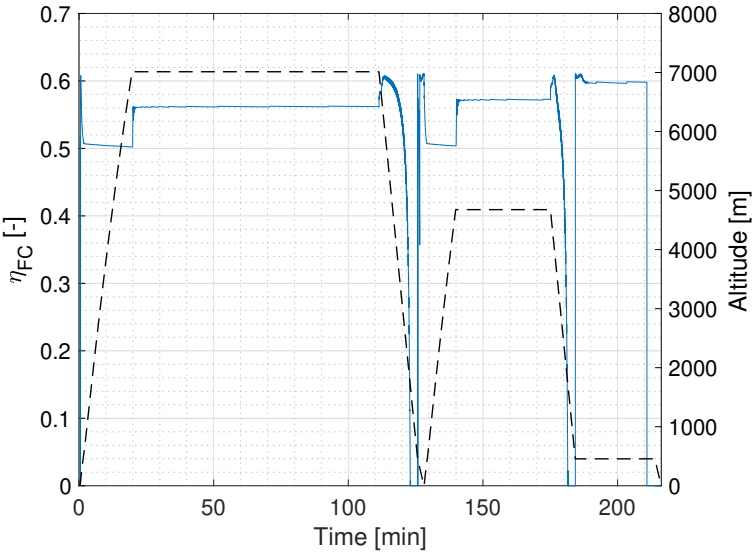

Figure 4.28: *Time histories of the fuel cell efficiency(blue) and altitude (black) for the A70LH2-2035i.*

the efficiency is around 56-57%.

Figure 4.29 displays the time history of the pressure inside the LH2 tank during the flight. The pressure is represented by the yellow line, while the green line represents the minimum pressure necessary to feed the fuel cell system and the red line is the maximum tank pressure. The maximum tank pressure is the pressure at which hydrogen starts to be vented, in order to contain the pressure within the limits. The tank pressure depends mostly on the amount of heat that enters the tank and the fuel flow that exits the tank. The amount of heat that enters the tank is higher when the outside temperature is higher, hence at low altitude. On the other hand, the outgoing hydrogen flow rate is higher during high power phases, such as climb and cruise. The amount of heat that enters the tank wall during the flight mission is represented by the red line in Figure 4.30.

We can see that it decreases as the altitude increases. On the other hand, the yellow line outlines the extra heat that is necessary to vaporize LH2 in order to provide FCs with the necessary hydrogen flow rate. This extra heat drops to zero at the end of the first descent and at the beginning and end of loiter over the alternate airport, towards the end of the mission. In these phases, the fuel cell hydrogen flow rate is close to zero and the natural heat is high enough to trigger the pressure relief valve that vents some hydrogen out in order to limit the tank pressure. The flow rate of vented hydrogen is shown by the blue line in Figure 4.31. Some venting occurs also during take-off because the initial pressure of the tank is set

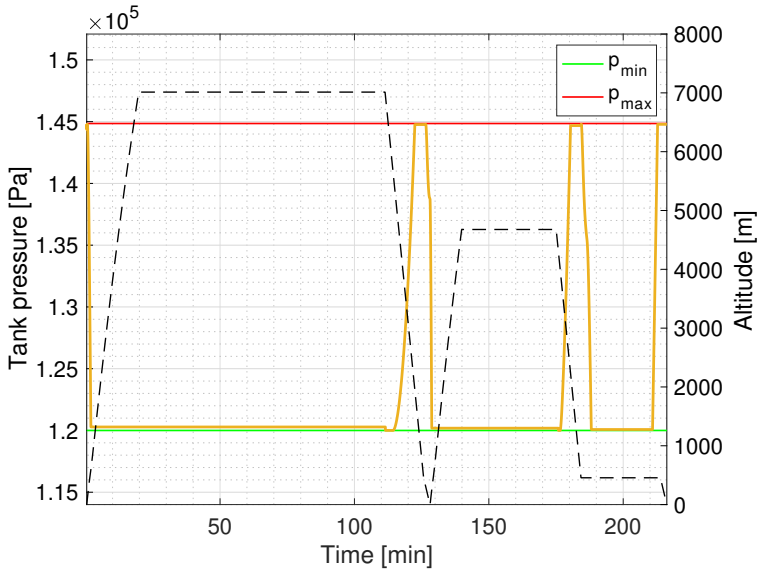

Figure 4.29: *Time history of the LH2 tank internal pressure for the A70LH2-2035i.*

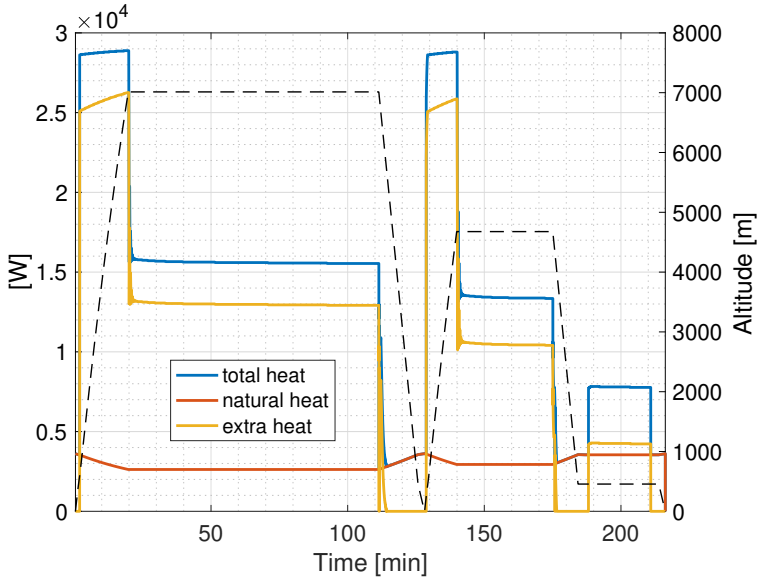

Figure 4.30: *Time history of the LH2 tank heat flow for the A70LH2-2035i.*

equal to the maximum one and, despite a very high hydrogen flow rate for the FCs, some boil-off is present.

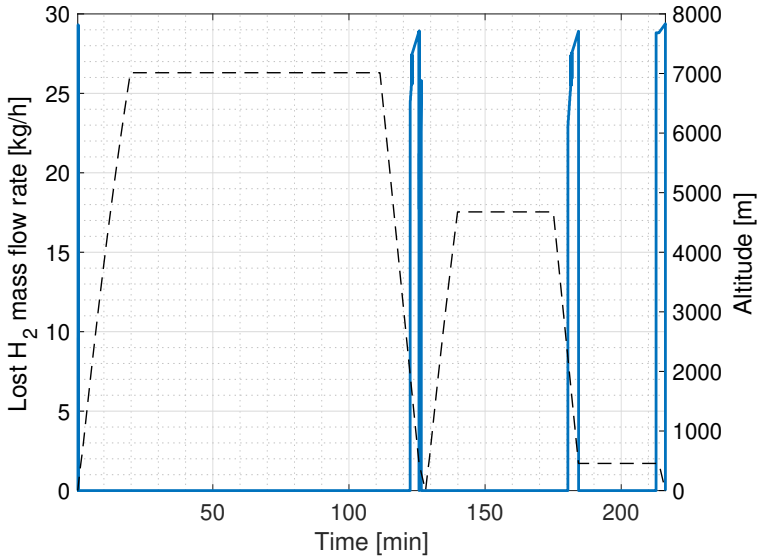

Figure 4.31: *Time history of the LH2 tank boil-off losses for the A70LH2-2035i.*

4.7 Towards conceptual design

In order to move from the preliminary sizing solution, such as that produced by HYPERION and obtain a more complete conceptual design solution, it is necessary to go trough the sizing of the geometry and iterate the preliminary sizing process until the two solutions converge. This is commonly known as a Class I aircraft design solution and involves the geometrical design of the whole aircraft, including weight of the subcomponents (wing, fuselage, tail, landing gear) and aerodynamic performance estimation [121].

A full Class I aircraft design methodology was implemented in the TITAN tool. TITAN is a MATLAB code created combining two tools, HYPERION and AiRcraft GeOmetry Sizing (ARGOS). The latter is the tool taking care of the geometric sizing and is detailed in the next section.

ARGOS development is still undergoing and is currently in an initial stage. For this reason, only a concise description of the tool will be given with a preliminary application in Chapter 11 of the thesis.

4.7.1 Geometry sizing

ARGOS is a crucial component of the encompassing TITAN code. ARGOS is a tool implementing Class I sizing methodologies for geometric sizing and can provide a better estimate of the subcomponent's weights and aerodynamic drag polar than HYPERION. However, ARGOS fully relies on HYPERION for the power-train sizing. In Figure 4.32 a flow chart

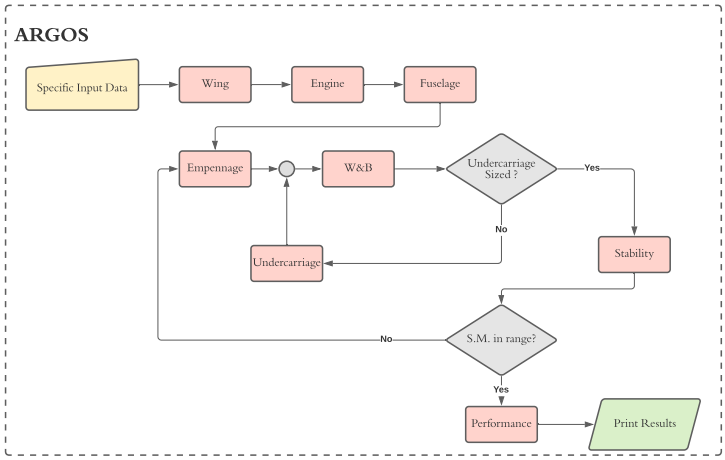

Figure 4.32: *Flowchart of the main building blocks of ARGOS.*

of ARGOS is illustrated. The first step is the wing design: the airfoil is selected based on the necessary aerodynamic characteristics (target L/D or stall coefficient). After that, an innovative lifting line theory for twisted wings is used through a function to compute the wing taper ratio, twist angle and setting angle minimizing the induced drag [137].

Then, the fuselage sizing follows. The procedure for the fuselage can find the best external diameter and length based on the selection of an optimal slenderness ratio. The internal dimensions are calculated taking into account the cabin layout for passengers and cargo. Successively, the external dimensions of the fuselage are found. An important aspect to determine the sizing of the fuselage is the type of power-train (THE, FCHE). In many cases, there is the need to find room for hosting batteries, fuel tanks and PGS. In this case, the PGS is placed in the tail cone. For what concerns hydrogen tanks, GH2 tanks are placed on top of the cabin because they occupy a large volume and their shape is constrained due to the high pressure (cylindrical shape). This usually leads a fuselage diameter which is larger than it would have been on a conventional airplane. On the other hand, LH2 tanks can be fitted behind the passenger's cabin as the shape is not constrained by pressurization limitations and the weight is usually

much more contained than GH2 tanks. It is remarked that the choice of the locations for the components discussed above should be verified on the basis of applicable certification requirements, once such requirements are enforced for this new aircraft categories.

At this point, the other aircraft components are sized, such as the empennages and the landing gear. Finally, the *Weight and Balance* module estimates all the weights and centre of gravity positions for all the subcomponents.

All the steps described above run inside an optimization loop that guarantees the static margin to remain within the requested range. In particular, the sizing of the horizontal tail is repeated to meet the request. Once the full geometry has been defined, the parasite drag coefficient is calculated. For each configuration (gear up/down, flaps up/down) it is possible to obtain the analytical drag polar and the performance indices (such as the lift-to-drag ratio), using the component build method suggested in [107]. As anticipated, the ARGOS tool is still in its infancy. Nevertheless, it is able to size traditional tube and wing configurations with aft tail and has been validated in [138]. Future developments will include support to DEP and non traditional configurations: canard wing, three surface aircraft, blended wing-body, trussed-braced wing, tail cone propeller, etc.

4.7.2 The coupling with power-train sizing

The coupling of HYPERION and ARGOS in TITAN represents a complete tool for the conceptual design of hybrid-electric aircraft. The design process begins when HYPERION provides an initial estimation of the overall wing sizing (surface and span), and a weight breakdown of the aircraft: non-propulsive air-frame mass, PGS system, fuel, batteries and electric motors, and hydrogen tanks in case of a FC-Hybrid architecture. Afterwards, ARGOS uses input data from two different sources: the output data from HYPERION and a specific information about the aircraft configuration. For a reliable solution, the output weights from both tools must be equal. Thus, an iterative loop is implemented through TITAN in which the ARGOS output for the non-propulsive airframe mass and the aerodynamic data (parasite drag) is utilized for a new solution of HYPERION. This process is repeated until the output MTOM from both converge. When they successfully converge, the convergence histories, as well as a CAD drawing and the related numerical results are printed. A schematic of this logic is in Figure 4.33.

An application of TITAN will be shown in Part II of the thesis, concerning

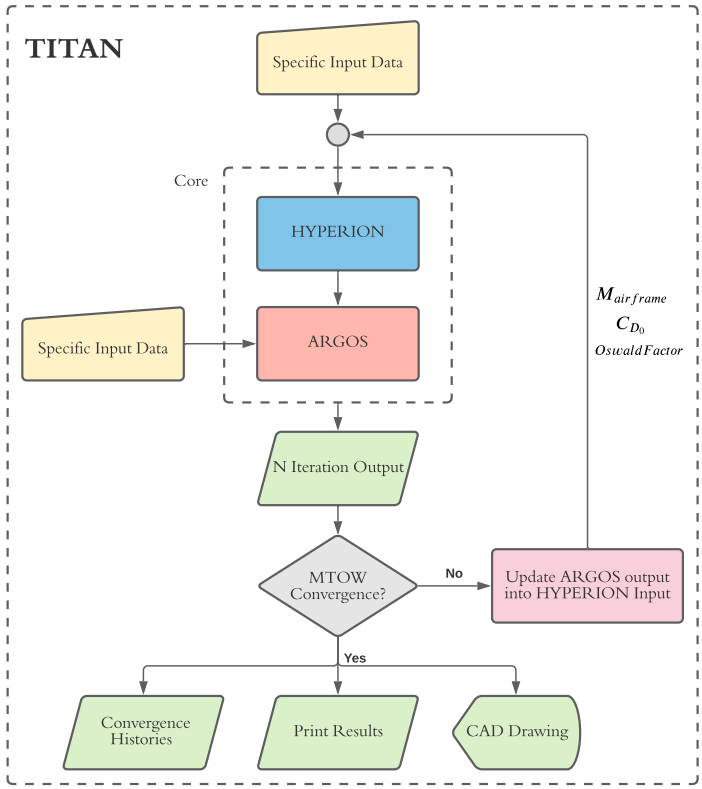

Figure 4.33: *Flowchart of the main building blocks of TITAN.*

the conceptual design of the miniliner.

4.8 Conclusion

The present chapter introduced a novel methodology aiming to perform the preliminary sizing of innovative, electrically-powered fixed-wing aircraft, providing a comprehensive and flexible tool for preliminary sizing loops. The methodology can deal with pure-electric (battery-based) airplanes, serial hybrid-electric and fuel-cell driven airplanes as well. A validation effort including several conventional aircraft across widely different weight categories, from low-end CS-23 to CS-25 models, has been carried out, together with some similar studies involving pure-electric and hybrid-electric aircraft. Examples of these studies have been detailed here. Based on this methodology, a number of design exercises have been pursued. The present chapter, involving a 4-seat and a 70-passenger airplane in multiple versions, provides an illustration of the flexibility and power in tackling widely different design cases, in view of fully-fledged design exercise as the one presented in the second part of this thesis.

CHAPTER 5

AIRPORT INFRASTRUCTURES FOR INNOVATIVE AIRCRAFT

In the frame of MAHEPA, a great deal of research is carried out in providing estimations on the scalability of the developed technologies for application to the upper end of FAR-23/CS-23, and even FAR-25/CS-25 aircraft. This may lead regional air transportation to be the next application scenario for HE propulsion after the current activities targeting the GA segment. In this regard, recent studies provide promising predictions for fuel reduction for commuter aircraft and narrow body liners [139]. Market studies concerned with the estimation of the potential passenger demand for short-haul air transportation have been recently carried out, up to providing the definition of optimal route networks aimed at capturing at best future opportunities arising by the enhancement of citizen mobility as it is going to be discussed in Chapter 8 and [140, 141].

Despite the large amount of ongoing research related to HE propulsion, little information is available regarding the necessary infrastructure on the ground for permitting the operation of PE and HE aircraft ([142]). The

existing airport framework was not designed for this new type of aircraft and the setup of a suitable ground infrastructure is necessary [143]. A need for an increased electric power supply has to be accounted for in the reconfiguration of an existing airport. Indeed, the price of electric energy would come to represent a more relevant cost than in nowadays budgets. The energy purchase price is typically a function of time, changing greatly over a daily or weekly period - reaching up to two times and four times the minimum respectively, over these time frames, [144]. A smart scheduling of the recharging activities should be pursued to reduce the energy supply cost.

Smart recharge planning is clearly connected with the technological constraints inherent to available on-board systems and ground recharging facilities [145, 146]. These can be reduced to two basic types [147], Battery Plug-in Chargers (BPCs) and Battery Swapping Stations (BSSs). BPCs are conceptually similar to fuel refilling stations. The large scale spread of terrestrial Electric Vehicles (EVs) has pushed a capillary diffusion of fast or semi-fast BPCs. Many standards and connectors have been designed for the automotive field, like SAEJ1772, CCS, CHAdeMo and Tesla Superchargers. On the other hand, examples of aircraft charging operations for propulsive purposes are confined to few models such as Pipistrel Alpha Electro, NASA Green Flight Challenge competitors, IFB-Stuttgart e-Genius and Pipistrel Taurus G4 [148]. The recharge happens trough an external 60 kW DC charger, that is able to recharge the battery in 15 minutes. A major shortcoming associated with BPCs is the fact that heavier and higher-performing aircraft – e.g. today's liners – would need amounts of battery energy in the order of MWh (3.5-7 MWh for an aircraft the weight of a B737-800, depending on the mission [149]), which in turn would translate into an unacceptably long recharging time, totally incompatible with the usual turnaround of a liner. The usual 90 kVA power lines and connectors currently deployed to supply aircraft systems on ground could be multiplied to increase power supply, but besides procurement cost for the hardware, this would impact on the peak power required from the grid, which is responsible for part of the energy supply cost, together with the actual energy acquired from the grid. In the Italian energy supply scenario, the cost of allowed peak power is responsible for 20% of the overall electric energy cost for a typical user [144].

An alternative to BPCs are BSSs, which allow recharging batteries while unplugged from an aircraft [150–152]. Provided a matching number of unplugged batteries is available, a smart scheduling of the recharge, simultaneously compatible with air operations and such to minimize power acquisition cost, can be envisaged. Clearly, a larger amount of batteries

represents a higher acquisition cost and an increased logistic effort (batteries need to be transported from and to the aircraft, as well as safely stored after recharge and before being plugged in). Furthermore, similar to BPC, recharging power is limited for a single BSS, hence a higher number of simultaneous battery recharges would imply a larger number of BSSs, with an ensuing higher acquisition cost.

These factors – required energy/power supply, number of BPCs and BSSs, and number of batteries – constitute the main output of a sizing problem where the schedule of air operations, i.e. number and time frames, is given as the input. From the viewpoint of a ground operator, the reconfiguration of an airfield for operations with PE or HE aircraft should imply defining these quantities, in order to grant minimum procurement and operative costs. A different scenario is represented by airfields where a single company is simultaneously acting as ground operator and owner of a fleet. In some cases, most typically on smaller airfields serving as bases for flying schools, the operations of that fleet make for nearly the total of all air operations. For such scenario, the study of fleet switching to innovative propulsion should account for the procurement cost of novel aircraft, such to grant the same operativity level of a conventional fuel-burning fleet, yielding an extended sizing problem, where an optimal number of aircraft is obtained as an output, together with a suitably sized ground infrastructure. The latter scenario is of great interest today, when the economic profitability of fleet switching to electric propulsion has to be assessed in detail. Lower absolute costs for both procurement and operations, as well as its limited impact on the existing air transport system, make the flying school or aero club case more likely to translate into a real field application.

This methodology has been implemented in the Airport Recharging Equipment Sizing (ARES) tool and applied to a number of study cases ranging from smaller local GA aerodromes to large airports. An application of ARES to the reconfiguration of the Milano Bresso (ICAO Code: LIMB) airport will be presented next. This airport is operated by the company Aero Club Milano [153], which acts as airport manager, and owns the aircraft fleet used for instructional as well as sport flights. Finally, the ARES will be applied to the reconfiguration of Athens International Airport (ICAO Code: LGAV), since it was the European airport with the highest number of propeller-driven regional aircraft movements in 2019. Indeed, propeller-driven regional aircraft, from 40 to 70 seats, are considered the first step for the scalability of HE propulsion from general aviation to airliners.

A part of the work presented was developed with the contribution of

the following MSc students in the frame of their thesis project: Federico Bigoni, Alejandro Moreno-Perez. Results related to this activity have been published in [154–160].

5.1 Methodology

5.1.1 General

The ability of sizing the charging infrastructures for a given schedule of aircraft movements in a given airport will represent a fundamental element in drafting future operational scenarios for future PE and HE air transportation. The problem involves a large number of variables and parameters related to the type, cost, usage, and operating life of aircraft, batteries, charging devices, as well as to the characteristics of the electricity supply.

A feasible and reliable solution is sought here by casting this question as an optimization problem, by establishing an appropriate objective function to be minimized under all relevant constraints. The objective function is represented by the total cost related to battery charging operations. The constraints reflect aircraft, airport, and electric grid operational models, as well as technology limitations. The formulation is cast as a Mixed Integer Linear Programming (MILP) problem, where Boolean, integer and real variables are involved. This is applied to a given duration in time for which a detailed flight scheduling is known. The solution is provided as the optimal values of the number of needed charging devices, the number of necessary batteries, and the detailed time scheduling of the charging process.

The present formulation is inspired by the approach described in [150], where an optimization framework is set for automotive applications. However, as a result of the fundamentally different modes of operations of aircraft on scheduled flights when compared to land EV, the extension of the cited approach to airport operations implied a major reformulation involving almost all the ingredients of the MILP problem, from the definition of the cost function, to a large part of the necessary constraints. As an example of the numerous differences that naturally arise from the widely diverse fields of application, we remark that in [150], the operation of a BSS to support a fleet of ground vehicles is considered, according to a day-ahead scheduling process, including possible uncertainties in battery demand and in electricity price. The procurement cost of the BSS is not considered, as well as that of the EVs. In the present case, we consider both BSSs and BPCs as alternative to one another or in a mixed setting, including their

procurement cost. Indeed, given the current uncertainty about the convenience of providing either plug-in recharge or battery swap, especially for larger aircraft models, we introduced the possibility to rely on both type of devices. The procurement cost of the airplanes is also included in the present formulation, as it may be of interest whenever the fleet is operated by the same company that manages the airport recharging infrastructures (as it may be for GA airports). Also, here the battery demand is known *a priori*, as it depends strictly on the flight schedule, which—contrary to private cars—is known ahead in detail. Therefore, we did not consider uncertainties in battery demand and, as all battery requests must be satisfied, a penalty for the inability to satisfy such demand is not necessary. Also, we did not consider uncertainties in electricity price.

Recently, an approach that shares many elements with the present one has been published [142]. Instead of using a MILP formulation, scheduling theory is employed to solve a similar problem. However, some differences in the framework can be seen: the solution is allowed to divert from the predetermined flight scheduling, only battery swapping is considered, only one type of battery is considered, some battery-related and aircraft-related constraints are relaxed, and the price of electricity is constant in time, so that minimizing the electricity cost equates to minimizing the peak-power draw.

5.1.2 Preliminary Definitions

In seeking for the minimum of the cost function J as a function of an array of optimization variables $\mathbf{x}$, the dynamics of the recharging operations are integrated over a time duration L, subdivided in a number of slots of length l_t, providing a discrete time grid for the problem. The set of all time slots is denoted by T and each time slot is identified by the index $t \in T$. Therefore, $L = \Sigma_{t \in T} l_t$. The set of all batteries is denoted by I and each battery is identified by the index $i \in I$. The set of all aircraft types, which are in a one-to-one relationship with battery types and charger types, is denoted by G and each aircraft type/battery type/charger type is identified by the index $g \in G$.

The battery demand over time is defined by the flight scheduling at the airport, with the request for a fully charged battery pack before each take-off. The cost function and constraint equations will be described in the following, together with the necessary provisions to set the problem in a MILP framework.

5.1.3 Cost Function

From the standpoint of an airport operator, the goal is to grant an assigned operational capability to satisfy a given flight schedule, while minimizing procurement and operational costs. Therefore, the cost function J is defined as the sum of all involved costs over the time duration L as

$$J = C^e + C^p + C^{\mathrm{BSS}} + C^{\mathrm{BPC}} + C^b + C^a \tag{5.1}$$

where C^e represents the cost of the electric energy purchased from the grid, C^p the cost of the corresponding peak power, C^{BSS} and C^{BPC} the procurement costs of the BSSs and BPCs, C^b the cost of the batteries, and C^a the cost of the airplanes. The latter may or may not be included, according to the application, as it will be seen in the following application studies. Each cost component in Equation (5.1) is discussed below.

The cost of the energy supply C^e is bound to the energy amount E_t purchased from the grid in the time slot t and to the corresponding monetary value per energy unit λ_t. Due to the very low frequencies in the evolution of both quantities as functions of time (compared to a daytime scale), providing definitions in discrete time is more typical to this type of problem. Therefore, it is possible to write

$$C^e = \sum_{t \in T} \lambda_t E_t, \tag{5.2}$$

where the value of E_t represents the energy acquired in the time slot t.

The cost of peak power can be expressed as

$$C^p = \max_{t \in T} \left(\frac{E_t}{l_t} \right) c_p \frac{d}{30} \tag{5.3}$$

where the ratio E_t/l_t represents required power in the time slot t, while c_p represents the cost per unit peak-power per month, and d the number of days in the considered analysis. This is simply the time duration expressed in days, so that $d = L/1,440$, when L is given in minutes.

The procurement cost of the BSS can be written as

$$C^{\mathrm{BSS}} = \sum_{g \in G} N_g^{\mathrm{BSS}} c_g^{\mathrm{BSS}} \frac{d}{d_g^{\mathrm{BSS}}}, \tag{5.4}$$

where c_g^{BSS} is the acquisition cost per unit of the BSS and d_g^{BSS} the expected lifespan of the device, measured in days. Therefore, d/d_g^{BSS} represents the relative extension of the analysis over the expected lifespan of the

device. The unit cost of the BSS can be defined, based on a technological regression, as a function of the BSS rated charging power p_g^{BSS}:

$$c_g^{\mathrm{BSS}} = \left(a_1 \ln p_g^{\mathrm{BSS}} - a_0\right)\left(1 + \chi_g^{\mathrm{BSS}}\right), \tag{5.5}$$

where the suggested values for the coefficients are $a_1 = 14,601$€ and $a_0 = 19,968$€ [161], while the coefficient $\chi_g^{\mathrm{BSS}} \geq 0$ takes charger maintenance costs into account.

In a similar fashion, the procurement cost of the BPC can be written as

$$C^{\mathrm{BPC}} = \sum_{g \in G} N_g^{\mathrm{BPC}} c_g^{\mathrm{BPC}} \frac{d}{d_g^{\mathrm{BPC}}}, \tag{5.6}$$

where c_g^{BPC} is the acquisition cost per unit of the BPC and d_g^{BPC} the expected lifespan of the device, measured in days. The unit cost of the BPC can be defined in the same way as seen for the BSS, as a function of the BPC rated charging power p_g^{BPC}.

The cost model for batteries provides the expression

$$C^b = \sum_{g \in G} N_g^b \bar{c}_g^b \tag{5.7}$$

where $\bar{c}_g^b$ is a weighted cost per battery. It should be noted that, theoretically, when considering a sufficiently long time frame for the cost computation, driving the number of total batteries to a minimum would not imply a lower overall battery cost, but only a lower initial procurement cost. A lower number of batteries would imply that each of them should sustain more charge and discharge cycles. This in turn would decrease their life more rapidly, implying that more batteries would be needed in the long run, with an ensuing higher overall cost. On the other hand, a higher number of spare batteries would entail a higher initial procurement cost and their efficient use would be associated in turn to a higher number of charges. Therefore, the C^b term makes sense only on a time frame sufficiently limited with respect to the battery lifespan. With this in mind, $\bar{c}_g^b$ was written as

$$\bar{c}_g^b = c_g^b \frac{d}{d_g^b} \tag{5.8}$$

where c_g^b is the cost per battery. The term d/d_g^b represents the ratio between the length of the simulation and the expected battery life. The value of d_g^b will influence the weight that the battery cost will have compared to the other terms of the cost function. The reasoning above does not take into account the problem of cell ageing, in case the usage of the batteries

is very prolonged in time. This does not happen in the application cases studied so far, as shown by the examples provided in Section 5.2, where the average battery replacement time is always well below two years. However, different approaches may be easily considered in case cell ageing is of interest, such as changing the value of d_g^b, in order to drive the solution to an initial acquisition of less batteries to be replaced quickly as as result of a very frequent usage.

Finally, the aircraft procurement cost C^a, whenever necessary for the analysis, can be arranged similarly to Eqs. (5.4) and (5.6), that is proportional to the number of aircraft N_g^a needed for the scheduled operations, yielding

$$C^a = \sum_{g \in G} N_g^a c_g^a \frac{d}{d_g^a} \tag{5.9}$$

where c_g^a is the aircraft procurement cost per unit and d_g^a the expected lifespan of the aircraft.

5.1.4 Constraints

The parameters influencing the components of the cost function need to satisfy an array of constraints, which reflect both technological limits and models of the recharging processes. As seen in the following, these constraints can be formalized as a set of 23 relations: 7 equations and 16 inequalities.

Battery State of Charge The SOC $S_{i,t}$ of the i-th battery at time index t should always range between a minimum S_g^{min} and a maximum S_g^{max}, as required by the device own technology limitations. This is expressed by

$$\sum_{g \in G} s_{i,g} \left(1 - x_{i,t}^o - x_{i,t}^b\right) S_g^{min} \leq S_{i,t} \leq \sum_{g \in G} s_{i,g} \left(1 - x_{i,t}^o - x_{i,t}^b\right) S_g^{max}, \tag{5.10}$$

where $s_{i,g}$ is a binary parameter indicating if the i-th battery is of type g:

$$s_{i,g} = \begin{cases} 1, & \text{if battery } i \text{ is of type } g, \\ 0, & \text{otherwise.} \end{cases} . \tag{5.11}$$

This allows to handle different types of battery technologies, represented by the G set, each one employed—in principle—on a different type of airplane. The binary variable $x_{i,t}^o$ is active when a battery is currently in use on a flying airplane, while $x_{i,t}^b$ models other types of unavailability,

such as when a battery is disembarked from an airplane and transferred to a BSS:

$$x^o_{i,t} = \begin{cases} 1, & \text{if battery } i \text{ is in use on an aircraft at time } t, \\ 0, & \text{otherwise,} \end{cases} \tag{5.12}$$

$$x^b_{i,t} = \begin{cases} 1, & \text{if battery } i \text{ is unavailable at time } t, \\ 0, & \text{otherwise.} \end{cases} . \tag{5.13}$$

Equation (5.10) shows that $S_{i,t} = 0$ when $x^o_{i,t}$ or $x^b_{i,t}$ are equal to one. Indeed, an unavailable battery can be seen as a battery with a zero SOC that cannot be recharged.

Battery Availability The variables $x^o_{i,t}$ and $x^b_{i,t}$ are linked to a third binary variable $x_{i,t}$, that becomes unitary when the i-th battery is requested at time t:

$$x_{i,t} = \begin{cases} 1, & \text{if battery } i \text{ is requested at time } t, \\ 0, & \text{otherwise.} \end{cases} . \tag{5.14}$$

All flights are supposed to last m time slots. When the i-th battery is not available because it is engaged in a flying aircraft, $x^o_{i,t}$ must be equal to one for the entire length of the flight:

$$x^o_{i,t} = x_{i,t-m} + x_{i,t-(m-1)} + \cdots + x_{i,t}. \tag{5.15}$$

The battery becomes newly available for recharge when the flight mission ends, and the next equation is needed:

$$x^b_{i,t+m} = x_{i,t}. \tag{5.16}$$

In order to better illustrate the application of $x^o_{i,t}$, $x^b_{i,t}$ and $x_{i,t}$, an example is provided in Table 5.1, referred to the case of battery swapping. This refers to the case when the i-th battery is requested in the time slot $t = 1$ and a flight mission lasts $m = 3$ time slots.

Battery Readiness for Use Naturally, every battery must be fully charged before being employed on an aircraft. Hence, the following equation is needed:

$$S_{i,t-1} \geq \sum_{g \in G} s_{i,g} x_{i,t} S^{max}_g. \tag{5.17}$$

Table 5.1: *Example application of binary variables $x^o_{i,t}$, $x^b_{i,t}$ and $x_{i,t}$.*

Phase	(A)	(B)	(C)	(D)	(E)
t	0	1	2	3	4
x_i	0	1	0	0	0
x^o_i	0	1	1	1	0
x^b_i	0	0	0	0	1

A The battery is charging in the BSS.
B The battery is requested and employed on an aircraft, the flight mission begins.
C The flight mission continues.
D The flight mission ends.
E The depleted battery is removed from the aircraft and brought to the BSS for recharging.

Battery State of Charge Congruence Congruence must be imposed between every battery's state of charge at the beginning and at the end of the simulation:

$$S_{i,t=0} = S_{i,t=t_f}. \tag{5.18}$$

Battery Charging Power The battery charging rate cannot exceed a technological limit expressed by a nominal $P_g^{\max}$ value. This yields the conditions below, for both BPC and BSSs:

$$0 \leq P^{BPC}_{i,t} \leq \sum_{g \in G} s_{i,g} \left(1 - x^o_{i,t}\right) P_g^{\max}, \tag{5.19}$$

$$0 \leq P^{BSS}_{i,t} \leq \sum_{g \in G} s_{i,g} \left(1 - x^o_{i,t} - x^b_{i,t}\right) P_g^{\max}. \tag{5.20}$$

Exclusive Recharging Two additional binary variables $y^{\text{BPC}}_{i,t}$ and $y^{\text{BSS}}_{i,t}$ are added to exclude simultaneous recharging of the same battery from a BPC and a BSS:

$$y^{\text{BPC}}_{i,t} = \begin{cases} 1, & \text{if battery } i \text{ is recharging at a BPC at time } t, \\ 0, & \text{otherwise,} \end{cases} \tag{5.21}$$

$$y^{\text{BSS}}_{i,t} = \begin{cases} 1, & \text{if battery } i \text{ is recharging at a BSS at time } t, \\ 0, & \text{otherwise.} \end{cases} . \tag{5.22}$$

Their sum is constrained to be unitary at most;

$$y^{\text{BPC}}_{i,t} + y^{\text{BSS}}_{i,t} \leq 1. \tag{5.23}$$

Using these variables, the following equations, mimicking Equations (5.19) and (5.20), must be considered:

$$y_{i,t}^{\text{BPC}}\, P^{min} \leq P_{i,t}^{BPC} \leq y_{i,t}^{\text{BPC}} \sum_{g \in G} s_{i,g}\, P_g^{\max}, \tag{5.24}$$

$$y_{i,t}^{\text{BSS}}\, P^{min} \leq P_{i,t}^{BSS} \leq y_{i,t}^{\text{BSS}} \sum_{g \in G} s_{i,g}\, P_g^{\max}, \tag{5.25}$$

so that the recharging power of a BPC or BSS charger may be non-zero and not higher than the maximum allowed only if the corresponding binary variable states that the charger is active. Note that P^{min} may assume an arbitrary small positive value.

Recharge continuity In a setting where moving a battery to a BSS or plugging another in a BPC involves manpower or the use of machines, battery charging should happen in consecutive time slots, from minimum to maximum SOC. To enforce this, the following relations are added:

$$y_{i,t}^{\text{BPC}} \geq y_{i,t-1}^{\text{BPC}} - \left\lfloor \frac{S_{i,t-1}}{\sum_{g \in G} s_{i,g} S_g^{max}} \right\rfloor, \tag{5.26}$$

$$y_{i,t}^{\text{BSS}} \geq y_{i,t-1}^{\text{BSS}} - \left\lfloor \frac{S_{i,t-1}}{\sum_{g \in G} s_{i,g} S_g^{max}} \right\rfloor. \tag{5.27}$$

The term to which the floor symbol is applied in the right-hand side of the previous equations is always null whenever the battery SOC is less than the maximum allowed for that battery type. This means that $y_{i,t}^{\text{BPC}}$ or $y_{i,t}^{\text{BSS}}$ must equal unity until the battery is fully charged. Of course, the charging power can assume any value allowed by Eqs. (5.24) and (5.25).

Flight Schedule To satisfy the flight schedule requirements, the following equation is enforced:

$$\sum_{i \in I} s_{i,g} x_{i,t} = b_{g,t}, \tag{5.28}$$

where the $b_{g,t}$ represents the battery demand for a battery type g at time t, as derived from the flight schedule, while the minimum number of necessary batteries is given by

$$N_g^b = \sum_{i \in I} s_{i,g} z_i. \tag{5.29}$$

The new binary variable z_i is such that

$$z_i = \begin{cases} 1, & \text{if battery } i \text{ is at least used once,} \\ 0, & \text{if battery } i \text{ is never used.} \end{cases}. \tag{5.30}$$

Therefore, to take into account the usage of the batteries, the following equation is needed:

$$\sum_{t \in T} x_{i,t} \leq |T| \, z_i, \tag{5.31}$$

where $|T|$ represents the cardinality of T. When $z_i = 0$, the battery i cannot be used, as $x_{i,t}$ is forced to vanish. If battery i is required, the algorithm sets $z_i = 1$. When this happens, $x_{i,t}$ can assume an arbitrary value, otherwise it is forced to zero. This prevents that batteries that are never used remain in the set I (which is initialized by a guess value).

Number of Chargers and Aircraft Finally, the minimum number of BSSs, BPCs and aircraft are related to the the binary variables $y_{i,t}^{\mathrm{BPC}}$ and $y_{i,t}^{\mathrm{BSS}}$ through the following inequalities:

$$N_g^{\mathrm{BSS}} \geq \sum_{t \in T} \sum_{i \in I} s_{i,g} y_{i,t}^{\mathrm{BSS}}, \tag{5.32}$$

$$N_g^{\mathrm{BPC}} \geq \sum_{t \in T} \sum_{i \in I} s_{i,g} y_{i,t}^{\mathrm{BPC}}, \tag{5.33}$$

$$N_g^a \geq \sum_{t \in T} \sum_{i \in I} s_{i,g} \left(x_{i,t}^o + x_{i,t}^b + y_{i,t}^{\mathrm{BPC}} \right), \tag{5.34}$$

relating the integer variables N_g^{BSS}, N_g^{BPC}, and N_g^a to the binary variables that describe the usage of all batteries on aircraft, their unavailability, and their being recharged for all time slots in the simulation.

In addition, the total number of batteries can exceed or be lower than the number of aircraft only if at least one BSS is used. Therefore, an equation is needed that matches the number of airplanes N_g^a and the number of batteries N_g^b, taking into account the number of spare batteries that can be present when using BSSs:

$$-M \, N_g^{\mathrm{BSS}} \leq N_g^b - N_g^a \leq M \, N_g^{\mathrm{BSS}}, \tag{5.35}$$

where M is a large, user-defined integer.

Global Energy Balance The energy amount acquired from the grid in a time slot must corresponding to the integral of the recharge power, so that

$$E_t = l_t \sum_{i \in I} \left(P_{i,t}^{BPC} + P_{i,t}^{BSS} \right), \tag{5.36}$$

where the sum must be carried out on the number of active charging devices (BSS and BPC).

Battery Energy Balance A further constraining equation is represented by the energy balance for the i-th battery, yielding

$$S_{i,t} = \left(1 - x^o_{i,t} - x^b_{i,t}\right) \left[S_{i,t-1} + \frac{\eta_c \, l_t \, \left(P^{BSS}_{i,t} + P^{BPC}_{i,t}\right)}{E^B_g}\right] + x^b_{i,t} S^{min}, \quad (5.37)$$

where η_c is the efficiency of the recharging process.

5.1.5 Linearization

The problem described above is nonlinear due to the battery energy balance, Equation (5.37). The nonlinear character arises because the continuous variables $S_{i,t}$, $P^{BSS}_{i,t}$, and $P^{BPC}_{i,t}$ are multiplied by the combination of binary variables $\left(1 - x^o_{i,t} - x^b_{i,t}\right)$. In order to cast the problem within a MILP setting, a series of actions is taken, obtaining a convenient linearization of the such balance.

First, considering Eqs. (5.19) and (5.20), $P^{BPC}_{i,t}$ and $P^{BSS}_{i,t}$ are set to zero if the battery is in use or unavailable. Therefore, there is no need to multiply them again for $\left(1 - x^o_{i,t} - x^b_{i,t}\right)$. Hence, Equation (5.37) can be rewritten as

$$S_{i,t} = \left(1 - x^o_{i,t} - x^b_{i,t}\right) S_{i,t-1} + \frac{\eta_c \, l_t \, \left(P^{BPC}_{i,t} + P^{BSS}_{i,t}\right)}{E^B_g} + x^b_{i,t} S^{min}, \quad (5.38)$$

which is still nonlinear. The next step is to reformulate the latter equation, at the price of increasing the total number of constraints. To do so, the first term in the right-hand side is substituted by an auxiliary variable $q_{i,t}$ such that

$$0 \leq q_{i,t} \leq \left(1 - x^o_{i,t} - x^b_{i,t}\right) S^{max}_g \quad (5.39)$$

and

$$q_{i,t} \leq S_{i,t-1}. \quad (5.40)$$

Hence, the new auxiliary variable is equal to $S_{i,t-1}$ if the battery is available, and zero otherwise. Therefore, making use of $q_{i,t}$, Equation (5.38) can be efficiently replaced by the combination of Eqs. (5.39) and (5.40) together with

$$S_{i,t} = q_{i,t} + \frac{\eta_c \, l_t \, \left(P^{BPC}_{i,t} + P^{BSS}_{i,t}\right)}{E^B_g} + x^b_{i,t} S^{min}. \quad (5.41)$$

5.1.6 Problem Statement

For the mathematical formalization of the problem described above, the optimization variables are represented by 15 arrays grouped in the global array $\mathbf{x}$ defined as

$$\begin{aligned}\mathbf{x} = \Big(&\{S_{i,t}\}, \left\{P_{i,t}^{BPC}\right\}, \left\{P_{i,t}^{BSS}\right\}, \{E_t\}, \{x_{i,t}\}, \left\{x_{i,t}^{b}\right\}, \left\{x_{i,t}^{o}\right\}, \left\{y_{i,t}^{\mathrm{BPC}}\right\}, \left\{y_{i,t}^{\mathrm{BSS}}\right\}, \\ &\{z_i\}, \{q_{i,t}\}, \left\{N_g^b\right\}, \left\{N_g^{\mathrm{BSS}}\right\}, \left\{N_g^{\mathrm{BPC}}\right\}, \left\{N_g^a\right\}\Big),\end{aligned} \tag{5.42}$$

and are detailed in Table 5.2. Through the derivations detailed in Section 5.1.3, it is seen that the cost function J depends on $\mathbf{x}$. The problem statement is then

$$\begin{aligned}&\underset{\mathbf{x}}{\text{minimize}} && J(\boldsymbol{x}) \\ &\text{subject to} && \text{Eqs. (5.10, 5.15, 5.16, 5.17, 5.18, 5.19, 5.20, 5.23} \\ &&& \text{5.24, 5.25, 5.36, 5.26, 5.27, 5.28, 5.29, 5.31} \\ &&& \text{5.32, 5.33, 5.34, 5.35, 5.39, 5.40, 5.41),}\end{aligned} \tag{5.43}$$

with the constraints holding $\forall t \in T$, $\forall i \in I$, and $\forall g \in G$. Table 5.3 shows the ARES input parameters, while Table 5.4 lists the output data (in addition to the values of the optimization variables). The MILP problem was implemented in MATLAB® and solved using the GUROBI solver [162].

Table 5.2: *ARES optimization variables.*

Variable	Type	Description
$x_{i,t}$	binary	Request status of battery i at time t
$x_{i,t}^{b}$	binary	Unavailability status of battery i at time t (on ground)
$x_{i,t}^{o}$	binary	Unavailability status of battery i at time t (in flight)
$y_{i,t}^{\mathrm{BPC}}$	binary	BPC charging status of battery i at time t
$y_{i,t}^{\mathrm{BSS}}$	binary	BSS charging status of battery i at time t
z_i	binary	Auxiliary variable to account for battery i usage
$q_{i,t}$	integer	Auxiliary variable for linearity of battery i at time t
N_g^b	integer	Number of type g batteries
N_g^{BSS}	integer	Number of type g BSS
N_g^{BPC}	integer	Number of type g BPC
N_g^a	integer	Number of type g aircraft
$S_{i,t}$	real	State of charge of battery i at time t
$P_{i,t}^{BPC}$	real	BPC charging power of battery i at time t
$P_{i,t}^{BSS}$	real	BSS charging power of battery i at time t
E_t	real	Consumed electric energy at time t

Table 5.3: *ARES input parameters.*

Battery-related	
I	Set of batteries
G	Set of airplane/battery/charger types
$\{s_{i,g}\}$	Binary parameter indicating if battery i is of type g
$\{E_g^B\}$	Stored energy of a battery of type g
$\{b_{g,t}\}$	Demand of a battery of type g at time t
$\{P_g^{\max}\}$	Maximum charging power of a battery of type g
η_c	Battery charging efficiency
η_d	Battery discharging efficiency
S^{min}	Depleted battery state of charge
$\{c_g^b\}$	Procurement cost of a battery of type g
$\{\bar{c}_g^b\}$	Weighted cost of a battery of type g
$\{d_g^b\}$	Expected life of a battery of type g
Charger-related	
$\{p_g^{\text{BSS}}\}$	Maximum power of a BSS charger of type g
$\{p_g^{\text{BPC}}\}$	Maximum power of a BPC charger of type g
$\{c_g^{\text{BSS}}\}$	Procurement cost of a BSS charger of type g
$\{c_g^{\text{BPC}}\}$	Procurement cost of a BPC charger of type g
$\{\chi_g^{\text{BSS}}\}$	Coefficient for BSS maintenance cost
$\{\chi_g^{\text{BPC}}\}$	Coefficient for BPC maintenance cost
$\{d_g^{\text{BSS}}\}$	Expected life of a BSS charger of type g
$\{d_g^{\text{BPC}}\}$	Expected life of a BPC charger of type g
Aircraft-related	
$\{c_g^a\}$	Procurement cost of an aircraft of type g
$\{d_g^a\}$	Expected life of an aircraft of type g
Energy supply-related	
λ_t	Electric energy price at time t
c_p	Electric power cost per month
Simulation-related	
T	Set of time slots
L, d	Simulated time duration
l_t	Length of a time slot
M	Large integer

Table 5.4: *ARES output parameters.*

C^a	Total aircraft procurement cost
C^b	Total battery cost
C^{BSS}	Total BSS cost
C^{BPC}	Total BPC cost
C^e	Electric energy cost
C^p	Electric power cost
$\{E_t\}$	Consumed electric energy at time t
J	Cost function

5.2 Results

The methodology described above was tested on two case studies. The first concerns the reconfiguration of a GA aerodrome, the Milano–Bresso airport, home of an historical flying school. The second focuses on the adaptation of a large regional hub, the Athens international airport, which currently hosts a massive traffic of turboprop flights.

The Milano–Bresso study addresses a case that is likely to be among the first to be implemented in the future, given the relative maturity of PE and HE technologies for smaller airplanes in the GA segment. The Athens study addresses a case of high interest on a longer time horizon, should the current research on the scalability of HE technologies allow to assume that large turboprop aircraft may be conveniently replaced by new, environmentally-friendly models carrying the same payload.

5.2.1 Milano–Bresso Airport

The Milano–Bresso airport "Franco Bordoni-Bisleri" (ICAO code: LIMB), built in 1912, is located in the Milan metropolitan area, Italy. It features a 1,080 m × 30 m asphalt runway and is the home of Aero Club Milano (ACM) since 1960. The ACM fleet, providing flying school, leisure flight and air taxi services, is currently composed of 21 aircraft, 20 of which are single-engine propeller-driven models. In the current analysis, it has been hypothesized to switch from the current aircraft models, mainly Cessna C172 and Piper PA-28 four-seaters, to a homogeneous fleet of HE aircraft inspired by the Pipistrel Panthera Hybrid. This four-seater is the HE version of the conventionally-powered Panthera, featuring a cutting edge serial HE power-train, introduced in Section 4.3.5.

The basic features of the aircraft and its battery pack are reported in Table 5.5. Among them, minimum battery life is provided for two refer-

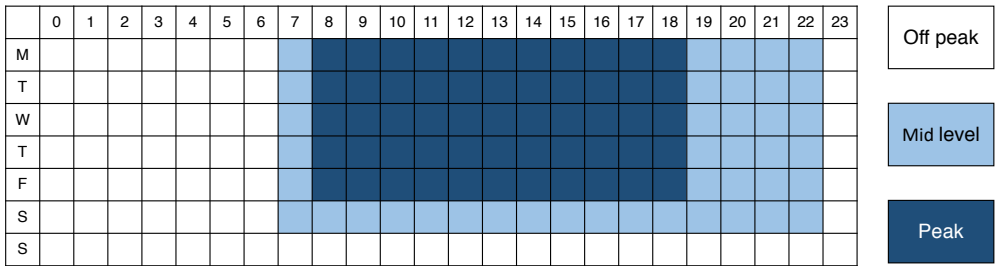

Figure 5.1: *Italian electricity pricing policy scheme.*

ence values of the Depth of Discharge (DOD). As for the aircraft cost, considering that it is not yet marketed, we assumed a value of 450,000 €, which appeared representative for a stock purchase. Although not used here, a possible approach to estimate such cost has been recently proposed in [163].

Table 5.5: *Panthera Hybrid main specifications.*

Item	Value
No. pax	4
MTOW	1,315 kg
Rated power	200 kW
Max. cruising speed	177 KTAS
Range	>1,000 nm
Battery Cost	15,000 €
Battery nominal capacity	13.8 kWh
Battery useful capacity	11.0 kWh
Battery life @ 100% DOD	500 cycles
Battery life @ 75% DOD	800 cycles
Charging efficiency	93%
Discharging efficiency	85%
Charging Power	60 kW

In order to analytically set up the sizing problem, the recharge power values p_g^{BSS} and p_g^{BPC} of the ground recharging devices have been defined at the nominal recharge power of the aircraft, *i.e.* 60 kW. Similarly, the maximum battery SOC, the recharge efficiency η_c, and the unit cost c_g^B have been defined based on the data in Table 5.5. The unit cost of the recharging devices c_g^{BSS} and c_g^{BPC} has been fixed at 39.8 k€, with $\chi_g^{\text{BSS}} = \chi_g^{\text{BPC}} = 0.1$ (10% overhead for maintenance), based on Equation (5.5) for the considered recharge power [161].

The average electric energy price for the first quarter of 2018 in Italy was considered for the present analysis. The Italian electricity pricing is very

complex and includes fixed, transport and system fees.

Since 2007, the pricing scheme has been based on three time-dependent fares: F1–Peak, F2–Mid-level, and F3–Off-peak. The scheme is summarized in Figure 5.1, where the rows represent the days of the week and the columns the hours of the day. The electricity consumption is billed according to a different consumption charge depending on the time slot during which it is used. Therefore, the energy-related cost of electricity λ_t changes according to the time of the day and day of the week. According to Figure 5.1, the three fares do not apply to Saturdays, when only F2 and F3 are adopted, and to Sundays, when only F3 is employed. Numerical values of λ_t and c_p for LIMB are reported in Table 5.6.

Table 5.6: *Electricity prices employed for LIMB reconfiguration.*

Energy charge λ_t	
F1	0.1482 €/kWh
F2	0.1449 €/kWh
F3	0.1286 €/kWh
Power charge c_p	
	4.8104 €/kW/month

LIMB is open to Visual Flight Rules (VFR) traffic only, and operations take place from 08:00 local time to 30 minutes past sunset [153]. Due to these reasons, the number of departures varies during the year. For the present sizing purposes, movements occurred in November 2017 have been considered, since it turned out that this is the most demanding month of the year. In fact, because of fewer daylight hours available, operations are packed in eight hours only and consequently the number of take-offs per hour increases. In addition, the number of flights increases during the weekend, since there are more people willing to fly in those days. The average hourly flight schedule in November 2017 is reported in Table 5.7. This schedule has been employed as the variable $b_{g,t}$, which represents the number of departures at every t. We assumed that every flight takes one hour, as this is a typical value for ACM flight school activities. This schedule has been expanded by reducing the length of each time step l_t to 15 minutes, in order to increase accuracy.

Initially, the ARES procedure was applied to the case of the Most Demanding Day (MDD) only, which is usually Saturday; subsequently, it has been extended to the entire week. The first case examined is restricted to the use of BPCs only, without the possibility to resort to BSSs. This is due to the fact that the Panthera Hybrid, in its present configuration, does

Table 5.7: *Average weekly departure scheme at LIMB.*

h	5	6	7	8	9	10	11	12	13	14	15	16	17	18	19	20
M	0	0	0	0	0	0	0	0	0	0	0	0	0	0	0	0
T	0	0	0	0	2	1	2	1	1	2	2	1	0	0	0	0
W	0	0	0	2	1	2	2	1	2	3	2	0	0	0	0	0
T	0	0	0	2	2	3	2	1	2	3	2	0	0	0	0	0
F	0	0	0	1	1	3	1	3	3	4	3	0	0	0	0	0
S	0	0	0	6	6	5	4	4	5	7	3	0	0	0	0	0
S	0	0	0	3	7	5	2	5	4	6	4	0	0	0	0	0

Table 5.8: *LIMB infrastructural sizing summary.*

Quantity	Unit	Value		
No. of recharges	-	39	39	136
No. of batteries	-	11	12	12
No. of chargers	-	2 BPCs	2 BSSs	2 BSSs
No. of aircraft	-	11	10	10
Average battery replacement	Years	0.62	0.67	1.35
Peak power	kW	56	56	56
Energy consumption	kWh	410	410	1,430
Electric energy cost	€	58	57	191
Electric power cost	€	9	9	63
Total cost	€	596	570	3844
		MDD-BPCs only	MDD	Entire Week

not support battery swapping. Table 5.8 reports the main results of the sizing exercise: the number of recharges corresponds to the input provided by the flight schedule, while all other parameters represent outputs of the procedure. As seen in the left column reporting the values for the MDD in this case, two BPCs are needed. The number of aircraft to fulfil the flight schedule is 11 and it necessarily coincides with the number of batteries. The value of the cost function amounts to 596 € for the MDD. This can be ameliorated if the optimizer is left free to choose the best combination of BPCs and BSSs. Indeed, by looking at the center column reporting the values for this enhanced case, a value for the cost function of 570 € is achieved, with a saving of 4.3%. In this case, the optimizer provides a solution using two BSSs and, as a result, a different trade-off is obtained, where the number of aircraft necessary for fulfilling the flight schedule is lowered to 10, while the number of batteries is risen to 12, implying two spare batteries. Clearly, the additional cost of this added equipment is more than balanced by the need of one aircraft less in the fleet.

Table 5.8 also reports the values for the solution extended to the entire

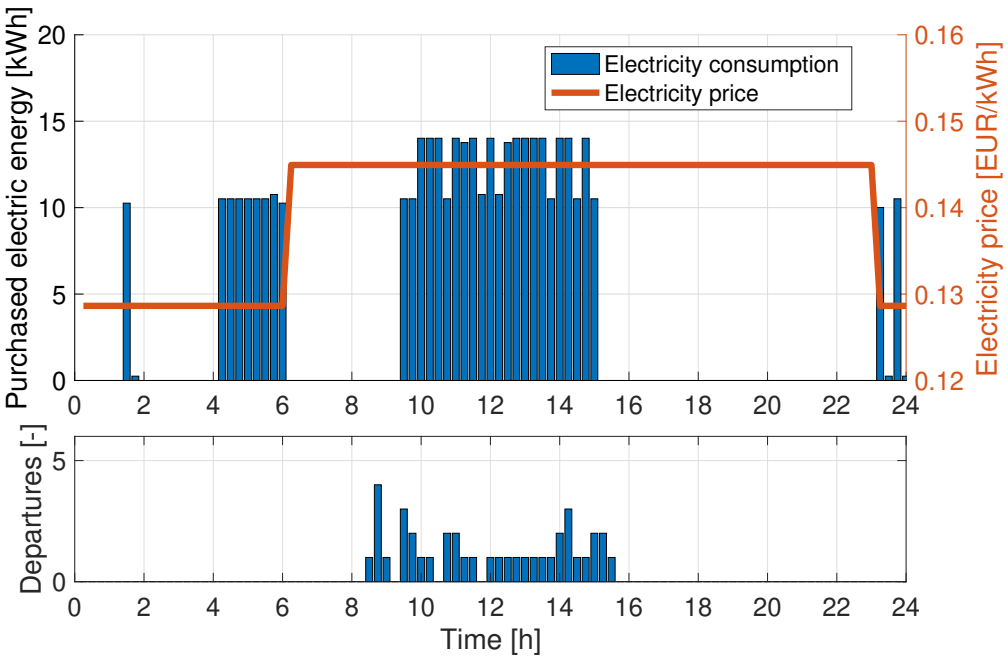

Figure 5.2: *Energy expenditure (top) and departure schedule (bottom) at LIMB for the Most Demanding Day case – BPC only.*

week that encompasses the MDD, again with the optimizer free to choose any combination of BPCs and BSSs. It is remarked that the number of aircraft necessary for fulfilling the flight schedule in both cases (39 and 136 flights) is ten, or half of the current fleet size. Also, the number of batteries and BSSs in both cases is the same. The average battery life is less than seven months in the MDD case, while it raises to 28 months when considering the entire week, a case in which battery usage is more evenly distributed. No difference is observed also with regard to the peak value of the electric power drawn from the grid. Looking at the value of the cost function, the MDD amounts to less than 15% of the entire week.

For the MDD case with BPCs only, the outcome in terms of the time history of electricity consumption E_t is displayed in Figure 5.2. In the lower plot, bars show the daily flight schedule, in terms of departures every 15-minute time slot. In the upper plot, blue bars represent the purchased electric energy necessary to recharge the batteries for all time slots, while the orange line indicates the electricity price variation during the day. It is possible to note that night hours, when energy price is lower, are exploited to charge all the batteries before the first flight session begins at 08:30. The time scheduling of the battery charging during night hours, with an accumulation before the rise in electricity fare, is not specially

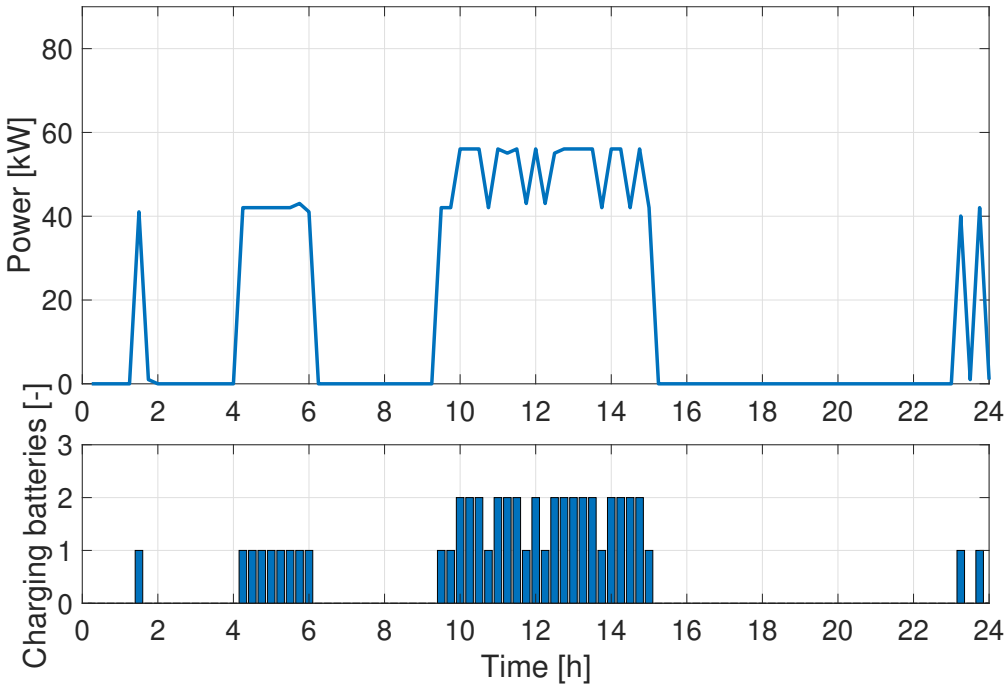

Figure 5.3: *Power consumption (top) and battery charging schedule (bottom) at LIMB for the Most Demanding Day case – BPC only.*

meaningful, as any time slot may be chosen, provided that a single battery is charged within it. The first flights are performed until there are no more fully charged ones available, so that depleted ones are recharged during the day hours up to 15:00. Once the last charged battery is delivered, and no more flights are scheduled, depleted batteries are not recharged before the electricity price decreases again, to take advantage of night-time fares. The power consumption for the same case is reported in the upper plot of Figure 5.3, while the lower plot displays the number of charging batteries at each time slot. As seen during daytime there are instances in which two batteries are recharged at the same time, although not at full power. The maximum requested power is clearly lower at night and peaks during the day. Finally, Figure 5.4 portrays the state of charge of the batteries $S_{i,t}$ throughout the day. Battery charging is a continuous process, with the restriction that a battery must be fully charged before the next one can be plugged in the same charger. The rows in the grid represent each battery, while the columns represent the 15-minute time slots. The cells are colored whenever the battery is plugged in a BPC (blue) or a BSS (green). The color is shaded to represent the SOC, with white corresponding to $S_{i,t} = 0$ and full color with $S_{i,t} = 1$. It is seen that batteries are often fast-charged to fulfil the demand, taking a single time

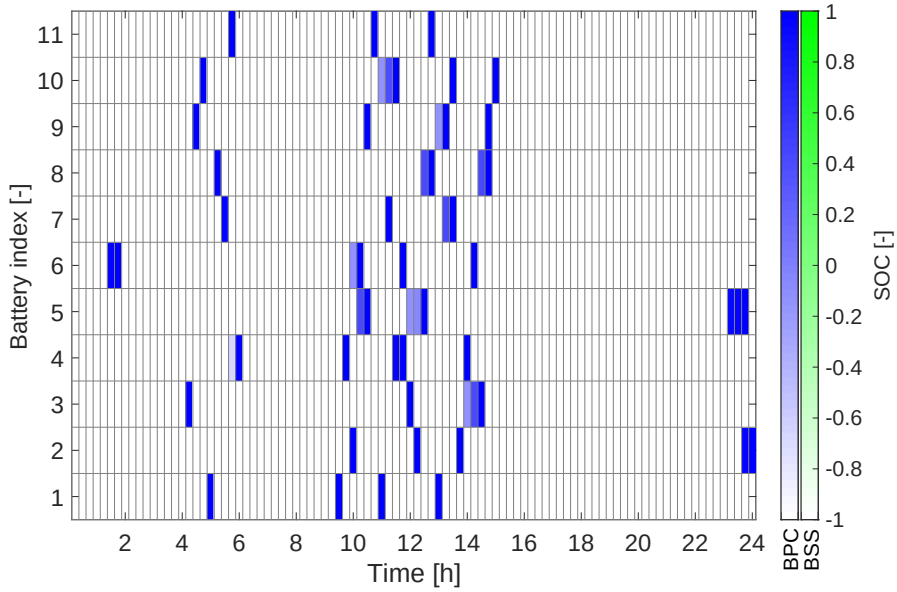

Figure 5.4: *Battery state of charge time evolution at LIMB for the Most Demanding Day case – BPC only.*

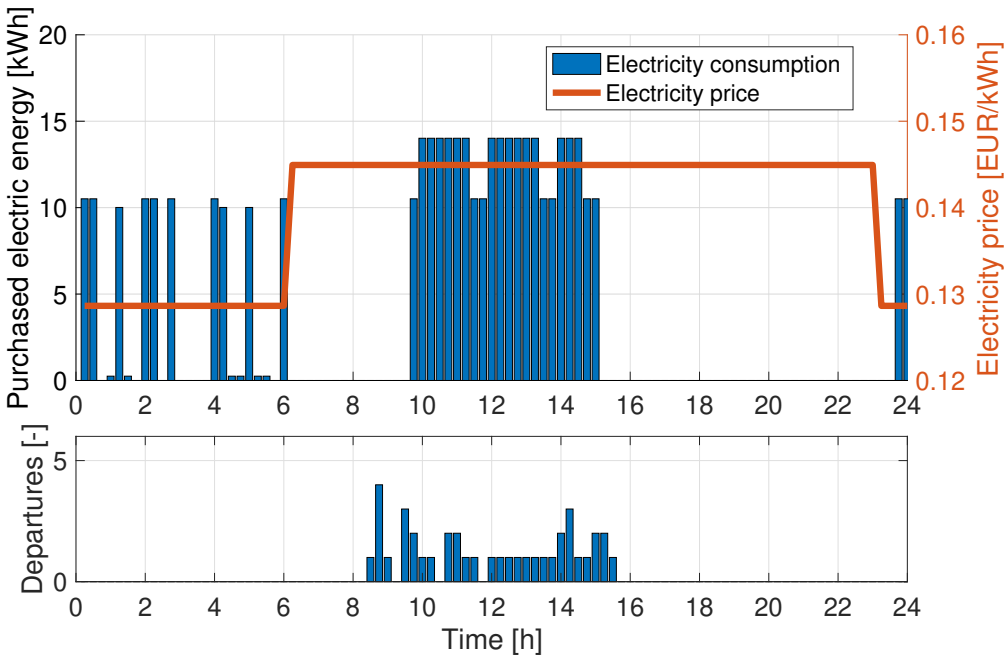

Figure 5.5: *Energy expenditure (top) and departure schedule (bottom) at LIMB for the Most Demanding Day case.*

slot, and therefore being represented by single full-coloured squares. As seen, the solution provides three recharges for five batteries and four for six batteries in the MDD.

For the fully optimal MDD case, resulting in BSSs only, Figure 5.5 provides the time history of energy consumed and Figure 5.6 that of the power required. Again, the sparse pattern seen in the recharging schedule during night hours has no special value. The general behavior observed in both energy and power is similar to the case of using only BPCs, with some differences in the need to recharge two batteries at the same time (13 instances instead of 16 in the previous case). As seen in Figure 5.7, compared to the BPC-only solution, in this case batteries are more often fast-charged and the number of recharges varies from two for two batteries, to four for four batteries in the MDD. This lowers the cycles accumulated in the BSS solution, as seen in the values for the time to replace the batteries in Table 5.8.

Taking the whole week into account, starting with Monday (from 0 to 24 h) and ending with Sunday (from 144 to 168 h), the results shown in Figures 5.8 and 5.9 are obtained. No flights are scheduled on Monday, so almost nothing happens until Tuesday night when the batteries used

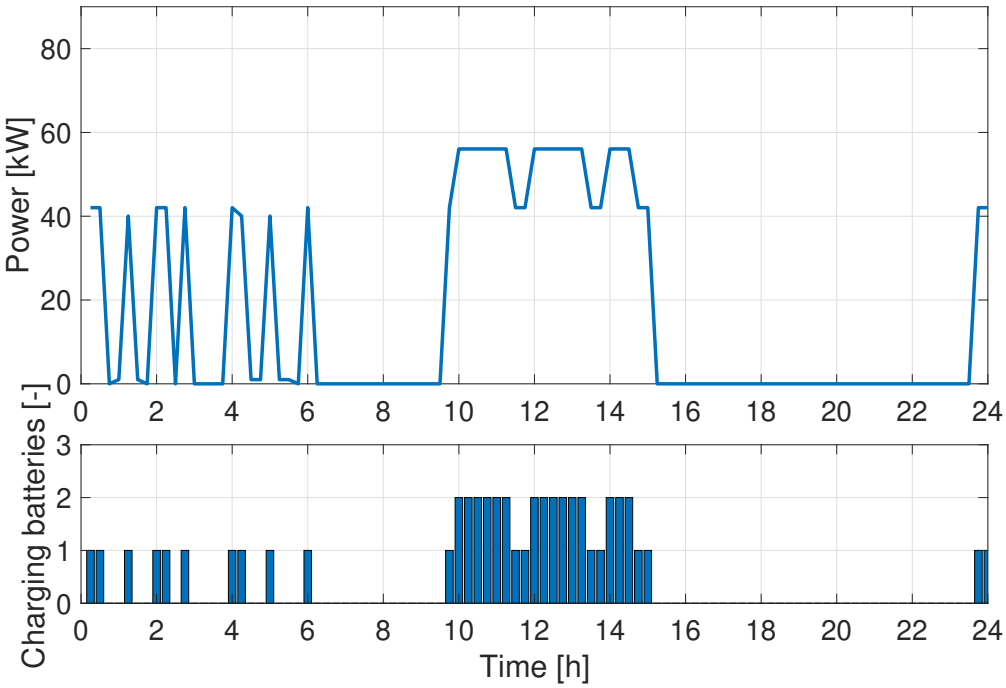

Figure 5.6: *Power consumption (top) and battery charging schedule (bottom) at LIMB for the Most Demanding Day case.*

during daytime hours are recharged. As seen, the batteries were charged during Sunday and Monday night. This strategy is repeated up to Thursday (from 48 to 72 h) when it becomes necessary to recharge the batteries also during the day. It clearly appears that Saturday is the most demanding day, for both energy consumption and required power, followed by Sunday, which features a widely different energy pricing and therefore allows recharging during daytime hours even if the battery is not used for a flight in that day.

5.2.2 Athens International Airport

Athens International Airport "Eleftherios Venizelos" (ICAO code: LGAV) is the primary airport that serves the city of Athens and the region of Attica, Greece. It is the country's busiest airport, serving as the main hub of Aegean Airlines, the largest Greek airline by total number of passengers carried, as well as other Greek airlines. It has been selected for this study since it was the European airport with the largest number of propeller-driven regional aircraft movements in the years 2015–2019.[1] In partic-

[1]Eurostat data (Airport traffic data by reporting airport and airlines, 2020).

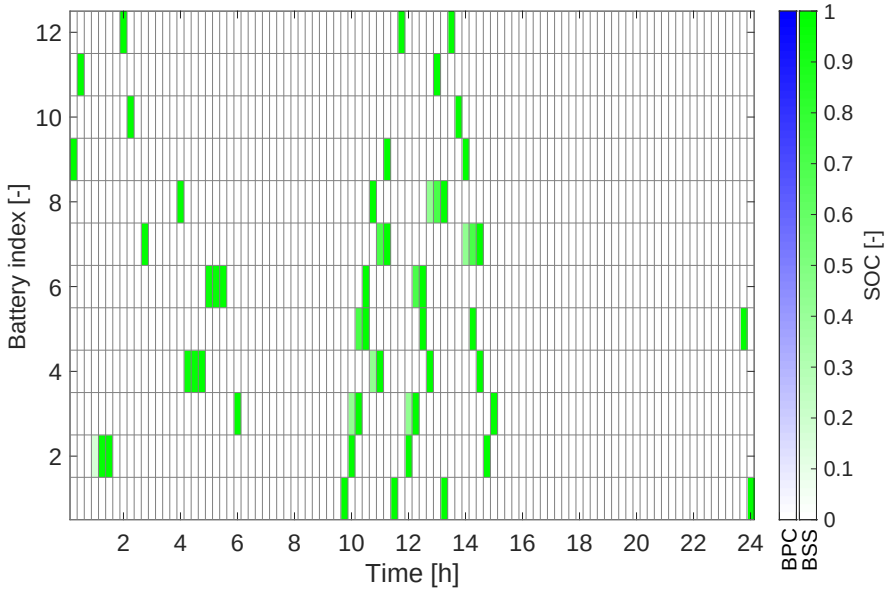

Figure 5.7: *Battery state of charge time evolution at LIMB for the Most Demanding Day case.*

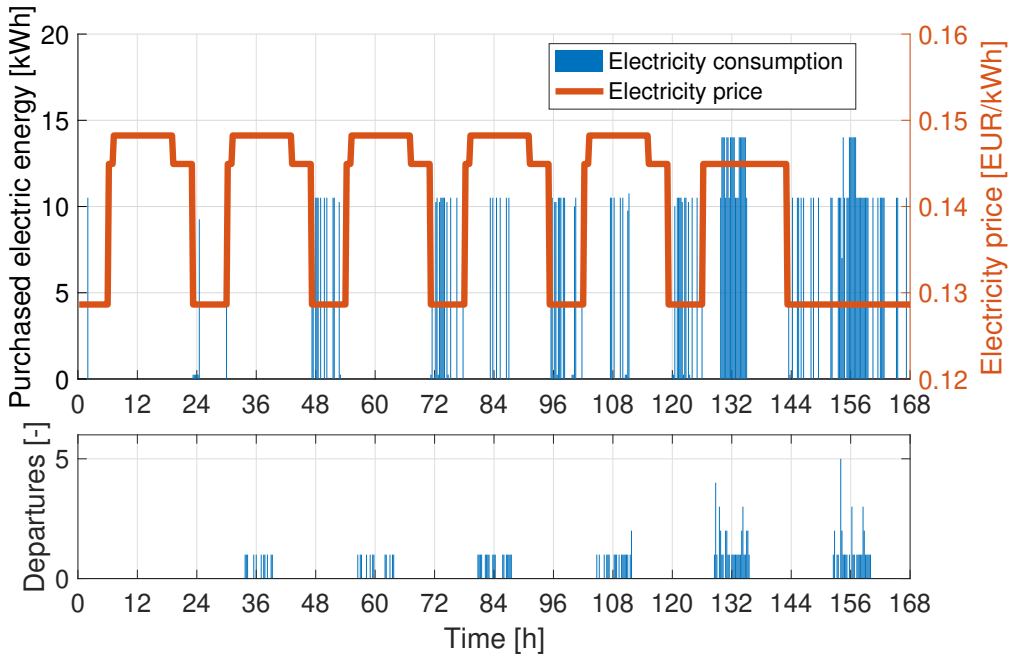

Figure 5.8: *Energy expenditure (top) and departure schedule (bottom) at LIMB for the entire week case.*

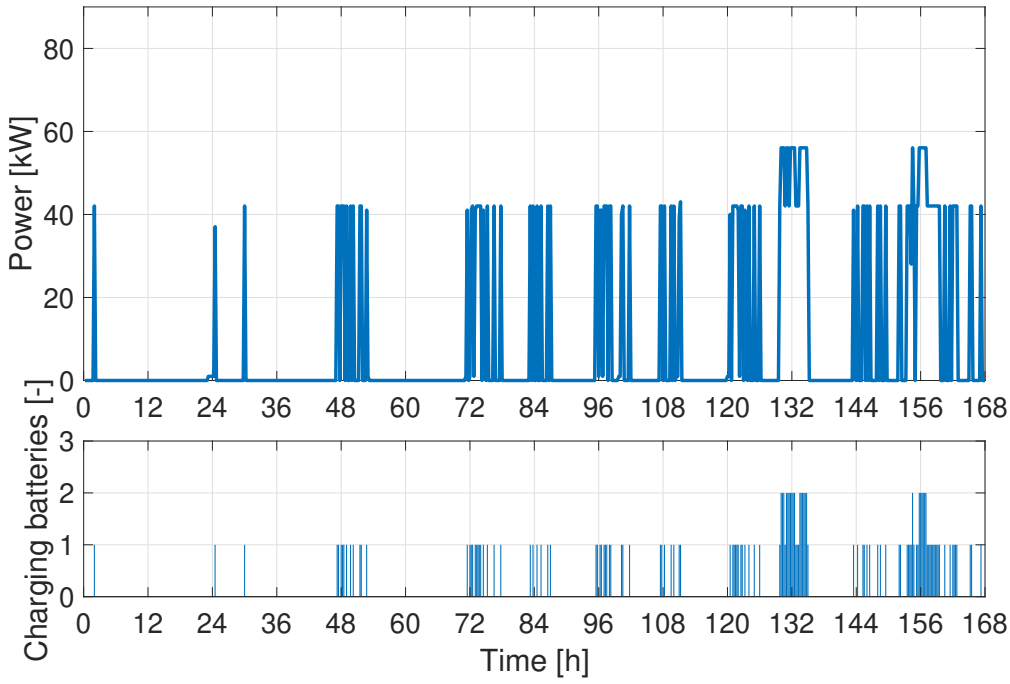

Figure 5.9: *Power consumption (top) and battery charging schedule (bottom) at LIMB for the entire week case.*

ular, regional flights in LGAV are still operated by turboprop aircraft, connecting the numerous Greek islands to the mainland. As propeller-driven regional liners appear interesting for the future implementation of environmentally-friendly HE models for short-haul transportation services, the LGAV study may be used to provide useful information for such an operational scenario.

The main regional airplanes operating at LGAV are the Bombardier Dash 8 Q400 (shortened as DH8 in the following), the ATR42, and the ATR72. These aircraft can carry 78, 48, and 70 passengers, respectively. In order to carry out a realistic analysis, we assumed to replace the current conventionally-powered fleet with new models featuring a serial HE power-train, such as those considered in the MAHEPA project. The sizing of the aircraft, including that of their propulsion systems, has been carried out through HYPERION, the preliminary sizing tool dedicated to PE and HE fixed-wing aircraft described in Chapter 4. In order to obtain such sizing, it is necessary to define a specialized mission profile in which all flight operations below a defined HETA are performed in a zero-emission PE mode. This includes taxi-out, take-off, initial climb, final descent, approach, landing, and taxi-in. Possibly loiter may be included as well. Above the HETA, the fuel-burning PGS is turned on, for providing energy during the rest of the flight phases, as well as for recharging the batteries, if needed. This strategy allows to drastically reduce chemical and noise emissions in the vicinity of the origin and destination airports and of the related overflown communities, and is considered an important advantage provided by serial HE power-trains. For the present analysis, the HETA was set to 3,000 ft.

The technical specifications of the electric-powered airplane design solutions are the result of a clean-sheet conceptual design loop starting from mission and certification requirements (*i.e.* they do not correspond to any 'retrofit' of existing models). For the sake of clarity, the serial HE airplanes sized through HYPERION are named as the mission performance corresponding model by adding an "HE-" prefix. The resulting battery capacity for each design solution is summarised in Table 5.9 together with the assumed corresponding budgetary price (including cells and battery pack), computed using 2018 Lithium-ion battery price values, *i.e.* approximately 176 €/kWh [35]. The assumed charging/discharging efficiency and battery life values are the same as seen in Table 5.5. The selected chargers maximum power has been raised to make a complete charge possible in a reasonable amount of time, given the sizeable increase in battery capacity with respect to the Milano–Bresso fleet. In particular, 200 kW and 400 kW rated power values for both BSS and BPC chargers were considered.

Table 5.9: *Aircraft battery characteristics for LGAV reconfiguration.*

Name	Pax	Battery capacity [kWh]	Battery Price [k€]
HE-DH8	78	1,400	253.4
HE-ATR42	48	1,000	184.8
HE-ATR72	70	1,300	237.6

Table 5.10: *Electricity prices employed for LGAV reconfiguration.*

Energy charge λ_t	
Daytime	0.0777 €/kWh
Nighttime	0.0648 €/kWh
Power charge c_p	
Daytime	10.5080 €/kW/month
Nighttime	2.5080 €/kW/month

In contrast to the Milano-Bresso study, complete departure/arrival data for the full year could not be retrieved for Athens International Airport. Therefore, an average daily flight schedule for the selected airplanes was estimated using public data.[2] While not sufficient to insure the capability to operate in the MDD, this preliminary investigation provides an illustration of the methodology and its potential in dealing with larger and more diverse case studies. During a typical day, there are approximately 30 departures that are relevant to the present analysis: 14 flights are performed with the DH8, 12 with the ATR42, and 6 with the ATR72. The flights are distributed during the day as reported in Figure 5.10. The length l_t has

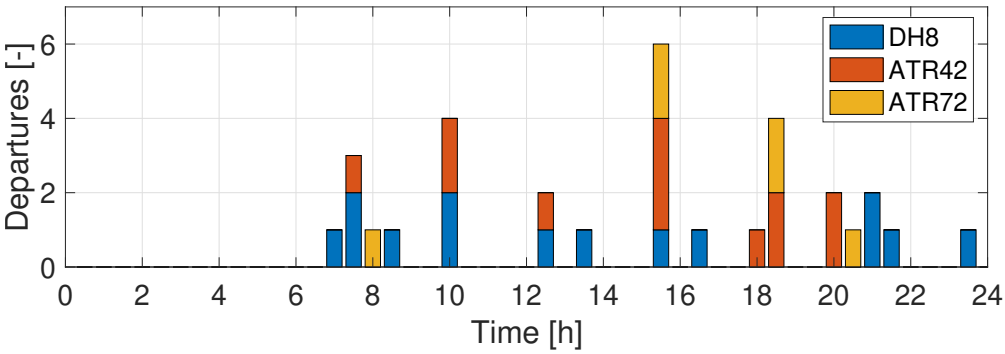

Figure 5.10: *Departure schedule at LGAV for the average day case.*

[2]The information retrieved on the Flight Radar 24 Live Air Traffic website was used (https://www.flightradar24.com/).

Table 5.11: *LGAV infrastructural sizing summary (the first, second, and third in the sums between parentheses refer to HE-DH8, HE-ATR42 and HE-ATR72, respectively).*

Quantity	Unit	Value	
No. of recharges	-	32 (14+12+6)	32 (14+12+6)
No. of batteries	-	24 (10+9+5)	21 (8+8+5)
No. of chargers	-	14 (6+5+3)	10 (4+3+3)
No. of BSSs	-	8 (4+3+1)	5 (2+1+2)
No. of BPCs	-	6 (2+2+2)	5 (2+2+1)
No. of aircraft	-	14 (6+6+4)	14 (6+6+4)
Average Battery replacement	Years	1.68	1.51
Energy consumption	MWh	36	36
Peak power	MW	2.6	2.9
Electric energy cost	€	2,531	2,502
Electric power cost	€	216	240
Total cost	€	44,908	44,263
		200 kW chargers	400 kW chargers

been set to 30 minutes in this case. No operations take place before 06:00 local time. We assumed that every aircraft performs a flight to another airport and comes back in three hours. Electricity prices in Greece for the year 2018 were assumed, as reported in Table 5.10. Unlike the Italian case, the energy and power components both depend on the time of the day, being set at different values for Daytime (weekdays, from 07:00 to 23:00) and Nighttime (weekdays, from 23:00 to 07:00, and weekends).

The results of the ARES procedure applied to the cases of 200 kW and 400 kW chargers are shown in Table 5.11 in a similar fashion to Table 5.8, here augmented by the detail of the different aircraft and battery types. It is observed that, when using 200 kW chargers, the number of aircraft necessary to fulfil the 32-flight schedule is 14, with six HE-DH8, six HE-ATR42, and four HE-ATR72. A mix of eight BSSs and six BPCs is needed to recharge a total of 24 batteries, *i.e.* ten more than the number of aircraft, to be swapped. The value of the cost function amounts to 44,908 €. When switching to 400 kW chargers, some important changes in the solution can be remarked. While the total cost is reduced by 1.43% and the necessary fleet is unchanged, the number of batteries is lowered to 21 (only seven spare) and the number of chargers to five BSSs and five BPCs. We note that the expected battery life is reduced, from one year and eight months to one year and six months, due to more frequent recharge cycles and that – for the same amount of energy drawn from the grid – the energy cost is slightly lower, meaning that less charging is necessary during Daytime as a result of the quicker recharge allowed by the higher power

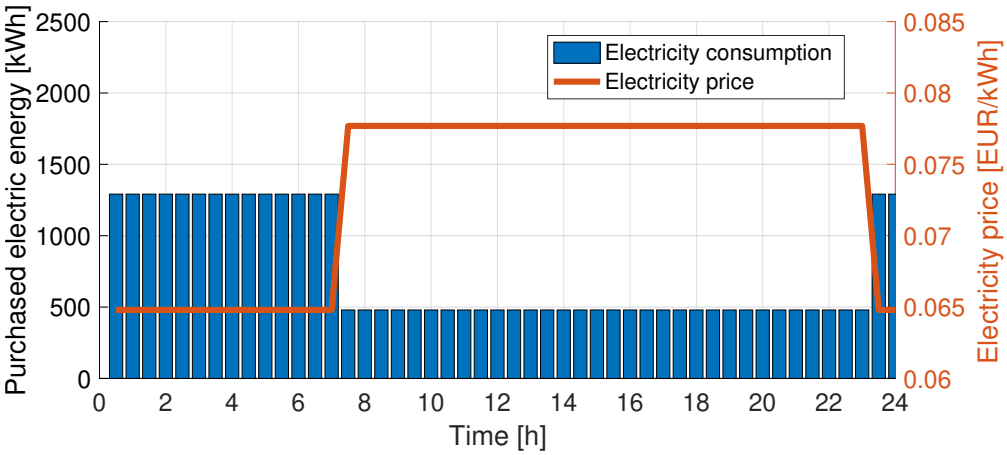

Figure 5.11: *Energy expenditure at LGAV for the average day case – 200 kW chargers.*

rating of the chargers. On the other hand, power cost is increased, hinting to a higher power drain on average.

Figure 5.11 provides the time history of energy consumption considering 200 kW chargers. As apparent, the solution provides constant nighttime and constant daytime energy drains, clearly with a much larger value for night hours when the energy and power pricing is lower. Figure 5.12 depicts the corresponding power consumption in the upper plot and the battery charging scheduling in the lower plot. Batteries are recharged continuously during the 24 hours, from a minimum of five to a maximum of fourteen simultaneously engaged. Notwithstanding the constant power required from the grid in the two time partitions, there are small variations in the number of batteries being simultaneously charged. This is due to the tuning of the power at with each battery is recharged and is clearly visible in Figure 5.13 reporting the battery state of charge $S_{i,t}$ throughout the day. In the figure, batteries from 1 to 10 are for the HE-DH8, from 11 to 19 for the ATR42, and from 20 to 24 for the ATR-72. Compared to the Panthera Hybrid case, the amount of energy stored in each battery is so high that even with the a nominal charger power higher than three times, the minimum time to fully recharge a battery ranges from five hours for the HE-ATR42 to seven hours for the HE-DH8. By looking at the coloured patterns, it is observed that in some cases, a battery of the HE-DH8 type may take up to 15 hours (which is more than double the nominal value) to recharge completely, at a reduced power setting.

Figure 5.14 provides the time history of energy consumption for the more powerful 400 kW chargers. Here, the constant pattern at night is basically

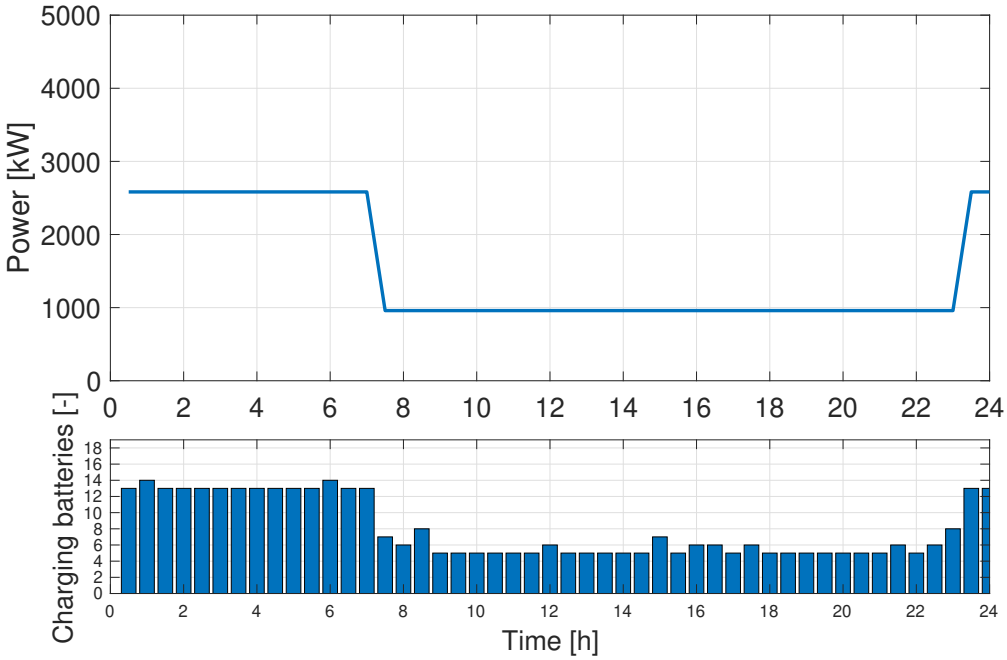

Figure 5.12: *Power consumption (top) and battery charging schedule (bottom) at LGAV for the average day case – 200 kW chargers.*

preserved, while a significant variation in the energy demand is seen during daytime. In fact, the chargers allow a quicker operation for each battery, so that all of them are completely recharged during nighttime and there is almost no need for continuing the process in the early daytime hours, at the rising of the energy and power pricing. Figure 5.15 illustrates the corresponding power consumption and the battery charging scheduling. The quicker recharging times, compared to the 200 kW case, are clearly visible, together with the power tuning that may change the recharge duration for a given battery. A maximum of nine batteries is simultaneously charged in this case. Figure 5.16 shows the time evolution of the battery state of charge, where now batteries from 1 to 8 are for the HE-DH8, from 9 to 16 for the HE-ATR42, and from 17 to 21 for the HE-ATR72. It is seen that the much faster recharging process (the maximum charging time is 5 h) allows more batteries to be served twice during the day when compared to the 200 kW case and even one to be charged thrice. Indeed, in the previous case, the batteries charged only once were 16 (67% of the total), while now they amount to 11 (52% of the total).

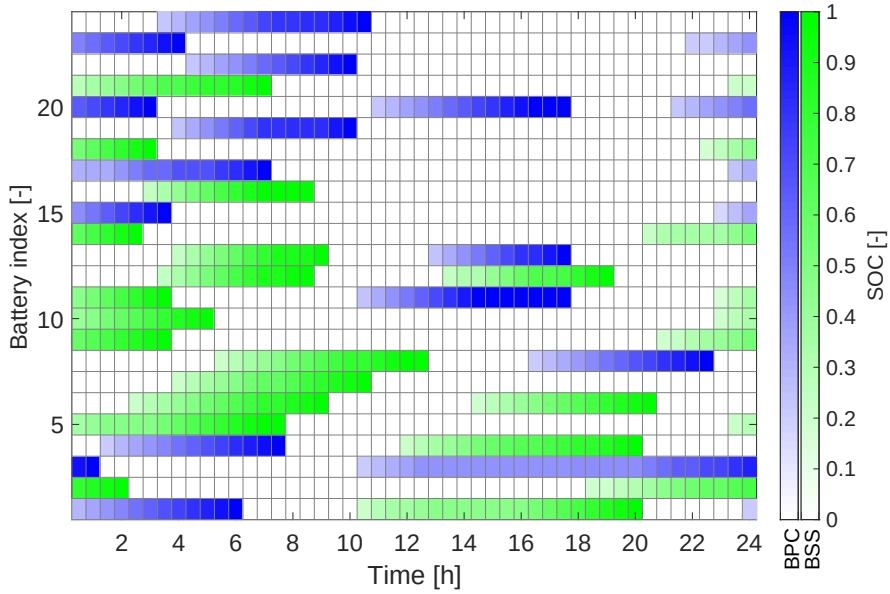

Figure 5.13: *Battery state of charge time evolution at LGAV for the average day case – 200 kW chargers.*

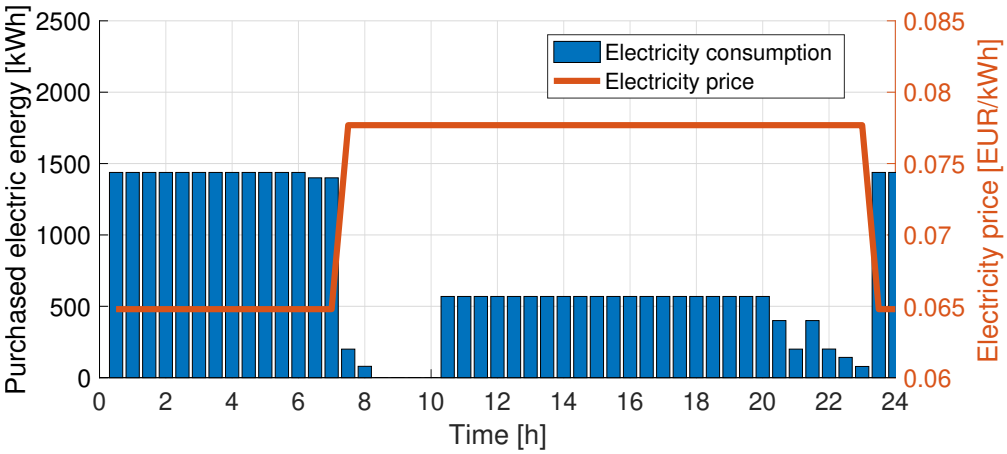

Figure 5.14: *Energy expenditure at LGAV for the average day case – 400 kW chargers.*

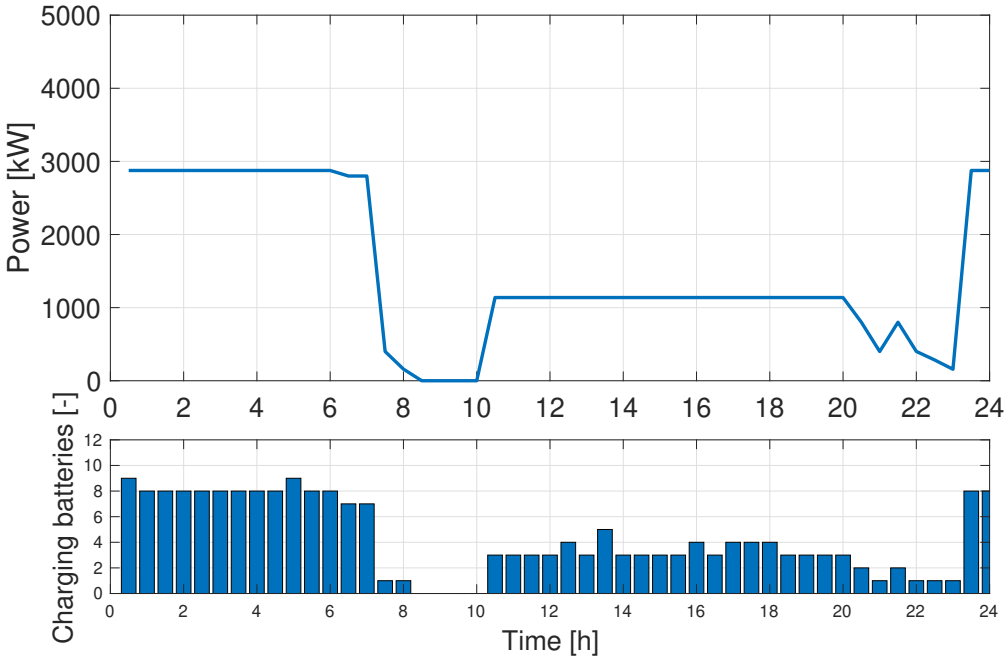

Figure 5.15: *Power consumption (top) and battery charging schedule (bottom) at LGAV for the average day case – 400 kW chargers.*

5.3 Conclusion

ARES, an original methodology solving the sizing of airport battery recharging infrastructure in support of an electric-powered fleet has been presented together with application studies. The underlying optimization algorithm provides the sizing solution together with the time planning of charging operations, in compliance with the predetermined flight scheduling at the airport, while minimizing procurement and operational costs. The method allows considering plug-in charging and battery swapping, either together or as alternatives. Due to the general approach in its formulation, ARES is suitable to extensive sensitivity studies on a large number of user-defined parameters. The discussed applications to a GA airport and to a large regional hub make use of real airport and aircraft data plus reasonable assumptions on the chargers' specifications, leading to feasible solutions that may be used as examples in the study of the general impact of transitioning from conventionally-powered to electric-powered aircraft fleets in the future.

Further developments of the ARES methodology shall consider other elements that may play a role in a a real case scenario. For example, the airport charging facility may provide ancillary services to the elec-

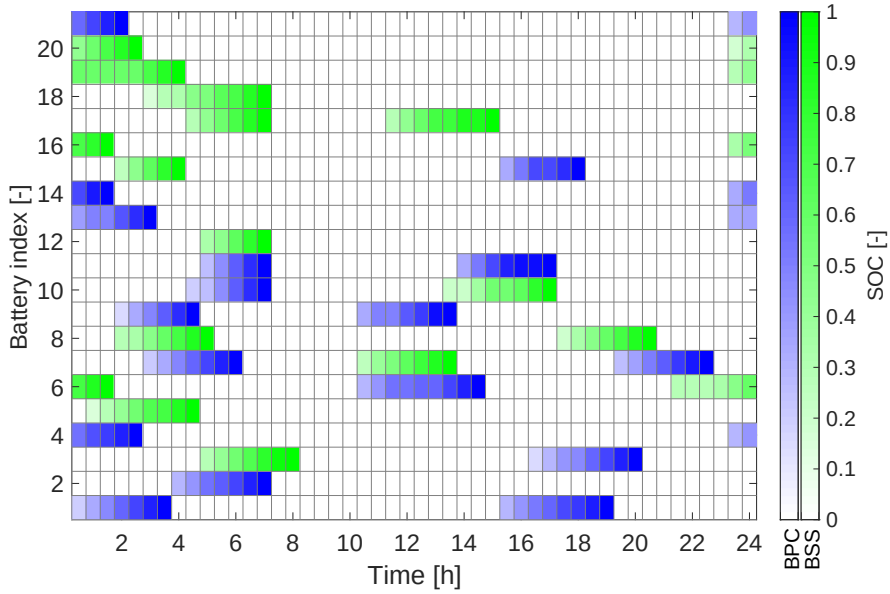

Figure 5.16: *Battery state of charge time evolution at LGAV for the average day case – 400 kW chargers.*

tric grid, such as intermittent renewable energy storage (from solar- and wind-energy production), peak power supply, frequency or voltage regulation and other Battery to Grid (B2G) and even Battery to Battery (B2B) applications. These possibilities will be investigated, also considering the possibility to alleviate the costs for the airport reconfiguration using the revenues brought by such grid-integration services. Among other elements that may be useful in application studies, the possibility to include the modeling of flight missions, to take into account residual battery state of charge higher than the minimum, can be considered. In addition, given the boosting interest in hydrogen-powered propulsion in aviation, in the quest for a more environmentally-sustainable air transportation system, an extension of the ARES methodology to encompass also hydrogen production, storage, and supply at airports is currently ongoing.

CHAPTER 6

ENVIRONMENTAL ASSESSMENT OF INNOVATIVE AIRCRAFT

New aircraft PE and HE power-trains may bring the most visible effects in the vicinity of airfields, where terminal manoeuvres and circuital patterns — the latter very frequent in training missions -– may be flown in pure- or partially-electric mode. Especially for lighter aircraft in the GA segment, capable of flying in and out smaller airfields often surrounded by densely populated areas, this new capability has the potential to increase public acceptance of near-ground air operations well beyond today's limits.

This in turn can increase the value of such airfields as elements of a diffuse infrastructure for the enhancement of citizens' mobility, for example by assuming a new role as nodes of a short-haul regional air transportation network. This implies the future use of CS-23 category commuters, provided with innovative environmentally-sustainable propulsion systems is roles such as the *microfeeder* and the *miniliner* introduced in Chapter 1.

In order to quantitatively evaluate the advantages of innovative electric

propulsion systems, to introduce a new performance parameter to be taken into account since an early stage in aircraft design, an acoustic and gaseous pollution prediction model would be required.

A part of the work presented was developed with the contribution of Luca Mariani, MSc student in the frame of his thesis. Results related to this activity have been published in [164–166].

6.1 Acoustic emissions

Comprehensive models capable of predicting the noise produced by an aircraft considered as a single emitter (instead of an assembly of different noise sources), include best-practice noise prediction procedures from European Civil Aviation Conference (ECAC) [167], which refer to the EUROCONTROL's Aircraft Noise and Performance (ANP) database [168]. Similar procedures are the foundation of such suites as Aircraft Noise CONtour (ANCON) [169], FLULA [170], SIMUL [171] and AzB [172]. ECAC procedures [167] provide the means for setting up and validating a comprehensive method for noise prediction, applicable to conventionally-powered aircraft and complying with accuracy standard. Such a method was assumed in this work for the validation of novel estimation procedures. The ECAC model is based on the principle of a standardized discretization of flight manoeuvres in proximity to the ground. The discretization resolution is tied to geometric quantities and flight mechanics parameters. The ANP database provides the values of the maximum Sound Pressure Level (SPL) and SEL, depending on the aircraft power setting and on the slant distance between the noise source and a receiver on ground for several aircraft models and corresponding engine options.

6.1.1 Proposed estimation approach

In order to build a noise prediction method applicable to aircraft featuring a hybrid-electric power-train, a bottom-up approach was followed. Firstly, suitable noise models for several airplane sub-components were considered, namely: propeller, airframe, thermal engine, gearbox, and electric motor. Inputs for such models include geometrical parameters, quantities describing the flight condition (propeller/thermal engine rotational speed, altitude, flight speed) and environmental conditions (air temperature). In particular, concerning the electric motor and gearbox, readily applicable models compatible with the current aeronautical application - i.e. power levels and power-to-weight ratios in the same range of existing electric or

hybrid-electric designs - are reported in [173]. The full list of noise models for the sub-components are detailed in [164].

Secondly, a global value of the SEL was obtained based on an energetic sum of the contributions from all considered sources, measured through the corresponding SPL values. In order to take into account the inaccuracy of the predictions for these sources, which would yield a highly inaccurate result if simply summed to each other, a source blending method was proposed, where each contribution is weighted by a blending coefficient to be determined. The proposed way of designing the blending coefficients is based on the tuning of the SEL obtained from the sub-component models to match the ANP database data.

The source blending method is based on the following expression for the SEL produced by the aircraft, $L_{E,A}$, as

$$L_{E,A}(d) = 10\log_{10}\left(\int_{t_1}^{t_2} 10^{x_1\frac{L^a_{p,A}(d,t)}{10}} + 10^{x_2\frac{L^p_{p,A}(d,t)}{10}} + 10^{x_3\frac{L^e_{p,A}(d,t)}{10}} + \right. \\ \left. + 10^{x_4\frac{L^m_{p,A}(d,t)}{10}} + 10^{x_5\frac{L^g_{p,A}(d,t)}{10}}\mathrm{d}t\right), \tag{6.1}$$

as a function of the slant distance d. The terms appearing in the time-integrated function $L^a_{p,A}(d)$, $L^p_{p,A}(d)$, $L^e_{p,A}(d)$, $L^m_{p,A}(d)$, $L^g_{p_\alpha,A}(d)$ represent the overall SPL values corresponding to the airframe, propeller, engine, electric motor, and gearbox, respectively. In Equation 6.1 the energetic sum appears modulated or weighted through a set of *blending coefficients* x_k, $k = 1, \ldots, 5$, which, ideally, should all equal 1. As significant uncertainty is associated with the prediction provided by each source, the proposed method provides a way to estimate the blending coefficients in an optimal fashion by minimizing a suitable error cost function. To this end, a set of eight GA single and twin-propeller aircraft in the ANP database were taken as a reference.

The ANP database provides SEL values for a number of aircraft in several weight categories. These were taken as reference values, based on the presumed accuracy of the method. The models for the considered noise sources were applied to the same conditions adopted for obtaining the values in the ANP database. Finally, the blending coefficients were validated by computing the SEL with the proposed source blending method and comparing the results with the output of the ANP database.

In order to check the suitability of the proposed prediction method to aircraft with novel propulsion systems, it is important to remark that for a hybrid-electric case more noise sources need to be considered than

those typical to conventionally-powered aircraft. In particular, the noise emissions of the electric motor and of the gearbox need to be evaluated.

In [164], the noise contribution of the electric motor and gearbox were compared to those of the propeller and reciprocating engine over a wide spectrum of power fractions and rotational speeds. It emerged that propeller and thermal engine emissions are always more intense than those pertaining to the electric motor and the gearbox, confirming an intuitive disparity between these sources.

Based on this analysis, the electric motor and gearbox noise components were ruled out for the case of GA hybrid-electric aircraft, in turn enabling the application of the source blending method based on the sole coefficients already designed for the conventional case, i.e. propeller, airframe, thermal engine.

The complete discussion introducing the source blending method and validating it is thoroughly elaborated in [164].

6.1.2 Example noise emission studies

The proposed source-blending prediction method can be deployed to analyze cases of practical interest and, in particular, to investigate the potential of pure-electric and hybrid-electric propulsion in mitigating noise pollution at airports.

The airport of Milano-Bresso, introduced in Section 5.2.1, has been selected as a test case for quantitative analyses presented herein. As anticipated, this airport is the home base of the ACM fleet, which is operated for instructional purposes and for pleasure flights. The fleet is mainly composed of both single-propeller and twin-propeller GA aircraft. Geographically located at the Northern border of the municipal area of Milan, Italy, the airport is completely surrounded by densely populated districts of the greater Milan area. This feature makes it a critical infrastructure with regards to noise and has fuelled an interest in the present analysis.

Based on a realistic description of the circuit around the runway of Milano-Bresso, two analyses are proposed in the present section. First, an assessment of the effect on the noise levels perceived on ground when some or all portions of the circuit are flown in pure-electric mode will be described in detail. To this aim, it will be hypothesized to fly a typical circuit by means of two different conventionally-powered aircraft, i.e. not provided with electric components in the power-plant. Several cases have been analysed where piston engines are conditionally activated in some clearly

identified legs of the circuit. In doing so, as no re-design of the aircraft is taking place, it is implicitly assumed that the necessary battery pack and pure- or hybrid-electric power-plant can be installed on board the existing aircraft without altering its maximum take-off weight and performance requirements. This retrofit can be conveniently evaluated by applying HYPERION, the preliminary sizing tool introduced in Chapter 4. That said, this comparative analysis produces valuable results to better understand in which parts of the circuit pure-electric propulsion (i.e. the deactivation of piston engines on hybrid-electric power-trains) may have a greater impact in terms of noise pollution.

Subsequently, a comparison is attempted between three existing aircraft, two conventionally-powered ones and the Pipistrel Panthera Hybrid (see Section 4.3.5, for an assigned circuit trajectory). For the Panthera Hybrid, it is assumed an activation/deactivation strategy for the PGS (i.e. the system coupling a piston engine with an electric generator that feeds the battery pack and/or the electric motor driving the propeller). This produces very promising results, which highlight the quantitative advantage implied by a fleet switching from ageing conventionally-powered models towards new hybrid-electric aircraft in the same weight category and with a similar mission profile.

6.1.2.1 Effect of power-train operational mode

The ECAC modelling approach [167] is applied to the discretization of the right-hand circuit of RWY 18, most commonly used in normal operation at Milano-Bresso. The circuit as typically flown by a Cessna 172R aircraft is presented in Figure 6.1 (left), and features a downwind leg at an altitude of 1 500 ft QNH. It is remarked that the discretization is not only geometrical, but also applies to flight mechanics parameters, as specified by ECAC guidelines. Two aircraft models, the Cessna T206H Stationair and the Piper PA-31-350 Navajo Chieftain, are considered as test-beds.

The prediction of noise emissions is carried out by computing the SEL on an assigned grid of sensors on ground. The source-blending method, with the coefficients computed in [164] can be applied to both aircraft, with the flight trajectory and flight mechanics parameters along the circuit assigned as input.

Sound exposure along the circuit ground track Initially, a grid of sensors is designed along the ground trace of the circuit. The adopted map of sensor points, represented by black dots, is displayed in Figure 6.1 (bottom). This plot also highlights the extension of the five legs in the traffic

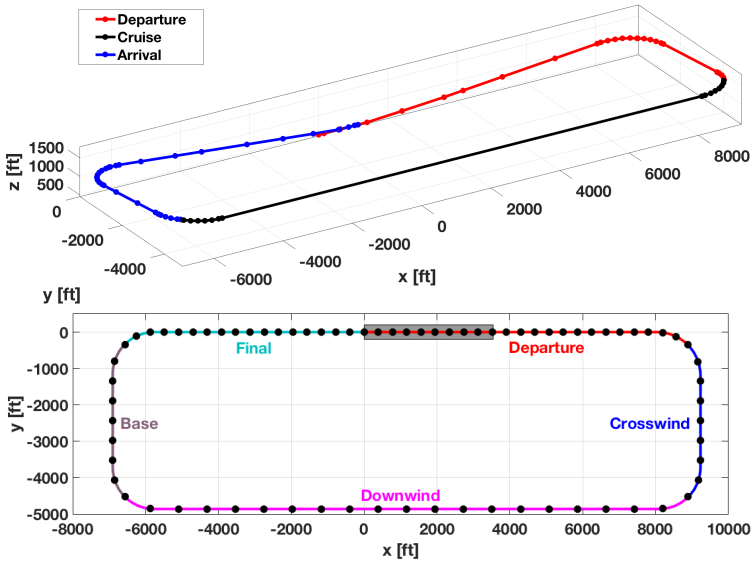

Figure 6.1: *Geometry discretization (top) and noise sensor placement (bottom) of the RWY 18 right-hand circuit at Milano-Bresso airport.*

circuit, namely: departure, crosswind, downwind, base, and final. The positioning of the grid follows the guidelines of ECAC validation scenarios [174]. As typical, the discretization is the result of a compromise between accuracy and computational cost, defined by means of a convergence analysis on the results. The main geometrical data of the grid are reported in Table 6.1. Clearly, the legs where altitude is changing more rapidly (departure and final) correspond to a finer discretization, whereas the downwind leg, where the aircraft is flying at constant altitude is associated to a looser discretization. The total number of sensors at this stage is 76. It is also worth mentioning that no transient is considered in the adopted noise emission models, so all changes in input and output variables involved in those models (e.g. power settings, rotational speed of the propeller, etc.) take place instantaneously.

As anticipated above, different power management strategies for flying

Table 6.1: *Grid characteristics for the ground track of the RWY 18 right-hand circuit at Milano-Bresso airport.*

Leg	Length (on ground) [ft]	Number of sensors	Resolution [ft]
Departure	8 990	24	391
Crosswind	4 360	9	545
Downwind	15 660	21	783
Base	4 370	9	546
Final	6 670	18	392

Table 6.2: *Piston engine conditional activation cases.*

ID	Circuit legs with piston engine activated
1	All
2	Departure, Crosswind
3	Departure, Crosswind, Downwind
4	Downwind
5	Downwind, Base, Final
6	Base, Final
7	None

the circuit are considered. Besides the extreme cases represented by using only the piston engine(s) (conventional propulsion case) or only the electric motor (pure-electric case), five further intermediate cases are investigated, as seen in Table 6.2. In order to present the results of the analysis in a concise form, as looking at the sensors one by one would be impractical, a more comprehensive measure is introduced. On account of the energetic nature of the SEL measurement, an energy-based spatial average $\overline{L_E}$ for an arbitrary piece of the ground track trajectory is computed based on the expression

$$\overline{L}_E = 10 \log_{10} \left(\frac{\int_{s_1}^{s_2} 10^{\frac{L_E(s)}{10}} \mathrm{d}s}{s_2 - s_1} \right), \tag{6.2}$$

where the SEL $L_E(s)$ is expressed as a function of the position along a segment of the ground track of the circuit, and s_1 and s_2 correspond to the initial and final extremes of that segment. respectively. By adopting the measurement in Equation 6.2 and applying it to each leg in the circuit, it is possible to obtain the results reported in Table 6.3 and Table 6.4 for the Cessna T206H and for the Piper PA-31-350, respectively. Both tables display the results of the application of conditional activation strategies for the piston engine listed in Table 6.2.

At a glance, a comparison of Table 6.3 and Table 6.4 points out a generally higher noise for the Piper PA-31-350. This is the result of a larger take-off weight, fuselage size, wing and tail areas, landing gear front section, and of a twin-engine configuration, as opposed to the smaller size and

Table 6.3: *Average SEL for the Cessna T206H.*

ID	Departure [dB]	Crosswind [dB]	Downwind [dB]	Base [dB]	Final [dB]	All legs [dB]
1	93.18	83.22	78.82	76.22	88.92	88.15
2	93.15	83.02	76.44	74.39	88.68	87.99
3	93.16	83.22	78.79	74.82	88.69	88.08
4	90.22	80.45	78.48	74.79	86.21	85.43
5	90.26	80.45	78.52	76.20	86.62	85.55
6	90.26	80.06	75.97	75.89	86.61	85.38
7	90.22	80.06	75.91	74.36	86.20	85.25

single-engine configuration of the Cessna T206H.

Comparing the legs to one another, it is possible to see that the noise exposure quotas pertaining to departure and final are the highest. For departure, this is the result of a combination of low distance from ground and high power setting. As for the sensors under the final leg, these are exposed to high noise from departure, which justifies the high values of this part (this will be evident from the sound exposure maps in the following).

Considering only the extreme piston engine deactivation strategies, i.e. Cases 1 and 7 in Table 6.2, it is possible to realize that the sensors under the crosswind leg are associated to SEL values immediately below those pertaining to departure and final, as a result of intermediate power settings and altitudes. Downwind and base are associated to the lowest SEL values, due to a higher distance from ground and lower power settings.

Analyzing the results in terms of conditional activation strategies, it is apparent that the pure-electric (Case 7) and all piston-powered (Case 1) scenarios are associated to the lowest and highest SEL values respectively. Looking at the intermediate cases, it can be seen that SEL values for each leg are roughly polarized around two extreme values. This means that when a leg is flown with the piston engine working, SEL values under that leg assume roughly an extreme, whereas when the piston engine is deactivated, the SEL values are always close to the opposite extreme. This polarization is further confirmed by the similarity between the SEL measures averaged over all legs for the Cases 4, 5, 6, and 7, i.e. when the piston engine is not running or it is run at low power (i.e. on downwind, base and final).

Sound exposure over airport area and surroundings To complement the analysis along the ground track of the circuit, a less refined grid of sensors has been adopted to quantify the SEL on the ground over a more extensive geometrical area. With reference to Figure 6.1(b), the new sensor grid extends between -15 000 ft and 15 000 ft in the direction of the runway centerline, and from -10 000 ft to 5 000 ft in the cross-centerline direction.

Table 6.4: *Average SEL for the Piper PA-31-350.*

ID	Departure [dB]	Crosswind [dB]	Downwind [dB]	Base [dB]	Final [dB]	All legs [dB]
1	97.25	87.83	83.19	80.30	91.72	92.03
2	97.22	87.69	80.66	78.66	91.33	91.83
3	97.22	87.83	83.17	78.99	91.34	91.94
4	93.68	85.01	82.96	78.97	88.84	88.87
5	93.75	85.01	82.99	80.29	89.49	89.05
6	93.75	84.73	80.34	80.04	89.47	88.83
7	93.67	84.73	80.29	78.64	88.82	88.65

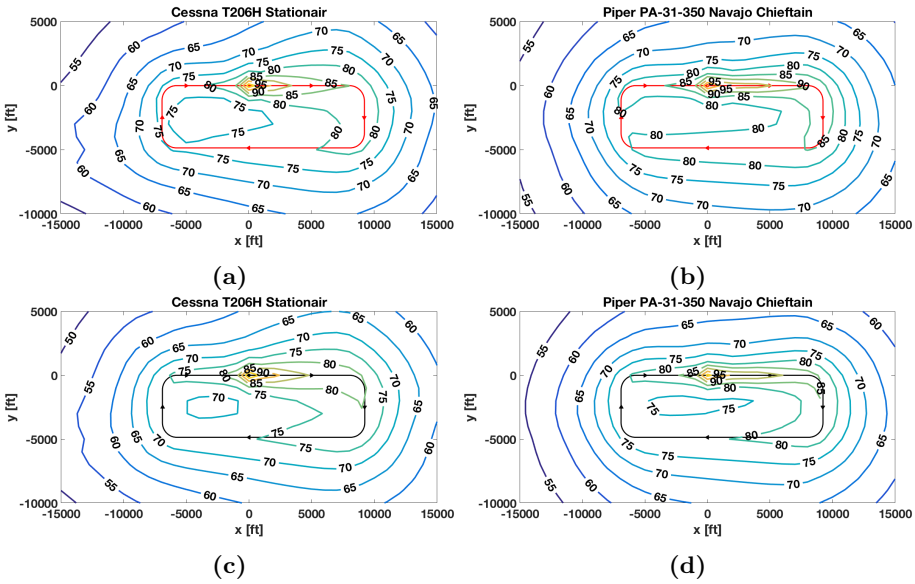

Figure 6.2: *SEL contour plots (in dB) over an extended sensor grid around Milano-Bresso airport: Case 1 (a) and Case 7 (c) for the Cessna T206H; Case 1 (b) and Case 7 (d) for the Piper PA-31-350.*

The resolution is 1 000 ft in both directions, yielding a total of 496 sensors, which allows to keep computational time to reasonable values.

The SEL contour lines associated to the extreme cases in Table 6.2 are reported in Figure 6.2 for the case of both aircraft models under investigation. With the adopted discretization, the computational time for a single plot in this figure is typically between 75 and 90 minutes for the PA-31 and the T206H, respectively, using a single dual-core `Intel® Core i5` processor.). In order to provide a quantitative description of the noise footprint, Table 6.5 and Table 6.6 display the areas A_{nl} contoured by a line corresponding to a given noise level nl (in dB). In both tables, the case ID refers to Table 6.2. From Table 6.5, it can be observed that in Cases 1,

Table 6.5: *SEL contoured areas for the Cessna T206H.*

ID	A_{70} [ft^2]	A_{75} [ft^2]	A_{80} [ft^2]	A_{85} [ft^2]	A_{90} [ft^2]	A_{95} [ft^2]	A_{100} [ft^2]
1	$2.1 \cdot 10^8$	$1.2 \cdot 10^8$	$4.4 \cdot 10^7$	$9.8 \cdot 10^6$	$2.8 \cdot 10^6$	$7.4 \cdot 10^5$	$8.8 \cdot 10^4$
2	$1.8 \cdot 10^8$	$8.9 \cdot 10^7$	$3.8 \cdot 10^7$	$9.6 \cdot 10^6$	$2.7 \cdot 10^6$	$7.2 \cdot 10^5$	$8.4 \cdot 10^4$
3	$2.0 \cdot 10^8$	$1.1 \cdot 10^8$	$4.3 \cdot 10^7$	$9.7 \cdot 10^6$	$2.7 \cdot 10^6$	$7.2 \cdot 10^5$	$8.5 \cdot 10^4$
4	$1.8 \cdot 10^8$	$9.4 \cdot 10^7$	$2.4 \cdot 10^7$	$4.7 \cdot 10^6$	$1.4 \cdot 10^6$	$2.6 \cdot 10^5$	
5	$1.9 \cdot 10^8$	$1.0 \cdot 10^8$	$2.5 \cdot 10^7$	$4.7 \cdot 10^6$	$1.4 \cdot 10^6$	$2.7 \cdot 10^5$	
6	$1.7 \cdot 10^8$	$7.6 \cdot 10^7$	$2.1 \cdot 10^7$	$4.7 \cdot 10^6$	$1.4 \cdot 10^6$	$2.7 \cdot 10^5$	
7	$1.6 \cdot 10^8$	$7.0 \cdot 10^7$	$2.0 \cdot 10^7$	$4.6 \cdot 10^6$	$1.4 \cdot 10^6$	$2.5 \cdot 10^5$	

2 and 3, when the piston engine is working in the departure and crosswind legs, i.e. at higher regimes, a core of higher noise intensity appears, which

especially from Figure 6.2(a) can be spotted along the ground track of the circuit, and in particular along the departure leg.

Comparing Cases 1 to 3 with 4 to 7, it can be seen that lower area values are associated to all noise levels for the four latter cases, and the core associated to the highest noise disappears in the same activation scenarios. This supports the results presented above in a more limited framework and is confirmed on the plot in Figure 6.2(c).

Table 6.6: *SEL contoured areas for the Piper PA-31-350.*

ID	A_{70} [ft^2]	A_{75} [ft^2]	A_{80} [ft^2]	A_{85} [ft^2]	A_{90} [ft^2]	A_{95} [ft^2]	A_{100} [ft^2]	A_{105} [ft^2]
1	$2.6 \cdot 10^8$	$1.8 \cdot 10^8$	$9.4 \cdot 10^7$	$2.6 \cdot 10^7$	$7.8 \cdot 10^6$	$2.4 \cdot 10^6$	$3.2 \cdot 10^5$	$3.6 \cdot 10^2$
2	$2.3 \cdot 10^8$	$1.6 \cdot 10^8$	$6.0 \cdot 10^7$	$2.4 \cdot 10^7$	$7.7 \cdot 10^6$	$2.3 \cdot 10^6$	$3.0 \cdot 10^5$	$1.9 \cdot 10^2$
3	$2.5 \cdot 10^8$	$1.7 \cdot 10^8$	$8.8 \cdot 10^7$	$2.6 \cdot 10^7$	$7.7 \cdot 10^6$	$2.4 \cdot 10^6$	$3.0 \cdot 10^5$	$2.0 \cdot 10^2$
4	$2.3 \cdot 10^8$	$1.6 \cdot 10^8$	$7.4 \cdot 10^7$	$1.3 \cdot 10^7$	$3.7 \cdot 10^6$	$6.1 \cdot 10^5$	$3.2 \cdot 10^4$	
5	$2.4 \cdot 10^8$	$1.7 \cdot 10^8$	$7.9 \cdot 10^7$	$1.4 \cdot 10^7$	$3.8 \cdot 10^6$	$6.6 \cdot 10^5$	$3.8 \cdot 10^4$	
6	$2.1 \cdot 10^8$	$1.4 \cdot 10^8$	$4.9 \cdot 10^7$	$1.3 \cdot 10^7$	$3.8 \cdot 10^6$	$6.6 \cdot 10^5$	$3.7 \cdot 10^4$	
7	$2.1 \cdot 10^8$	$1.4 \cdot 10^8$	$4.5 \cdot 10^7$	$1.2 \cdot 10^7$	$3.7 \cdot 10^6$	$6.1 \cdot 10^5$	$3.2 \cdot 10^4$	

The outcome of the analysis for the twin-engine Piper model is qualitatively similar to that for the Cessna single-engine aircraft. As observed, the configuration of this Piper model is forcibly associated to higher noise emissions than the Cessna aircraft. This is testified by the appearance of a top noise core of 105 dB in Table 6.6, whereas the corresponding value in Table 6.5 amounts to 100 dB. The generally more intense noise emission of the Piper PA-31-350 is testified also by the larger areas corresponding to the same SEL level, as can be seen from the comparison of corresponding columns on Table 6.5 and Table 6.6. This has a match in the stretched shapes of contoured areas associated to the highest noise levels in the (b) and (d) plots of Figure 6.2, pertaining to the Piper aircraft. By comparison, the contoured areas associated to the highest noise levels for the Cessna ((a) and (c) plots) are clearly more compact.

6.1.2.2 Effect of different propulsion systems

After assessing the effect of different piston engine activation strategies, without altering the actual structure of two existing conventionally-powered aircraft, an analysis is attempted on three more realistic test-beds.

Three aircraft models have been selected for the purpose: two are representative of conventionally-powered General Aviation 4-seaters, the vintage Cessna C172R Skyhawk and the modern Pipistrel Panthera; the third is the novel hybrid version of the latter, the Pipistrel Panthera Hybrid, that is currently being developed under the MAHEPA project. Concerning noise emissions, the blending coefficients have been identified for the class

of small GA airplanes and adopted for the three considered aircraft models [164].

Again, the case of the RWY 18 right-hand circuit of Milano-Bresso airport has been considered. As pointed out, the computation of sound exposure is based on the definition of a segmented aircraft trajectory and on the creation of a set of NPD data, made according to the source-blending method. The behavior of the flight mechanics parameters along the trajectory of the circuit has been simulated following the guidelines of the ANP database, starting from the data listed for a Cessna C172R. The guidelines have been emended considering the actual value of the altitude that must be kept over Bresso traffic circuit.

For the case of the Pipistrel Panthera in both its configurations, not included in the database, the same trajectory of the Cessna C172R has been assumed. Due to a general similarity in size, weight, and power, this assumption is considered reasonable. The aforementioned altitude limitations due to regulations over Milano-Bresso further reduce the uncertainty of such assumption – actually, all aircraft operating from this airport fly a very similar circuital trajectory. It also brings in as a plus the chance to assess differences in emissions only attributable to aircraft-specific features, and not to differences between trajectories.

For the case of the Panthera Hybrid, propelled by a series-hybrid powertrain, it has been assumed that the propeller is always driven by the brushless Siemens e-Motor SP150D. The power trend with respect to rotational speed is assumed linear, so that shaft power is directly proportional to rotational speed.

In order to keep it as close as possible to a realistic scenario, the Panthera Hybrid circuit flight has been analyzed assuming to activate the piston engine, a Rotax 914, only when the aircraft reaches the maximum allowable altitude, as operationally prescribed. In turn, this roughly corresponds to an engine activation along the downwind leg. Clearly, the two conventionally-powered aircraft are analyzed with the piston engine always running.

The SEL contour plots, computed on the same grid considered previously, are presented in Figure 6.3. As pointed out, from the three plots in Figure 6.3, it can be noted that the most intense SEL values are recorded in proximity to the departure leg, as this is characterized by the highest power settings and the lowest slant distances between the aircraft and the receiver on ground. The higher intensity of emissions in this phase is also responsible for relatively high SEL values on the ground track of the final leg. By comparison, the higher distance from ground typical of the down-

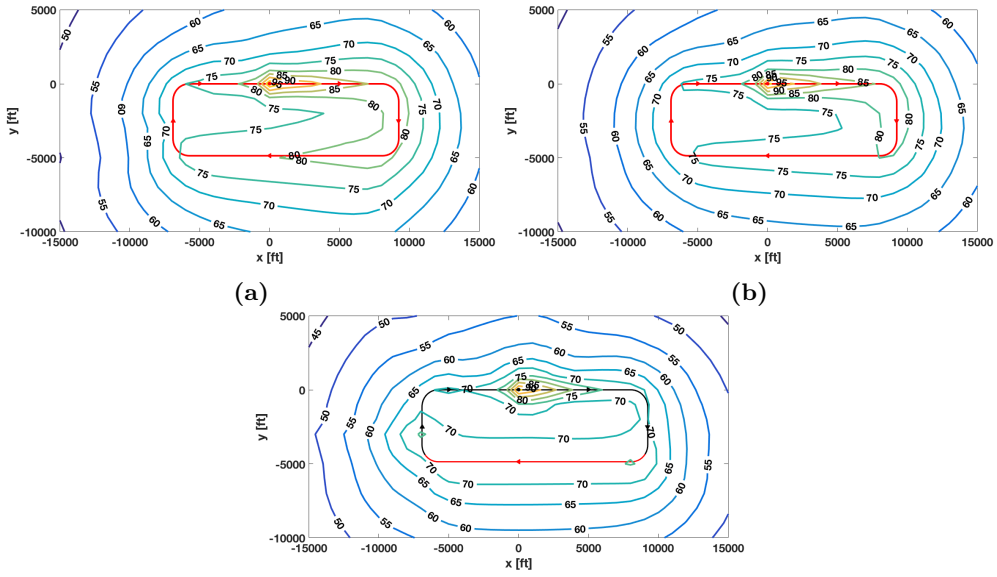

Figure 6.3: *SEL contour plots (in dB) over an extended sensor grid around Milano-Bresso airport: Cessna C172R Skyhawk (a), Pipistrel Panthera (b), Pipistrel Panthera Hybrid (c).*

wind leg, and the lower power settings of the base and final (the latter with the caveat just mentioned), are associated to a generally lower noise mark on ground for these legs.

Comparing the plots pertaining to the two conventional aircraft, these are qualitatively similar, but a difference in the extreme values can be noticed far from the circuit, especially port of the aircraft along the downwind leg, showing a generally lower noise footprint for the Panthera. Inside the circuit (i.e. in the immediate vicinity of the runway and aerodrome area) more significant differences can be appreciated in the shapes of the contour plots, but the values of the SEL are generally similar for both aircraft.

The Panthera Hybrid case displays some marked differences with the other two cases. Looking at the regions out of the circuit, the SEL is generally significantly lower for this aircraft, especially closer to high-power legs (departure, crosswind). It can be noticed also that the SEL gradient along the departure leg is more pronounced for the hybrid-electric case. Looking at the downwind leg, the activation of the piston engine at maximum regime in this phase produces a 70 dB contour line parallel to the downwind leg, which contrasts with the noise intensity decay registered for the two conventional airplanes.

To quantitatively compare the results in Figure 6.3, the same approach adopted for Table 6.5 and Table 6.6 has been adopted in Table 6.7 for the three aircraft considered in this phase. Considering in a first stage the

Table 6.7: *SEL contoured areas for the Cessna C172R Skyhawk, Pipistrel Panthera, and Pipistrel Panthera Hybrid.*

Aircraft	A_{70} [ft^2]	A_{75} [ft^2]	A_{80} [ft^2]	A_{85} [ft^2]	A_{90} [ft^2]	A_{95} [ft^2]	A_{100} [ft^2]
Cessna C172R	$1.9 \cdot 10^8$	$1.1 \cdot 10^8$	$3.4 \cdot 10^7$	$6.2 \cdot 10^6$	$1.9 \cdot 10^6$	$2.5 \cdot 10^5$	
Pipistrel Panthera	$1.8 \cdot 10^8$	$9.0 \cdot 10^7$	$2.8 \cdot 10^7$	$7.4 \cdot 10^6$	$2.6 \cdot 10^6$	$6.0 \cdot 10^5$	$1.6 \cdot 10^4$
Pipistrel Panthera Hybrid	$7.9 \cdot 10^7$	$8.3 \cdot 10^6$	$4.1 \cdot 10^6$	$1.9 \cdot 10^6$	$5.5 \cdot 10^5$	$9.0 \cdot 10^3$	

two conventionally-propelled models, it can be noticed that, somewhat unexpectedly, SEL higher than 100 dB is produced by the conventional Panthera, which is also associated to the largest contoured areas for SEL values of 85 dB and above, i.e. performing somewhat worse than the older C172R. Looking at the emission maps in Figure 6.3, such effect is likely due to the take-off phase, as SEL higher than 85 dB is registered only near the departure leg. A possible explanation for this effect is linked to Dobrzynski's model for piston engine noise [175], which accounts only for maximum power and not for its actual value. The conventional Panthera version is equipped with a 260-hp Lycoming IO-540-V, which is much more powerful than the Lycoming IO-360-L2A installed on the Cessna C172R Skyhawk. This results into a generally higher engine noise and, consequently, also into a larger exposure level for the conventional Panthera during take-off and climb, i.e. two phases in which the contribution of the engine is mostly relevant.

On the other hand, the areas relative to the lower SEL values are higher for the Cessna C172R Skyhawk than the conventional Panthera (e.g. the 80 dB and the 75 dB lines). Looking at the emission maps in Figure 6.3, this difference is associated with a different behavior in the first part of the downwind leg, and may be related to the landing gear contribution to the overall aircraft noise. As engine power is not at its maximum value over this leg, the engine and propeller noise emission levels are comparable to the airframe contribution, in turn mainly related to landing gear, greater than wing noise level and for a flap deflection assumed null. Considering the Panthera, landing gear retraction has been assumed in the generation of the NPD data adopted for this flight phase, whereas the Cessna C172R Skyhawk is equipped with a fixed landing gear, contributing to the difference in overall aircraft noise. Focusing now on the Panthera Hybrid, the lower contoured areas in Table 6.7 confirm the generally lower noise footprint of this aircraft, as observed. There are also in this case locations where the SEL reaches 95 dB, but the corresponding contoured area is two orders of magnitude smaller than the value pertaining to the

Cessna C172R Skyhawk and conventional Pipistrel Panthera. The region contoured by the 90 dB and the 85 dB lines is three-times smaller for the Panthera Hybrid with respect to Cessna C172R Skyhawk, as a result of the different gradient in proximity to the departure leg, as observed. The area enclosed by the 85 dB line for the Panthera Hybrid roughly matches that associated to the 90 dB level for the Cessna C172R Skyhawk.

Considering the lowest exposure levels, a more interesting comparison is made with respect to the conventional Panthera, associated to lower values than the Cessna C172R Skyhawk. Looking at the 75 dB and 80 dB levels, the corresponding enclosed region is one order of magnitude larger for the conventional Panthera than for its hybrid-electric version. Since the aerodynamic and structural characteristics are the same for the two aircraft, such behavior is due to the effect of the electric component of the power-train.

On the other hand, the area contoured by the 70 dB line for the case of the Panthera Hybrid is only 2.2 times smaller than the corresponding value for the conventional Panthera, as a result of the large 70 dB area produced on both sides of the downwind leg, as noted in Figure 6.3(c).

6.2 Chemical emissions

Available methods for the prediction of chemical emissions are classified in three tiers and follow a standard set by the EEA [176]. The goal of the existing methods is computing chemical emissions at a system level. To this aim, low tier methods apply average data taken from national databases to estimate the number of movements from all airport in a nationwide system and make use of statistical emission data for aircraft. These methods are not sufficiently accurate to resolve the difference between the emission performance of two similar aircraft in a given category and flying an assigned trajectory, as of interest in this study. On the other hand, top-tier methods (class 3B) make use of precise characterization of the aircraft trajectory and flight performance characteristics, and can be profitably applied here.

The same discretization of the flight trajectory adopted for the acoustic analysis (see Section 6.1) and complying with ECAC standard is considered here. The LTO cycle, otherwise associated to a predetermined flight time (lower tier methods), can be computed accurately based on the time actually spent over each leg of the arrival and departure procedures, based on nodal values of speed and geometry data of the discretized trajectory.

A key-factor in the estimation of chemical emissions is the emission index $I_{j,k}$, defined for a chemical component k and a trajectory leg j. Databases for estimating this quantity are available from EEA especially for jet engines. Instead, for piston engines such data can be derived from the detailed database by Yakovitch [177], where emission indices for CO, NO_x, and Uncombusted Hydro-Carbon (UHC) are provided as a function of the fuel flow. On the other hand, the emission of CO_2 is computed based on a pre-determined proportion with respect to the quantity of AVGAS 100LL fuel burned, i.e. 3.067 gCO_2/gfuel.

A further dependence of the emission index for aspirated engines is from outside air temperature. This has been modelled by FOCA [178] through a linear law for CO and UHC, whereas no change is expected with temperature for NO_x.

According to EEA standard, the mass released in the atmosphere for the k-th chemical and due to all contributions from the N_l segments along a trajectory can be computed from Equation (6.3),

$$m_k = N_e \sum_{j=1}^{N_l} I_{j,k} \dot{m}_{F_j} t_j \tag{6.3}$$

where $\dot{m}_{F_j}$ is the fuel flow, t_j the time spent by the aircraft in the j-th leg. Finally, N_e is the number of engines. As mentioned in Section 6.1.2.1, the LTO cycle is computed below 3,000 ft, hence the mass in Equation (6.3) corresponds only to the legs of the terminal manoeuvres under this altitude. This is not a significant constraint for the case of light-powered aircraft of interest here, which fly terminal manoeuvres typically far within this threshold. The database by Yakovitch provides values for the emission indices and fuel flow, classifying them as related to five flight phases – namely take-off, climb-out, cruise, approach and final approach. In order to compute $\dot{m}_{F_j}$ and $I_{j,k}$ from the database for each segment in the considered terminal manoeuvres (see Figure 6.1), a segment needs to be attributed to one of these categories. Differently from the noise pollution analysis, no scatter is considered for chemicals, hence the total LTO mass is a primary endpoint of the computation procedure. To better assess the potential polluting effect of each emitted mass, considering the strong imbalance between mass and harmful effects of some components (like CO_2 and NO_x), the social cost corresponding to each pollutant has been computed as in Equation (6.4)

$$C_k = €_k m_k, \tag{6.4}$$

where C_k is the cost per chemical component and k is the social cost per unit mass of the k-th chemical. Values for the latter can be obtained from

the literature [56], and the adopted values are reported in Table 6.8 these refer to currency value in 2008).

Table 6.8: *Social cost per unit mass for the considered chemicals released by internal combustion engines*

Chemical	$€_k$ [€/kg]
CO_2	0.035
CO	0.09
UHC	4.47
NO_x	10.05

6.2.1 Example chemical emission studies

6.2.1.1 Effect of power generation system use

A comparison of the emission of chemicals for different aircraft has been carried out in the same scenario described in Section 6.1.2.1. Considering a Cessna T206H Stationair and a Piper PA-31-350 Navajo Chieftain, a single engine and twin-engine configuration respectively, the masses released over the five legs of a circuit are reported in Table 6.9 and Table 6.10. Results are proposed for one engine only in the case of the Piper (Table 6.10).

These data show that the Cessna aircraft produces a generally higher mass per engine. As the engines are actually very similar for the two aircraft, this effect is mainly due to the flight trajectory parameters. In particular, as the trajectory is very similar for the two aircraft – only slight discrepancies exist in the access to the crosswind and early downwind legs, as the Cessna climbs faster than the Piper and reaches circuit altitude earlier – the difference is due to airspeed. The higher speed performance of the Piper allows it to fly the circuit faster, hence reducing the time spent

Table 6.9: *Released masses of chemicals, Milano-Bresso RWY 18 right-hand circuit, Cessna T206H Stationair.*

Circuit leg	mCO_2 [g]	mCO [g]	mUHC [g]	mNO_x [g]
Departure	3,884.70	1,320.10	35.5	6.8
Crosswind	1,065.00	178.5	10.3	10.4
Downwind	3,714.40	622.5	36	36.3
Base	783.9	212.4	9.4	3.3
Final	1,578.20	467.6	19.3	4.3

Table 6.10: *Released masses of chemicals, Milano-Bresso RWY 18 right-hand circuit, Piper PA-31-350 Navajo Chieftain. Computation for one engine only.*

Circuit leg	mCO_2 [g]	mCO [g]	mUHC [g]	mNO_x [g]
Departure	3,330.60	1,168.50	30.3	4.1
Crosswind	1,134.70	398.1	10.3	1.4
Downwind	2,566.60	445.6	24.8	24.4
Base	524.7	142.7	6.3	6.3
Final	1,196.20	354.3	14.6	3.2

Table 6.11: *Comparison of social cost associated to a single circuit, for different activation strategies of the power generation system.*

ID	Cessna T206H [€]	Piper PA-31-350 [€]
1	1.99	2.901
2	0.781	1.217
3	1.593	2.325
4	0.811	1.108
5	1.208	1.684
6	0.397	0.576
7	0	0

over each leg, in turn reducing emissions. For crosswind, the balance is in favour of the Cessna, as part of this leg is flown in cruise mode (lower power setting), as circuit altitude is reached earlier for this aircraft, as just observed. Considering next the same power generation systems activation strategies presented in Table 3.5, under the hypothesis of operating an ideal hybrid-electric version of the two aircraft taken as example (with the same weight and power performance), the results presented in Table 6.11 are obtained, in terms of social cost for the whole circuit. It is immediately apparent that the overall cost is generally higher for the twin-engined Piper aircraft, but by a ratio which is clearly less than 2. This confirms that the number of engines is not the only driver of cost, but the higher airspeed plays a relevant mitigation role.

6.2.1.2 Comparison of different aircraft

An investigation of the scenario proposed in 3.1.7.2 is proposed also in terms of chemical emissions. Here a Cessna C172R, a Pipistrel Panthera and a Pipistrel Panthera Hybrid fly the same circuit, and the corresponding chemical emissions are predicted. Due to the relevant disproportion be-

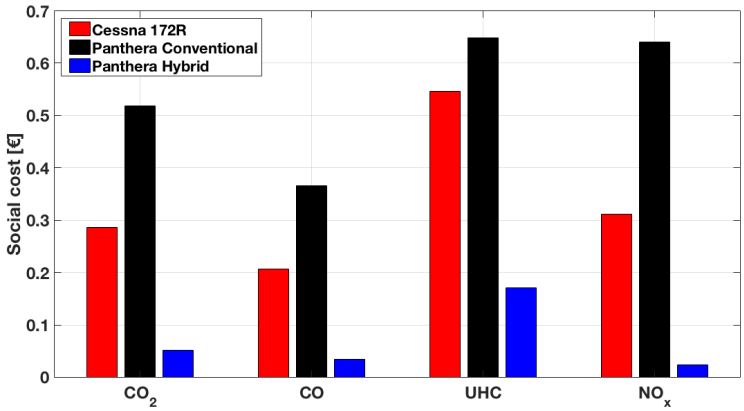

Figure 6.4: *Comparison of social cost corresponding to a Milano-Bresso RWY 18 right-hand circuit flown by a Cessna C172R, Pipistrel Panthera and Panthera Hybrid.*

tween mass and social cost, a comprehensive comparison is more straightforward on the latter performance index. The hybrid version of the Panthera is flown in purely electric mode except above 1,000 ft ground, i.e. basically for the downwind leg. The results of the analysis are synthetically shown in Figure 6.4 . It is noteworthy that from Figure 6.4 it is possible to compute the total mass of each chemical released by each aircraft, using the data in Table 6.8. The largest contribution to social cost goes generally to the conventional version of the Panthera, which is based on a 260 hp powerplant, whereas the Cessna C172R mounts a less powerful 160 hp engine. The power generation systems of the Panthera Hybrid is also different, besides being activated only for a limited part of the circuit. Looking at the results for the UHC, it can be observed that the proportion between the three aircraft, by comparison to the picture for CO_2 and CO, largely similar to each other, is here in favour of the conventional Panthera. This is specifically due to the better performance of the engine of this aircraft (Lycoming IO-540-V). The opposite happens for NO_x, which appears better (lower emissions) for the Cessna C172R. In general terms, the highest social cost is due to UHC, which despite being associated to a more limited cost per unit mass than NO_x, are released in very relevant amounts.

6.3 Conclusion

The present chapter presents results from a new practical procedure to predict the noise produced and propagated by an aircraft featuring a

novel pure- or hybrid-electric power-train in the vicinity of an airport. The procedure is applied to two case studies, both set in the the circuit around the Milano-Bresso city airport. In the first case, the effect of the various activation strategies of a fuel-burning power generation system is taken into account, demonstrating the efficacy of some of such strategies in significantly reducing the noise perceived on the ground. Ideal hybridized variants of two existing aircraft have been introduced for testing in this study. In the second example, a comparison is made between existing conventionally-powered aircraft and the Pipistrel Panthera Hybrid, a hybrid-electric aircraft currently in an advanced development stage. In terms of noise reduction, the ability of the hybrid-electric architecture is clearly demonstrated, thus quantitatively documenting the gain provided by this novel type of power-trains and confirming the ability of the proposed noise estimation approach through sensible results.

The same trajectory segmentation needed to carry out acoustic analyses has been adopted for the assessment of chemical emissions. This has allowed to deploy very accurate methods for the prediction of the social cost of chemicals released by example ideal or existing hybrid-electric aircraft, to the same realistic test case adopted for the acoustic analysis. This analysis too has shown the potential of hybrid-electric power-trains in reducing social cost, thus potentially raising public acceptance and increasing the value of smaller airfields in the air transport infrastructure.

Part II

On the design of a zero emission commuter aircraft

CHAPTER 7

THE MINILINER CONCEPT

A key-element in understanding the applicability and profitability of novel electric-powered aircraft is the quantitative analysis of the air transport network they can support. Thanks to the stark reduction in noise and chemical emissions, especially during terminal manoeuvrers (see Chapter 6), airliners endowed with this new type of propulsion may operate from secondary airports and smaller airfields, collectively referred to as SAs, often located very close to towns or in densely populated areas, which are nowadays constrained by traffic limitations to reduce social cost and public annoyance. The upgrade of these overlooked assets to the role of nodes in a new air transportation infrastructure would be possible especially when coupled with a fleet of pure-electric or hybrid-electric commuter airplanes capable to take off and land from small SAs. Such a miniliner, specifically designed for passenger transportation on short and very-short haul routes, may be used in two flavours.

The first, here referred to as *microfeeder*, is intended to be operated in a hub-and-spoke service, used to feed major airports from smaller cities and open country territories, in an effort to ease the accessibility of medium-

and long-range flights. The second, here termed *intercity liner*, is intended to operate a point-to-point service, used to connect smaller cities and open country territories, mainly for daily commuting journeys. Both services may reveal as key components in the future development of a more connected continental transportation network through enhanced, environmentally sustainable regional air travel, especially in territories with inefficient ground transportation services to major airports or between towns. In particular, they may decisively contribute to the European Flightpath 2050 vision of a transportation system offering virtually any EU citizen the possibility to complete any intra-continental journey in no more than 4 hours, door-to-door.

This second part of the thesis will go trough the design process of the miniliner. Chapter 8 will show some market studies that will be used to set up the TLAR in Chapter 9. Finally, Chapter 10 and Chapter 11 illustrate the application of the preliminary sizing tool HYPERION and the conceptual design tool TITAN to the design of the miniliner, testing different power-train architectures and providing also sensitivity analysis on the design parameters.

7.1 Microfeeder

The goal of the microfeeder service is feeding international hub flights: passengers can be carried to big international airports (hubs) flying from SA scattered in the neighbouring territory, instead of taking the car and/or public transportation.

The idea behind this concept is trying to reduce the usually long travel time that it takes to go from someone's home to the nearest hub. Figure 7.1 depicts the Italian situation, showing the road distance in minutes between Italian towns with more than 20,000 inhabitants and the nearest hub. Bars in the figure show the distribution of this distance, while the orange line represents the integral of the distribution. Without accounting for parking times, 53.4% of citizens living in these towns cannot reach the nearest hub in less than 1 hour by car. The situation is dramatically different depending on the area (north, centre or south Italy) with an average travel time ranging from 55 to 100 minutes. Moreover, the situation is expected to be worse if smaller towns and villages are taken into account.

One example that shows the efficacy of the microfeeder service is depicted in the maps of Figure 7.2. This map shows the connection between the Estonian town of Kuressaare and Riga International Airport (EVRA) in Latvia, one of the biggest hubs of the region. In this particular case,

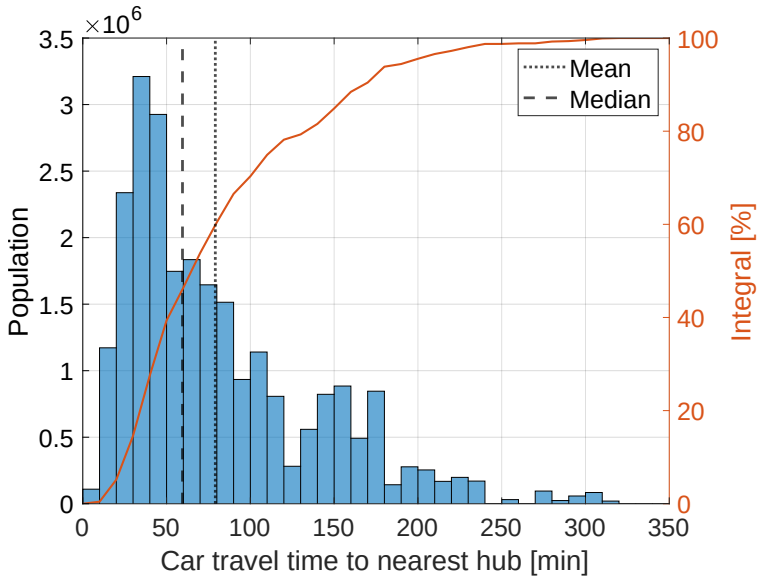

Figure 7.1: *Car travel time distribution to go to the nearest hub in Italy.*

the car would take almost 6 h (even more by train), but the microfeeder service only 1 h 16 min: 6 minutes car driving from Kuressaare to the nearest small airport, 40 minutes airport times (ckeck in, check out, etc.) and 30 minutes flight time, cruising at 200 KTAS. The microfeeder would be 4.7 times faster than the car alternative.

7.2 Intercity liner

The *intercity liner* service is a point-to-point transportation system for day to day commuting and business travel. The idea is providing a faster and greener alternative to ground based systems, mostly fossil-fuel based like cars, thanks to the miniliner hybrid-electric propulsion. From a European perspective, there is a good portion of European citizens who commute outside of the region where they live: 6% or 12 million of the 193 million people working in the EU aged 15-64 years in 2018 commuted to work within their country of residence from one area to another. The Benelux, the United Kingdom and, in particular, Norway have the highest share of interregional commuters with respect to the total number of employed people as depicted in Figure 7.3.

When considering the Italian case, nearly half a million people cross regional borders every day to go to work or study in Italy (according to the latest 2011 census). Moreover, more than 75% of the commuting is done

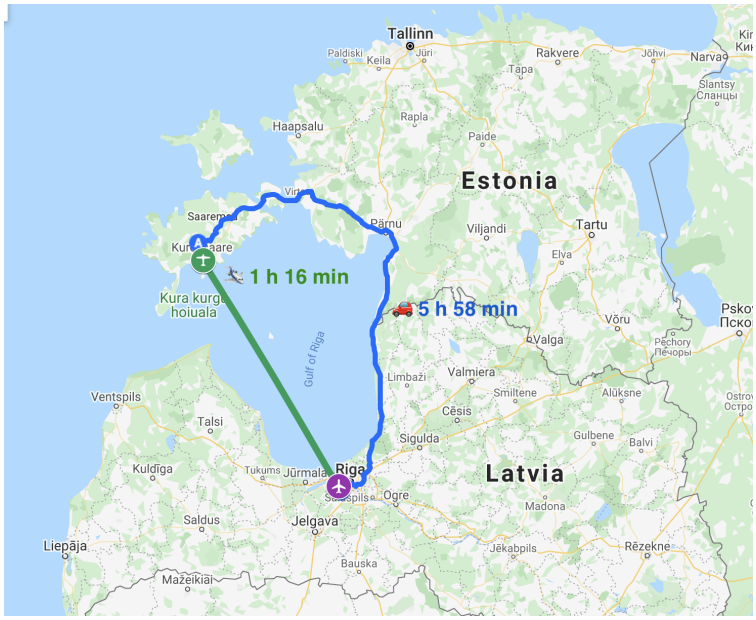

Figure 7.2: *Example of microfeeder route.*

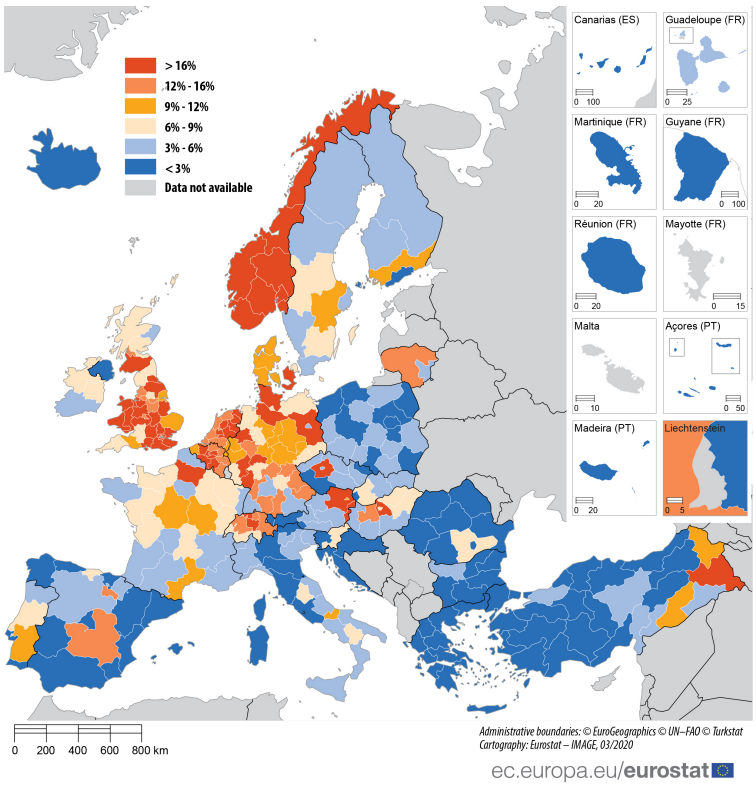

Figure 7.3: *Employed people commuting to another region within their country in Europe in 2018.*

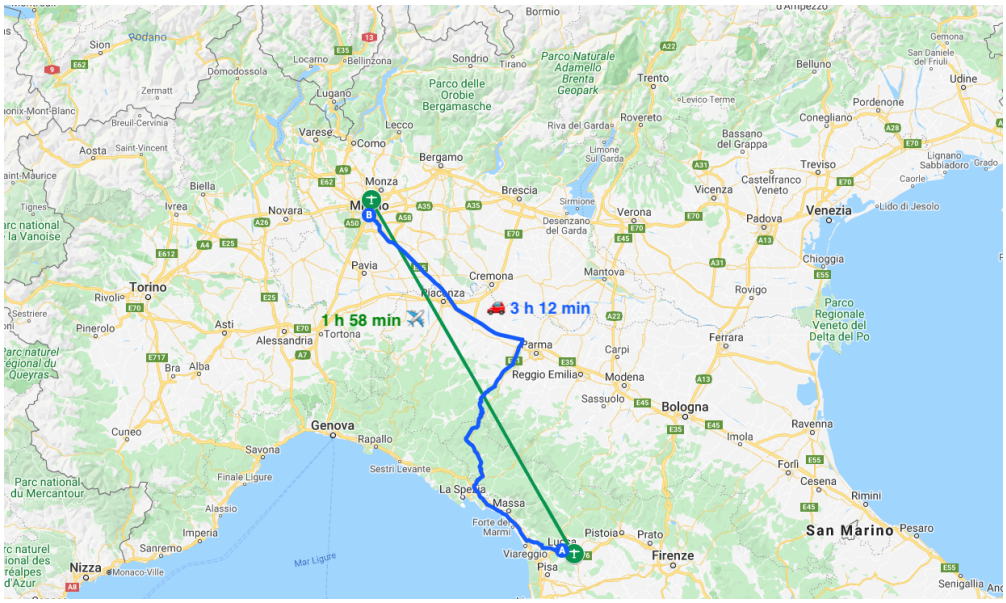

Figure 7.4: *Example of intercity liner service.*

using private cars, with a very small fraction being shared (carpooling). Car is predominant among workers, which makes up to 66% of total commuting population, while students prefer public means of transport. It is expected that the miniliner will be specially interesting in those cases where the commuting distance is long.

One example of the intercity liner service is depicted in Figure 7.4. A person living in Lucca (Tuscany) but working in Milan (Lombardy), could take the car to the nearest airport (Lucca-Tassignano Airport, 8.5 km from the city centre) and from there take the miniliner to Bresso Airport (LIMB), in the neighbourhood of Milan. The full car travel takes 3 h and 12 min without traffic. This time can be reduced to 1 h and 58 min, including 40 min extra time to check-in/check out at the local airports and the car time from the SAs to the city centres.

CHAPTER 8

MARKET STUDIES

This chapter shows the results of several market studies carried out to assess the potential demand for the miniliner and drive the decision of Top Level Aircraft Requirements (TLAR) detailed in the next chapter.

A part of the work presented was developed with the contribution of the following MSc students in the frame of their thesis project: Raouf Ibrahim (initial studies in the microfeeder potential demand estimation), Davide Gabrielli (microfeeder potential demand estimation), Germán García González (miniliner potential demand estimation). Results related to this activity have been published in [140, 141, 179].

8.1 Aerodrome studies

The starting point for the estimation of the potential demand for a miniliner service is the assessment of the existing and potential aerodrome infrastructures in a geographical area of interest. Based on the current European scenario, three types of aerodromes are identified (Table 8.1):

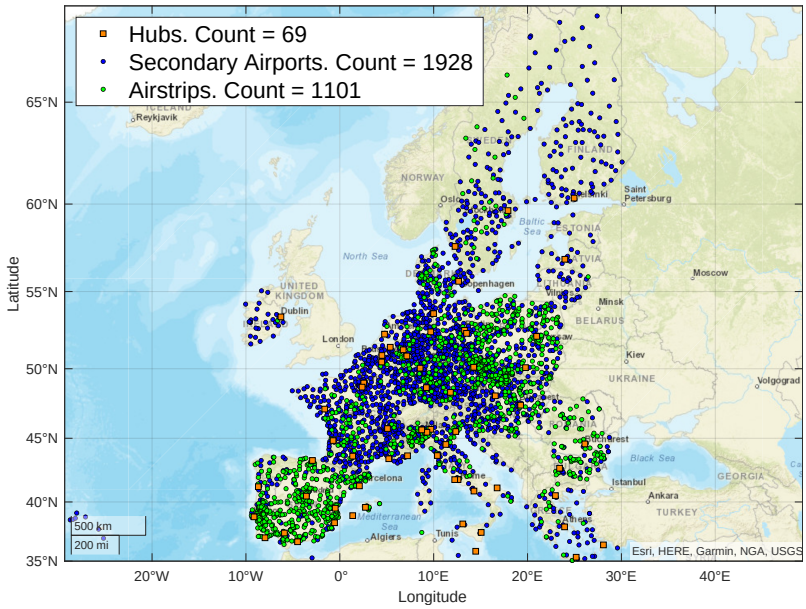

Figure 8.1: *Map of all aerodromes in Europe.*

1. **Major airports**, which are most typically adopted as hubs, support a volume above 5,000,000 passengers per year.
2. **Secondary airports**, which are below such threshold.
3. **Airfields**, by far the majority of aerodrome infrastructures in any European country, which are mainly used for sport and leisure flight. Airfields do not feature an ICAO code.

The set of secondary airports and airfields, collectively referred to as SAs is the asset that may be exploited by the miniliner transport network. The existing SAs with runways longer than 100 m have been identified through an analysis of the European data available on `openAIP.net` considering EU27 countries: Austria, Belgium, Bulgaria, Croatia, Republic of Cyprus, Czech Republic, Denmark, Estonia, Finland, France, Germany, Greece, Hungary, Ireland, Italy, Latvia, Lithuania, Luxembourg, Malta, Netherlands, Poland, Portugal, Romania, Slovakia, Slovenia, Spain and Sweden. Data about passenger traffic was taken from Eurostat[1]. A total of 3,029 SAs were taken into account. A map of all the airports and SAs in Europe is displayed is Figure 8.1

The runway length distribution of the selected SAs is shown in Figure 8.2. The average runway length is 996 m, with minimum and maximum values of 108 m and 4,000 m, respectively. The shape of the distribution shows

[1]https://ec.europa.eu/eurostat/web/products-datasets/-/avia_tf _apal

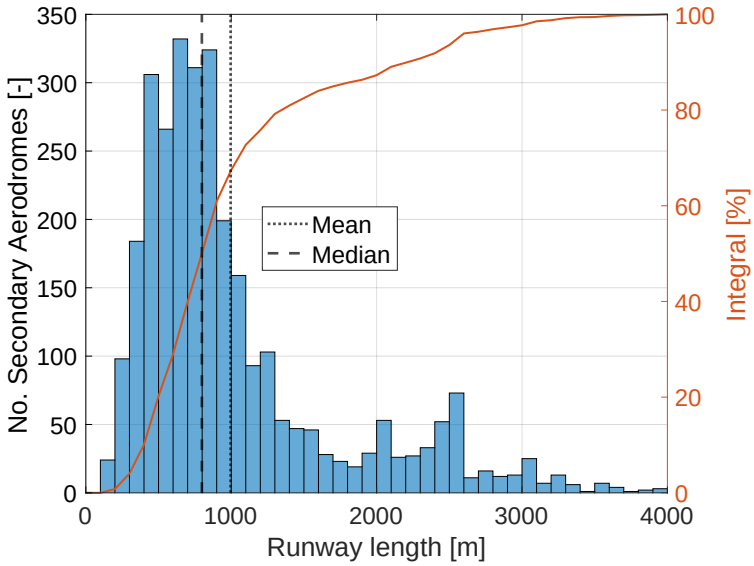

Figure 8.2: *Runway length distribution of European SAs.*

Table 8.1: *Survey of airports and airfields in Europe.*

Group	Type	Description	Quantity
Hubs	Hubs	$\geq$ 5M pax/year	69
Secondary aerodromes	Secondary airports	$<$ 5M pax/year	1928
	Airfields	no ICAO code	1101
Total			3098

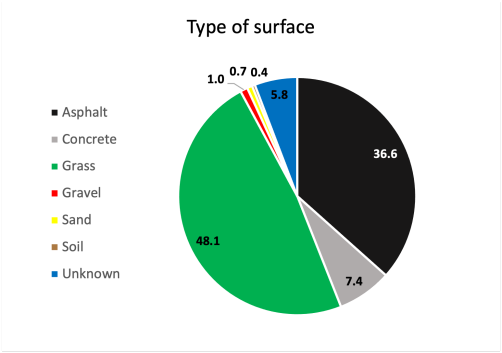

Figure 8.3: *Type of runway surface of European SAs.*

a marked asymmetry, with many runways shorter than the mean value. The median value is, in fact, 798 m, while the standard deviation is 698 m. The red curve in Figure 8.2, represents the integral of the runway length distribution and helps to further understand the situation. It is interesting to notice that runways 600 m or longer represent 75% of the total, 800 m or longer 50%, and 1,000 m or longer 35%. Of all SAs, 44% have either concrete or asphalt runways, while 48% feature a grassy surface. Other types of surfaces are gravel, soil and sand, which together account for less than 3% of the total (to visualise this data, see Figure 8.3).

Another interesting aspect of making use of SAs is the distance s_{SA} between any SA and the nearest one (Figure 8.4). Due to the very fine grid of existing SAs, considering only runways longer than 800 m (1376 SAs: 1,214 airports and 200 airfields), the mean value of s_{SA} is 66 km, while the median value is 40 km. Even more interestingly, 80% of SAs have another SA within 75 km range. This result may imply the need for short diversion distances for the miniliner.

8.2 Mission profile

Due to their nature, *intercity liner* and *microfeeder* services are expected to cover short distances. For this reason, high altitude flight might not be possible and cabin pressurization can be avoided. However, the lack of pressurization system, despite providing a significant weight saving, can limit the maximum cruising altitude and restrict the maximum rate of climb and rate of descent. For instance, pressure gradients related to high and low rates could bring passenger discomfort and eventually aural pain, in particular at very high rate of descents.

Figure 8.5 shows that in order to have a cruise at 8000 ft, with a cruising

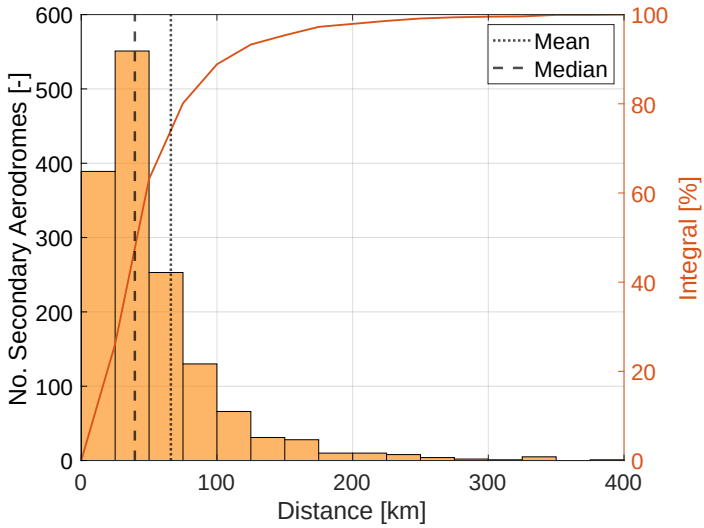

Figure 8.4: *Distance between one SA and the nearest one in Europe.*

speed of 200 KTAS (corresponding to 177 KEAS) the route has to be longer than 200-330 km depending on the rate of climb. Using the baseline values for commercial liner cabin altitude variation patterns (500 ft/min for the rate of climb and 300 ft/min for the rate of descent) the minimum range in order to climb to 8000 ft is 225 km. On shorter missions, the flight would not include a cruise phase but only climb and descent.

8.3 Analysis of ground transportation

An analysis of the existing European ground transportation system was carried out. The goals were the identification of possible transport mode competitors for the miniliner services and the evaluation of the *ground transportation efficiency* on a local territorial basis, in order to provide information for the areas where a miniliner service can be more competitive and time-efficient. To do so, Eurostat data[2] was analysed, leading to the mapping of Europe with respect to the density of the ground transportation infrastructures. The total length of motorways and railways measured in meters divided by the country area in squared kilometres was used to derive the ground transportation efficiency, as the overall ground network density. Figure 8.6 shows the distribution of such index across European countries. As reported, the maximum values are reached in Central Europe, with a peak in Belgium, while minimum values are found especially in North-Easternmost and South-Easternmost countries.

[2]https://ec.europa.eu/eurostat/web/products-datasets/-/tgs00003

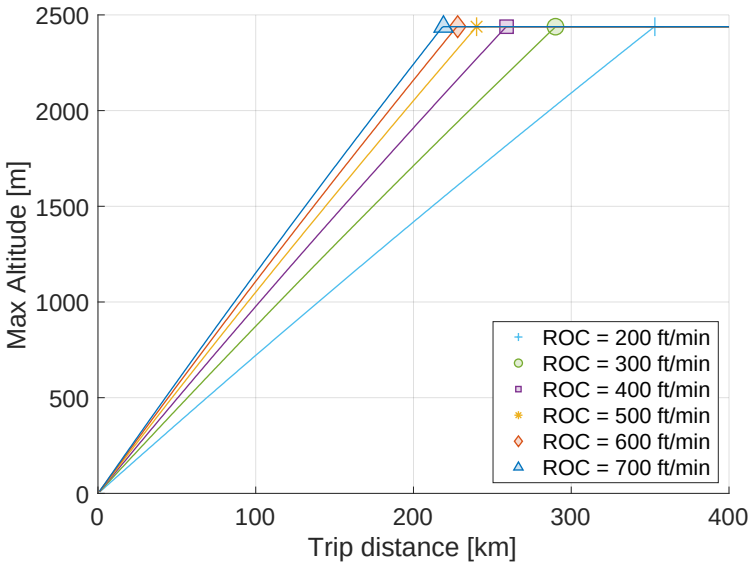

Figure 8.5: *Maximum cruise altitude for a given range.*

This analysis leads to the general classification of European countries highlighted in Figure 8.6. As apparent, the wide differences in the ground transportation efficiency values found across Europe yield the possibility of a clustering in three subsets. In fact, discrete jumps (marked in red in the figure) are found between the values for Romania and Portugal, and for Hungary and the Czech Republic. This inspires the definition of three subsets with high, medium, and low ground transportation efficiency. This study is considered preliminary to the analysis of selected cases seen as representative of the different conditions encountered in the three country subsets.

8.4 Potential demand estimation methodology

On the basis of the known aerodrome infrastructure, a vast number of routes may be traced connecting all locations. It is clearly crucial to be able to adequately downselect possibly interesting routes from such a large set. For this market study, a selection is enforced according to a time-saving criterion: the air routes which guarantee a minimum time advantage with respect to the car alternative are considered, while the others are discarded. Air route distances have been calculated by referring to orthodromic distances, whereas car travel distances and times have been gathered through HERE Maps APIs [180].

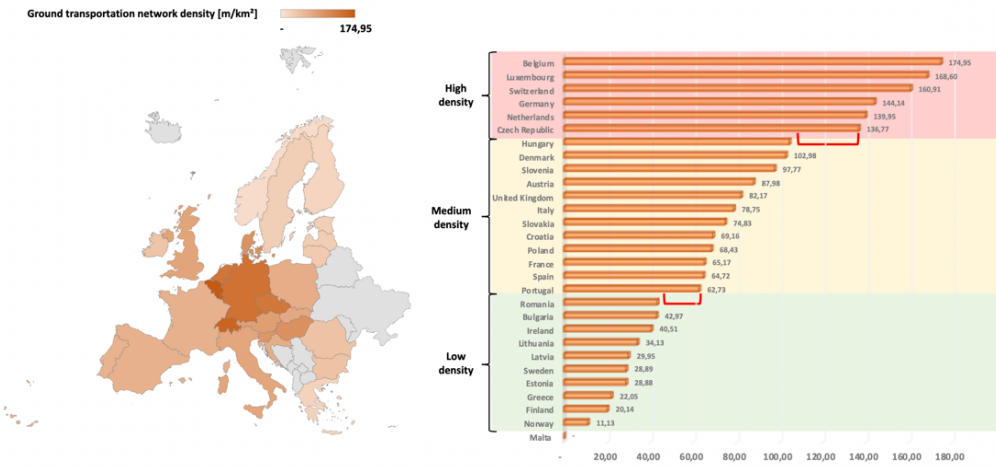

Figure 8.6: *Ground transportation network density map in Europe (left) and related country clustering (right).*

8.4.1 Identification of route catchment area

For a *microfeeder* service, the travel time is retrieved as the sum of the time t^{T-S} needed to reach a SA S from the considered municipal area T using land-based means and the travel time t^f of the miniliner flight from the SA to the hub. The latter is clearly a function of the flight performance characteristics of an assumed aircraft, and is obtained from a set of components:

$$t^f = t^{c-in} + t^{ta} + t^{to-lnd} + t^{t-in} + t^{t-out} + t^c \tag{8.1}$$

where the variables on the right-hand side are (from left to right): the time durations for check-in t^{c-in}, aircraft turnaround t^{ta}, take-off and landing t^{to-lnd}, taxi-in t^{t-in}, taxi-out t^{t-out}, and block cruise t^c (including climb, cruise, and descent flight phases). It is remarked that only the last term actually depends on the trip distance, while other terms are constant.

Given the previous travel time definitions, the catchment area for a route traced between a SA S and a hub H is defined based on the positive evaluation of the following time constraints:

$$\frac{t^{T-H}}{t^{T-S} + t^f} \geq k \tag{8.2}$$

$$t^{T-H} - \left(t^{T-S} + t^f\right) \geq t_{ref} \tag{8.3}$$

Equation (8.2) represents an imposed, significant time advantage of the novel miniliner-based transport solution with respect to the usual, purely

ground-based one, where k is a parameter that can be defined by the analyst at will and t^{T-H} is the term indicating the land-based mean travel time to go to the hub. Equation (8.3) further stresses this advantage, imposing a minimum difference of a duration t_{ref}. This can be explained for instance by considering a possibly higher fare of the miniliner solution with respect to a purely ground-based one. Adding a more significant time difference between the two services in favour of the miniliner may balance out a possible slight economical shortcoming of this solution.

For the *intercity* service, the travel time is given by the sum of the time $t^{T_1-S_1}$ needed to reach the nearest SA (S_1) from the departure town T_1 using land-based means, the miniliner travel time, t^f, and the time $t^{S_2-T_2}$ to go by land-based means from the arrival SA (S_2) to the destination town T_2. The constraints for the *intercity* case are equivalently

$$\frac{t^{T_1-T_2}}{t^{T_1-S_1}+t^f+t^{S_2-T_2}} \geq k \tag{8.4}$$

$$t^{T_1-T_2} - \left(t^{T_1-S_1}+t^f+t^{S_2-T_2}\right) \geq t_{ref} \tag{8.5}$$

where $t^{T_1-T_2}$ is the time that it takes to go from the departure town T_1 to the destination town T_2 using land-based means of transport.

8.4.2 Microfeeder potential demand estimation algorithm

8.4.2.1 Route function

The application of Equations (8.2), (8.3), to all considered municipal areas and aerodromes allows defining a number of connections between hubs and SAs, representing a potential traffic demand. This can be expressed in terms of the total number of passengers P_i with an advantage in reaching the i-th hub via the miniliner. However, this data, based only on demography (geographic distribution of the population), may not be sensitive enough to the potential travel interest of the local population. As a second factor, the local distribution of wealth, represented by the national gross domestic product (GDP), is thus considered. Therefore, for the pair represented by the i-th hub and the j-th SA, the corresponding route is associated to a demographic level D_{ij}, bound to the population size, and to an economic index G_{ij}, based on the GDP distribution, to represent the propensity to travel of the population associated to the route. Based on these parameters, it is possible to define the route value function $F_s\,(i,j)$

as

$$F_s\,(i,j) = \alpha\,\frac{D_{ij} - \min_{j\in H} D_{ij}}{\max_{j\in H} D_{ij} - \min_{j\in H} D_{ij}} + (1-\alpha)\,\frac{G_{ij} - \min_{j\in H} G_{ij}}{\max_{j\in H} G_{ij} - \min_{j\in H} G_{ij}} \tag{8.6}$$

where H represents the set of all hubs, and α is a tuning parameter defining the relative relevance of the economic aspect, with respect to a purely demographic datum.

8.4.2.2 Hub feeding demand

The analysis of the traffic potential of the connection routes must match with the actual feeding needs of the hubs. This can be quantified through the variables P_i^{arr} and P_i^{dep}, retrieved from publicly available databases and representing the number of passengers arriving and departing hourly from the i-th hub, respectively. In order to obtain a match between the actual airport needs and the potential traffic quota pertaining to each route connecting the i-th hub with secondary clusters, the following algorithm is proposed.

The values P_i^{arr} and P_i^{dep} are normalised by the population corresponding to the area connected to the considered hub, N, generating the following indices:

$$O_i = \frac{P_i^{arr}}{N}, \qquad D_i = \frac{P_i^{dep}}{N}, \tag{8.7}$$

where the values of O_i and D_i represent the normalised hourly number of passengers generated and attracted by the i-th hub, respectively. Next, the route value functions for all hub-SA pairs are normalised with respect to the sum of the route function values over the number of SAs, yielding

$$\varphi\,(i,j) = \frac{F_s(i,j)}{\sum_{j\in S} F_s(i,j)}, \tag{8.8}$$

where S represents the SA set. Finally, the hourly rate of generated (input) traffic on the routes from all hubs to a SA and the hourly traffic rate input on the route from the j-th SA to the hubs are defined as

$$o_j = \sum_{i\in H} \varphi(j,i)\,D_i, \qquad d_j = \sum_{i\in H} \varphi(i,j)\,O_i. \tag{8.9}$$

The potential hourly demand of the route from the i-th hub to the j-th SA is $G_{ji} = \varphi(j,i)\,D_i$, whereas the dual value from SA to hub is $g_{ij} = \varphi(i,j)\,O_i$. Both G_{ij} and g_{ji} are potential traffic demand parameters and are usually functions of the time of the day, as daily airport passenger flow in hubs typically features traffic peaks.

8.4.3 Intercity potential demand estimation algorithm

In order to estimate the number of people interested in traveling between any two towns using the *intercity liner* service, data about commuting habits from the Italian National Institute of Statistics was used. In particular, periodical censuses usually provide *matrices of commuting habits* estimating the number of people that commute daily for work or study reasons. The total traffic flow can be arranged in the form of a typical Origin-Destination (OD) matrix G such that

$$G = \begin{bmatrix} g_{11} & g_{12} & \cdots & g_{1n} \\ g_{21} & g_{22} & \cdots & g_{2n} \\ \cdots & \cdots & \cdots & \cdots \\ g_{n1} & \cdots & \cdots & g_{nn} \end{bmatrix} \tag{8.10}$$

where g_{ij} represents the commuter flow from the i-th town origin to the j-th destination. It is interesting to note that commuter traffic flow is bidirectional: those who travel in the morning will travel back in the afternoon/evening. Therefore, the "afternoon" OD matrix is simply the transpose of the "morning" OD matrix:

$$G_{\text{afternoon}} = G^T_{\text{morning}} \tag{8.11}$$

By evaluating of all route catchment areas relative to each entry of the OD matrix, the total potential demand can be estimated.

8.5 Potential demand estimation studies

The methodology described above has been applied to the study of a number of cases, in order to verify its capabilities to provide useful data for market studies dedicated to the design of the miniliner. In order to derive useful information on the effect of some of the TLAR on the demand-capturing capability of *microfeeder* and *intercity* services, parametric studies have been performed.

Here, results are shown as obtained by considering ranges of variation for the design values of the following performance parameters:

- Trip distance: from 100 to 300 km (*microfeeder*) and 600 km (*intercity*) with 50 km step increments (5 and 11 cases).
- Cruising speed: 200 ± 50 KTAS (3 cases).
- Take-off and landing distances: 800 ± 200 m (3 cases).

Cruising altitude is assumed at 4,000 ft. This is possibly reduced in case the trip is so short that the climb phase ends before reaching cruising altitude. Other mission profile parameters include optimal climb at a rate of climb of 500 ft/min and descent at cruising airspeed at a rate of descent of 250 ft/min.

The size threshold for towns considered in the analysis is 20,000 inhabitants. The constant part of the total travel time t^a is set to 40 min. The parameters defining the time advantage in Eqs. (8.2) are set as $k = 1.3$ and $t_{ref} = 30$ min.

8.5.1 Microfeeder service

Three case studies are presented in the following, all related to a possible feeding service for a single hub. These have been chosen as representative examples of the different conditions encountered across the European countries with respect to their ground transportation efficiency. Therefore, one case per each of the subsets identified in Section 8.3 was considered:

1. High ground transportation efficiency: Brussels Zaventem Airport (ICAO code: EBBR), Belgium.
2. Medium ground transportation efficiency: Venice Marco Polo Airport (ICAO code: LIPZ), Italy.
3. Low ground transportation efficiency: Riga Airport (ICAO code: EVRA), Latvia.

Neighbouring countries were also included in the analysis.

The graphs in Figure 8.7 refer to the case of selecting a maximum take-off and landing distance of 800 m (a "light" STOL case) for all the three scenarios, showing the potential passenger demand associated to the generated route networks. All quantities are displayed as functions of the range and parametrised with respect to cruising speed. It is apparent that in the EBBR and LIPZ case (Figures 8.7a and 8.7b) the potential demand that may be captured has a higher-than-linear rise with the increase of maximum trip distance, while the increase is significant, but less marked, in dependence of cruising speed. On the other hand, in Figure 8.7c for EVRA, the rise in the potential demand looks roughly linear with the increase of maximum trip distance. Moreover, EVRA results look insensitive to the value of cruising speed. This is clearly related to the low efficiency of ground transportation in the regions surrounding the hub under scrutiny, together with the relative sparsity of towns reaching the assumed threshold size. The values of the potential travellers for

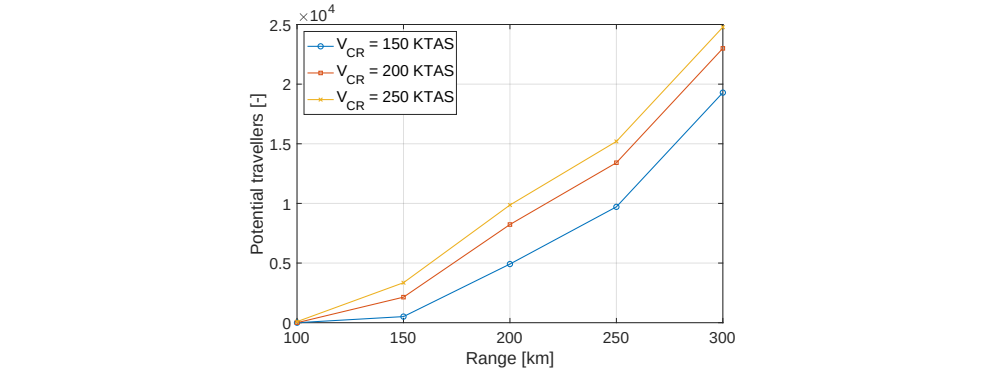

(a) *EBBR*

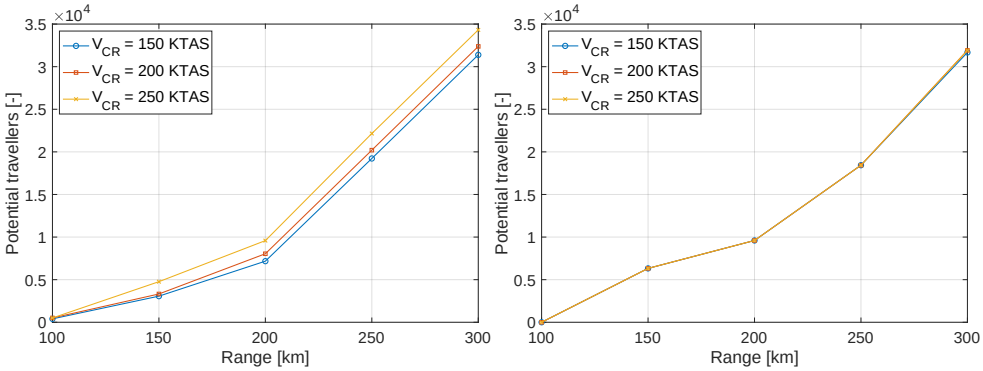

(b) *LIPZ*

(c) *EVRA*

Figure 8.7: *Potential demand estimation results for a microfeeder service to EBBR, LIPZ and EVRA in the case of 800 m long runways for SAs.*

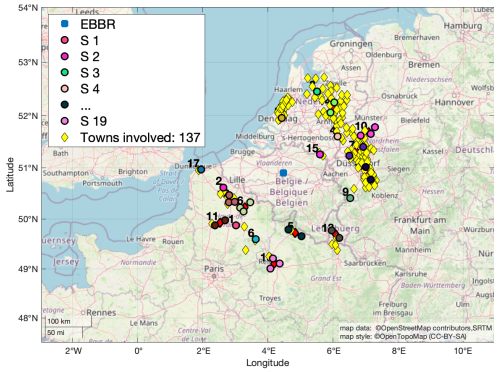

(a) *EBBR*

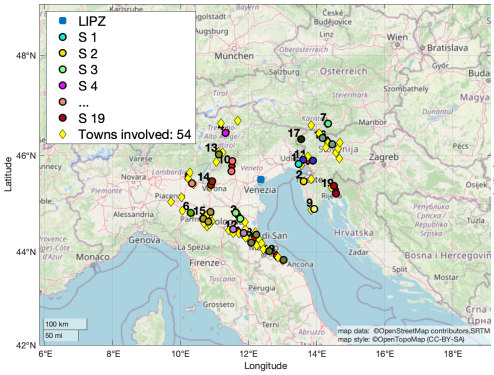

(b) *LIPZ*

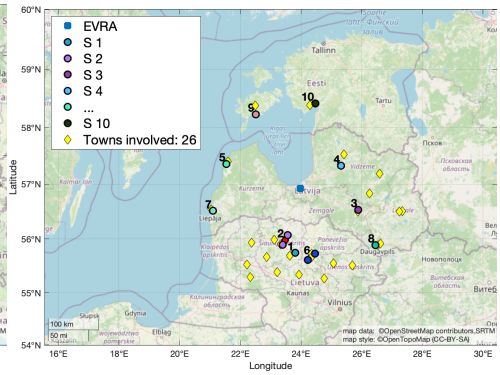

(c) *EVRA*

Figure 8.8: *Distribution of towns and SAs involved in a microfeeder service to EBBR, LIPZ and EVRA in the case of 800 m long runways for SAs and a cruising speed of 200 KTAS.*

EVRA are comparably higher with respect to the EBBR and LIPZ cases at medium values of the trip distance, and approximately the same at higher distance. Also, as a result of the high efficiency of ground transportation in the regions surrounding EBBR and LIPZ, the lower values for the trip distance provide poor results, since the *microfeeder* service cannot compete with alternative ground-based travel means. For the same case of picking SAs with 800 m long runways or more, Figure 8.8 shows the number and location of the towns and involved aerodromes when the maximum trip distance is 200 km.

Graphs in Figure 8.9 show the variation of potential travellers as functions of runway length and trip distance, with 200 KTAS cruising speed. Relatively small changes are observed in the potential demand with respect to runway length. The potential demand for LIPZ at 250 km trip distance seems to slightly increase when using 800 m runways or longer. This is possibly due to a better ground connection for SAs with a longer runway than for those with a shorter one.

8.5.2 Intercity service

The Italian case is assumed for the analysis of the *intercity* service. A *matrix of commuting habits* is included in the census of the Italian national institute of statistics (ISTAT), and updated every 10 years. In particular, this work is based on the commuting matrix G from the 15^{th} population and housing census from 2011[3].

The travelling demand of Italian commuters is presented in Figures 8.10 and 8.11 as a function of trip distance, cruising speed and runway length. Figure 8.12 depicts a related network map. The amount of potential commuters, clearly flattens towards a constant value, saturating around 300÷350 km trip distance. Significant variations with cruising speed and runway length are observed. For instance, looking at the 350 km value, a cruising speed increment of 50 and 100 kn from 150 KTAS increases the number of passengers by 26% and 57%, respectively. The effect of runway length is similar: the number of potential commuters rises by 68% using 600 m long runways, and 28% using 800 m long runways, with respect to the 1,000 m case.

[3]https://www.istat.it/it/archivio/157423

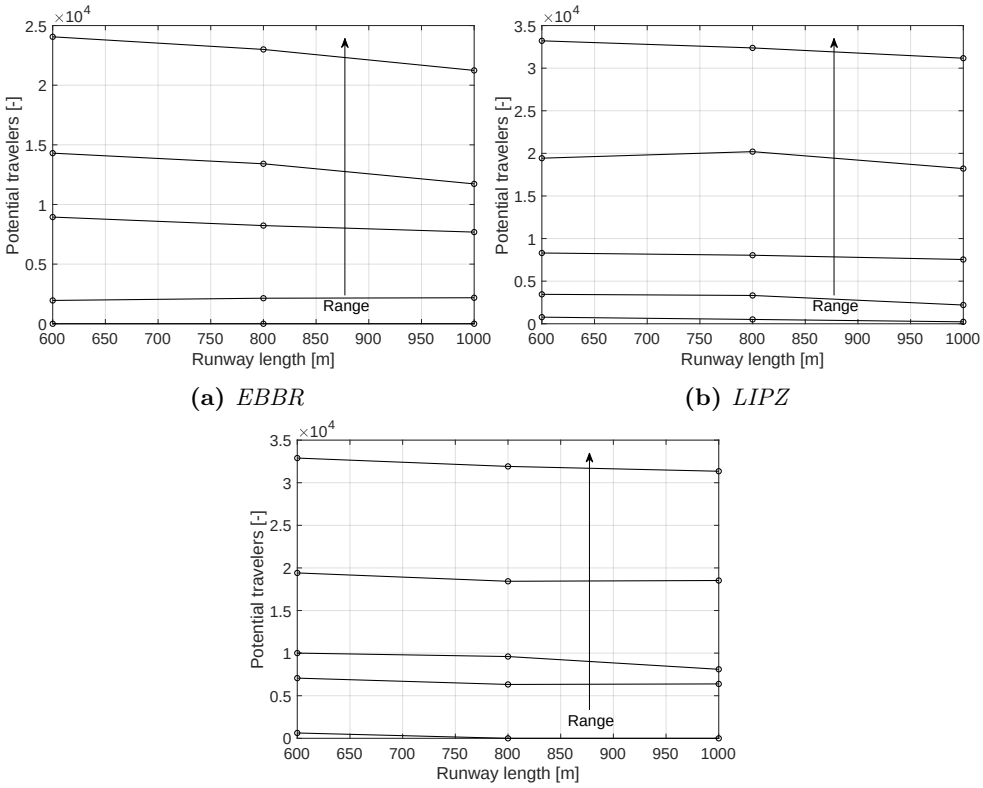

(a) *EBBR* **(b)** *LIPZ*

(c) *EVRA*

Figure 8.9: *Potential demand estimation results for a microfeeder service to EBBR, LIPZ and EVRA at 200 KTAS cruising speed for increasing values of the range: 100, 150, 200, 250, 300 km from bottom to top.*

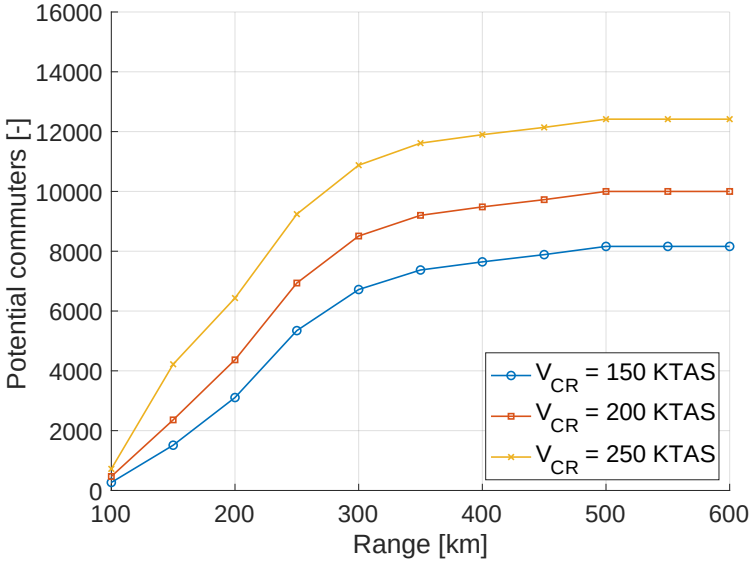

Figure 8.10: *Potential demand estimation for an intercity service in Italy: Variation with respect to cruising speed using runways longer than 800 m.*

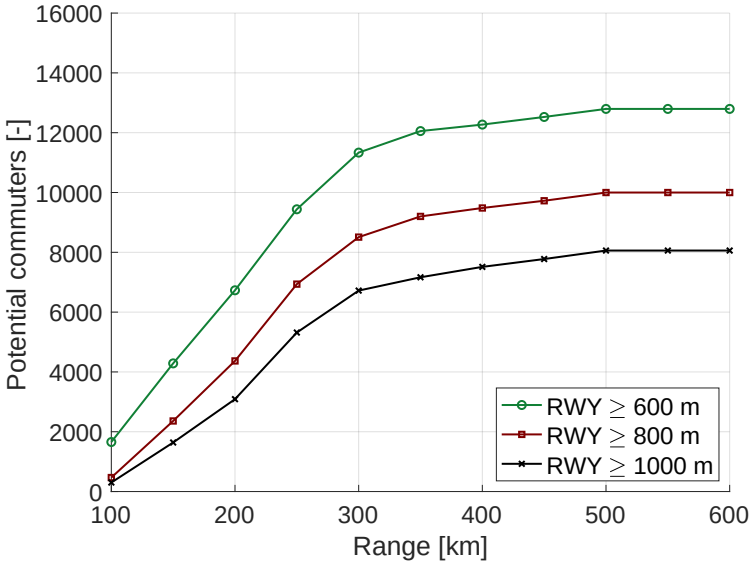

Figure 8.11: *Potential demand estimation for an intercity service in Italy: Variation with respect to runway length at 200 KTAS cruising speed.*

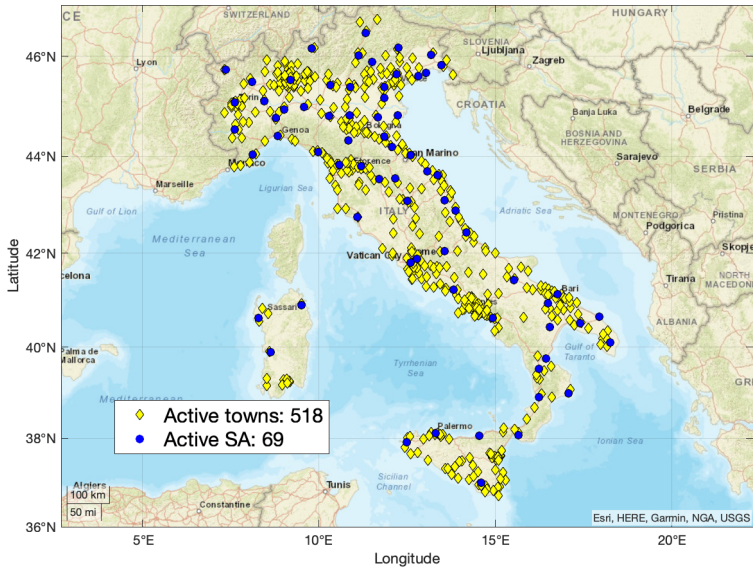

Figure 8.12: *Distribution of towns and SAs involved in an intercity service in Italy with a range of 350 km, runways longer than 800 m and 200 KTAS cruising speed.*

8.5.2.1 Airport times and time gain sensitivity analysis

The effect of the parameters k and t_{ref} are visible in Figure 8.13, which shows the distribution of the pairs t^{T1-T2} (x-axis) representing the road travel time and $t^{T_1-S_1} + t^{mf} + t^{S_2-T_2}$ (y-axis) representing the travel time with the miniliner. As seen, increasing or decreasing t_{ref} moves up and down the time difference constraint boundary (Equation 8.5), represented by the solid black line. However, this constraint has a limited effect, if any, in the current configuration. Modifying k rotates around the origin the time gain constraint boundary (Equation 8.4), represented by the dashed black line. In particular, decreasing k makes the boundary steeper and hence, less restrictive. Also, increasing the aircraft performance or reducing the airport times (the latter amounting to 40 minutes), moves down the point cloud introducing more potential town pairs.

The influence of the airport times and the time gain parameter k has a deep effect on the number of potential travelers. This is presented in 8.14, where the absolute time difference t_{ref} is not considered due to its lower effect. The rationale behind this study is that nominal airport times were selected with the *microfeeder* service in mind, in which the passenger continue the trip after disembarking from the miniliner, to take an international flight. In the *intercity* liner, this is no longer the case. The commuters are expected to be light travelers, so shorter check-in, turnaround and, in general airport associated times could be achieved. Also, time gain

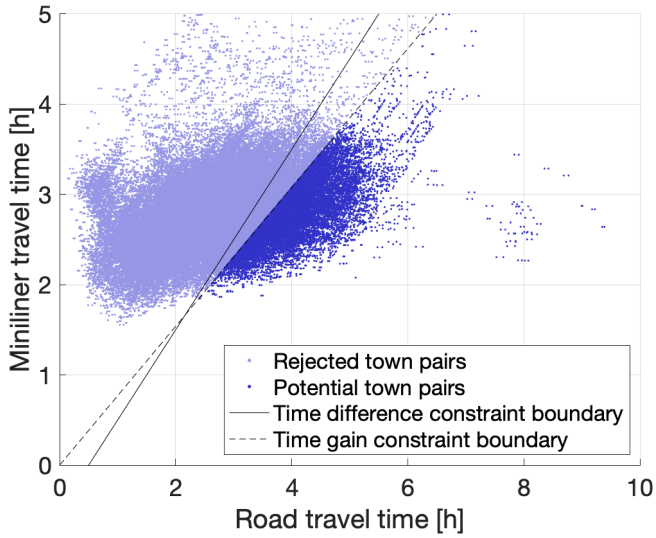

Figure 8.13: *Miniliner travel time and road time for all the town pairs, including trip constraints.*

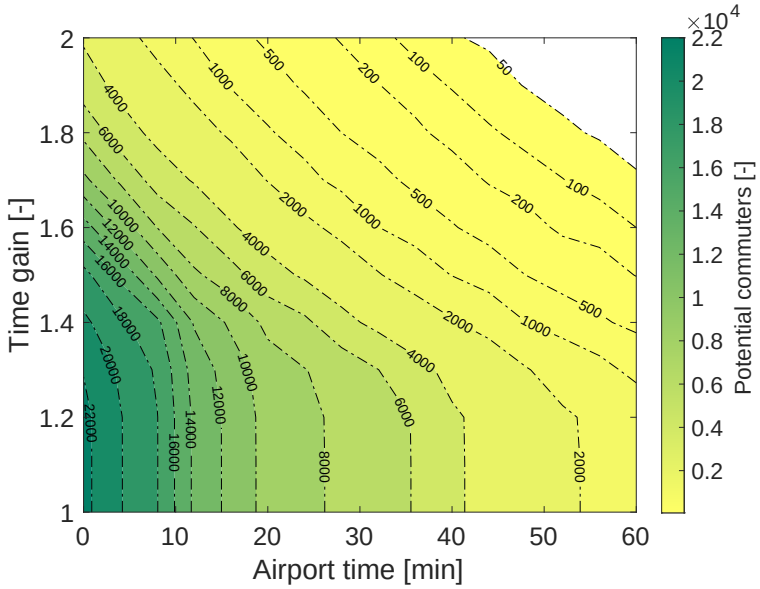

Figure 8.14: *Potential commuters with respect to overall airport time and time gain parameter.*

expectations may be different for commuters. In the figure, a range of 200 km, a cruising speed of 200 KTAS and a minimum runway length required of 800 m are considered. Airport times are added up and treated as a block. This exposes the considerable impact airport times have on the potential demand. In the trivial case of vanishing airport times, more than 22,000 commuters are potentially willing to use the service. On the other hand, with airport times between 40 minutes (the nominal value) and one hour, this number is reduced by one order of magnitude, to 1,000÷4,000 commuters. The effect of increasing the time gain parameter k is less relevant and provides an increase in the potential demand that quickly reduces with increasing airport time.

CHAPTER 9

TOP-LEVEL AIRCRAFT REQUIREMENTS FOR THE MINILINER

The application studies in Chapter 8 highlight the importance of primary aircraft performance of range, take-off/landing distances, and cruising speed in the ability to capture the travel needs of potential customers. These results are exploited in the definition of the Top Level Aircraft Requirements (TLAR) for the design of the miniliner. The TLAR will be used in the next chapter to derive preliminary sizing solutions using the HYPERION tool introduced in Chapter 4. To this end, the technological framework and the possible choices about the power-train architecture are also discussed in this chapter.

9.1 Power-train architecture and technology

Two types of power-train architectures are considered as candidates for the miniliner: the serial THE and FCHE power-trains as they offer greater innovative potential with respect to other options as shown in Chapter 1.

Table 9.1: *Technology parameters adopted for the preliminary sizing of the miniliner.*

	Symbol	2025
Battery specific energy [Wh/kg]	e_b	260
Battery specific power [W/kg]	p_b	1,670
EM specific power [W/kg]	p_m	7,533
ICE specific power [W/kg]	p_g	2,947
FC specific power [W/kg]	p_g	2,130
GH2 tank gravimetric index [%]	μ_g	10.0

Table 9.2: *Specifics of the PGS-ICE for the miniliner.*

Power Generation System - ICE		
PGS type	[-]	turboshaft
PGS specific power	[W/kg]	2,947
Electricity generator efficiency	[-]	0.95
η_{tg} at maximum power	[-]	0.256
De-rating altitude	[ft]	10,000

The reference year for the entry into service of the miniliner is 2030. Five years are expected for novel technology to be certified, so the reference year for the technology employed in the power-train is set to 2025.

In order to start the design process with HYPERION, it is necessary to assume some values for the EM specific power, the FC/ICE specific power, battery specific power and energy and the tank gravimetric index, in the case of GH2 hydrogen tank. A summary of these quantities is provided in Table 9.1 for the year 2025. This table is similar to Table 4.19. The main difference is that, with a conservative approach in mind, we assumed that the leading battery technology for the year 2025 will still be LIB, especially considering safety critical applications, such as air transport. Hence, the technological values for the year 2025 are linearly interpolated between 2020 and 2035i values of Table 4.19. The limit on the battery minimum and maximum state of charge are set to 25% and 85%. EM extra power is assumed as 25% while the EM efficiency is constant and equal to 0.95. In the case of ICE PGS, the proposed engine type is a turboshaft and its properties are summarised in Table 9.2. The de-rating altitude of the ICE and the maximum thermal efficiency η_{tg} are assumed considering engines already employed on existing large commuters. For what concerns the fuel cell system, the specifics are gathered in Table 9.3

Table 9.3: *Specifics of the PGS-FC for the miniliner.*

Fuel cell system		
Electric system efficiency	[-]	0.95
Fuel cell area	[cm^2]	300
Operating voltage	[V]	600
Operating pressure	[bar]	2.5
Operating temperature	[K]	353
Compressor efficiency	[-]	0.88

9.2 Mission requirements

9.2.1 Design range

Studies on the potential demand showed that the trip distance has the bigger effect in increasing the number of potential travellers. In particular, it seems to have an exponential effect in the *microfeeder* case for high and medium density countries, and a linear effect in the low density countries. On the other hand, the influence of trip distance is completely different for the *intercity liner* service. In this case the potential demand curve flattens reaching a plateau region for increasing trip distance. In both cases, there is no potential demand for trip distances lower than 100 km, since the ground alternative turns out to be more efficient. While data on the *microfeeder* case shows that increasing the range over 300 km could be beneficial, the exponential trend of the curves seems to continue beyond that point, a value of 300 km was considered looking at the saturation limit of the *intercity* case.

One of the main objectives of the miniliner concept is its ability to be operated without needing a fully-developed infrastructure, being capable to operate on remote airfields which might not have the necessary infrastructure for refuelling and/or recharging the batteries. For this reason, the trip distance of 300 km is to be considered as one hop of an overall longer mission, possibly including more hops. The number of hops is selected taking into account the nature of the two services. For the *microfeeder* service, the miniliner is expected to come and go from/to a hub and we assumed that hubs will be equipped with both recharging and refuelling infrastructure. On the other hand, only 290 airports among all the 3029 SAs are actually used for commercial transport as of today. (December 2020[1]). This corresponds to roughly 1 out of 10 SAs. Assuming

[1] `https://ec.europa.eu/eurostat/databrowser/view/avia_if_arp/default/table?lang=en`

that today's commercial airports will more easily see an upgrade of their infrastructure than airfields that are currently used for leisure flight, we can imagine that only 1 out 10 SAs will feature refueling and recharging stations.

However, asking for 10 hops of 300 km each results in a total range of 3000 km, which is more than that of many regional airplanes and is considered out of scope. Hence, an educated guess of 3 hops seems to be a good compromise. Since every hop will be characterised by climb and descent, an additional 100km can be considered if we refer to the overall design range of the aircraft.

9.2.2 Take-off and landing distance

The first effect of selecting a value for the take-off and landing distance is cutting a percentage of the existing SAs. In particular, half of all the SAs feature a runway longer than 800 m. Reducing this value to 600 m, brings in an additional 25%, while increasing it to 1000 m removes 15% of all the SAs. The effects on potential demand are related to the increase/reduction of the resulting available network of SAs for the miniliner. However, the impact on the *intercity* service and on the *microfeeder* service is very different. In the first case, the potential demand changes by a similar amount, (compare Figure 8.11), but in the *microfeeder* it has very little effect (see Figure 8.9). Hence, the middle value of 800 m was selected. Of course, both the take-off and the landing distance are considered equal. Since more than half of the SAs features a grassy airstrip, the miniliner has to be able to take-off and land also from runways with this type of pavement.

9.2.3 Cruising speed and altitude

The cruising speed is set to 150 KTAS, as this value shows good results, in terms of potential demand, especially in countries with a medium or low *ground transportation efficiency*. This value of TAS is requested at 4000 ft, chosen as an average value for the cruise altitude of the miniliner. The service ceiling is selected to be 2480 m (8000 ft) with a non pressurized fuselage: the limited trip distance (less than 300 km) does not require reaching high altitude, so no pressurization is necessary. 8000 ft corresponds to the maximum cabin altitude used in pressurized airplanes [181].

9.2.4 Climb and descent

As discussed in Section 8.2, in order to avoid passenger discomfort during the flight, the rate of climb and descent are limited to 500 and 250 ft/min respectively, as these are the values currently adopted when depressurizing and pressurizing the cabin in commercial airplanes [181]. The climb CAS is set to the best rate of climb airspeed, while the descent CAS is equal to cruise airspeed, as typical for propeller-driven airplanes.

9.2.5 Loiter and reserves

The current requirement for reserve fuel is to have enough fuel for diversion to the alternate airport plus the necessary amount for 45 min loiter over the alternate airport. However the regulation applicable for the fuel reserve does not affect the certification process but is only specific for operations. Moreover, the minimum distance of the alternate airport is not prescribed. In this case, the market studies suggest that 90% of SAs with runway longer than 800 m have another SA nearer than 100 km. Hence this value was chosen as the diversion range.

9.3 Payload and crew

The miniliner is conceived as a 19-seater, belonging to the Level 4 cathegory of CS-23 regulation. Each passenger is expected to bring one carry-on bag and a checked luggage. For the sizing, a total of 100 kg + 20 kg checked luggage per passenger is used.

Fully autonoums flight and single-pilot operations would be desirable for such an innovative miniliner. Nevertheless, the very short time horizon (2030) for the deployment of the miniliner does not encourage to consider these options. Hence, for the design process, two pilots are expected, 100 kg each. This mass can also account for future equipment to support fully autonoums flight. No additional cabin crew is considered, as there is no specific requirements for airplanes up to 19 seats.

9.4 Aerodynamics and configuration

High and low speed drag polars are derived during the preliminary sizing process, however target values in terms of aspect ratio and lift-to-drag ratio are required. The same values of the Dornier 228 are chosen for the aspect ratio, 9, and the desired lift-to-drag ratio, 14, corresponding to a

Table 9.4: *Aerodynamic data of the miniliner.*

Aspect ratio	[-]	9
Zero lift drag coefficient	[-]	0.029
$C_{L_{max}}$	[-]	1.04
$C^{TO}_{L_{max}}$	[-]	1.62
$C^{LND}_{L_{max}}$	[-]	2.61
η_P	[-]	0.75

zero lift drag coefficient of 0.029. The maximum lift coefficients, $C_{L_{max}}$ in clean configuration, $C^{TO}_{L_{max}}$ in take-off configuration and $C^{LND}_{L_{max}}$ in landing configuration are, once again, selected as those of the Dornier 228 and are reported in Table 9.4 together with the rest of the aerodynamic data. The chosen configuration involves two propellers with constant propeller efficiency ($\eta_P = 0.75$) connected to the EMs.

9.5 Summmary of design specifications

All the input data necessary for the design is summarized in Table 9.5.

Table 9.5: *Design parameters of the miniliner.*

	Measurement unit	**Value**
No. Passengers	[-]	19
No. Crew	[-]	2
Pressurization	[-]	NO
Regulation	[-]	CS-23
Aerodynamic properties		
Wing aspect ratio	[-]	9.0
Oswald factor clean	[-]	0.80
Oswald factor with TO flaps	[-]	0.80
Oswald factor with LND flaps	[-]	0.75
$C_{L_{max}}$ clean	[-]	1.04
$C^{TO}_{L_{max}}$ with TO flaps	[-]	1.62
$C^{LND}_{L_{max}}$ with LND flaps	[-]	2.61
C_{D_0}	[-]	0.03
ΔC_{D_0} due to gear	[-]	0.020
ΔC_{D_0}due to TO flaps	[-]	0.015
ΔC_{D_0} due to LND flaps	[-]	0.045

Performance requirements		
Stall CAS at LND	[kn]	68.0
Max cruise CAS	[kn]	141.4
Max cruise CAS altitude	[ft]	4000
Max rate of climb	[ft/min]	500
Service ceiling	[ft]	8000
TO distance	[m]	800
LND distance	[m]	800
Sizing mission		
Payload	[kg]	2,280
Climb CAS	[kn]	107
Cruise CAS	[kn]	141
Descent CAS	[kn]	141
Departure altitude	[ft]	0
Cruise altitude	[ft]	4,000
Loiter altitude	[ft]	1,500
Landing altitude	[ft]	0
Rate of climb	[ft/min]	500
Rate of descent	[ft/min]	-350
Design range	[km]	1,000
Diversion range	[km]	100
Residual end-of-mission stored fuel	[%]	5
HETA (for THE only)	[ft]	1,500
Electric Motors		
No. Engines	[-]	2
Propeller efficiency	[-]	0.75
Electric Motor efficiency	[-]	0.95
Electric Motor specific power	[W/kg]	7533
Electric Motor overrating	[-]	0.25
Power Generation System - ICE		
PGS type	[-]	turboshaft
PGS specific power	[W/kg]	2,947
Electricity generator efficiency	[-]	0.95
PGS thermal efficiency at max power	[-]	0.256
De-rating altitude	[ft]	10000.00

Power Generation System - FC		
PGS specific power	[W/kg]	2,947
Electric system efficiency	[-]	0.95
Fuel cell area	[cm^2]	300
Operating voltage	[V]	600
Operating pressure	[MPa]	0.25
Operating temperature	[K]	353
Compressor efficiency	[-]	0.88
Battery		
Battery specific power	[W/kg]	1,670
Battery specific energy	[Wh/kg]	260
Minimum battery state of charge	[%]	25
Maximum battery state of charge	[%]	85
Gaseous hydrogen tank		
Gravimetric index	[-]	0.10
Nominal pressure	[MPa]	70
Liquid hydrogen tank		
Minimum pressure	[MPa]	0.120
Maximum pressure	[MPa]	0.145

CHAPTER 10

PRELIMINARY SIZING OF THE MINILINER

A preliminary sizing of the miniliner with the TLAR gathered in Chapter 9 is carried out, considering different architectures for the power-train and including sensitivity analyses of the miniliner performance, as well as the technological parameters. The sizing is done using the HYPERION tool introduced in Chapter 4.

10.1 Preliminary sizing solutions

10.1.1 Sizing matrix plot

Figure 10.1 shows the SMP for the miniliner, with the selected design point. As it concerns a multi-engine airplane, OEI requirements as found in FAR23/CS-23 appear, similarly to Figure 4.20. The design point is chosen at the intersection between the stalling speed and the take-off distance constraints, being very close to the line representing OEI balked landing.

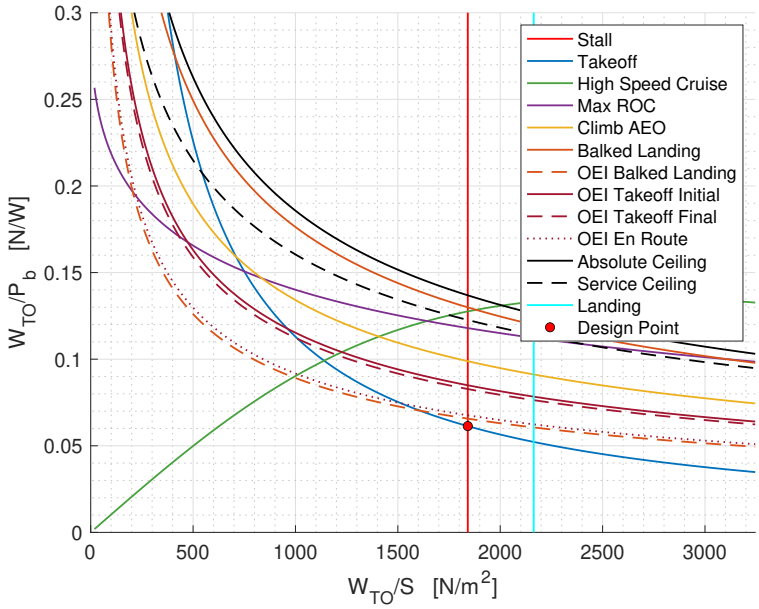

Figure 10.1: *Sizing matrix plot of the miniliner.*

The resulting wind loading is 1841.5 N/m^2 and the power loading is 61.4 N/kW.

10.1.2 Effect of power-train architecture

Three solutions, corresponding to different power-train architectures have been tested for the miniliner:

1. M19THE: serial thermal hybrid-electric.
2. M19GH2: fuel cell hybrid-electric with GH2 tank.
3. M19LH2: fuel cell hybrid-electric with LH2 tank.

In order to compare the three solutions, the corresponding mass breakdowns are reported in Figure 10.2. The MTOM of M19THE is 13.3 tonnes compared to 19.0 t of M19GH2 and 7.5 t of M19LH2.

For M19THE, the heaviest elements, apart from the non propulsive mass of 6765 kg or 50.8% of the MTOM represented by the light blue bar, are the fuel and the battery (blue and yellow bars). These two elements represent 13.5% and 12.9% of the MTOM. The BP is sized to allow take-off and flight below the HETA. HETA is set right below the loiter altitude, 1500 ft. Compared to BP and fuel, the EM and PGS mass (green and orange bars) are one order of magnitude lower, weighing 302 kg and 258

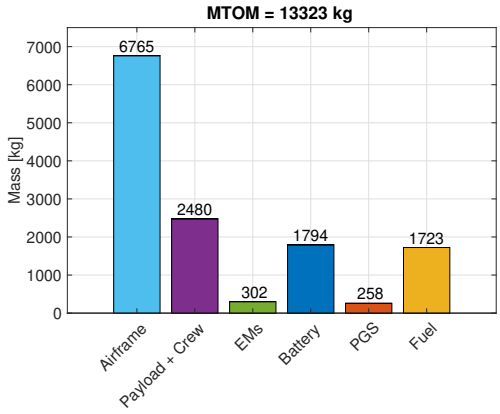

(a) *Thermal hybrid-electric solution.*

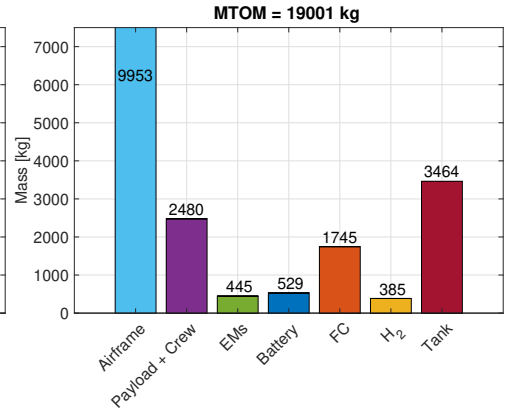

(b) *Gaseous hydrogen solution.*

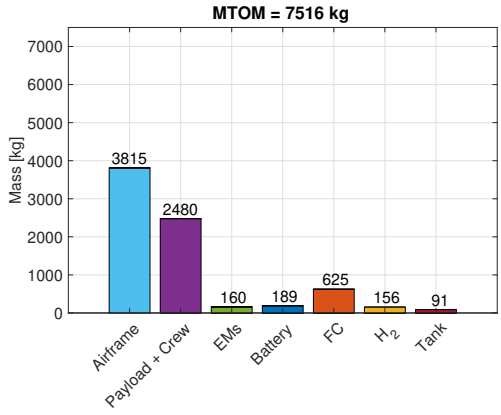

(c) *Liquid hydrogen solution.*

Figure 10.2: *Mass breakdown of the miniliner in three different propulsion architectures.*

kg respectively.

The MTOM of the FCHE solution with GH2 tanks, M19GH2, is instead the heaviest among the three solutions. The power-train element that contributes the most to the MTOM is the mass of the hydrogen tank. GH2 tank weighs 3465 kg, almost 18.2% of the MTOM and 39.7% more than the payload. The reason behind such high value of tank mass is the low gravimetric index, $\mu_g = 10\%$, that makes the tank mass 9 times larger than the mass of hydrogen (385 kg, yellow bar). Also the fuel cell system mass, orange bar, amounts to a relevant fraction of the MTOM: 9.2% or 1745 kg. It is remarked that fuel cells are sized for maximum continuous power and are used together with batteries to reach peak power such as during take off or OEI situations. As a consequence of the overall weight toll of the tank, fuel cells, batteries and electric motors, the airframe mass

jumps to 9953 kg, 52.3% of the MTOM.

The lightest solution among the tested power-train architectures is M19LH2, which weighs only 56% of M19THE and 40% of M19GH2. Looking at the detailed mass breakdown, we can understand that M19LH2 is the winner mainly becuse of the much lighter tank, with respect to M19GH2. The gravimetric index of M19LH2 tank is, in fact, 63.2%. This value is six times larger than the gravimetric index of M19GH2. Indeed, LH2 tanks, working at much lower pressure than GH2 tanks, are usually much lighter, despite the additional insulation thickness necessary to keep the tank thermally isolated. The second heaviest element of M19LH2 is the fuel cell system. It amounts to 625 kg, around 8.3% of the MTOM. It is interesting to notice that the value for the MTOM of M19LH2 is the only one, among M19THE, M19GH2 and M19LH2 to be lower, by 12.8%, than the current CS-23 design mass limit of 8,618 kg, a rather promising result.

Since M19LH2 seems to be the winning solution in terms of lower MTOM, non propulsive mass and lower fuel consumption, the FCHE architecture with LH2 tanks is the selected one for the miniliner and will be, from now on, simply called M19.

All the graphs pertaining to the solutions M19THE and M19GH2 are collected in Appendix C.

10.1.3 The candidate solution

The value for the wing reference surface of M19 is 40.0 m^2 and the installed electric motor maximum continuous power is 1201.9 kW. If we compare this result with the reference 19-seater used for validating the HYPERION tool in Chapter 4, this represents a 25% increase with respect to the Do228NG, while the installed power is lower by 14.3%.

Figure 10.3 shows the time evolution of the energy stored on board, in terms of BP state-of-charge (blue line), PGS throttle (red line) and hydrogen tank level (yellow line). The dashed line in Figure 10.3 outlines the flight profile, in terms of altitude. First of all, we can see that the battery SOC drops by roughly 20% in the first phases of the flight. After that, the SOC is kept constant at 85% and then drops again for the go-around. Finally, the battery is depleted up to the residual SOC at the end of the mission. The hydrogen tank level, instead, decreases continuously up to the minimum value of 5% at the end of the flight. The PGS-FC throttle reaches 100% only during take-off and during the go-around phase, lying

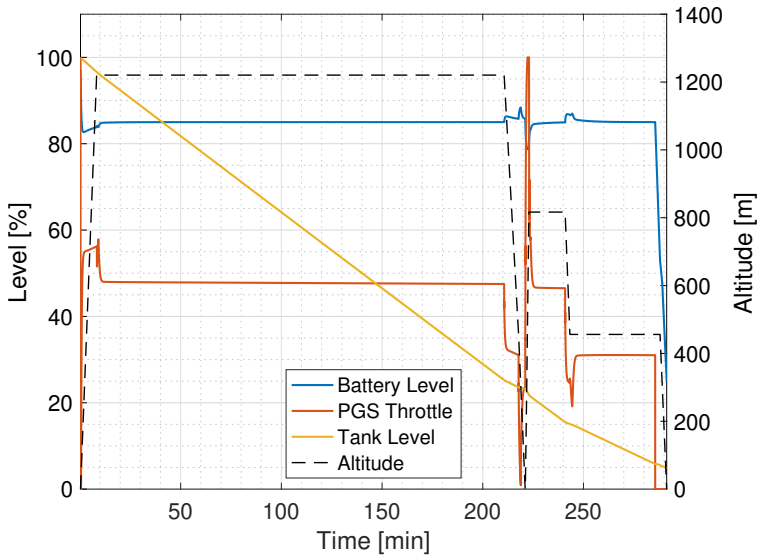

Figure 10.3: *Time histories of battery state of charge (blue), PGS throttle (red), fuel quantity (yellow), and altitude (black) for M19.*

at 43% during cruise and 26% during the loiter. This trend mimics that of the red line in Figure 10.4.

Indeed, Figure 10.4 shows the share of power coming from the BP (blue line), and the PGS (red line) resulting in the EM output power (green line). It is readily seen that the PGS line is quite uniformly overlapped to that of the EM output power, with the battery providing power only during transients and high peak power phases (take-off and go-around).

The efficiency of the fuel cell system, η_{FC}, is depicted in the plot of Figure 10.5. η_{FC} remains constant for most parts of the mission, and is around 58%. Such high value comes as a consequence of the sizing of the fuel cells, sized for maximum continuous power, and their usage at a lower power setting. In fact, as outlined in Section 3.2.2, η_{FC} decreases with rising power and has a maximum at low power.

Figure 10.6 displays the time history of the pressure inside the LH2 tank during the flight. The pressure is represented by the yellow line, while the green line represents the minimum pressure necessary to feed the fuel cell system and the red line is the maximum tank pressure. The maximum tank pressure is the pressure at which hydrogen starts to be vented, in order to contain the pressure within the limits. The tank pressure reaches the maximum value only at the beginning of the flight, where this is set as an initial condition, and at the end of the flight, with two additional spikes occurring during the first approach and at the beginning of loiter.

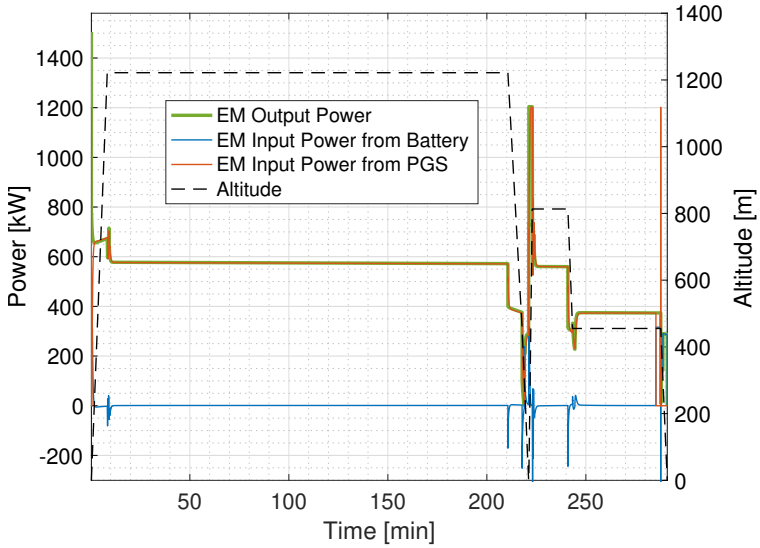

Figure 10.4: *Time histories of shaft power (green), BP power (blue), PGS power (red), and altitude (black) for M19.*

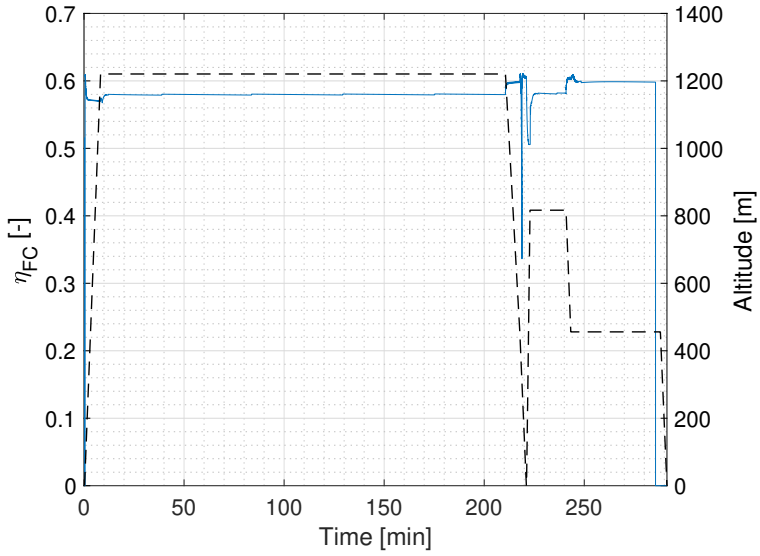

Figure 10.5: *Time histories of the fuel cell efficiency (blue) and altitude (black) for M19.*

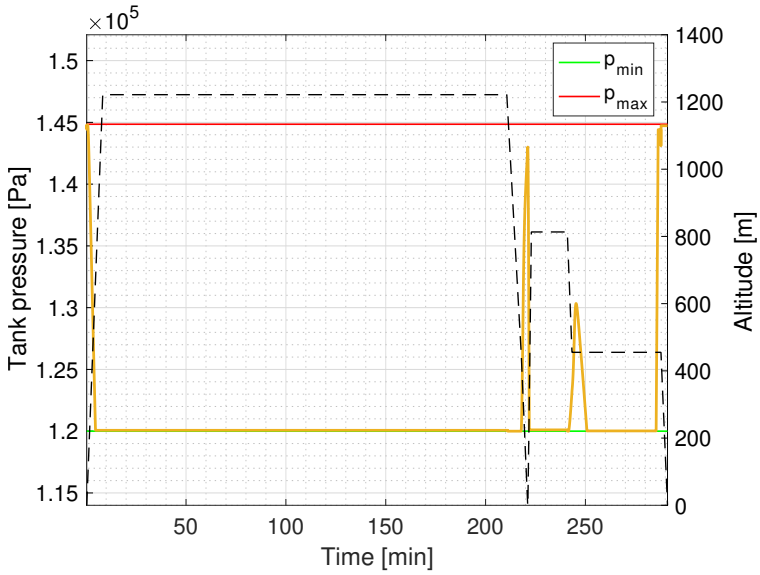

Figure 10.6: *Time history of the LH2 tank internal pressure for M19.*

However, these two spikes do not touch the red line boundary. For the rest of the flight the pressure lies low at the minimum level. This behaviour of the pressure comes as a consequence of the fuel flow provided to the FCs and of the heat entering the tank, shown in Figure 10.7. We can see as the natural heat entering the tank (red line in the plot) is higher at take-off, first approach and final approach phases. Extra heat to gasify some LH2 is necessary throughout the flight, see the yellow line in Figure 10.7, apart for the aforementioned flight phases. Finally, the resulting time history of the vented hydrogen is reported in Figure 10.8. The flow rate of vented hydrogen is shown by the blue line in the figure. Venting occurs only when the tank pressure reaches the upper bound of Figure 10.6. Since this happens only during take-off and at the end of flight, hydrogen is expelled only in these phases.

10.2 Trade studies on mission requirements

10.2.1 Sensitivity to payload and range

The payload-range diagram depicted in Figure 10.9 shows the MTOM of M19 when the design solution is found for different values of the design range R and payload mass M_l. All the other TLAR are left untouched, including fuel reserves and the diversion to the alternate airport. The colours of the plot that indicate the value of M_{TO} range between dark blue

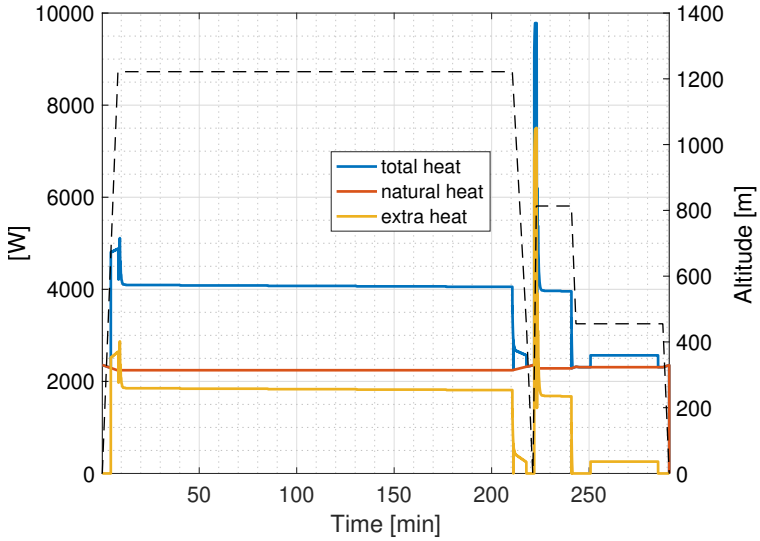

Figure 10.7: *Time history of the LH2 tank heat flow for M19.*

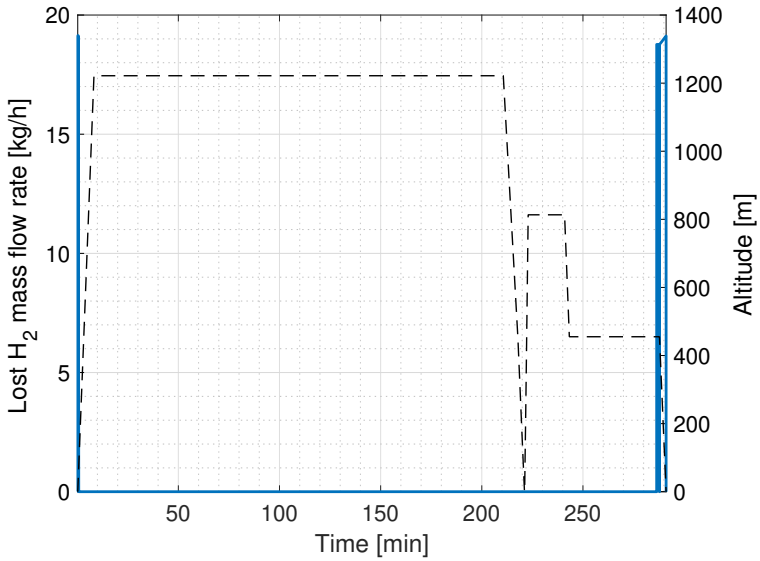

Figure 10.8: *Time history of the LH2 tank boil-off losses for M19.*

(6000 kg) and yellow (9000 kg). In addition to the contoured areas, red markers in Figure 10.9 pinpoint possible solutions with varying passenger mass, assumed between 100 kg/pax and 120 kg/pax, including luggage. The red line, instead, represents the CS-23 mass limit, well above the selected solution obtained considering 120 kg/pax.

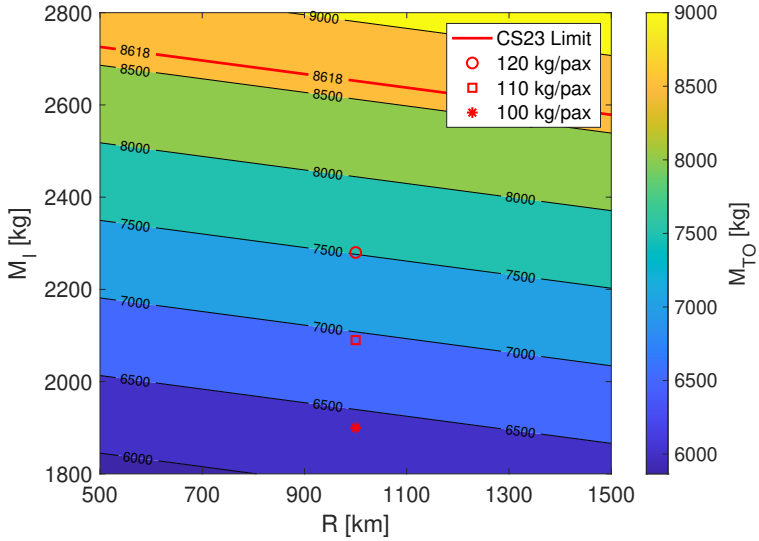

Figure 10.9: *Sizing solution for M19 at different values of payload and range.*

10.2.2 Sensitivity to cruising speed and take-off distance

Figure 10.10 groups a series of subplots showing the effect of cruising speed V_{CR} and take-off distance s_{TO} on several quantities of interest for M19. The values of cruising speed and take-off distance used for these sensitivity analysis are the same tested in Chapter 8 for the market studies. Let us first remark that the cruising speed is expressed in KTAS and that the landing distance is varied together with the take-off distance.

Figure 10.10a shows the variation of the MTOM. In this plot, the reference design point is indicated with a red circle and corresponds to $V_{CR} = 150$ kn and $s_{TO} = 800$ m. The red line in this figure indicates the mass limit of CS-23.

First of all, let us study the effect of increasing the cruising speed. Moving from 150 KTAS to 200 KTAS, with $s_{TO} = 800$ m, M_{TO} and the wing surface S are increased (Figure 10.10b) by roughly 5%. This is possibly driven by the 20% increase in the installed power as shown by Figure 10.10c that is reflected in the 20% higher fuel cell and battery mass, M_g and M_b, in

Figure 10.10d. On the other hand, decreasing the take-off (and landing) distance to 600 m has a much bigger impact on all the graphs of Figure 10.10. In particular, the M_{TO} increases by 10%, while the installed power, as well as the battery and the fuel cell system mass, jump to +40%. As a result of the higher M_{TO}, the fuel mass is incread by 8%.

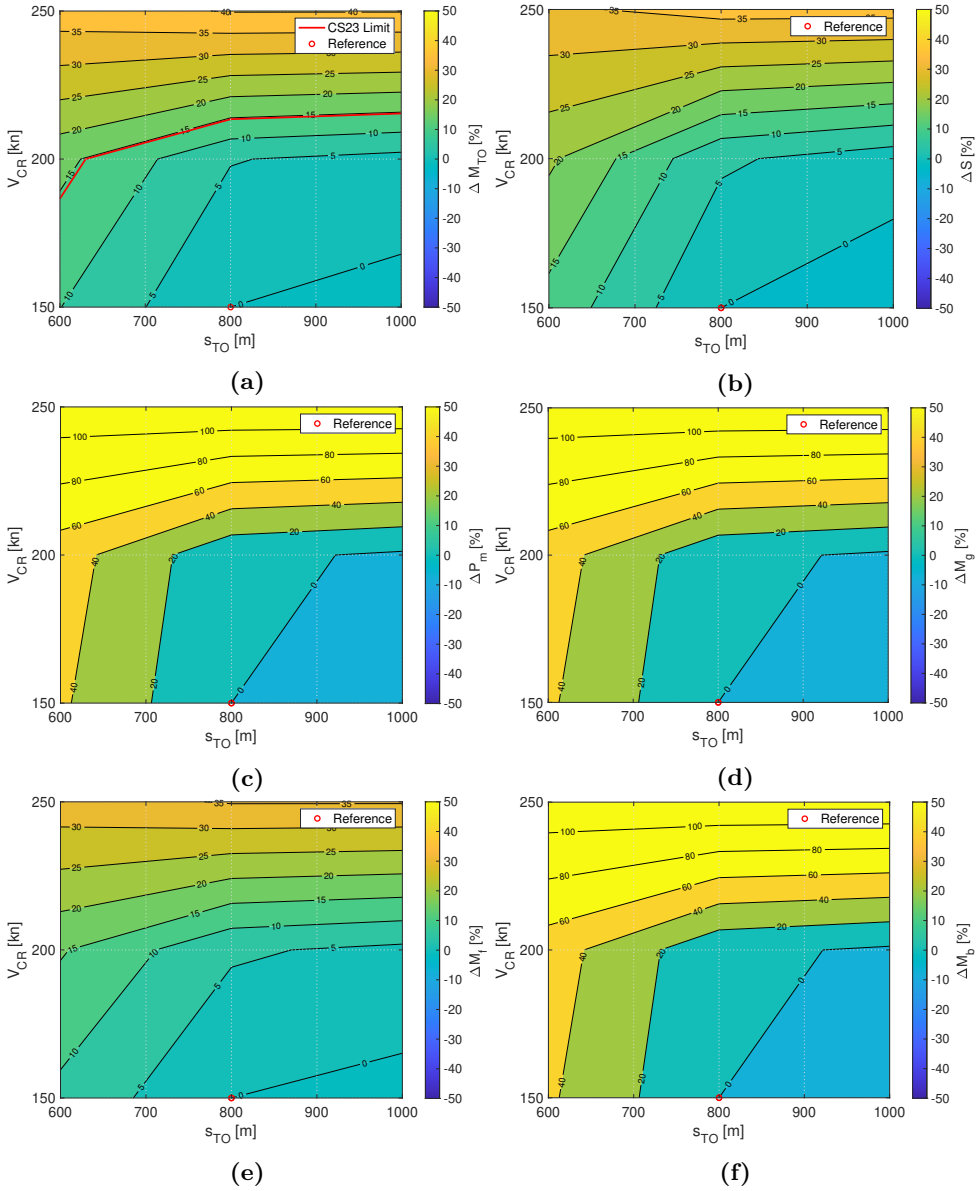

Figure 10.10: *Sensitivity of M19 to the take-off distance and cruising speed.*

10.3 Trade studies on technology parameters

10.3.1 Empty mass fraction

The design of M19 relies on historical regressions for what concerns the non propulsive mass, M_a as shown in Chapter 4. In particular, the non propulsive mass is gathered from the estimation of the empty mass fraction in historical regressions such as that of Figure 4.2.

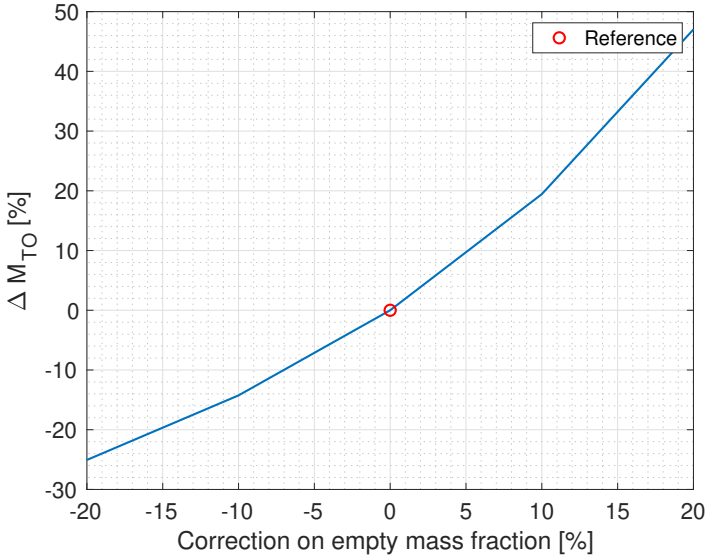

Figure 10.11: *Sensitivity of M19's MTOM to empty mass fraction.*

Figure 10.11 depicts the variation of M_{TO} with respect to a correction factor on the empty mass fraction. It is immediately clear that the increase or decrease of the empty mass fraction has an asymmetrical behaviour on the M_{TO}. For instance, raising the empty mass fraction by 20% boosts the MTOM up by 45%. On the contrary, only 25% of M_{TO} is saved when the empty fraction is reduced by 20%. This underlines the importance of estimating the empty mass fraction in the correct way.

10.3.2 Fuel cell technology

Another sensitivity analysis on fuel cells specific power is shown in the graphs of Figure 10.12. The nominal FC specific power, p_g is varied of plus or minus 30% with respect to the nominal value in Table 9.1. Analogously to the sensitivity on the empty mass fraction, an asymmetrical behaviour is present also for this analysis. For instance, increasing the FC specific

power by 30% reduces M_{TO} by 5%, while a reduction of p_g of 30% pushes the MTOM up by 11%. This behaviour is similar for all the quantities shown in Figure 10.12, but on different scales. In particular, the mass of the PGS-FC system ranges between +55% and -25% when reducing or increasing p_g (Figure 10.12d)

10.3.3 Battery technology

A sensitivity on the M19 solution with respect to battery specific power p_b and battery specific energy e_b is given in Figure 10.13. The reference values assumed for these two parameters are $p_b = 1670$ W/kg and $e_b = 210$ Wh/kg as detailed in Table 9.1. Observing all the graphs of Figure 10.13, apart from Figure 10.13f, we see that the variation of M_{TO}, S, P_m, P_g and M_f are limited within the interval $[-2\%, +4\%]$ with Δp_b and Δe_b in the range $[-30\%, +30\%]$. The battery mass instead, M_b, is more directly influenced and varies between -25% (blu area of Figure 10.13f) and +45% (yellow area). All graphs show a minimum in the upper right region, corresponding to the highest increments of e_b and p_b.

The biggest takeaway of this sensitivity analysis is that the improvement of energy density e_b brings little positive effects in all cases, while the specific power p_b has a more important impact. This is particularly visible in Figure 10.13f, where the mass of the battery is almost insensitive to specific energy variations. It is also interesting to notice that the hydrogen mass, Figure 10.13e, increases a little bit whenever the battery mass decreases. The explanation of this could be linked to how the battery is sized. The battery is, in fact, sized to provide the extra power necessary to boost the fuel cells. Hence, increasing p_b and keeping a constant value of e_b the battery mass gets lower. Nonetheless, the battery stored energy $E_b = M_b e_b$ decreases too. Hence, the missing energy has to be added as additional fuel.

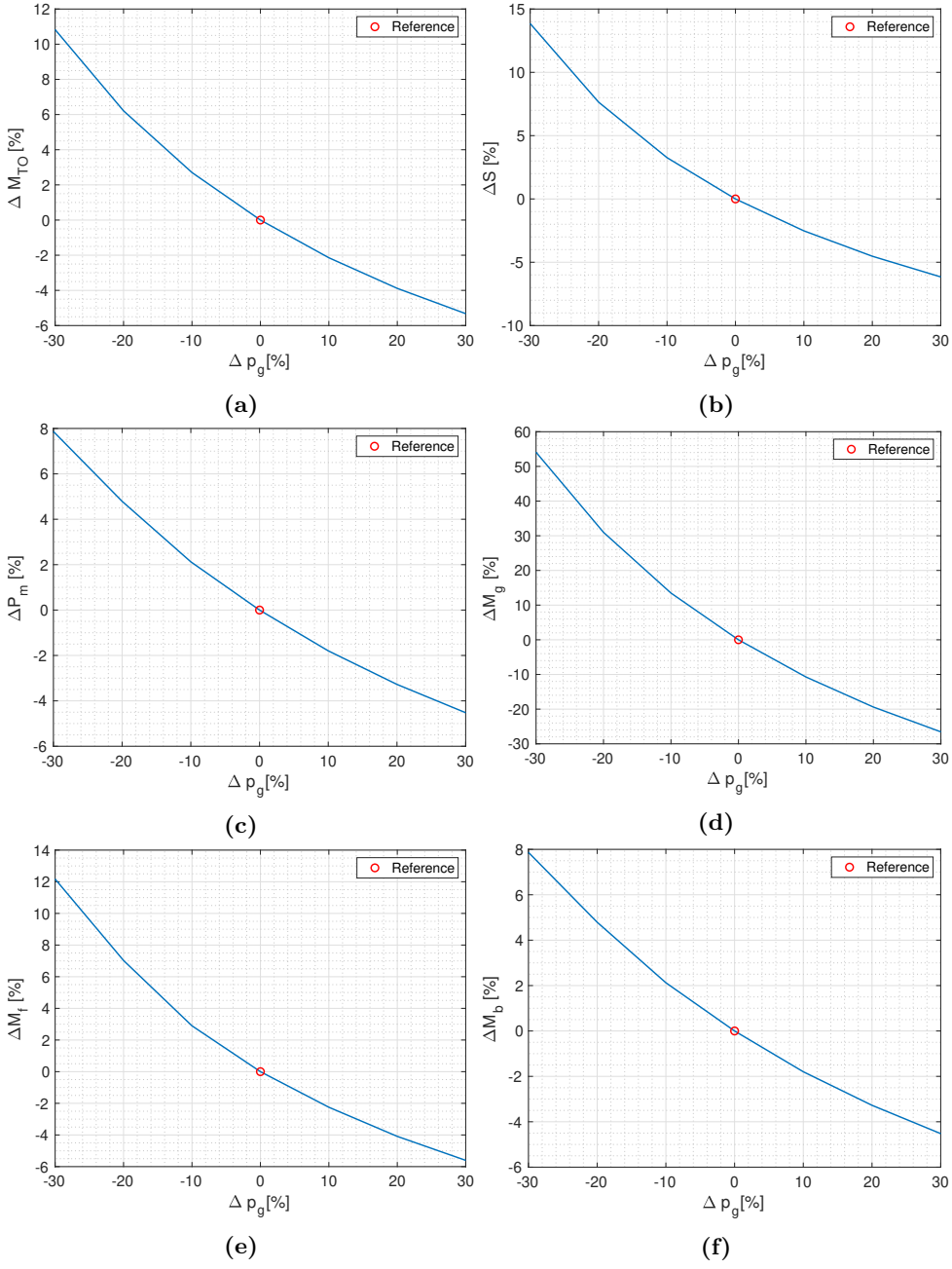

Figure 10.12: *Sensitivity of M19 to the fuel cell specific power.*

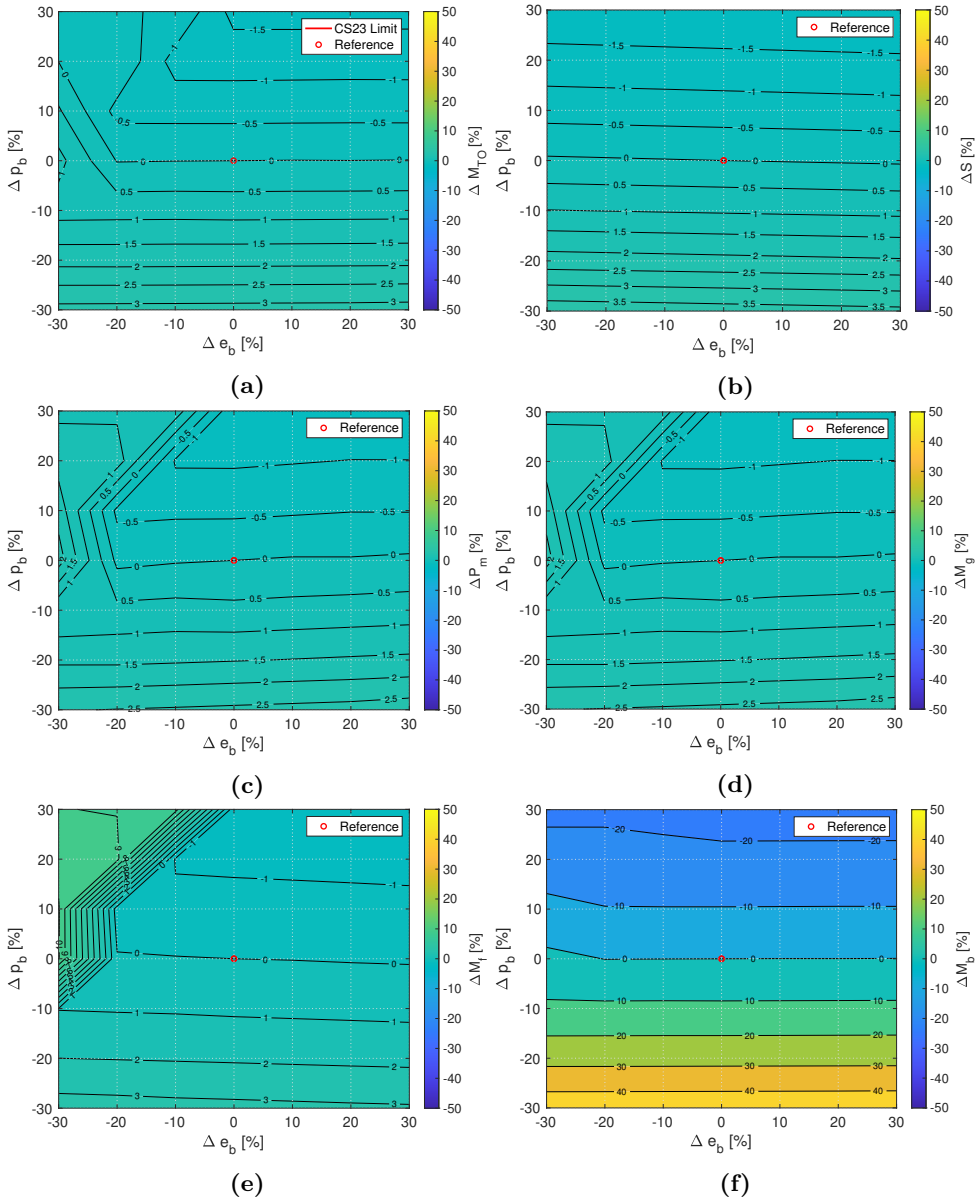

Figure 10.13: *Sensitivity of M19 to the battery specific energy and battery specific power.*

CHAPTER 11

TOWARDS A CONCEPTUAL DESIGN OF THE MINILINER

This chapter shows a preliminary application of the TITAN tool introduced in Section 4.7. TITAN is able to perform a full Class I conceptual design loop for hybrid-electric aircraft and couples the preliminary sizing tool HYPERION and the geometrical sizing tool ARGOS. The design process begins with the preliminary sizing of M19 obtained with HYPERION and presented in Chapter 10. The wing sizing (surface and span) and the weight breakdown of the aircraft (airframe, PGS, fuel, BP, EMs and tank mass) are passed to ARGOS. ARGOS performs a better estimate of the non-propulsive mass and of the aerodynamic properties (parasite and induced drag) and sends the solution back to HYPERION. This process is repeated until the output MTOM of both tools, HYPERION and ARGOS converges.

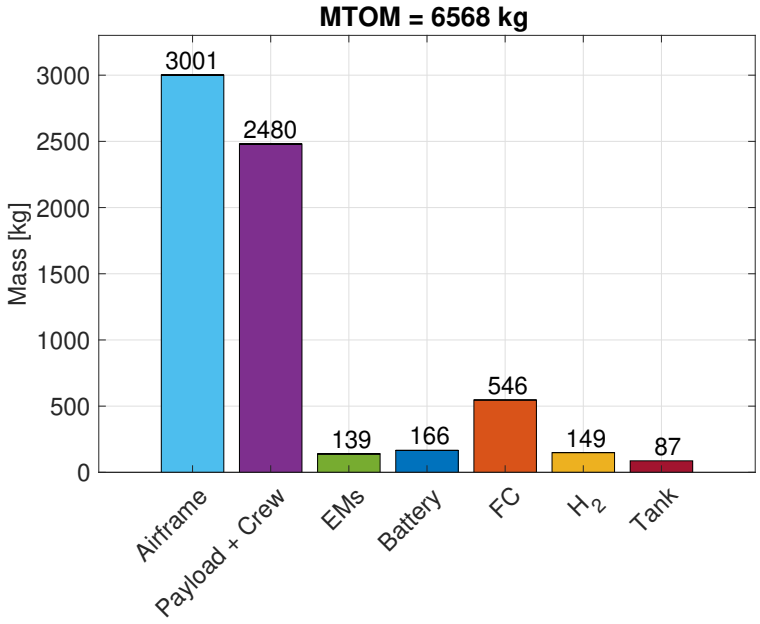

Figure 11.1: *Mass breakdown of the M19 TITAN solution.*

11.1 Mass breakdown

The mass breakdown of the full solution found with TITAN is shown in Figure 11.1. The final MTOM is equal to 6589 kg, a result that is 12.3 percent lower than the solution found by HYPERION in Chapter 10. Such weight difference is related to the non propulsive airframe mass, the light blue bar of Figure 11.1, reduced by 21.8% with respect to the values in Figure 10.2c. The fuel cell system mass in the TITAN solution weighs 55 kg less than the solution of HYPERION (-8.8%). Analogously, the battery mass and the EM mass are lower by a similar amount: -8.7%. The couple hydrogen+hydrogen tank is 4.9% lighter. Table 11.1 lists all the mass breakdown elements of the TITAN and HYPERION solutions and provides the relative error among the two.

The airframe mass resulting in TITAN is obtained from a detailed mass estimation process that is performed for each aircraft subcomponent, namely: wing, horizontal tail, vertical tail, fuselage, landing gear and other. The term other includes the mass of the control surfaces, air conditioning, instrumentation, furniture and other items. The full list of masses is shown in Table 11.2. The heaviest contribution, as expected, is given by the structural mass of the fuselage, followed by the wing, tail and landing gear. It is interesting to notice that the term Other amounts to 47.4% of the overall airframe mass. This highlights that this term can be partic-

Table 11.1: *TITAN and HYPERION M19 solutions compared.*

	Units	TITAN	HYPERION	Difference
Airframe	kg	3001	3815	-21.3%
Payload + Crew	kg	2480	2480	0.0%
EMs	kg	139	160	-13.1%
Battery	kg	166	189	-12.2%
PGS (FC)	kg	546	625	-12.6%
Fuel (H_2)	kg	149	156	-5.1%
Tank	kg	87	91	-4.4%
MTOM	kg	6568	7516	-12.6%
Wing Surface Area	m^2	35.0	40.0	-12.5%
Wing Span	m	17.8	19.0	-6.3%
EMs Maximum continous power	kW	1,051	1,202	-12.6%
PGS (FC) power	kW	1,106	1,265	-12.6%

Table 11.2: *Mass breakdown of M19 subcomponents.*

	Original
Wing	555.5
Fuselage	599.0
H-Tail	51.0
V-Tail	90.1
Landing Gear	292.2
Other	1413.2
OEM	3,939.0
MZFM	6,419.0
MTOM	6,568.0

ularly critical in the design of very innovative aircraft configurations and propulsion systems and should be better derived in a later stage of the design process.

11.2 Convergence process

With the purpose of obtaining reliable results from the TITAN tool, the solution must converge towards the final result reducing the discrepancy between the HYPERION and the ARGOS solutions. In this case, the convergence process is done minimizing the relative error between the HYPERION and ARGOS MTOM. The error convergence threshold was set to 10^{-3}.

Figure 11.2 contains 6 subfigures showing the effect of this convergence process. For example, Figure 11.2a depicts the value of the MTOM as found by HYPERION and ARGOS at each iteration, while Figure 11.2b shows the relative error between HYPERION's value of the MTOM and ARGOS's.

In particular, TITAN gets the airframe mass M_a and the parasite drag coefficient C_{D_0} from the ARGOS solution before beginning a new iteration in HYPERION. As it can be seen in Figure 11.2c, HYPERION does not have an imposed value of M_a in the 1^{st} iteration. In the 1^{st} iteration, HYPERION uses the statistical relations of Chapter 4 to compute the aircraft's empty weight fraction. For the successive iterations, the value from the ARGOS solution is utilized. By updating M_a each iteration, a more accurate estimation of the power-train components weight is done in HYPERION, as both solutions progressively come to convergence.

It can be observed (Figure 11.2d) that the wing loading (W/S) for HYPERION converges to a constant value that coincides with that of the sizing matrix plot. The ARGOS solution must arrive to the W/S design condition imposed by HYPERION; thus, as the aircraft weight decreases, the wing surface area must also decrease as shown by Figure 11.2e.

Concerning the parasite drag coefficient, C_{D0} the final value is larger than the initial estimation. Given that the wing surface area decreases, the overall aircraft wetted area also decreases; hence, the Reynolds number is lower as the aircraft's characteristic length decreases, producing a higher viscosity effect which translates into higher parasite drag coefficient (Figure 11.2f).

Table 11.3: *Liquid hydrogen tank of M19.*

	Units	Original
Length	m	2.38
Diameter	m	1.19
Insulation Thickness	mm	2.6
Structural Thickness	mm	20.0
Volume	m^3	2.21
Mass λ	kg	87.0
Gravimetric Index	$-$	63.1%

11.3 Geometry and lofting

The three plots in Figures 11.3a, 11.3b, 11.3c show the three views of M19 as designed by TITAN.

The orange boxes on the wing represent the EMs. EMs are fitted inside nacelles which are embedded in the wing and are physically connected to the propellers.

The BP is placed in the mid section of the high wing and is represented by the flashing green box. We can see that the volume occupied by the battery seems to be pretty small (0.071 m^3). This is due to the fact that the battery serves as a power booster and not as a main energy source.

For what concerns the hydrogen system, the FCs are located in the tail cone, the usual location for APUs on conventionally fuelled aircraft, and the entire fuel cell system is represented by the pink box. The volume of the fuel cell was estimated starting from the regressions present in Section 3.2.2 which are based on existing fuel cell systems and is 0.42 m^3. Balance of plant equipment, such as air compressors and humidifier, could be fitted in the tail cone as well.

Finally the LH2 tank, drawn as the blue box, is placed behind the passenger cabin. The shape of the tank is a capsule with hemispherical heads and cylindrical shell. Table 11.3 summarises the specifics of the LH2 tank of M19. The gravimetric index turns out to be identical to that of the design performed by Hyperion: 63.1%.

The 3D view of Figure 11.4 illustrates the arrangement of both payload and power-train elements within M19. For what concerns the payload, the figure shows a 1+1 seating arrangement per row. The cargo hold is placed right behind the passenger cabin, and is represented by the dark green cylinder in Figure 11.4.

With the help of the views and Table 11.4 we can see that the overall length of the fuselage is 19.48 m and the width is 1.70. The tail is a so called *traditional tail* and features an horizontal surface of 6.13 m^2 and a vertical surface of 3.94 m^2. The wing surface amounts to 35.02 m^2, that

Table 11.4: *Main geometrical quantities of M19.*

	Units	**Original**
Wing Area S_w	m^2	35.02
Wing Span b	m	17.75
Wing Taper λ	$-$	0.39
Wing Thickness ration t_c	$-$	0.16
Fuselage Length L_f	m	19.48
Fuselage Width D_f	m	1.70
H-Tail Area S_h	m^2	6.14
V-Tail Area S_v	m^2	4.15

is 12.5% less than the M19 solution found in Chapter 10. The wing span amounts to 17.8 m. The wing plan-form is trapezoidal, with a taper ratio of 0.39 and a thickness ratio of 0.16.

11.4 Discussion

From the three views of M19 in Figures 11.3a, 11.3b, 11.3c and the 3D representation of Figure 11.4 one may wonder whether a tube-and-wing configuration is a good one for a FCHE airplane using hydrogen stored in liquid form. At a glance, only a fraction of the fuselage is used to host the payload, drifting away from what is common with conventionally-fuelled airplane. Certainly the tube-and-wing concept has become the industry standard due to a series of incremental optimizations which happened across the last century: introduction of the integral wing tanks, optimized wing structure, extra-light fuselage furniture, carbon composites fuselage structure and so on. The tube-and-wing option represents also a good starting point for keeping the production costs low and for compatibility with the existing airport infrastructure. However, the switch towards a different propulsion system can lead to drastic changes in the aircraft configurations.

For what concerns the wing, the volume inside the wingbox of Figure 11.4 does not host fuel as it is common for conventional propulsion. For sure, some of this space will be needed for cables and power electronics that drive the EMs, but the sizing of the wing still appears suboptimal. Un-

fortunately, it might be particularly difficult to fit LH2 tanks inside the wing, since they need to be slightly pressurised and well insulated.

Without the need for fuel tanks inside the wing, a longer and thinner braced wing could be adopted [182]. Another option to effectively increase the aspect ratio is that of resorting to a box-wing, connecting the tail with a thinner wing. Both options, the trussed-braced wing and the box-wing, could achieve significant reductions in induced drag per unit and make the overall wing-tail system lighter [183].

Another possibility to optimize and reduce the size of the wing could be that of using a canard, instead of an aft tail. The wing can be smaller as part of the lift is effectively produced by the canard and the usual shift of the aircraft centre of gravity towards the nose could be counterbalanced by the presence of the heavy hydrogen tank placed in the rear of the cabin [122].

Also, a different distribution of thrust among small on-wing-propellers moved by EMs, opposed to a two-propeller electric configuration, can lead towards a smaller wing. DEP could be conveniently employed to increase the wing loading and get a reduced wing area at the cost of increasing the complexity of the control system. Conversely, if the wing surface is not reduced, DEP can improve the take-off and landing performance.

Other possible configurations that are more suitable to host large hydrogen tanks could be employed. For instance, a Flying-V shape [184] or a Blended Wing Body (BWB) configuration [185]. These concepts can reduce the total wetted area of the airplane, and, with a larger centre section, improve structural efficiency. Hence, the airplane is basically rendered into a flying wing with a delta-shaped wing/fuselage, large enough for the passenger cabin and GH2 or LH2 tanks.

The design of M19 presented here is not optimal from a configuration point of view, but represents a starting point and shows the design capability of the HYPERION and TITAN tools. There is need to further explore the wide design space that emerges from the introduction of HE propulsion and several aspects will be addressed in future versions of the methodologies. As a demonstration that the work is already on-going, Figure 11.5 depicts a possible version of the miniliner with DEP and a tail cone propeller. This is only one of the many exotic configurations already under investigation using TITAN, among the large series of follow-up works that are continuing under the MAHEPA and UNIFIER19 projects.

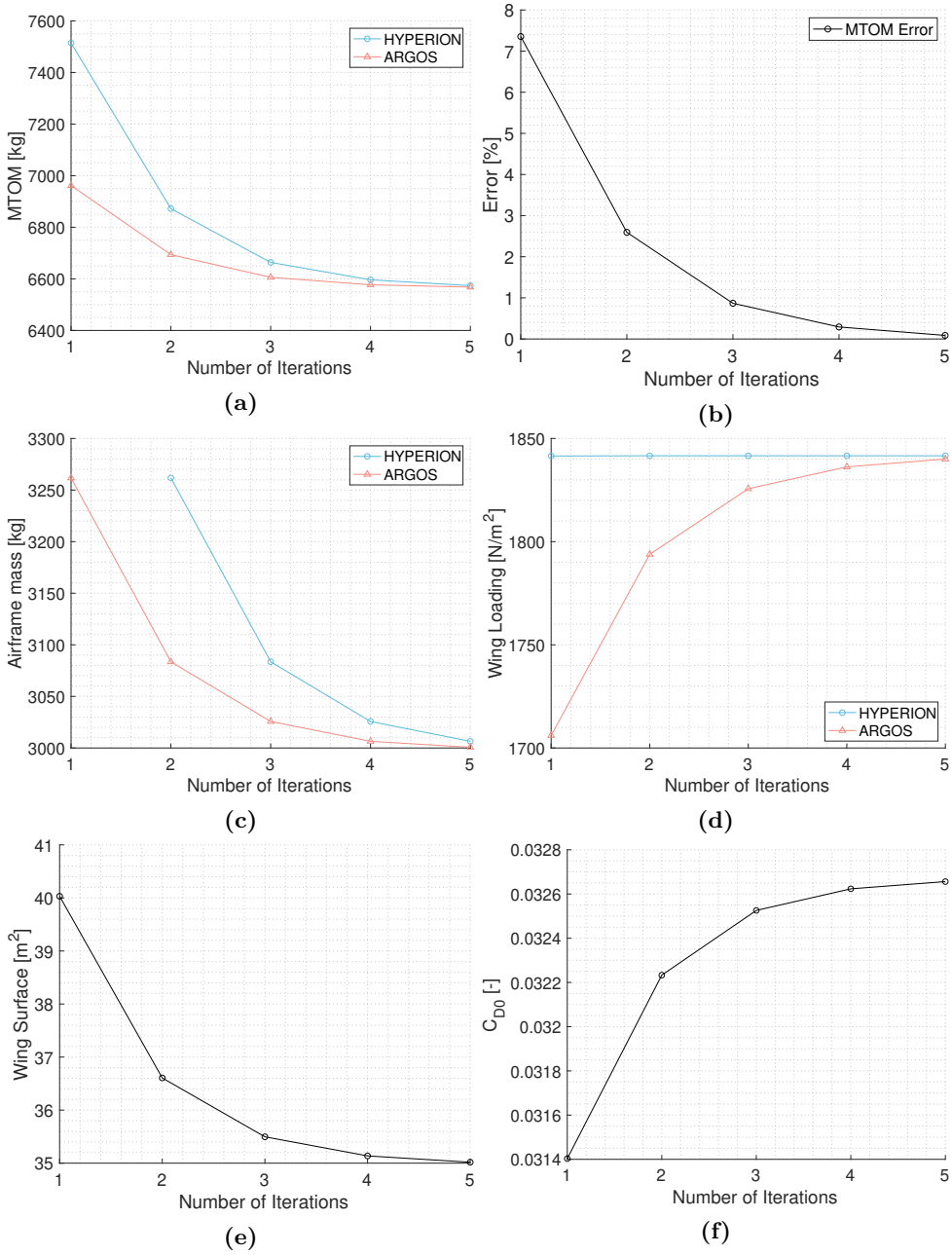

Figure 11.2: *HYPERION and ARGOS convergence process.*

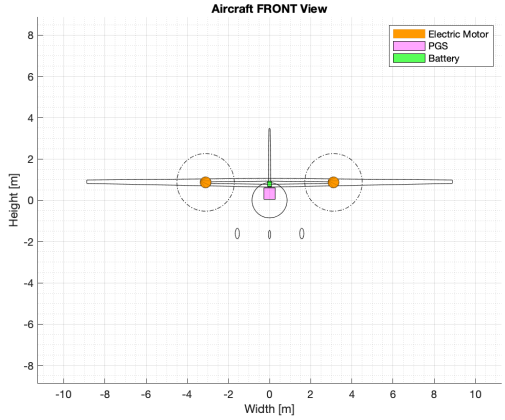

(a)

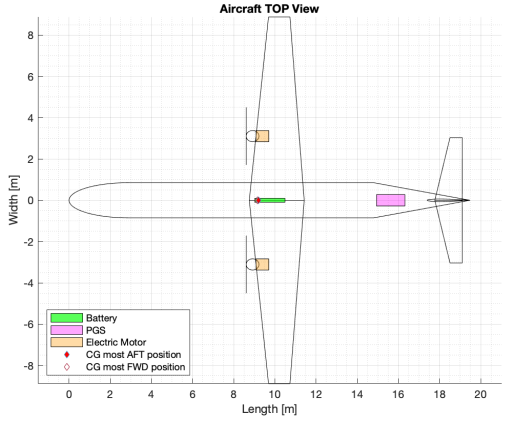

(b)

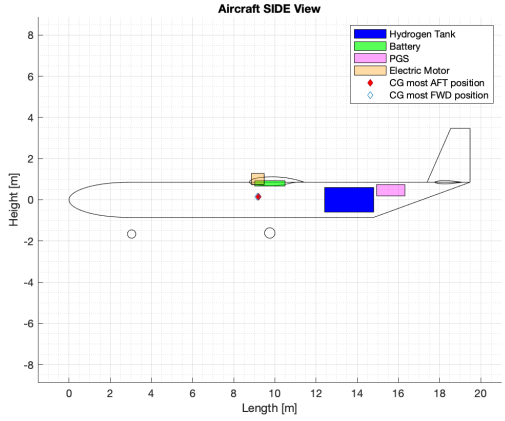

(c)

Figure 11.3: *Three views of M19.*

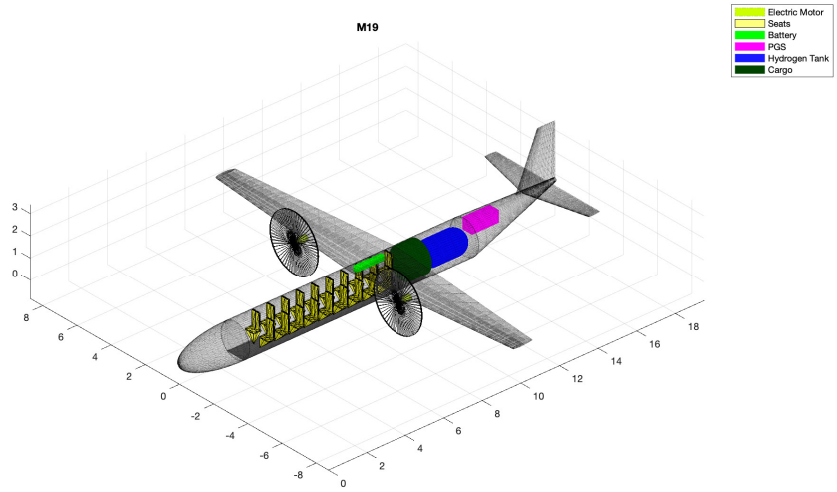

Figure 11.4: *3D view of M19 TITAN solution.*

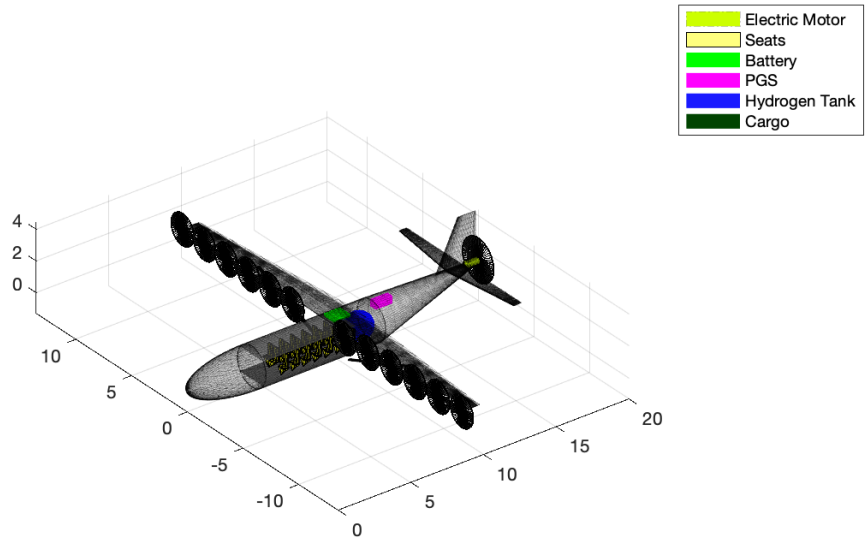

Figure 11.5: *Example of innovative configuration of M19 with DEP and tail cone propeller, obtained with TITAN.*

CHAPTER 12

CONCLUSION

This thesis presented a broad array of contributions regarding the design of hybrid-electric airplanes and scenario studies concerning sustainability and ground infrastructure. The core of this work is represented by the three methodologies introduced in Part I:

- **HYPERION** is a novel methodology to perform the preliminary sizing of innovative, electrically-powered fixed-wing aircraft, providing a comprehensive and flexible tool for conceptual/preliminary design loops. HYPERION can deal with propeller-driven PE airplanes, as well as serial THE and FCHE ones. The method is capable to find a mass breakdown that includes the mass of the non-propulsive airframe, PGS, fuel, BP, EMs and tank mass in case of FCHE. The methodology combines the ability to resort to historical-statistical estimations and direct modelling of aircraft main subsystems, in a modular fashion. Additionally, the value of the wing surface and span, together with the installed power of EMs, BP, thermal engine and FCs are returned. A thorough validation effort including several conventional aircraft across widely different weight classes has been

carried out. The considered categories of aircraft go from low-end CS-23 to CS-25 models, namely: GA, small commuter, large commuter and large regional. In addition to this, another validation is shown for an existing hybrid-electric aircraft and a pure-electric aircraft with DEP. Based on this methodology, a number of design exercises have been pursued. First of all a 4-seater GA is designed with a serial THE and a PE power-train. The FCHE solution, instead, has been found for a large regional 70-seater, looking at different technological scenarios for what concerns the battery and FC technology. Two options are considered for the storage of the hydrogen: GH2 and LH2 tanks. The HYPERION tool has been completed with the geometrical sizing tool ARGOS. The two codes, together, form the TITAN tool which is able to carry out a complete Class I conceptual design loop. Compared to HYPERION, TITAN can also return the geometry of the wing, fuselage, horizontal/vertical tail and landing gear.

- **ARES** is an original methodology to model and optimally size a ground battery recharging system in support of an electric-powered fleet. Two major recharge options are considered: BPC and BSS. BSSs can be employed if the aircraft batteries can be loaded and unloaded from the aircraft before or after a flight, while BPCs are capable of recharging the battery without unplugging it. A further element which is modelled is the varying price of electricity provided by the electric grid. The underlying optimization algorithm, using a MILP scheme provides the sizing solution together with the time planning of charging operations, in compliance with the predetermined flight scheduling at the airport, while minimizing procurement and operational costs. Due to the general approach in its formulation, ARES is suitable to extensive sensitivity studies on a large number of user-defined parameters. The discussed applications to a GA airport and to a large regional hub make use of real airport and aircraft data plus reasonable assumptions on the chargers' specifications, leading to feasible solutions that may be used as examples in the study of the general impact of transitioning from conventionally-powered to electric-powered aircraft fleets in the future.

- **CHANCES** is a novel method introduced in order to assess the acoustic pollution and chemical emissions of aircraft equipped with a novel hybrid-electric power-train. Concerning acoustic pollution, a method blending the output of several noise sources on board the aircraft to obtain an overall figure comparable to that of comprehensive methods based on database (currently inapplicable to hybrid-electric aircraft) has been proposed. The coefficients are tuned in the case of

conventionally-powered aircraft, and applied to hybrid-electric aircraft, making possible to quantitatively assess the advantages provided by an innovative power-train in terms of acoustic pollution around the reference case of an existing GA airport. The same trajectory segmentation needed to carry out acoustic analyses has been adopted for the assessment of chemical emissions. This has allowed to deploy very accurate methods for the prediction of the social cost of chemicals released by example ideal or existing hybrid-electric aircraft, to the same realistic test case adopted for the acoustic analysis. This analysis too has shown the potential of hybrid-electric power-trains in reducing social cost, thus potentially raising public acceptance and increasing the value of smaller airfields in the air transport infrastructure.

These methodologies have been integrated in the design framework for the preliminary sizing and early conceptual design of the zero emission 19-seat miniliner.

The results of an original, extended analysis of the future market for miniliner applications have been discussed in order to obtain indications for the miniliner top-level aircraft requirements. In particular, the market studies highlight the importance of primary aircraft performance of range, take-off/landing distances, and cruising speed in the ability to capture the travel needs of potential customers. This community-friendly aircraft, in fact, is specifically conceived to be used in the roles of hub *microfeeder* and *intercity* liner. Therefore, market studies dedicated to these two service options were necessary to guide the determination of the aircraft design requirements and since both air transportation segments are not yet developed, predictions concerning future market opportunities were needed.

First of all, an analysis of the existing system of secondary aerodromes in Europe was performed, considering runway length, surface type and geographic distribution, showing its potential in supporting a diffuse regional network. This database has been used to provide a set of possible routes for which the travelling demand has been estimated. This process relies on the assessment of a definite advantage for travellers when using the miniliner instead of cars or trains, in terms of time saving, as this is assumed of crucial importance. The method is currently being extended to take into account further aspects of the travellers' motivation in choosing for flying with the miniliner, such as cost and comfort.

Then, the preliminary sizing of the miniliner is carried out showing that the most promising solution, in terms of power-train architectures is the fuel cell hybrid-electric with liquid hydrogen tanks. Conversely, gaseous

hydrogen tanks are too heavy and do not allow a sensible design solution. The thermal hybrid-electric solution lies in the middle, but still shows an MTOM greater than the CS-23 limit. Sensitivity analysis showed that the selection of range, take-off distance and cruising speed has a relevant impact on the resulting design. The effect of technology parameters, such as fuel cell specific power and battery technology, can be very different. For example, changing the fuel cell specific power brings to an asymmetrical behaviour of the design solution, i.e. if the fuel cell specific power is increased the weight saving is a lot smaller than the weight penalty resulting from a reduction of the fuel cell specific power. The sensitivity on battery specific energy and power has, on the whole, a much contained effect, with variations on the MTOM within 4%.

Finally, the first attempt for a full Class I conceptual design was performed. This sizing lowers the MTOM of the miniliner to 6568 kg. This exercise was carried out considering a traditional architecture for the wing and the tail. The battery pack is small enough and can be fitted inside the wing. On the other hand, the liquid hydrogen tank is placed behind the cabin and makes the fuselage longer. The fuel cell system is located right behind the tank, inside the tail cone, a space usually reserved for the APU on conventionally driven airplanes. This location should, in principle, allow for positioning of the balance of plant equipment necessary for the fuel cell operation.

12.1 Work performed by the author

The material presented here is the result of a team effort in which the author had a prominent role, individually developing a large part of it and supervising a number of MSc thesis students.

Concerning Part I, the author is solely responsible for the technology review (Chapter 2) and the achievement of all the results in Chapters 4 and 5. The author participated in the development and implementation of all the original formulations discussed in Chapters 3 to 6 and contributed to the achievement of the results discussed in Chapter 6.

Concerning Part II, the author participated in the development and implementation of the original formulation discussed in Chapter 8 and in the setup of the case study carried out in Chapters 9 to 11, being solely responsible for the achievement of all the results shown in Chapters 8 to 11.

12.2 Future outlook

As stated in the Introduction, the work described in this thesis is part of a much wider research path and some of the things we have been doing were left out of this manuscript. Moreover, despite the large effort done so far, there are several aspects of hybrid-electric propulsion that need further investigations and many things that could be improved in the methodologies developed.

Among the work in progress the following methodological developments are found:

- **SHARONA**: a procedure for the assessment of the capability of a regional network system based on electric-powered commuter aircraft, christened Short-Haul Air Route Optimal Network Assessment (SHARONA) was developed to complete the potential demand estimation studies introduced in Chapter 8. This optimization algorithm defines a complete air transportation network for the territory at hand, being capable to capture the highest possible share of the potential demand, based on the availability of a given aircraft fleet [141].
- **AHRES**: the ARES methodology is being expanded to hydrogen refilling stations. The new ARES formulation, named Airport Hydrogen Refilling Equipment Sizing (AHRES) is still based on a MILP approach but instead of finding the optimal recharging schedule, it finds the best refilling schedule for an airport hosting hydrogen-fuelled airplanes. In particular, the tool is able to decide when to produce hydrogen using electrolyzers based on the cost of electricity and the flight schedule that must be served. The infrastructure is sized in terms of storage tanks, buffer tanks, distribution pipelines and dispensing units.

Further activities related to the present work are presently being considered. Among them the following are worth mentioning:

- Further coupling of HYPERION and ARGOS within TITAN: although a preliminary sizing tool offers exceptional versatility, the conceptual design solution is far more interesting and satisfying from an engineering perspective. The TITAN tool is still at an infant stage of development and currently supports only traditional tube and wing architectures. The extension of TITAN to non conventional configurations, such as truss-braced wing, blended wing body, variable incidence wing, is going to be the next step in the development

of the methodology.

- Battery modelling in TITAN: the energy-in-the-box approach to model the performance of the BP adopted in HYPERION works fine and provides sensible results. However, a more accurate battery model should be used to include some aspects of battery operations in the design loop. For instance, the monitoring of the battery state of health could lead to different power management strategies during the flight of a hybrid-electric airplane and yield to different sizing of BP and PGS.
- Optimal design: one big takeaway we have learnt while building the methodologies for the design of hybrid-electric airplanes is that the sizing of every item (battery, fuel, PGS) is coupled with each other. Not only the sizing, also the use strategies, such as energy management strategies of Section 4.1.10 can definitely change the design solution. This problem can be addressed in an optimal way, resorting to suitable optimization tools.
- Thermal management system and inclusion of cooling drag: electrical components located within the aircraft interior need cooling to dissipate the waste heat they produce. This aspect can be particularly relevant in the design process and also leads to the rise of the so-called *cooling drag*. Heat exchangers are possibly needed and might add a weight toll to the design solution.
- Further developments of the ARES methodology shall consider other elements that may play a role in a real case scenario. For example, the airport charging facility may provide ancillary services to the smart electricity grid, such as intermittent renewable energy storage (from solar- and wind-energy production), peak power supply, frequency or voltage regulation and other B2G and even B2B applications.
- The CHANCES tool will be further developed for the prediction of the noise of larger aircraft. The lack of consolidated data from existing prototypes in higher weight categories makes the task very demanding. Ultimately, CHANCES should be used directly within TITAN to drive the design process towards the minimization of noise and chemical emission.

Appendices

APPENDIX A

DATABASE

This Appendix contains a set of tables with data on existing electric motors for aeronautical applications, fuel cell systems and gaseous hydrogen tanks.

Table A.1: *Database of electric motors for aeronautical applications*

Name	Manufacturer	Mass [kg]	Peak power [kW]	Max Cont. Power [kW]	Diameter [m]	Axial Length [m]	Operating Voltage [V]	Efficiency [-]
magni500	MAGNIX	135		560	0.652	0.729	750	93
EVD250-115P2	EVDRIVE	110	560	320	0.386	0.492	700	
magni250	MAGNIX	72		280	0.559	0.536	750	93
SP260D	SIEMENS	50	260	260	0.418			
SP260D-A	SIEMENS	44	260	260			580	0.95
HVH410-075	REMY	98	310	235	0.49	0.202	700	0.95
S230 LAB	SIEMENS	50	261	230	0.418	0.3	580	95
HVH410-150	REMY	140	315	225	0.49	0.277	700	0.95
EMRAX 348	EMRAX	42	380	210	0.348	0.107		
SP200D	SIEMENS	49		204			850	
EVD250-115P1	EVDRIVE	54	280	175	0.426	0.356	700	
EVD250-90P1	EVDRIVE	46	300	175	0.311	0.282	700	
S170 LAB	SIEMENS	24.4		170			580	95
HVH250-115	REMY	57.2	350	160	0.215	0.302	700	0.95
HSM1-10.18.22	BRUSA	76	220	145	0.328	0.34		
HVH250-090	REMY	49	330	130	0.215	0.277	700	0.95
EVD250-90S1	EVDRIVE	46	150	125	0.326	0.282	700	
EMRAX 268	EMRAX	20.5	200	107	0.268	0.091	800	0.95
Panthera Hybrid - Generator	COMPACT DYNAMICS	28	100	100	0.302	0.29	450	0.95
YASA P400 R	YASA	100	160	100	0.305	0.0804	750	96
HSM1-10.18.13	BRUSA	51	185	93	0.328	0.25		
SP70D	SIEMENS	26	92	79				
Panthera Hybrid - Motor	COMPACT DYNAMICS	12	150	75	0.23	0.16	450	0.962
HSM1-6.17.12	BRUSA	51.5	120	70	0.328	0.25	450	
YASA 750 R Motor	YASA	37	100	70	0.368	0.098	750	
EMRAX 228	EMRAX	12.4	109	62	0.228	0.086		
YUNEEC PD 60	YUNEEC	30		60	0.28	0.209	133	
SP55D	SIEMENS	26	72	55				
PEM 60 MVLC	PIPISTREL	20	60	50				
E-811 ELECTRIC	PIPISTREL	22.7	57.6	49.2	0.268	0.091	450	
EngineUS	EngineUS Safran	18		45				94
EMRAX 208	EMRAX	9.4	68	41	0.208	0.085	550	
EMRAX 207	EMRAX	9.1	70	40	0.208	0.085	550	
YUNEEC PD 40	YUNEEC	19		40	0.24	0.163	133	
LANGE EA42	Lange Aviation Antares 20E	29.12	38.5	38.5	0.25	0.272		
EMRAX 188	EMRAX	7.3	52	30	0.188	0.077	430	95
REB 90	ROTEX ELECTRIC	23	80	30	0.27	0.212	350	
REX90	ROTEX ELECTRIC	17	60	25	0.219	0.203	380	
REB 50	ROTEX ELECTRIC	12.5	40	20	0.266	0.121	250	
FES SILENT 2	Silent 2	7.3	22	20	0.18		116	95
YUNEEC PD20	YUNEEC	8.2		20	0.2	0.133	67	
REB 30	ROTEX ELECTRIC	8.2	30	15	0.266	0.101	120	
RET 60	ROTEX ELECTRIC	7	25	15	0.17	0.123	250	
REX50	ROTEX ELECTRIC	7.9	28	15	0.216	0.094	120	
NASA X57	NASA	3.6		10.5	0.157	0.0345	460	93
YUNEEC PD10	YUNEEC	4.5		10	0.16	0.114	67	
REB 20	ROTEX ELECTRIC	8.5	20	8	0.266	0.111	120	
REX30	ROTEX ELECTRIC	5.2	20	8	0.216	0.0806	63	
RET 30	ROTEX ELECTRIC	4.1	15	6	0.17	0.074	120	
REG 30	ROTEX ELECTRIC	1.95	10	5	0.114	0.072	55	
REG20	ROTEX ELECTRIC	1.45	7	3	0.114	0.063	50	
Electravia GMPE 102	Electravia GMPE 102	13.3	19		0.206	0.182	74	93
Electravia GMPE 104	Electravia GMPE 104	13.8	26		0.206	0.182		93
Electravia GMPE 205	Electravia GMPE 205	14.7	37		0.206	0.182	111	0.93

Table A.1: *Database of electric motors for aeronautical applications*

Name	Manufacturer	Mass [kg]	Peak power [kW]	Max Cont. Power [kW]	Diameter [m]	Axial Length [m]	Operating Voltage [V]	Efficiency [-]
Electra 1	Electric Aircraft Corporation Electra 1	12	14				74	0.85
ELECTRO 2	Electro Light 2	7	19.4					
Geiger HDP 10	GEIGER	3.75	12.5		0.215	0.171	58	0.93
Geiger HDP 13.5	GEIGER	4.7	13.5		0.215			
LAK 17B FES	LAK 17B FES	7.3	35.3					
ELECTRIC 40/30 Taurus Electro G2	PIPISTREL	11	40					
SP90G	SIEMENS	13	65		0.224	0.18		
S85 WATTSUP	SIEMENS	14	85					

Table A.2: *Database of existing fuel cell systems for transportation application. From [63, 186].*

Manufacturer/Model	Type	Specific Power [W/kg]	Power Density [W/L]
Horizon AeroStack A-200	PEMFC	400	278
Horizon AeroStack A-500	PEMFC	434	162
Horizon AeroStack A-1000	PEMFC	571	224
Lynntech Gen IV	PEMFC	250	263
Protonex ProCore	PEMFC	74	71.5
Protonex UAV C-250	PEMFC	208	185
Spectronik FLY-300	PEMFC	545.5	320.7
DOE 2015 Status	PEMFC	659	640
PEM Fuel Cell Stack	PEMFC	967	846

Table A.3: *Database of existing gaseous hydrogen tanks for transportation application*

Manufacturer	Model	Nominal working pressure at 15° C [MPa]	Outside diameter [mm]	Overall length [mm]	Tank Mass [kg]	Water volume [l]	Hydrogen capacity [kg]	Gravimetric Index [-]
HEXAGON	A	20.0	315.0	1060.0	16.0	46.0	0.7	0.042
WORTHINGTON	ALT881DK	24.8	410.0	2743.0	109.8	277.5	4.9	0.043
HEXAGON	C	25.0	503.0	2342.0	94.0	350.0	6.0	0.060
HEXAGON	B	25.0	541.0	2783.0	164.0	450.0	8.0	0.047
HEXAGON	D	30.0	509.0	2342.0	112.0	350.0	7.2	0.060
WORTHINGTON	ALT604	31.0	183.0	533.0	5.5	9.2	0.2	0.035
WORTHINGTON	ALT817	34.5	402.0	844.0	43.6	68.4	1.6	0.035
WORTHINGTON	ALT836U	34.5	432.0	1003.0	59.4	90.2	2.1	0.034
WORTHINGTON	ALT909S	34.5	419.0	2667.0	117.0	273.7	6.4	0.052
WORTHINGTON	ALT909	34.5	419.0	3048.0	130.6	312.9	7.3	0.053
HEXAGON	F	35.0	509.0	2342.0	112.0	350.0	8.4	0.070
HEXAGON	E	35.0	420.0	3190.0	101.0	312.0	7.5	0.069
WORTHINGTON	ALT962	43.1	439.0	2976.0	190.5	304.1	8.4	0.042
WORTHINGTON	ALT962L	43.1	439.0	3048.0	197.3	311.8	8.6	0.042
WORTHINGTON	ALT1015LP	46.5	445.0	3048.0	217.7	312.9	9.2	0.041
HEXAGON	H	50.0	531.0	2424.0	229.0	347.0	10.7	0.045
HEXAGON	G	50.0	565.0	3277.0	280.0	530.0	16.5	0.056
WORTHINGTON	ALT1015	51.7	452.0	3048.0	224.5	312.9	10.0	0.043

Table A.3: *Database of existing gaseous hydrogen tanks for transportation application.*

Manufacturer	Model	Nominal working pressure at 15° C [MPa]	Outside diameter [mm]	Overall length [mm]	Tank Mass [kg]	Water volume [l]	Hydrogen capacity [kg]	Gravimetric Index [-]
HEXAGON	K	70.0	420.0	845.0	43.0	64.0	2.6	0.057
HEXAGON	L	70.0	440.0	1050.0	59.0	76.0	3.1	0.050
HEXAGON	I	70.0	319.0	906.0	34.0	36.0	1.4	0.040
HEXAGON	M	70.0	530.0	2050.0	185.0	244.0	9.8	0.050
HEXAGON	N	70.0	530.0	2154.0	188.0	244.0	9.8	0.050
HEXAGON	J	70.0	238.0	1600.0	29.0	39.0	1.6	0.052
WORTHINGTON	ALT1154	70.0	600.0	900.0	137.4	111.0	4.3	0.030
HEXAGON	O	95.0	515.0	2783.0	365.0	254.0	12.4	0.033
WORTHINGTON	ALT1063	106.0	482.0	1587.5	253.1	90.0	4.6	0.018

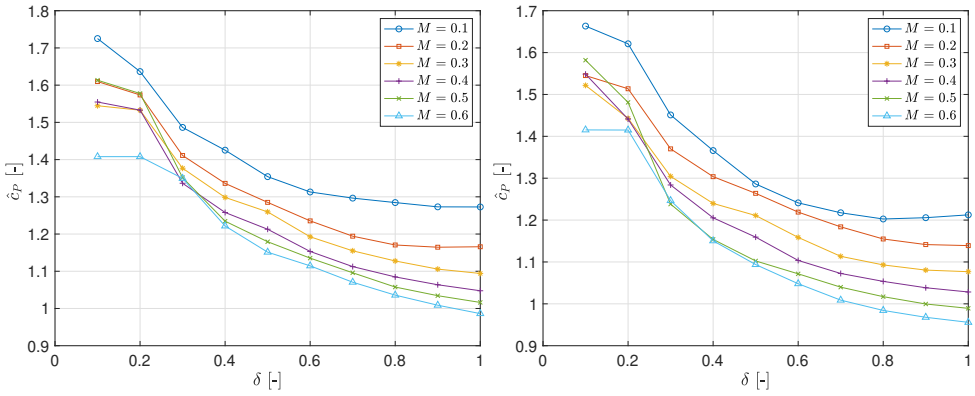

(a) *0 ft*

(b) *5,000 ft*

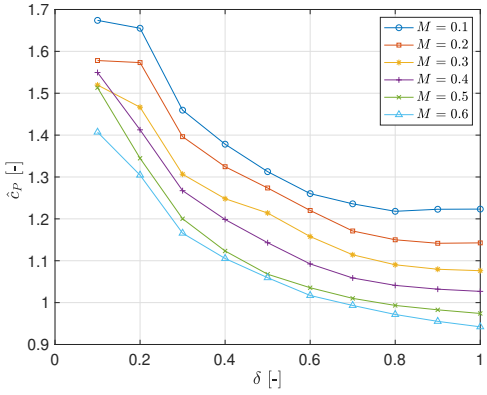

(c) *10,000 ft*

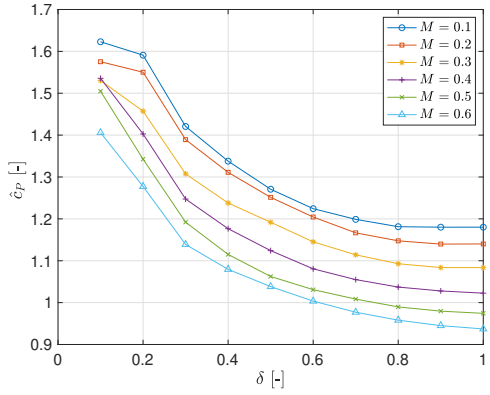

(d) *15,000 ft*

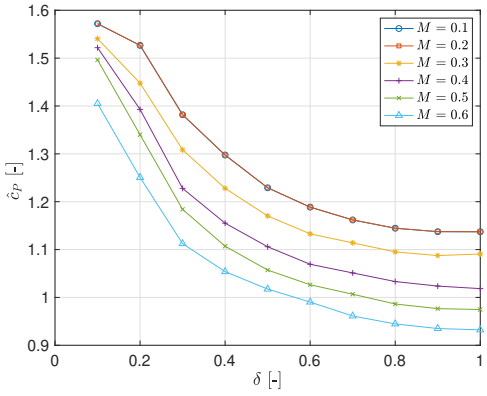

(e) *20,000 ft*

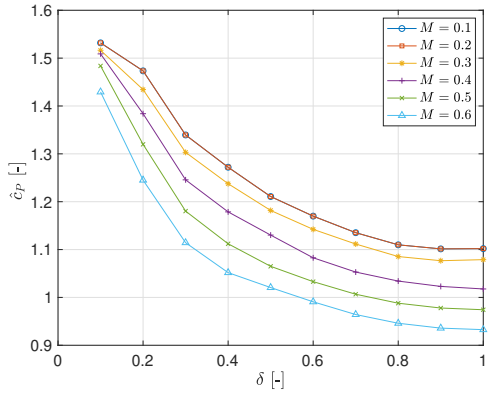

(f) *25,000 ft*

Figure A.1: *Dependence of normalised brake specific fuel consumption $\hat{c}_P$ vs throttle δ and Mach number M for turboshaft engine model from [107] at different altitude.*

APPENDIX B

COMPLEMENTARY PRELIMINARY SIZING RESULTS

This Appendix gathers additional plots regarding the preliminary sizing exercises of Chapter 4.

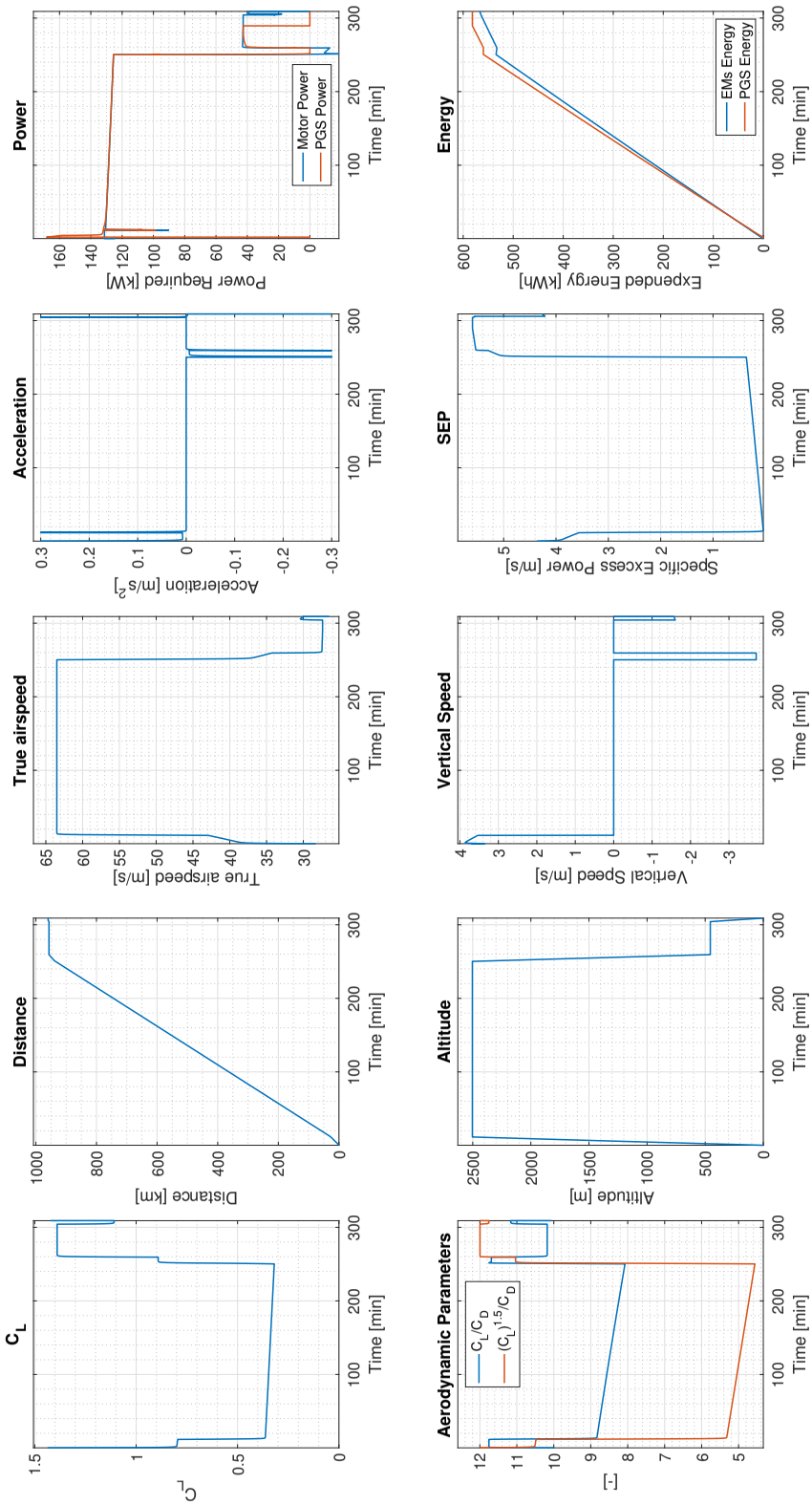

Figure B.1: *Time histories of the sizing mission for the A4THE.*

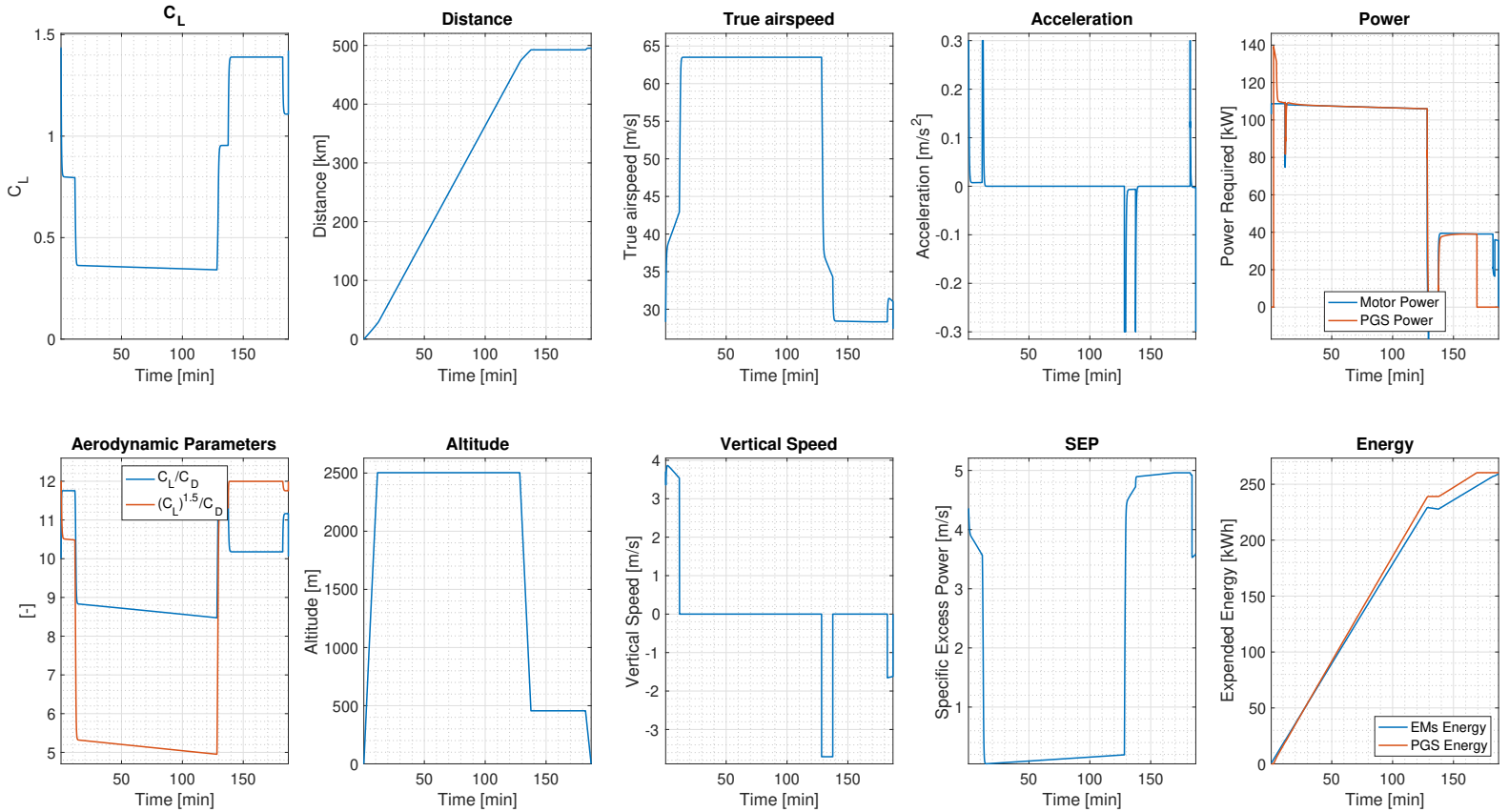

Figure B.2: *Time histories of the sizing mission for the B4THE.*

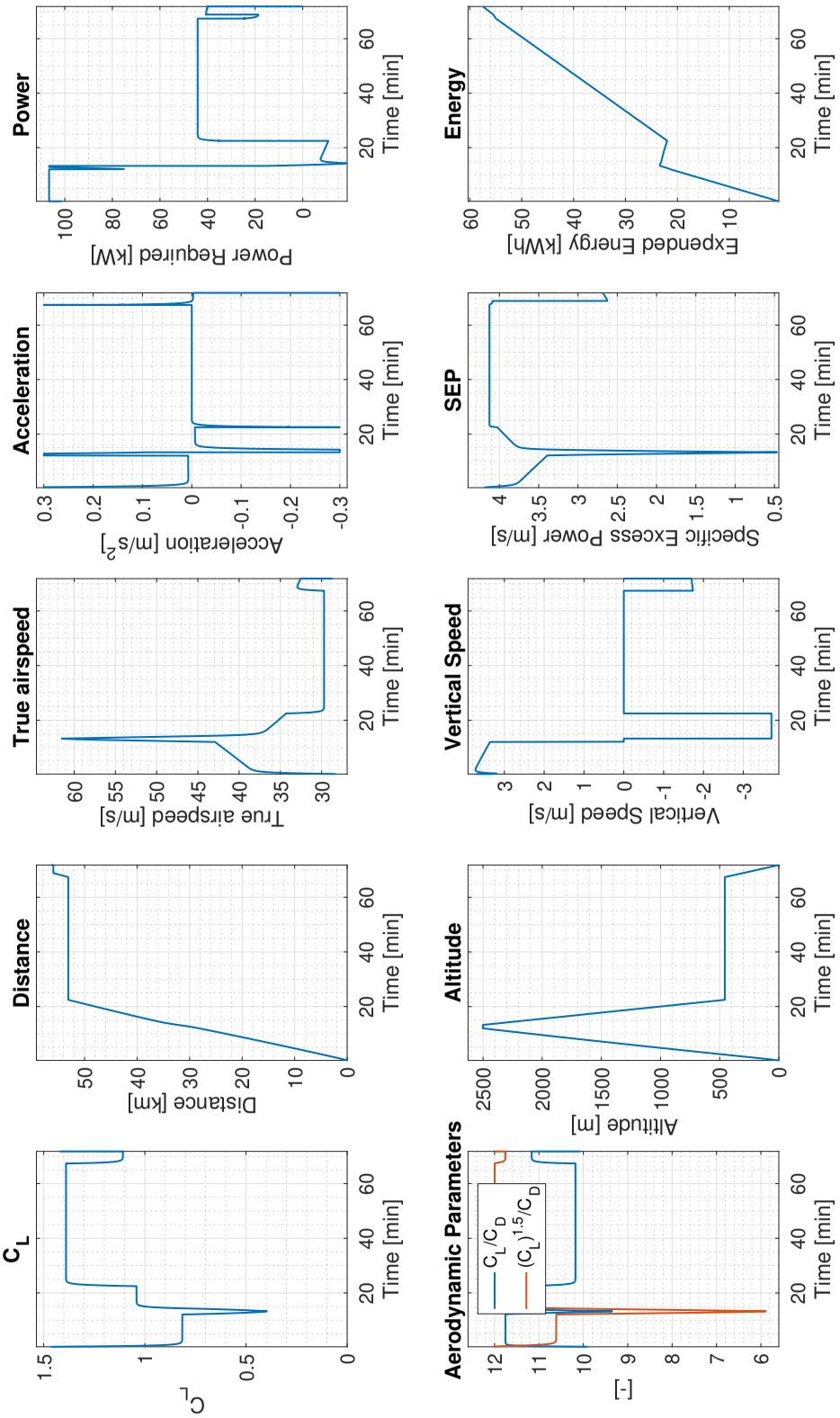

Figure B.3: *Time histories of the sizing mission for the B_4PE.*

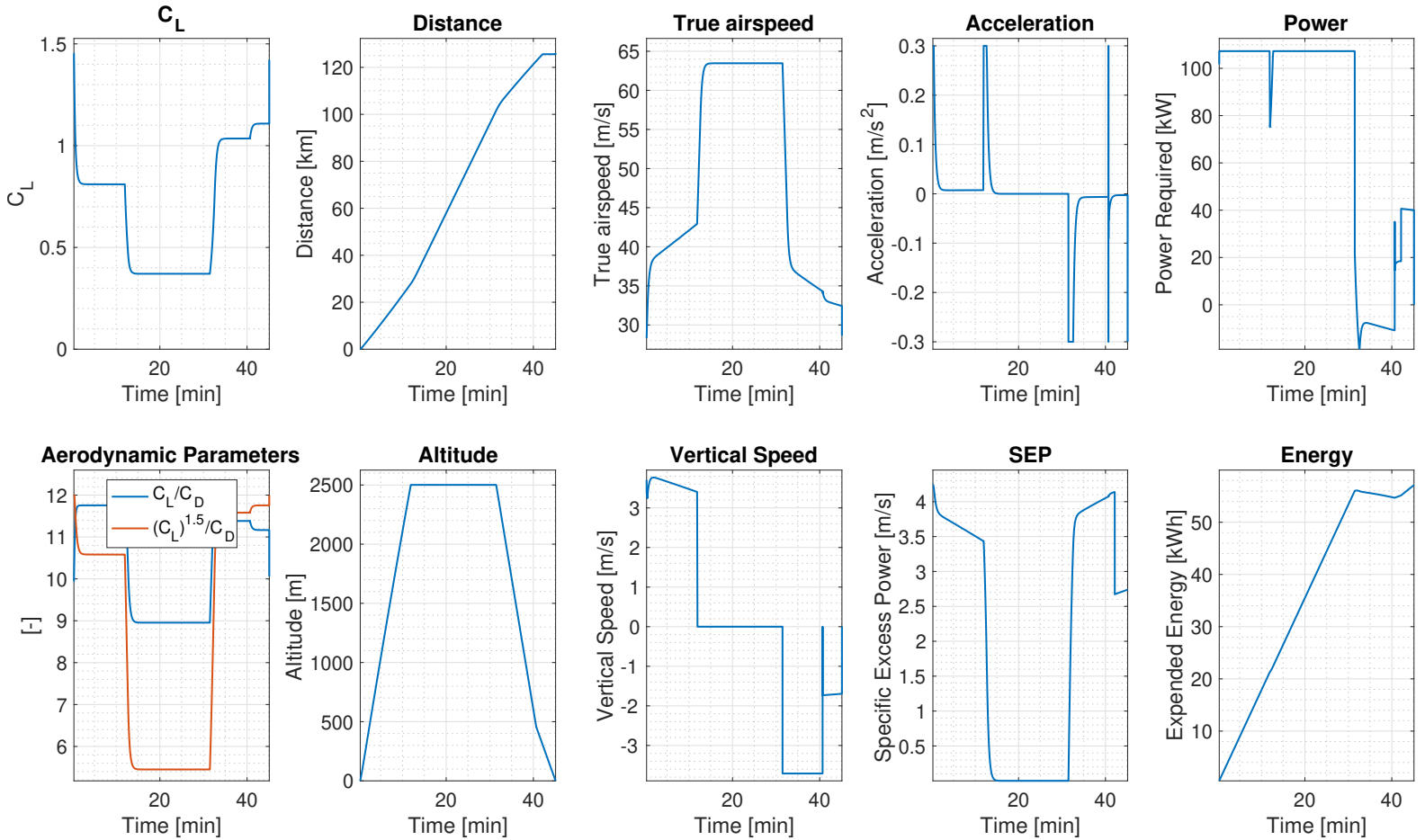

Figure B.4: *Time histories of the sizing mission for the B4PE without loiter.*

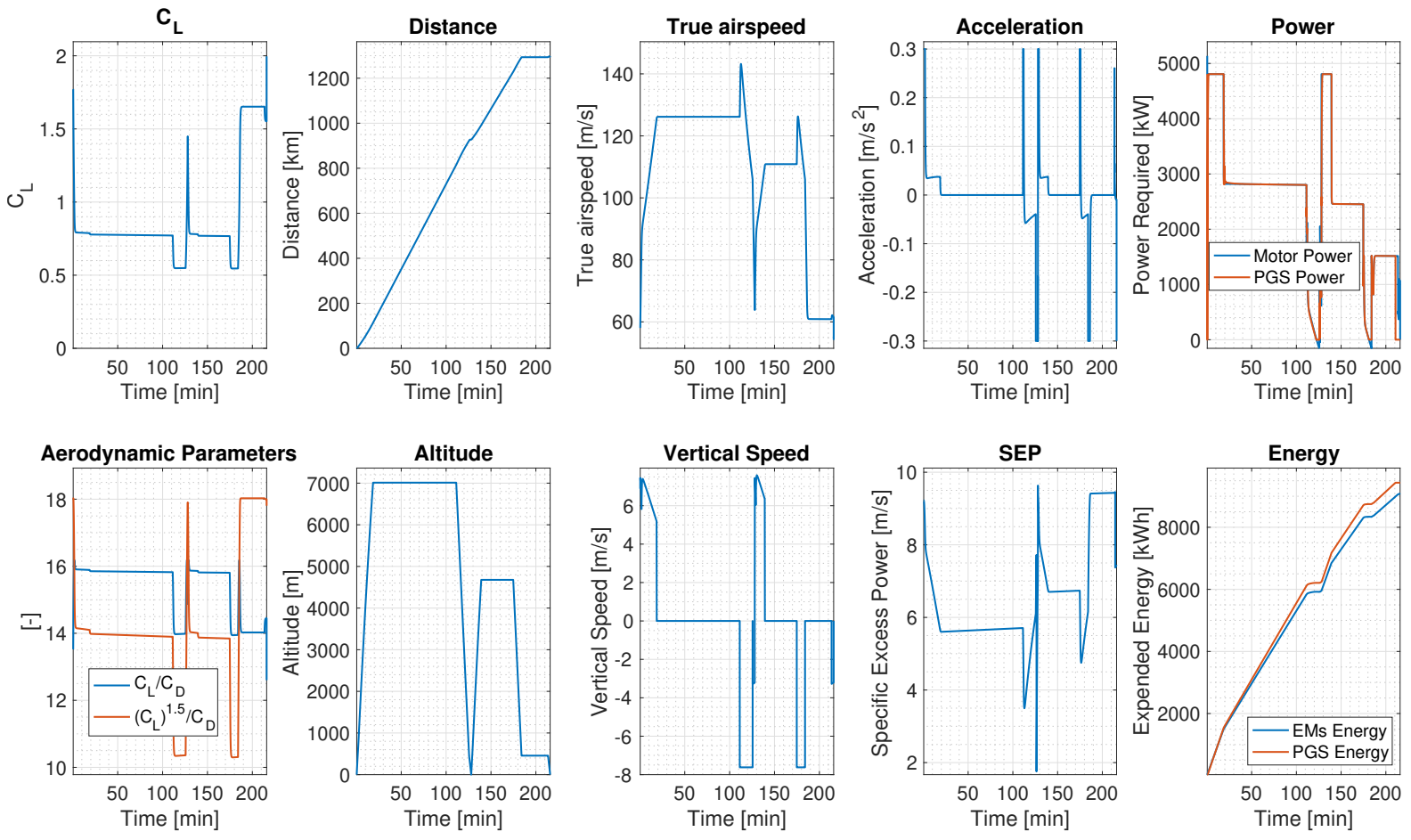

Figure B.5: *Time histories of the sizing mission for the A70GH2-2035i.*

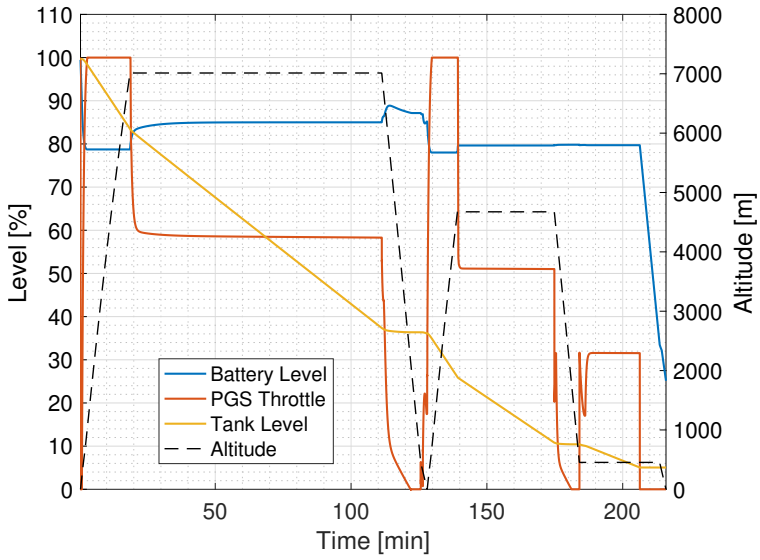

Figure B.6: *Time histories of battery state of charge (blue), PGS throttle (red), fuel quantity (yellow), and altitude (black) for the A70GH2-2035ii.*

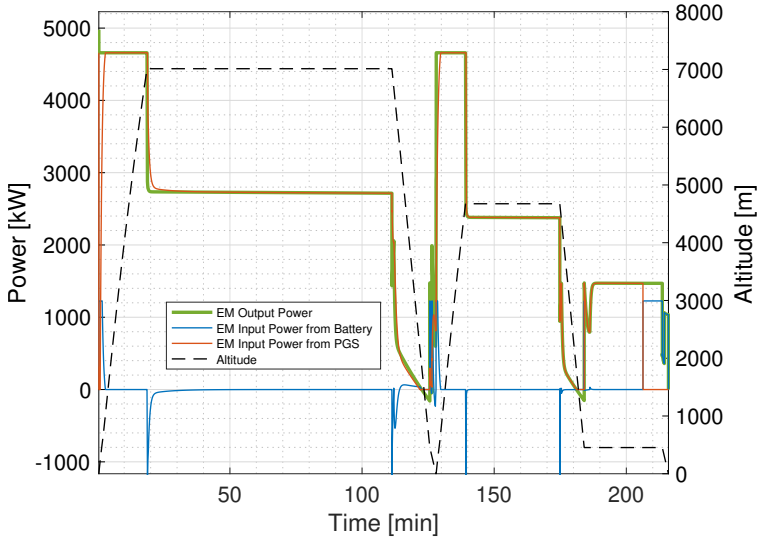

Figure B.7: *Time histories of shaft power (green), BP power (blue), PGS power (red), and altitude (black) for the A70GH2-2035ii.*

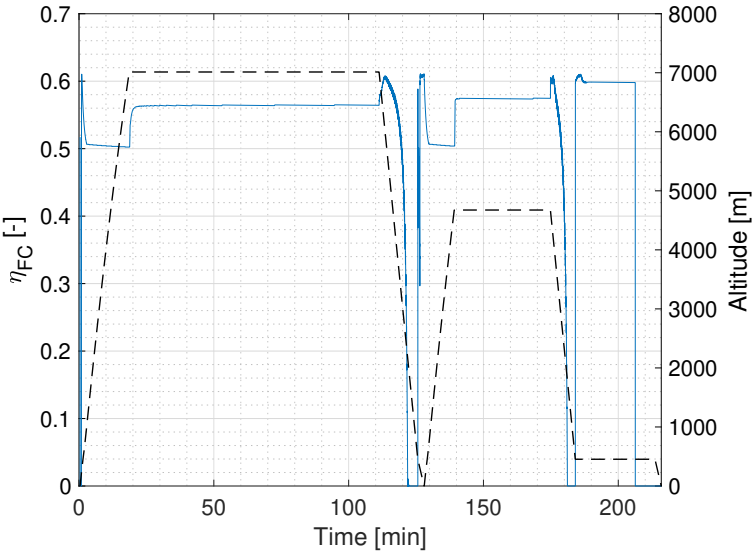

Figure B.8: *Time histories of the fuel cell efficiency(blue) and altitude (black) for the A70GH2-2035ii.*

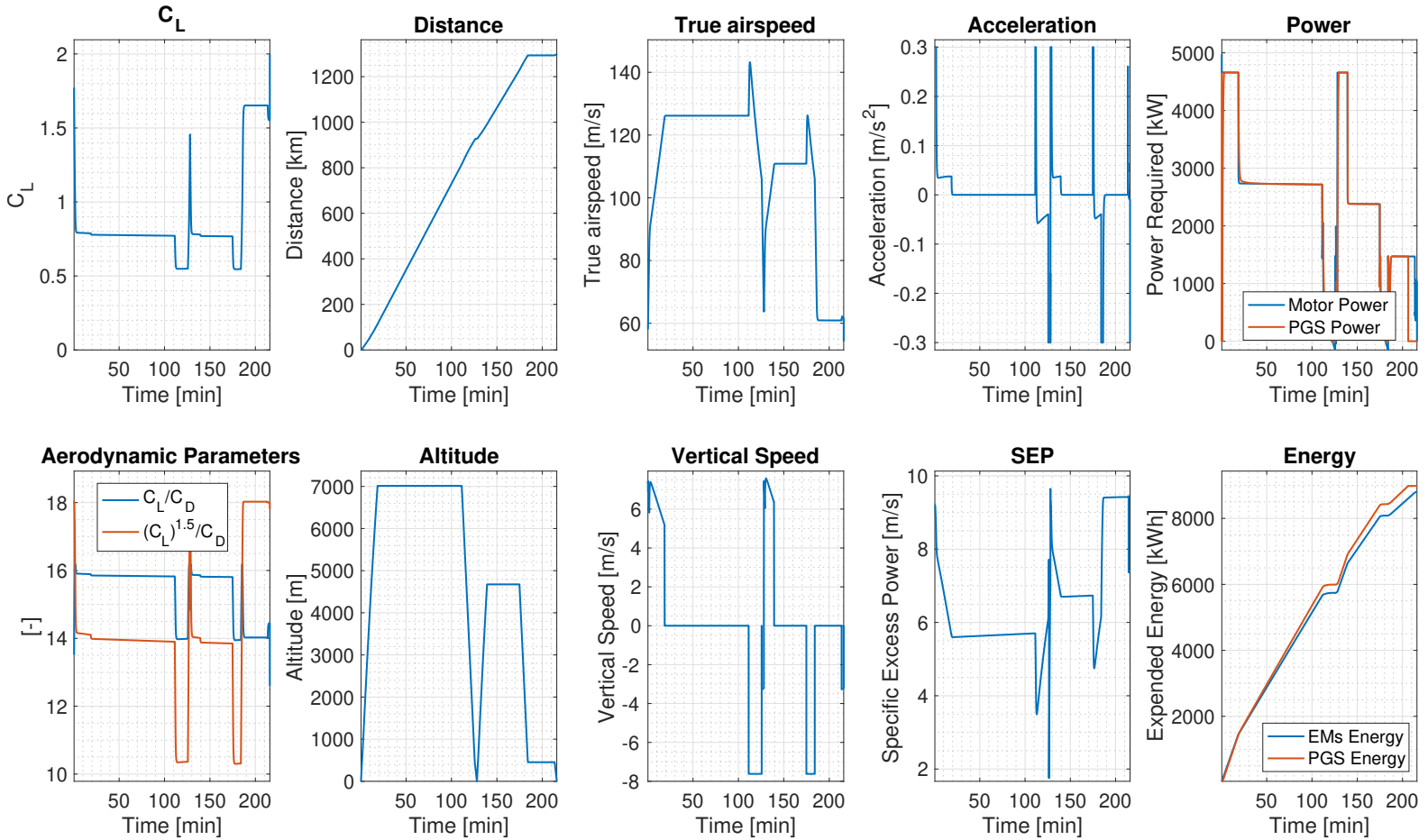

Figure B.9: *Time histories of the sizing mission for the A70GH2-2035ii.*

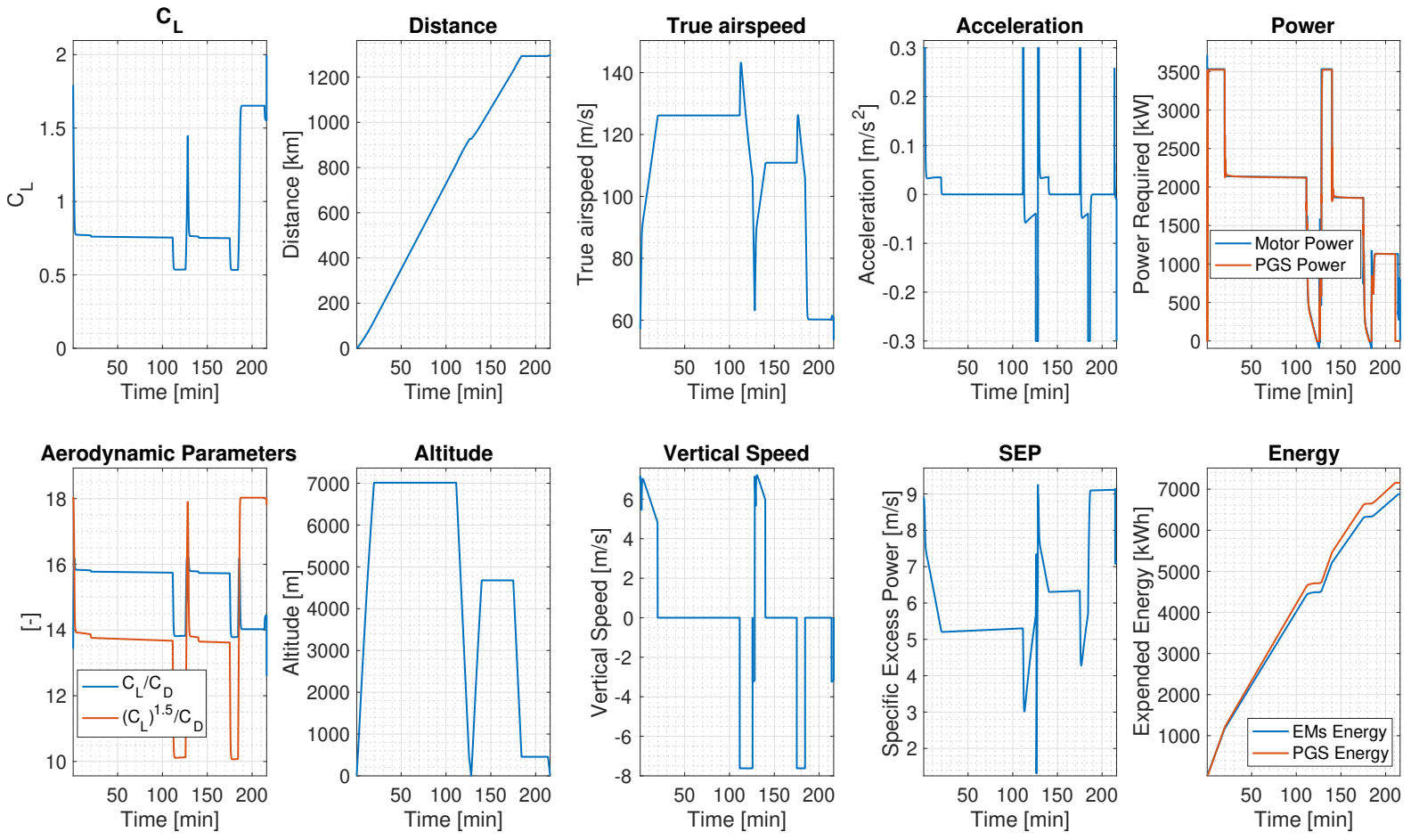

Figure B.10: *Time histories of the sizing mission for the A70LH2-2035i.*

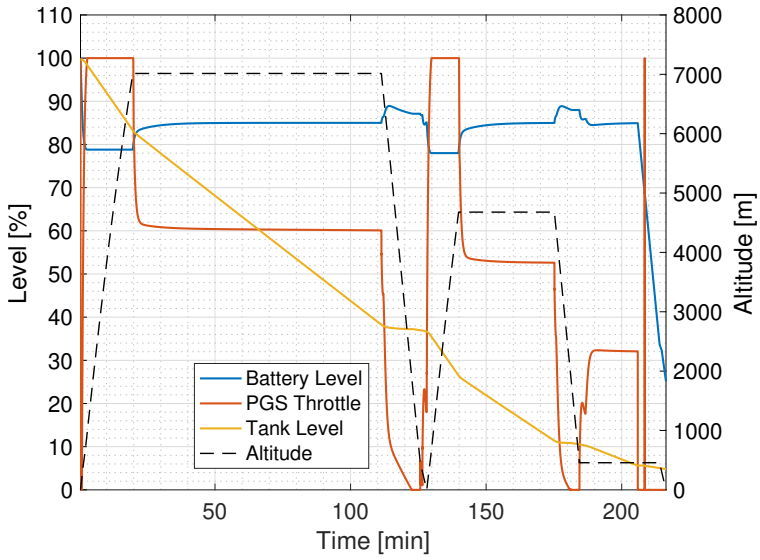

Figure B.11: *Time histories of battery state of charge (blue), PGS throttle (red), fuel quantity (yellow), and altitude (black) for the A70LH2-2035ii*

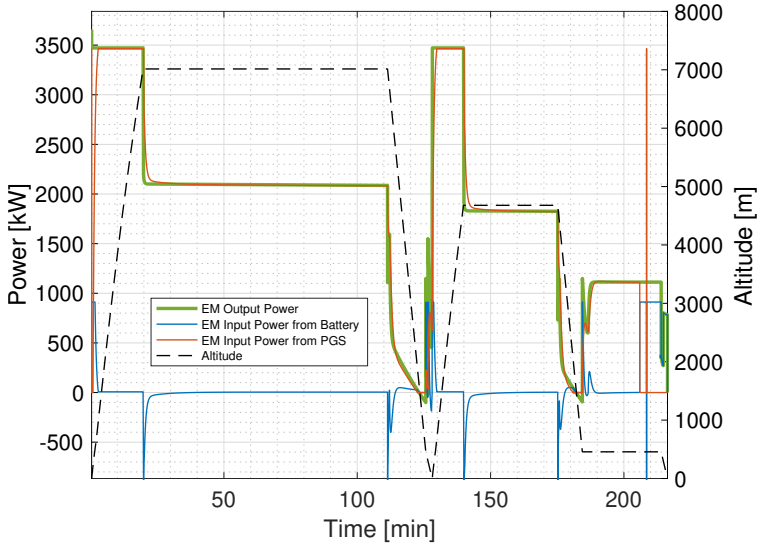

Figure B.12: *Time histories of shaft power (green), BP power (blue), PGS power (red), and altitude (black) for the A70LH2-2035ii*

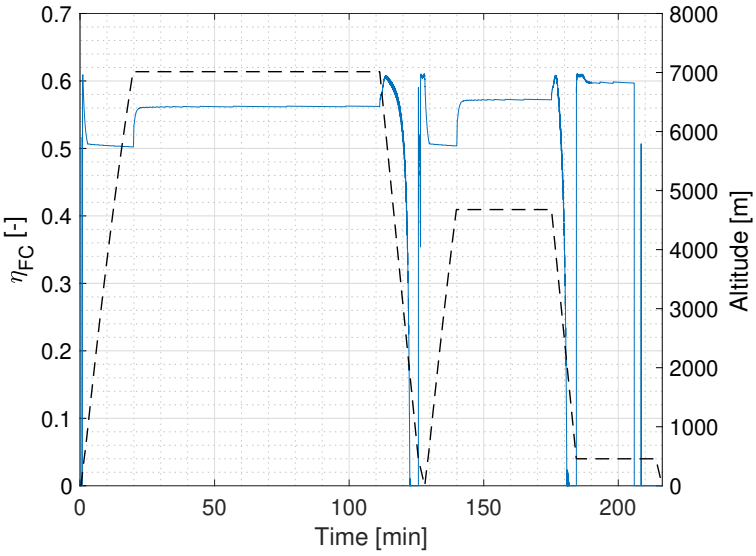

Figure B.13: *Time histories of the fuel cell efficiency(blue) and altitude (black) for the A70LH2-2035ii.*

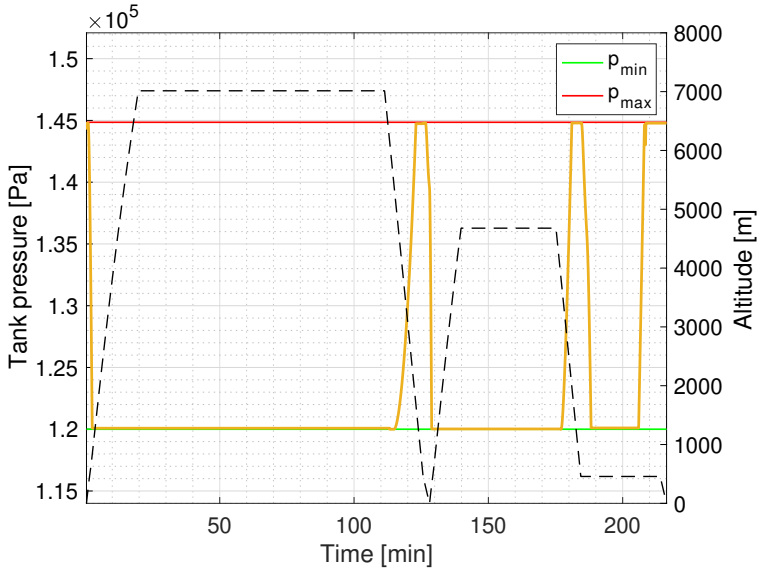

Figure B.14: *Time history of the LH2 tank internal pressure for the A70LH2-2035ii.*

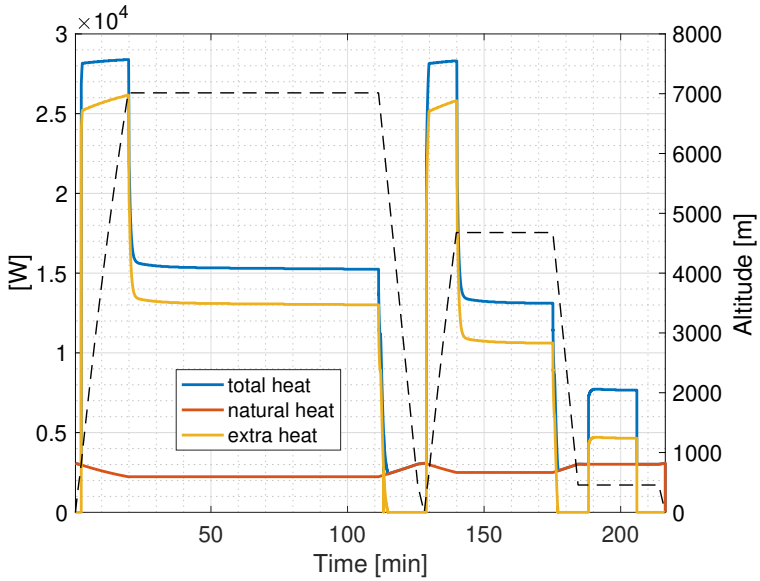

Figure B.15: *Time history of the LH2 tank heat flow for the A70LH2-2035ii.*

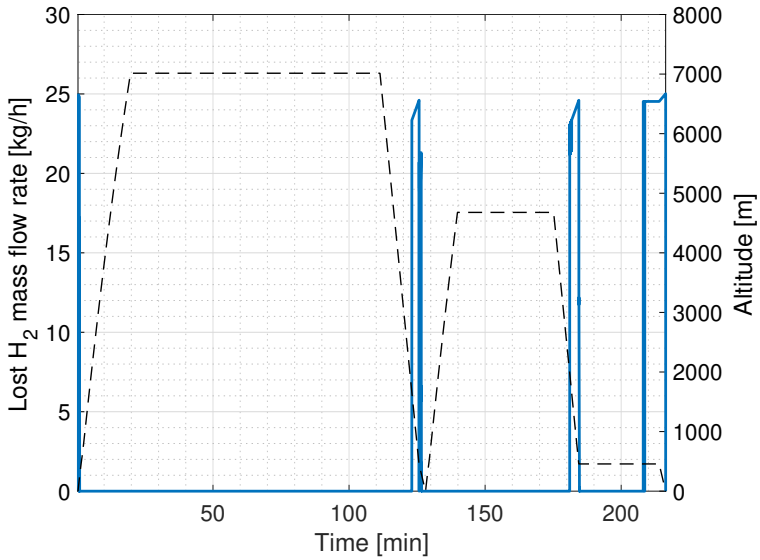

Figure B.16: *Time history of the LH2 tank boil-off losses for the A70LH2-2035ii.*

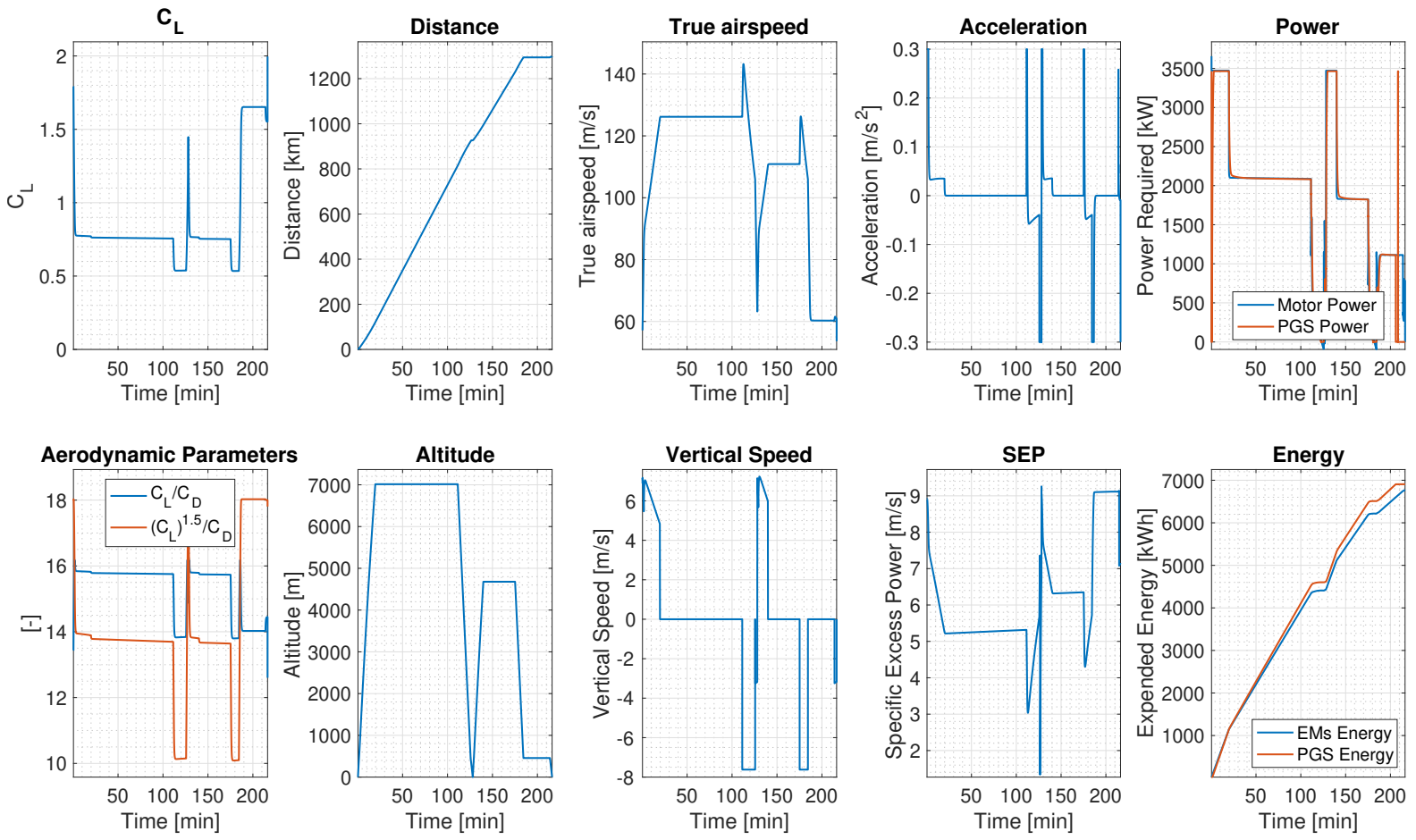

Figure B.17: *Time histories of the sizing mission for the A70LH2-2035ii.*

APPENDIX C

ADDITIONAL MINILINER SOLUTIONS

This Appendix contains the full set of plots for solutions M19THE, M19GH2 and M19LH2 introduced in Chapter 10.

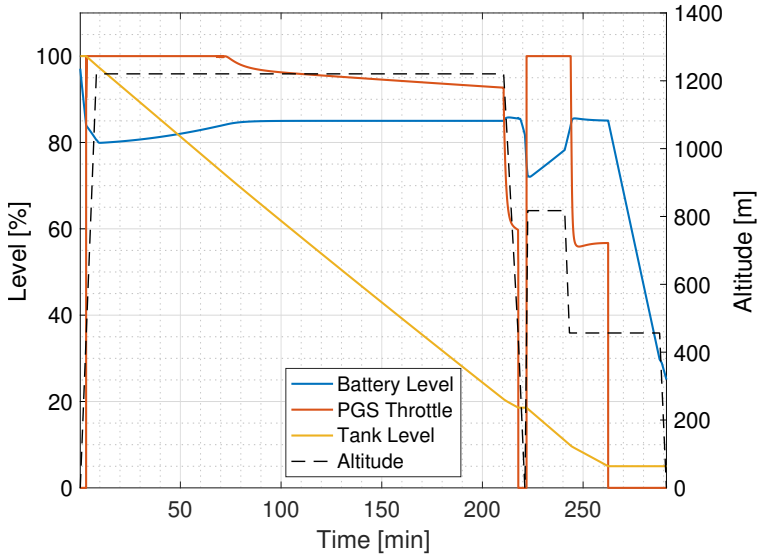

Figure C.1: *Time histories of battery state of charge (blue), PGS throttle (red), fuel quantity (yellow), and altitude (black) for the M19THE.*

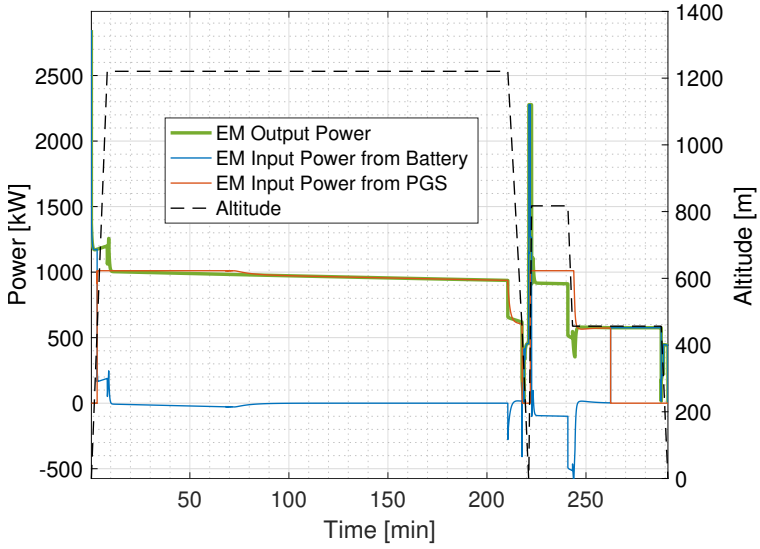

Figure C.2: *Time histories of shaft power (green), BP power (blue), PGS power (red), and altitude (black) for the M19THE.*

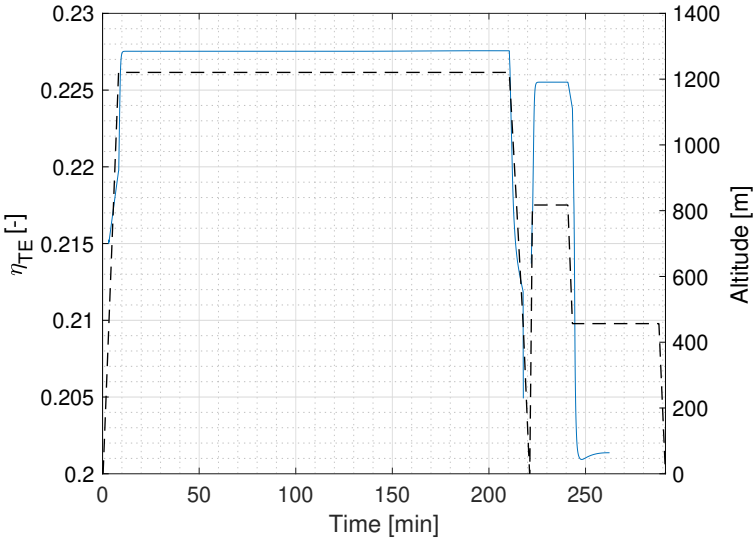

Figure C.3: *Time histories of the thermal engine efficiency(blue) and altitude (black) for the M19THE.*

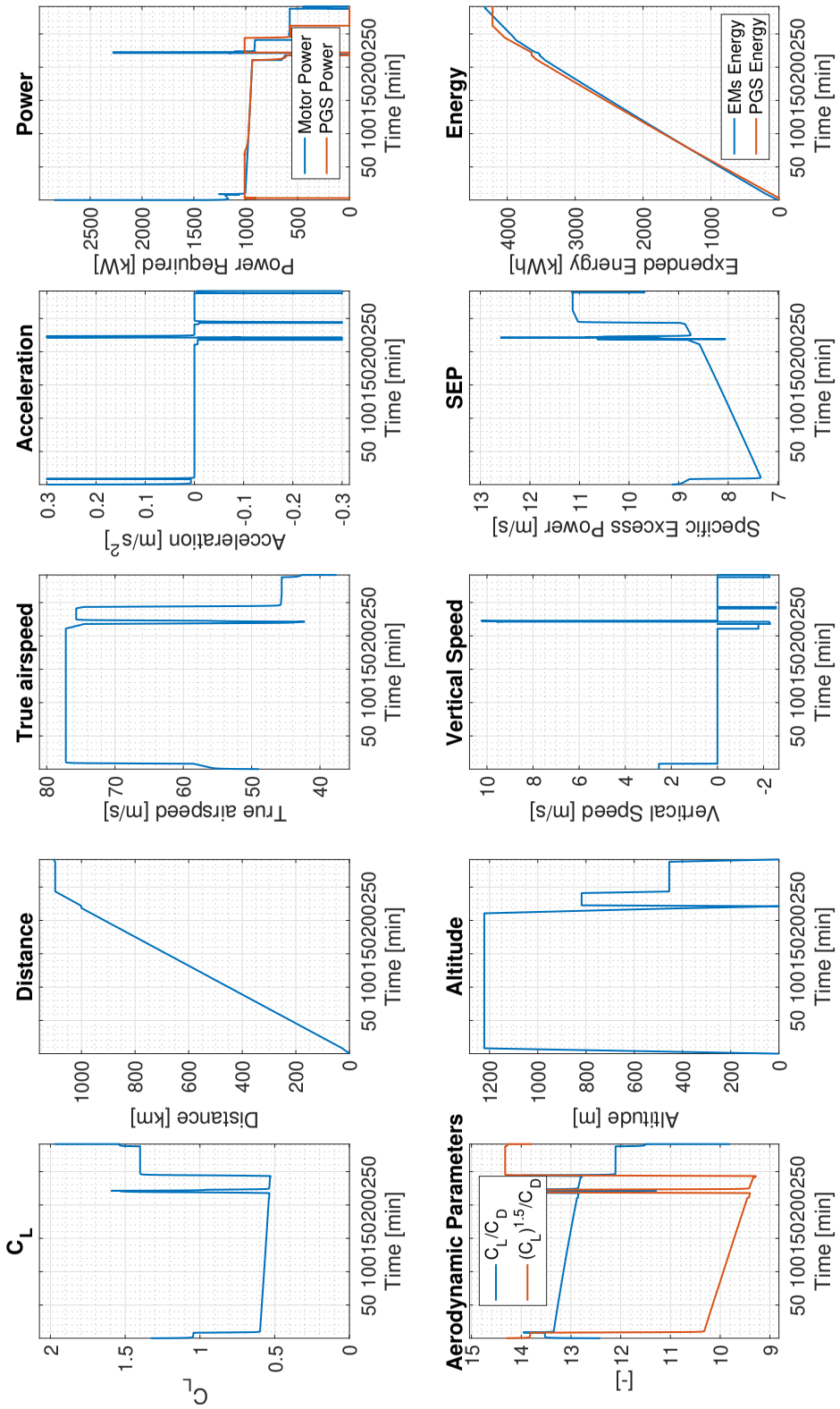

Figure C.4: *Time histories of the sizing mission for the M19THE.*

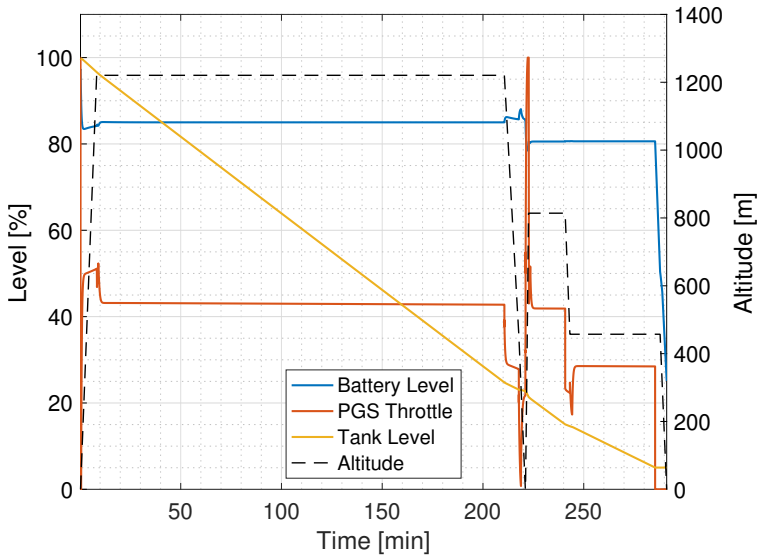

Figure C.5: *Time histories of battery state of charge (blue), PGS throttle (red), fuel quantity (yellow), and altitude (black) for the M19GH2.*

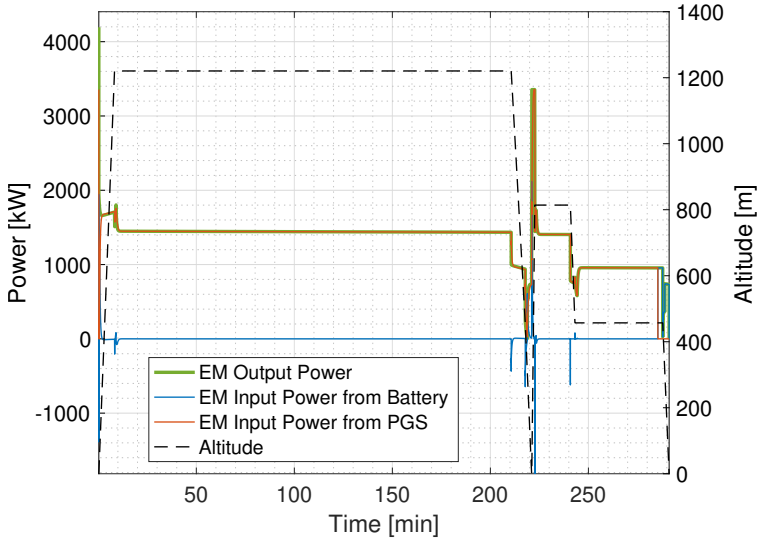

Figure C.6: *Time histories of shaft power (green), BP power (blue), PGS power (red), and altitude (black) for the M19GH2.*

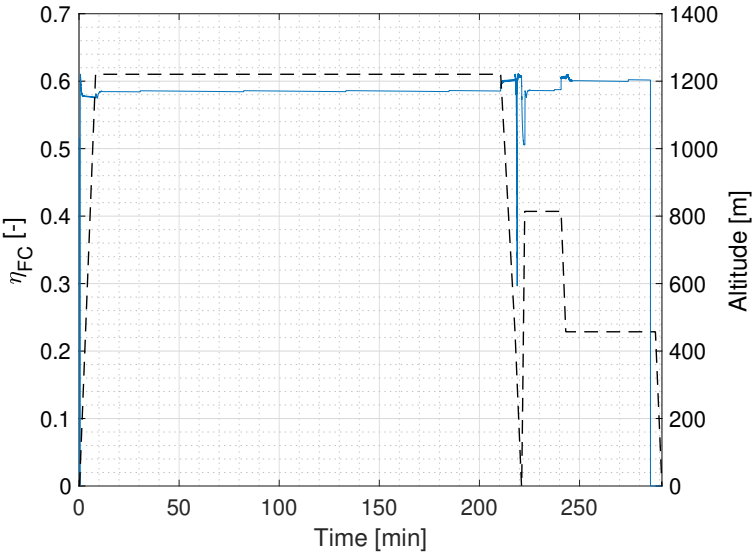

Figure C.7: *Time histories of the fuel cell efficiency(blue) and altitude (black) for the M19GH2.*

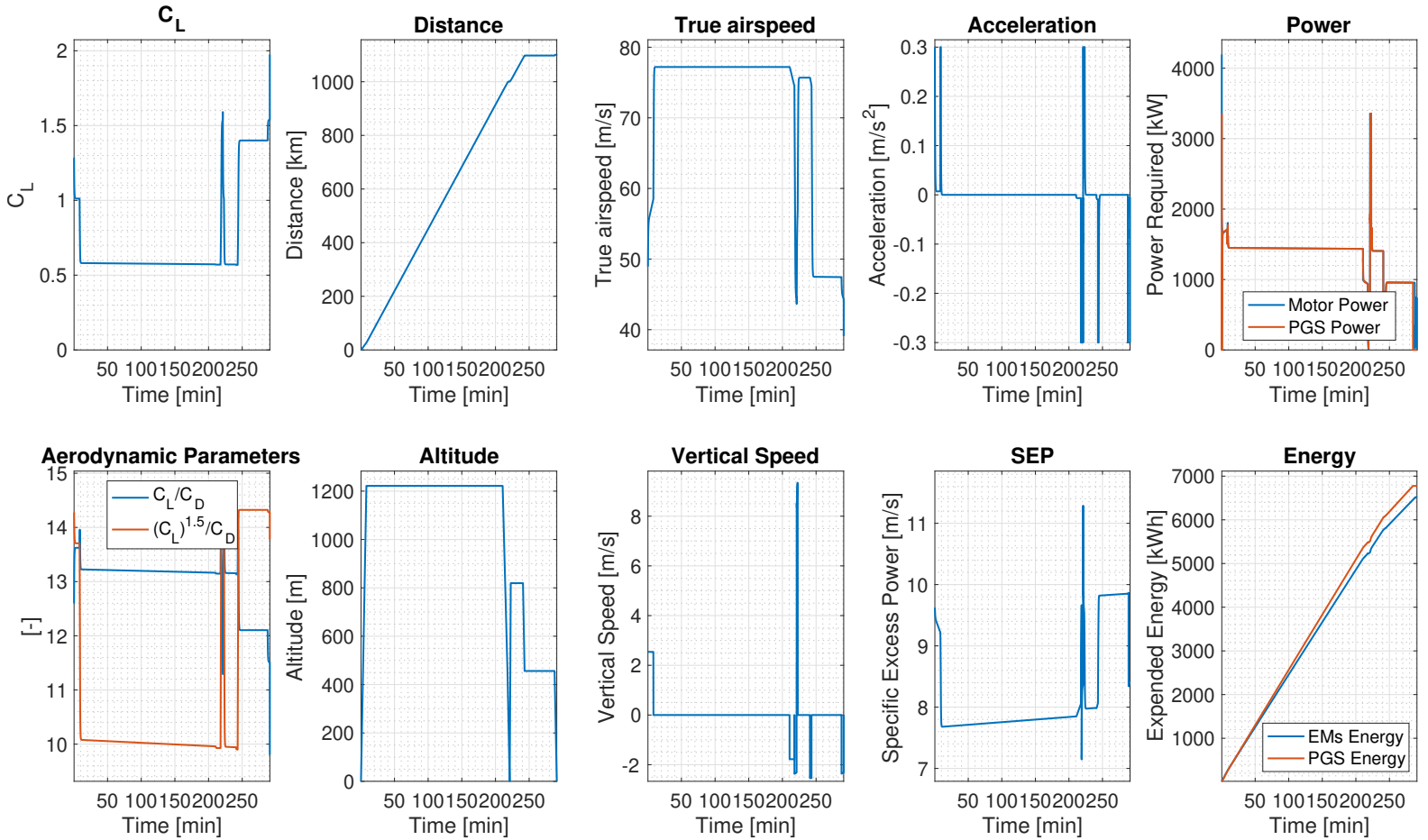

Figure C.8: *Time histories of the sizing mission for the M19GH2.*

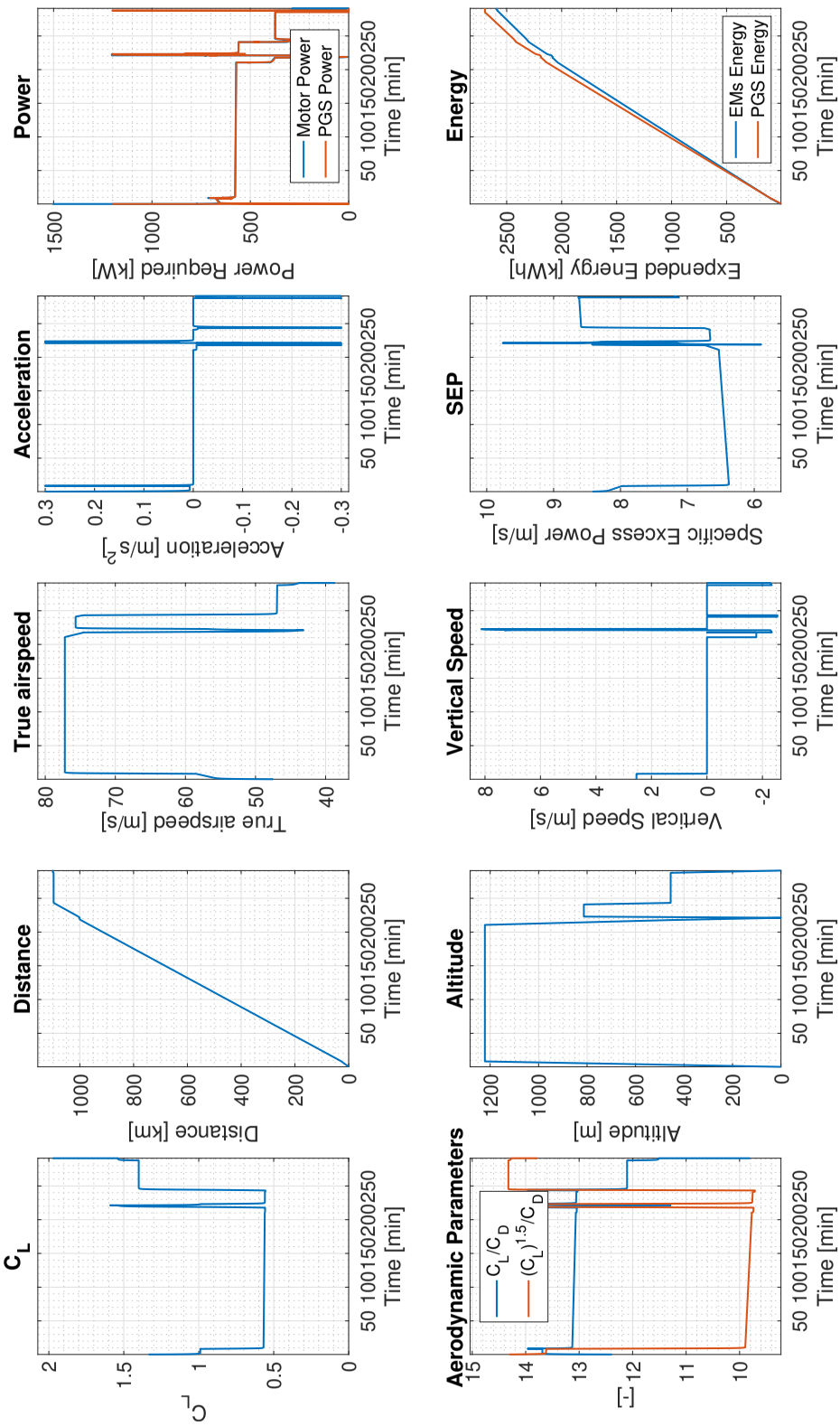

Figure C.9: *Time histories of the sizing mission for the M19LH2.*

BIBLIOGRAPHY

[1] M. Elkerbout et al. «The European Green Deal after Corona: Implications for EU climate policy». In: *CEPS Policy Insights* 2020–06 (2020) (cit. on p. XXXI).

[2] *EU nations aim high with plan to tax air travel*. URL: https://www.reuters.com/article/us-climate-change-eu-airlines/eu-nations-aim-high-with-plan-to-tax-air-travel-idUSKCN1TL1I7 (cit. on p. XXXI).

[3] B. J. Brelje and J. R. Martins. «Electric, hybrid, and turboelectric fixed-wing aircraft: A review of concepts, models, and design approaches». In: *Progress in Aerospace Sciences* (2018) (cit. on p. XXXIII).

[4] A. R. Gnadt, R. L. Speth, J. S. Sabnis, and S. R. Barrett. «Technical and environmental assessment of all-electric 180-passenger commercial aircraft». In: *Progress in Aerospace Sciences* 105 (Feb. 2019), pp. 1–30. DOI: 10.1016/j.paerosci.2018.11.002 (cit. on pp. XXXIII, 17, 19, 35, 36).

[5] S. Kallas et al. «Flightpath 2050 Europe's Vision for Aviation». In: *Report of the High Level Group on Aviation Research, European Commission, Brussels, Belgium, Report No. EUR* 98 (2011) (cit. on p. 3).

[6] ICAO. *Environmental report 2016*. Montreal, QC, 2016 (cit. on p. 4).

[7] IATA. *A global approach to reducing aviation emissions*. Montreal, QC, 2009 (cit. on p. 4).

[8] A. Drake. «NASA environmentally responsible aviation (ERA) N+ 2 advanced vehicle study». In: *50th AIAA Aerospace Sciences Meeting*. 2012 (cit. on p. 4).

[9] C. S. Dorbian, P. J. Wolfe, and I. A. Waitz. «Estimating the climate and air quality benefits of aviation fuel and emissions reductions». In: *Atmospheric Environment* 45.16 (May 1, 2011), pp. 2750–2759. DOI: 10.1016/j.atmosenv.2011.02.025 (cit. on p. 5).

[10] B. J. Brelje and J. R. Martins. «Electric, hybrid, and turboelectric fixed-wing aircraft: A review of concepts, models, and design approaches». In: *Progress in Aerospace Sciences* 104 (Jan. 2019), pp. 1–19. DOI: 10.1016/j.paerosci.2018.06.004 (cit. on pp. 5–7, 29, 30).

[11] C. Pornet and A. T. Isikveren. «Conceptual design of hybrid-electric transport aircraft». In: *Progress in Aerospace Sciences* 79 (Nov. 1, 2015), pp. 114–135. DOI: 10.1016/j.paerosci.2015.09.002 (cit. on p. 7).

[12] J. Ribeiro et al. «Environmental assessment of hybrid-electric propulsion in conceptual aircraft design». In: *Journal of Cleaner Production* 247 (Feb. 2020), p. 119477. DOI: 10.1016/j.jclepro.2019.119477 (cit. on pp. 7, 17, 19, 21).

[13] B. Cox, W. Jemiolo, and C. Mutel. «Life cycle assessment of air transportation and the Swiss commercial air transport fleet». In: *Transportation Research Part D: Transport and Environment* 58 (Jan. 2018), pp. 1–13. DOI: 10.1016/j.trd.2017.10.017 (cit. on p. 7).

[14] F. C.H. J. Undertaking. *Hydrogen-Powered Aviation: A fact-based study of hydrogen technology, economics, and climate impact by 2050*. Brussels, Belgium, 2020 (cit. on p. 10).

[15] A. Friedlander, R. Zubrin, and T. L. Hardy. *Benefits of slush hydrogen for space missions*. Tech. rep. National Aeronautics and Space Administration, 1991 (cit. on p. 11).

[16] L. Trainelli and I. Perkon. «A Milestone-Setting Project in Hybrid-Electric Aircraft Technology Development». In: *More Electric Aircraft Conference (MEA 2019)*. Toulouse, France, 2019 (cit. on pp. 11, 89).

[17] D. Erzen, F. Oliviero, and L. Trainelli. «Conceptual Design of a Near-Zero Emission and Cost-Efficient Regional Air Mobility Solution». In: *10th EASN International Conference*. September 2–4,2020 (cit. on p. 14).

[18] A. Rolando, F. Salucci, L. Trainelli, C. E. D. Riboldi, and Y. M. Khan. «On the Design of an Electric-Powered Micro-Feeder Aircraft». In: *1st Aerospace Europe Conference (AEC 2020)*. Bordeaux, France, February 25–28, 2020, pp. 1–11 (cit. on p. 14).

[19] C. E. D. Riboldi, L. Trainelli, and F. Biondani. «A Sizing Procedure for Structural Batteries in Hybrid-Electric Aircraft». In: Advanced Aircraft Efficiency in a Global Air Transport System Conference (AEGATS 2018). Accepted: 2018-11-16T12:05:29Z. 2018, pp. 1–8 (cit. on p. 15).

[20] A. Bernasconi et al. «Aircraft with electric batteries, in particular a hybrid aircraft». U.S. pat. 20190263498A1. P. di Milano. Library Catalog: Google Patents. Aug. 29, 2019 (cit. on p. 15).

[21] C. E. D. Riboldi, L. Trainelli, and F. Biondani. «Structural Batteries in Aviation: A Preliminary Sizing Methodology». EN. In: *Journal of Aerospace Engineering* 33.4 (July 2020). Publisher: American Society of Civil Engineers, p. 04020031. DOI: 10.1061/(ASCE)AS.1943-5525.0001144 (cit. on p. 15).

[22] A. N. Varyukhin, V. Zakharchenko, A. Vlasov, M. V. Gordin, and M. Ovdienko. «Roadmap for the Technological Development of Hybrid Electric and Full-Electric Propulsion Systems of Aircrafts». In: *2019 International Conference on Electrotechnical Complexes and Systems (ICOECS)*. 2019 International Conference on Electrotechnical Complexes and Systems (ICOECS). Ufa, Russia: IEEE, Oct. 2019, pp. 1–7. DOI: 10.1109/ICOECS46375.2019.8949910 (cit. on p. 16).

[23] X. Lü, P. Wang, L. Meng, and C. Chen. «Energy optimization of logistics transport vehicle driven by fuel cell hybrid power system». In: *Energy Conversion and Management* 199 (Nov. 2019), p. 111887. DOI: 10.1016/j.enconman.2019.111887 (cit. on p. 16).

[24] C. Depcik et al. «Electrifying Long-Haul Freight-Part II: Assessment of the Battery Capacity». In: *SAE International Journal of Commercial Vehicles* 12.2 (Jan. 25, 2019), pp. 02–12–02–0007. DOI: 10.4271/02-12-02-0007 (cit. on p. 16).

[25] F. Schlachter. «No Moore's Law for batteries». In: *Proceedings of the National Academy of Sciences* 110.14 (Apr. 2, 2013). Publisher: National Academy of Sciences Section: Opinion, pp. 5273–5273. DOI: 10.1073/pnas.1302988110 (cit. on p. 16).

[26] J. Rohacs and D. Rohacs. «Energy coefficients for comparison of aircraft supported by different propulsion systems». In: *Energy* 191 (Jan. 2020), p. 116391. DOI: 10.1016/j.energy.2019.116391 (cit. on pp. 16, 17).

[27] W.-J. Kwak et al. «Lithium–Oxygen Batteries and Related Systems: Potential, Status, and Future». In: *Chemical Reviews* (Mar. 5, 2020), acs.chemrev.9b00609. DOI: 10.1021/acs.chemrev.9b00609 (cit. on pp. 16, 20).

[28] N. Nitta, F. Wu, J. T. Lee, and G. Yushin. «Li-ion battery materials: present and future». In: *Materials Today* 18.5 (June 1, 2015), pp. 252–264. DOI: 10.1016/j.mattod.2014.10.040 (cit. on pp. 16, 21).

[29] G. E. Blomgren. «The Development and Future of Lithium Ion Batteries». In: *Journal of The Electrochemical Society* 164.1 (Dec. 1, 2016). Publisher: IOP Publishing, A5019. DOI: 10.1149/2.0251701jes (cit. on p. 16).

[30] B. Khandelwal, A. Karakurt, P. R. Sekaran, V. Sethi, and R. Singh. «Hydrogen powered aircraft : The future of air transport». In: *Progress in Aerospace Sciences* 60 (July 1, 2013), pp. 45–59. DOI: 10.1016/j.paerosci.2012.12.002 (cit. on p. 16).

[31] *Basic to Advanced Battery Information from Battery University*. URL: https://batteryuniversity.com/ (visited on 11/12/2020) (cit. on p. 17).

[32] R. Korthauer, ed. *Lithium-Ion Batteries: Basics and Applications*. en. Berlin, Heidelberg: Springer Berlin Heidelberg, 2018. DOI: 10.1007/978-3-662-53071-9 (cit. on p. 17).

[33] G. Zubi, R. Dufo-López, M. Carvalho, and G. Pasaoglu. «The lithium-ion battery: State of the art and future perspectives». In: *Renewable and Sustainable Energy Reviews* 89 (June 1, 2018), pp. 292–308. DOI: 10.1016/j.rser.2018.03.002 (cit. on p. 17).

[34] J. F. Peters, M. Baumann, B. Zimmermann, J. Braun, and M. Weil. «The environmental impact of Li-Ion batteries and the role of key parameters – A review». In: *Renewable and Sustainable Energy Reviews* 67 (Jan. 2017), pp. 491–506. DOI: 10.1016/j.rser.2016.08.039 (cit. on p. 17).

[35] *A Behind the Scenes Take on Lithium-ion Battery Prices*. BloombergNEF. Library Catalog: about.bnef.com Section: Report. Mar. 5, 2019. URL: https://about.bnef.com/blog/behind-scenes-take-lithium-ion-battery-prices/ (visited on 04/01/2020) (cit. on pp. 18, 149).

[36] J. E. Harlow et al. «A Wide Range of Testing Results on an Excellent Lithium-Ion Cell Chemistry to be used as Benchmarks for New Battery Technologies». In: *Journal of The Electrochemical Society* 166.13 (Sept. 6, 2019). Publisher: IOP Publishing, A3031. DOI: 10.1149/2.0981913jes (cit. on pp. 17, 19).

[37] S. Chung and A. Manthiram. «Current Status and Future Prospects of Metal–Sulfur Batteries». In: *Advanced Materials* 31.27 (July 2019), p. 1901125. DOI: 10.1002/adma.201901125 (cit. on pp. 19–21).

[38] L. Huang et al. «Electrode Design for Lithium–Sulfur Batteries: Problems and Solutions». In: *Advanced Functional Materials* (Mar. 12, 2020), p. 1910375. DOI: 10.1002/adfm.201910375 (cit. on p. 19).

[39] S. Urbonaite, T. Poux, and P. Novák. «Progress Towards Commercially Viable Li–S Battery Cells». In: *Advanced Energy Materials* 5.16 (2015). _eprint:

https://onlinelibrary.wiley.com/doi/pdf/10.1002/aenm.201500118, p. 1500118. DOI: 10.1002/aenm.201500118 (cit. on p. 19).

[40] *Licerion® high energy density, lithium-metal rechargeable battery*. Library Catalog: sionpower.com. URL: https://sionpower.com/ (visited on 04/01/2020) (cit. on p. 19).

[41] D. Lerwill. *OXIS Energy is close to achieving 500Wh/kg and is targeting 600Wh/kg with Solid State Lithium Sulfur technology*. Oxis Energy. Library Catalog: oxisenergy.com Section: Press Releases. Jan. 22, 2020. URL: https://oxisenergy.com/https-oxisenergy-com-wp-content-uploads-2020-01-500-and-600-whkg-pressor-pdf/ (visited on 04/01/2020) (cit. on p. 19).

[42] *Home*. Innolith Science and Technology GmbH. Library Catalog: innolith.com. URL: https://innolith.com/ (visited on 04/01/2020) (cit. on p. 19).

[43] R. a. M. ltd. *Global Lithium-Sulfur Battery Market 2018-2022 - Research and Markets*. Library Catalog: www.researchandmarkets.com. URL: https://www.researchandmarkets.com/reports/4535214/global-lithium-sulfur-battery-market-2018-2022 (visited on 04/01/2020) (cit. on p. 19).

[44] K. G. Gallagher et al. «Quantifying the promise of lithium–air batteries for electric vehicles». In: *Energy & Environmental Science* 7.5 (Apr. 17, 2014). Publisher: The Royal Society of Chemistry, pp. 1555–1563. DOI: 10.1039/C3EE43870H (cit. on pp. 20, 21).

[45] H. C. Lee et al. «High-Energy-Density Li-O2 Battery at Cell Scale with Folded Cell Structure». In: *Joule* 3.2 (Feb. 20, 2019), pp. 542–556. DOI: 10.1016/j.joule.2018.11.016 (cit. on pp. 21, 22).

[46] M. Huang, H. Nie, and M. Zhang. «Analysis of ground handling characteristic of aircraft with electric taxi system». In: *Proceedings of the Institution of Mechanical Engineers, Part D: Journal of Automobile Engineering* 233.6 (May 2019), pp. 1546–1561. DOI: 10.1177/0954407018764163 (cit. on p. 21).

[47] A. Misra. «Energy Storage for Electrified Aircraft: The Need for Better Batteries, Fuel Cells, and Supercapacitors». In: *IEEE Electrification Magazine* 6.3 (Sept. 2018), pp. 54–61. DOI: 10.1109/MELE.2018.2849922 (cit. on pp. 21, 23–25).

[48] X. Pu et al. «Recent Progress in Rechargeable Sodium-Ion Batteries: toward High-Power Applications». In: *Small* 15.32 (2019), p. 1805427. DOI: 10.1002/smll.201805427 (cit. on p. 21).

[49] B. B. Beenarani and C. P. Sugumaran. «Postulates of Supercapacitor and Performance Assessment Parameters: A Technical Overview». In: *Materials Today: Proceedings*. International Symposium on Functional Materials (ISFM-2018): Energy and Biomedical Applications 21 (Jan. 1, 2020), pp. 1911–1918. DOI: 10.1016/j.matpr.2020.01.275 (cit. on p. 23).

[50] P.-P. Sun et al. «Cu powder decorated 3D Mn-MOF with excellent electrochemical properties for supercapacitors». In: *Inorganica Chimica Acta* (2020). Publisher: Elsevier, p. 119629 (cit. on p. 23).

[51] B. Fan et al. «High-performance potassium ion capacitors enabled by hierarchical porous, large interlayer spacing, active site rich-nitrogen, sulfur Co-doped carbon». In: *Carbon* (2020). Publisher: Elsevier (cit. on p. 23).

[52] *Li-ion Capacitors - Yunasko is the developer and licensor of high power ultracapacitors*. URL: https://yunasko.com/en/products/lithium-ion-capacitors (visited on 04/01/2020) (cit. on p. 23).

[53] *Superdielectrics | Home*. URL: https://www.superdielectrics.com/ (visited on 04/01/2020) (cit. on p. 23).

[54] *Rolls-Royce and Superdielectrics explore supercapacitor technology*. Last Modified: 2018-05-22T16:49:20-04:00 Library Catalog: www.sae.org. URL: https://www.sae.org/news/2018/05/rolls-royce-and-superdielectrics-explore-supercapacitor-technology (visited on 04/01/2020) (cit. on p. 23).

[55] R. P. O'Hayre, S.-W. Cha, W. G. Colella, and F. B. Prinz. *Fuel cell fundamentals*. Third edition. Hoboken, New Jersey: John Wiley & Sons Inc, 2016. 1 p. (cit. on p. 24).

[56] S. E. Hosseini and B. Butler. «An overview of development and challenges in hydrogen powered vehicles». In: *International Journal of Green Energy* 17.1 (Jan. 2, 2020), pp. 13–37. DOI: 10.1080/15435075.2019.1685999 (cit. on pp. 24, 26, 29).

[57] J. A. Stockford, C. Lawson, and Z. Liu. «Benefit and performance impact analysis of using hydrogen fuel cell powered e-taxi system on A320 class airliner». In: *The Aeronautical Journal* 123.1261 (Mar. 2019), pp. 378–397. DOI: 10.1017/aer.2018.156 (cit. on p. 24).

[58] J. Wang, H. Wang, and Y. Fan. «Techno-Economic Challenges of Fuel Cell Commercialization». In: *Engineering* 4.3 (June 1, 2018), pp. 352–360. DOI: 10.1016/j.eng.2018.05.007 (cit. on p. 24).

[59] J. Büsselmann et al. «Analysis of HT-PEM MEAs' Long-Term Stabilities». In: *Energies* 13.3 (Jan. 24, 2020), p. 567. DOI: 10.3390/en13030567 (cit. on p. 24).

[60] T. Kadyk, C. Winnefeld, R. Hanke-Rauschenbach, and U. Krewer. «Analysis and Design of Fuel Cell Systems for Aviation». In: *Energies* 11.2 (Feb. 6, 2018), p. 375. DOI: 10.3390/en11020375 (cit. on pp. 24, 25).

[61] I. Staffell et al. «The role of hydrogen and fuel cells in the global energy system». In: *Energy & Environmental Science* 12.2 (Feb. 13, 2019). Publisher: The Royal Society of Chemistry, pp. 463–491. DOI: 10.1039/C8EE01157E (cit. on p. 24).

[62] A. Dicks and D. A. J. Rand. *Fuel cell systems explained*. Third edition. Hoboken, NJ, USA: Wiley, 2018. 1 p. (cit. on pp. 24, 25).

[63] *DOE Technical Targets for Fuel Cell Systems and Stacks for Transportation Applications*. Energy.gov. Library Catalog: www.energy.gov. URL: https://www.energy.gov/eere/fuelcells/doe-technical-targets-fuel-cell-systems-and-stacks-transportation-applications (visited on 04/01/2020) (cit. on pp. 25, 250).

[64] J. Andersson and S. Grönkvist. «Large-scale storage of hydrogen». In: *International Journal of Hydrogen Energy* 44.23 (May 3, 2019), pp. 11901–11919. DOI: 10.1016/j.ijhydene.2019.03.063 (cit. on p. 26).

[65] M. Hirscher et al. «Materials for hydrogen-based energy storage – past, recent progress and future outlook». In: *Journal of Alloys and Compounds* 827 (June 25, 2020), p. 153548. DOI: 10.1016/j.jallcom.2019.153548 (cit. on pp. 26, 28).

[66] SAE EUROCAE Fuel Cell Task Group. *Considerations for Hydrogen Fuel Cells in Airborne Applications*. SAE International. DOI: 10.4271/AIR7765 (cit. on pp. 26, 28).

[67] SAE EUROCAE Fuel Cell Task Group. *EUROCAE/SAE WG80/AE-7AFC Hydrogen Fuel Cells Aircraft Fuel Cell Safety Guidelines*. SAE International. DOI: 10.4271/AIR6464 (cit. on p. 26).

[68] E. Rivard, M. Trudeau, and K. Zaghib. «Hydrogen Storage for Mobility: A Review». In: *Materials* 12.12 (June 19, 2019), p. 1973. DOI: 10.3390/ma12121973 (cit. on pp. 26, 28).

[69] H. Barthelemy, M. Weber, and F. Barbier. «Hydrogen storage: Recent improvements and industrial perspectives». In: *International Journal of Hydrogen Energy* 42.11 (Mar. 2017), pp. 7254–7262. DOI: 10.1016/j.ijhydene.2016.03.178 (cit. on pp. 26, 28).

[70] D. Wang et al. «Development of regulations, codes and standards on composite tanks for on-board gaseous hydrogen storage». In: *International Journal of Hydrogen Energy* 44.40 (Aug. 2019), pp. 22643–22653. DOI: 10.1016/j.ijhydene.2019.04.133 (cit. on p. 26).

[71] *Gaseous hydrogen. Land vehicle fuel containers.* Standard. Geneva, CH: International Organization for Standardization, Oct. 2018 (cit. on p. 27).

[72] M. Zhang, H. Lv, H. Kang, W. Zhou, and C. Zhang. «A literature review of failure prediction and analysis methods for composite high-pressure hydrogen storage tanks». In: *International Journal of Hydrogen Energy* 44.47 (Oct. 2019), pp. 25777–25799. DOI: 10.1016/j.ijhydene.2019.08.001 (cit. on p. 28).

[73] E. Yamada and T. Mashiba. «Development of Technical Regulations for Fuel Cell Motorcycles in Japan-Hydrogen Safety». In: *World Electric Vehicle Journal* 10.3 (July 9, 2019), p. 48. DOI: 10.3390/wevj10030048 (cit. on p. 28).

[74] D. Halm et al. «Composite pressure vessels for hydrogen storage in fire conditions: Fire tests and burst simulation». In: *International Journal of Hydrogen Energy* 42.31 (Aug. 2017), pp. 20056–20070. DOI: 10.1016/j.ijhydene.2017.06.088 (cit. on p. 28).

[75] B. D. James, C. Houchins, J. M. Huya-Kouadio, and D. A. DeSantis. *Final Report: Hydrogen Storage System Cost Analysis.* DOE-SA–0005253, 1343975. Sept. 30, 2016, DOE–SA–0005253, 1343975. DOI: 10.2172/1343975 (cit. on p. 28).

[76] R. Moradi and K. M. Groth. «Hydrogen storage and delivery: Review of the state of the art technologies and risk and reliability analysis». In: *International Journal of Hydrogen Energy* 44.23 (May 3, 2019), pp. 12254–12269. DOI: 10.1016/j.ijhydene.2019.03.041 (cit. on p. 28).

[77] M. Genovese, D. Blekhman, M. Dray, and P. Fragiacomo. «Hydrogen losses in fueling station operation». In: *Journal of Cleaner Production* 248 (Mar. 1, 2020), p. 119266. DOI: 10.1016/j.jclepro.2019.119266 (cit. on p. 28).

[78] J. L. Sloop. *Liquid hydrogen as a propulsion fuel, 1945-1959.* Vol. 4404. Scientific, Technical Information Office, National Aeronautics, and Space ..., 1978 (cit. on p. 28).

[79] A. Silverstein and E. W. Hall. *Liquid hydrogen as a jet fuel for high-altitude aircraft.* Tech. rep. National Aeronautics and Space Administration Cleveland Oh Lewis Research Center, 1955 (cit. on p. 28).

[80] G. D. Brewer. *Hydrogen aircraft technology.* CRC press, 1991 (cit. on p. 28).

[81] D Kaminski-Morrow. «Tupolev's cryogenic Tu-155-20 years on». In: *Flight International, Aerospace and Aviation News, Aviation Industry & Airline Statistics* 2008 (2008) (cit. on p. 28).

[82] R. Rocheleau, M. Virji, and K. Bethune. *Fuel Cell Stack Testing and Durability in Support of Ion Tiger UAV.* Tech. rep. Geneva, CH: HAWAII NATURAL ENERGY INSTITUTE, 2010 (cit. on p. 28).

[83] A. Gomez and H. Smith. «Liquid hydrogen fuel tanks for commercial aviation: Structural sizing and stress analysis». In: *Aerospace Science and Technology* 95 (Dec. 2019), p. 105438. DOI: 10.1016/j.ast.2019.105438 (cit. on pp. 28, 29).
[84] D. Verstraete. «On the energy efficiency of hydrogen-fuelled transport aircraft». In: *International Journal of Hydrogen Energy* 40.23 (June 2015), pp. 7388–7394. DOI: 10.1016/j.ijhydene.2015.04.055 (cit. on p. 28).
[85] S. Sharifzadeh, D. Verstraete, and P. Hendrick. «Cryogenic hydrogen fuel tanks for large hypersonic cruise vehicles». In: *International Journal of Hydrogen Energy* 40.37 (Oct. 2015), pp. 12798–12810. DOI: 10.1016/j.ijhydene.2015.07.120 (cit. on p. 28).
[86] C. Winnefeld, T. Kadyk, B. Bensmann, U. Krewer, and R. Hanke-Rauschenbach. «Modelling and Designing Cryogenic Hydrogen Tanks for Future Aircraft Applications». In: *Energies* 11.1 (Jan. 3, 2018), p. 105. DOI: 10.3390/en11010105 (cit. on pp. 28, 45–47).
[87] S. M. Aceves et al. «High-density automotive hydrogen storage with cryogenic capable pressure vessels». In: *International Journal of Hydrogen Energy* 35.3 (Feb. 1, 2010), pp. 1219–1226. DOI: 10.1016/j.ijhydene.2009.11.069 (cit. on p. 29).
[88] J. Moreno-Blanco et al. «The storage performance of automotive cryo-compressed hydrogen vessels». In: *International Journal of Hydrogen Energy* 44.31 (June 21, 2019), pp. 16841–16851. DOI: 10.1016/j.ijhydene.2019.04.189 (cit. on p. 29).
[89] B. L. Salvi and K. A. Subramanian. «Sustainable development of road transportation sector using hydrogen energy system». In: *Renewable and Sustainable Energy Reviews* 51 (Nov. 1, 2015), pp. 1132–1155. DOI: 10.1016/j.rser.2015.07.030 (cit. on p. 29).
[90] R. H. B. Jansen. «Overview of NASA Electrified Aircraft Propulsion Research for Large Subsonic Transports». In: AIAA Propulsion and Energy 2017 Forum. Atlanta, GA, United States, July 10, 2017 (cit. on p. 30).
[91] T. Shinzato, S. Arakawa, H. Oyama, H. Saka, and T. Hayasaki. «Development of high-temperature superconducting motor for automobiles». In: *SEI Technical Review* 75 (2012), pp. 62–65 (cit. on p. 31).
[92] T. P. Dever et al. *Assessment of technologies for noncryogenic hybrid electric propulsion*. National Aeronautics and Space Administration, Glenn Research Center, 2015 (cit. on p. 31).
[93] E. National Academies of Sciences, Medicine, et al. *Commercial aircraft propulsion and energy systems research: reducing global carbon emissions*. National Academies Press, 2016 (cit. on p. 31).
[94] R. Schnell et al. «Assessment of a Turbo-Electric Aircraft Configuration with Aft-Propulsion Using Boundary Layer Ingestion». In: *Aerospace* 6.12 (Dec. 16, 2019), p. 134. DOI: 10.3390/aerospace6120134 (cit. on p. 31).
[95] K. S. Hariharan, P. Tagade, and S. Ramachandran. *Mathematical Modeling of Lithium Batteries: From Electrochemical Models to State Estimator Algorithms*. Springer, 2017 (cit. on p. 34).
[96] J. T. Warner. *The handbook of lithium-ion battery pack design: chemistry, components, types and terminology*. Elsevier, 2015 (cit. on p. 35).
[97] J. Larminie and J. Lowry. *Electric vehicle technology explained*. John Wiley & Sons, 2012 (cit. on pp. 36, 52).

[98] T. Christen and M. W. Carlen. «Theory of Ragone plots». In: *Journal of power sources* 91.2 (2000), pp. 210–216 (cit. on p. 36).

[99] G. Cinar, D. N. Mavris, M. Emeneth, A. Schneegans, and Y. Fefermann. «Development of parametric power generation and distribution subsystem models at the conceptual aircraft design stage». In: *55th AIAA Aerospace Sciences Meeting*. 2017, p. 1182 (cit. on p. 36).

[100] P. C. Vratny, C. Gologan, C. Pornet, A. T. Isikveren, and M. Hornung. «Battery pack modeling methods for universally-electric aircraft». In: *4th CEAS Air & Space Conference*. Linköping University Electronic Press Linköping, Sweden. 2013, pp. 525–535 (cit. on p. 36).

[101] C. Spiegel. *PEM fuel cell modeling and simulation using MATLAB*. Elsevier, 2011 (cit. on pp. 37, 40).

[102] D. Verstraete, P. Hendrick, P. Pilidis, and K. Ramsden. «Hydrogen fuel tanks for subsonic transport aircraft». In: *International Journal of Hydrogen Energy* 35.20 (Oct. 2010), pp. 11085–11098. DOI: 10.1016/j.ijhydene.2010.06.060 (cit. on p. 45).

[103] C. G. L. Miguel. «Liquid Hydrogen Aircraft Propulsion». MA thesis. Politecnico di Milano, 2020 (cit. on p. 47).

[104] M. H. Sadraey. *Aircraft performance: analysis*. VDM Publishing, 2009 (cit. on pp. 48, 66).

[105] G. J. J. Ruijgrok. *Elements of Airplane Performance*. Delft University Press, 2009 (cit. on p. 48).

[106] A. L.C. R. 2268. *Horsepower Correction Factors and Operating Techniques for Engine Development and Calibration*. Tech. rep. Avco Lycoming Corporation, 1960 (cit. on p. 48).

[107] D. Raymer. *Aircraft design: a conceptual approach*. American Institute of Aeronautics and Astronautics, Inc., 2018 (cit. on pp. 48, 66, 78, 80, 81, 83, 85, 120, 253).

[108] R. A. McDonald. «Electric propulsion modeling for conceptual aircraft design». In: *52nd Aerospace Sciences Meeting*. 2014, p. 0536 (cit. on pp. 51, 52).

[109] A. Straubinger et al. «An overview of current research and developments in urban air mobility–Setting the scene for UAM introduction». In: *Journal of Air Transport Management* 87 (2020), p. 101852 (cit. on p. 53).

[110] P. Della Vecchia, D. Malgieri, F. Nicolosi, and A. De Marco. «Numerical analysis of propeller effects on wing aerodynamic: tip mounted and distributed propulsion». In: *Transportation research procedia* 29 (2018), pp. 106–115 (cit. on p. 53).

[111] M. D. Patterson, M. J. Daskilewicz, and B. German. «Simplified Aerodynamics Models to Predict the Effects of Upstream Propellers on Wing Lift». In: *53rd AIAA Aerospace Sciences Meeting*. DOI: 10.2514/6.2015-1673. eprint: https://arc.aiaa.org/doi/pdf/10.2514/6.2015-1673 (cit. on pp. 53, 55, 56, 58).

[112] K. A. Deere et al. «Computational Analysis of a Wing Designed for the X-57 Distributed Electric Propulsion Aircraft». In: *35th AIAA Applied Aerodynamics Conference*. 35th AIAA Applied Aerodynamics Conference. Denver, Colorado: American Institute of Aeronautics and Astronautics, June 5, 2017. DOI: 10.2514/6.2017-3923 (cit. on pp. 53, 70).

[113] R. A. Marretta, G. Davi, G. Lombardi, and A. Milazzo. «Hybrid numerical technique for evaluating wing aerodynamic loading with propeller interference». In: *Computers & fluids* 28.8 (1999), pp. 923–950 (cit. on p. 53).

[114] F. Orefice, P. Della Vecchia, D. Ciliberti, and F. Nicolosi. «Aircraft conceptual design including powertrain system architecture and distributed propulsion». In: *2019 AIAA/IEEE Electric Aircraft Technologies Symposium (EATS)*. IEEE. 2019, pp. 1–20 (cit. on p. 53).

[115] T. Sinnige, N. van Arnhem, T. C. Stokkermans, G. Eitelberg, and L. L. Veldhuis. «Wingtip-mounted propellers: Aerodynamic analysis of interaction effects and comparison with conventional layout». In: *Journal of Aircraft* 56.1 (2019), pp. 295–312 (cit. on p. 53).

[116] A. Matrone. «Performance-based preliminary sizing of aircraft with distributed propulsion». MA thesis. Politecnico di Milano, 2019 (cit. on pp. 55, 71).

[117] R. de Vries, M. Brown, and R. Vos. «Preliminary Sizing Method for Hybrid-Electric Distributed-Propulsion Aircraft». In: *Journal of Aircraft* 56.6 (Nov. 2019), pp. 2172–2188. DOI: 10.2514/1.C035388 (cit. on p. 55).

[118] R. d. Vries, M. Hoogreef, and R. Vos. «Preliminary Sizing of a Hybrid-Electric Passenger Aircraft Featuring Over-the-Wing Distributed-Propulsion». In: *AIAA Scitech 2019 Forum*. _eprint: https://arc.aiaa.org/doi/pdf/10.2514/6.2019-1811. American Institute of Aeronautics and Astronautics. DOI: 10.2514/6.2019-1811 (cit. on pp. 55, 56, 58).

[119] K. Biber. «Estimating propeller slipstream drag on airplane performance». In: *Journal of aircraft* 48.6 (2011), pp. 2172–2174 (cit. on p. 55).

[120] J. Roskam. *Methods for estimating drag polars of subsonic airplanes*. Roskam Aviation and Engineering Corporation, 1971 (cit. on p. 56).

[121] J. Roskam. *Airplane design*. DARcorporation, 1985 (cit. on pp. 66, 67, 71, 78, 85, 118).

[122] M. H. Sadraey. *Aircraft design: A systems engineering approach*. John Wiley & Sons, 2012 (cit. on pp. 66, 67, 69, 71, 78, 108, 235).

[123] S. Yoo and J. Duensing. «Computational Analysis of the External Aerodynamics of the Unpowered X-57 Mod-III Aircraft». In: *AIAA Aviation 2019 Forum*. 2019, p. 3698 (cit. on p. 70).

[124] S. L. Schnulo et al. «Development of a Multi-Phase Mission Planning Tool for NASA X-57 Maxwell». In: *Electric Aircraft Technology Symposium, AIAA*. 2018, pp. 1–14 (cit. on pp. 70, 99).

[125] N. K. Borer et al. «Comparison of Aero-Propulsive Performance Predictions for Distributed Propulsion Configurations». In: *55th AIAA Aerospace Sciences Meeting*. 55th AIAA Aerospace Sciences Meeting. Grapevine, Texas: American Institute of Aeronautics and Astronautics, Jan. 9, 2017. DOI: 10.2514/6.2017-0209 (cit. on p. 70).

[126] C. B. Hoover et al. «Whirl Flutter Stability and Its Influence on the Design of the Distributed Electric Propeller Aircraft X-57». In: *17th AIAA Aviation Technology, Integration, and Operations Conference*. 2017, p. 3785 (cit. on p. 70).

[127] S. Clarke, M. Redifer, K. Papathakis, A. Samuel, and T. Foster. «X-57 power and command system design». In: *2017 IEEE Transportation Electrification Conference and Expo (ITEC)*. IEEE. 2017, pp. 393–400 (cit. on p. 70).

[128] C. A. T. Srl. *P2006T–Aircraft Flight Manual* (cit. on p. 70).

[129] L. Trainelli, C. E. Riboldi, F. Salucci, and A. Rolando. «A General Preliminary Sizing Procedure for Pure-Electric and Hybrid-Electric Airplanes». In: *1st Aerospace Europe Conference (AEC 2020)*. Bordeaux, France, February 25–28, 2020, pp. 1–10 (cit. on p. 76).

[130] L. Trainelli, N. Rossi, F. Salucci, C. E. D. Riboldi, and A. Rolando. «Preliminary Sizing and Energy Management of Serial Hybrid-Electric Airplanes». In: *Italian Associations of Aeronautics and Astronautics (AIDAA) 25th International Conference*. Roma, Italy, September 9–12, 2019 (cit. on p. 76).

[131] L. Trainelli, D. Comincini, F. Salucci, A. Rolando, and C. E. D. Riboldi. «Sizing and Performance of Hydrogen-Driven Airplanes». In: *Italian Associations of Aeronautics and Astronautics (AIDAA) 25th International Conference*. Roma, Italy, September 9–12, 2019 (cit. on p. 76).

[132] N. Rossi, F. Salucci, C. E. D. Riboldi, A. Rolando, and L. Trainelli. «A General Approach to the Conceptual Design of All-Electric and Hybrid-Electric Aircraft». In: *Advanced Aircraft Efficiency in a Global Air Transport System Conference (AEGATS 2018)*. Toulouse, France, October 23–25, 2018 (cit. on p. 76).

[133] L. Trainelli, F. Salucci, N. Rossi, C. E. D. Riboldi, and A. Rolando. «Preliminary Sizing and Energy Management of Serial Hybrid-Electric Airplanes». In: *XXV Congresso Nazionale AIDAA*. Roma, Italy, September 9–12,2019 (cit. on pp. 78, 85, 86, 103).

[134] C. E. D. Riboldi and F. Gualdoni. «An Integrated Approach to the Preliminary Weight Sizing of Small Electric Aircraft». In: *Aerospace Science and Technology* 58 (2016), pp. 134–149 (cit. on p. 85).

[135] C. E. D. Riboldi, F. Gualdoni, and L. Trainelli. «Preliminary Weight Sizing of Light Pure-Electric and Hybrid-Electric Aircraft». In: *Transportation Research Procedia* 29 (2018), pp. 376–389 (cit. on p. 85).

[136] A. Dubois et al. «Design of an electric propulsion system for SCEPTOR's outboard nacelle». In: *16th AIAA Aviation Technology, Integration, and Operations Conference*. 2016, p. 3925 (cit. on p. 99).

[137] W. Phillips. «Lifting-line analysis for twisted wings and washout-optimized wings». In: *Journal of aircraft* 41.1 (2004), pp. 128–136 (cit. on p. 119).

[138] A. Estrada Briz and I. Raimo. «A framework for hybrid-electric aircraft preliminary sizing». MA thesis. Politecnico di Milano, 2020 (cit. on p. 120).

[139] Y. Fefermann et al. «Hybrid-Electric motive power systems for commuter transport applications». In: *30th Congress of the International Council of the Aeronautical Sciences, Daejeon, Korea*. 2016, pp. 25–30 (cit. on p. 123).

[140] L. Trainelli, C. E. Riboldi, A. Rolando, and F. Salucci. «Methodologies for the initial design studies of an innovative community-friendly miniliner». In: *IOP Conference Series: Materials Science and Engineering*. Vol. 1024. 1. IOP Publishing. 2021, p. 012109 (cit. on pp. 123, 187).

[141] F. Salucci et al. «Capturing the Demand for an Electric-Powered Short-Haul Air Transportation Network». In: *AIAA SciTech 2021 Forum*. January 11–15, 2021, p. 0869 (cit. on pp. 123, 187, 243).

[142] C. Y. Justin, A. P. Payan, S. I. Briceno, B. J. German, and D. N. Mavris. «Power optimized battery swap and recharge strategies for electric aircraft operations». In: *Transportation Research Part C: Emerging Technologies* 115 (2020), p. 102605. DOI: https://doi.org/10.1016/j.trc.2020.02.027 (cit. on pp. 123, 127).

[143] M. Schmidt, A. Paul, M. Cole, and K. O. Ploetner. «Challenges for ground operations arising from aircraft concepts using alternative energy». In: *Journal of Air Transport Management* 56 (2016), pp. 107–117 (cit. on p. 124).

[144] *Servizio Elettrico Nazionale, Servizio di Maggior Tutela*. 2018 (cit. on p. 124).

[145] *Aircraft – Connectors for ground electrical supplies – Part 2: Dimensions*. Standard. Geneva, CH: International Organization for Standardization, April, 1985 (cit. on p. 124).
[146] N Sujitha and S Krithiga. «RES based EV battery charging system: A review». In: *Renewable and Sustainable Energy Reviews* 75 (2017), pp. 978–988 (cit. on p. 124).
[147] Y. Zheng et al. «Electric vehicle battery charging/swap stations in distribution systems: comparison study and optimal planning». In: *IEEE Transactions on Power Systems* 29.1 (2014), pp. 221–229 (cit. on p. 124).
[148] J. W. Langelaan et al. «Green flight challenge: aircraft design and flight planning for extreme fuel efficiency». In: *Journal of Aircraft* 50.3 (2013), pp. 832–846 (cit. on p. 124).
[149] C. Friedrich and P. A. Robertson. «Hybrid-electric propulsion for aircraft». In: *Journal of Aircraft* 52.1 (2014), pp. 176–189 (cit. on p. 124).
[150] M. R. Sarker, H. Pandžić, and M. A. Ortega-Vazquez. «Optimal operation and services scheduling for an electric vehicle battery swapping station». In: *IEEE transactions on power systems* 30.2 (2015), pp. 901–910 (cit. on pp. 124, 126).
[151] V. Bobanac, H. Pandzic, and T. Capuder. «Survey on electric vehicles and battery swapping stations: Expectations of existing and future EV owners». In: *2018 IEEE International Energy Conference (ENERGYCON)*. IEEE. 2018 (cit. on p. 124).
[152] C. A. Correa-Florez, A. Gerossier, A. Michiorri, and G. Kariniotakis. «Stochastic operation of home energy management systems including battery cycling». In: *Applied Energy* 225 (2018), pp. 1205–1218 (cit. on p. 124).
[153] *Aero Club Milano, Bresso - Italy*. 2018 (cit. on pp. 125, 140).
[154] L. Trainelli, F. Salucci, C. E. Riboldi, A. Ronaldo, and F. Bigoni. «Optimal Sizing and Operation of Airport Infrastructures in Support of Electric-Powered Aviation». In: *Aerospace* 8.2 (2021), p. 40 (cit. on p. 126).
[155] F. Salucci, L. Trainelli, C. E. Riboldi, and A. L. Rolando. «Sizing of Airport Recharging Infrastructures in Support to a Hybrid-Electric Fleet». In: *AIAA SciTech 2021 Forum*. January 11–15, 2021, p. 1682 (cit. on p. 126).
[156] F. Salucci, C. E. Riboldi, L. Trainelli, and A. Rolando. «Optimal Recharging Infrastructure Sizing and Operations for a Regional Airport». In: *1st Aerospace Europe Conference (AEC 2020)*. Bordeaux, France, February 25–28, 2020, pp. 1–8 (cit. on p. 126).
[157] C. E. D. Riboldi, F. Bigoni, F. Salucci, A. Rolando, and L. Trainelli. «Switching to electric propulsion: fleet and infrastructure sizing». In: *25th International Congress of the Italian Association of Aeronautics and Astronautics*. Rome, Italy, Septembre 9–12, 2019 (cit. on p. 126).
[158] F. Salucci, L. Trainelli, R. Faranda, and M. Longo. «An optimization Model for Airport Infrastructures in Support to Electric Aircraft». In: *2019 IEEE Milan PowerTech*. Milan, Italy, June 2019, pp. 1–5. DOI: 10.1109/PTC.2019.8810713 (cit. on p. 126).
[159] L. Trainelli, A. Rolando, C. Riboldi, and F. Salucci. «Evaluating the impact of fleet switching to hybrid-electric aircraft on airport infrastructures». In: *More Electric Aircraft Conference (MEA 2019)*. Toulouse, France, February 6–7, 2019, pp. 1–4 (cit. on p. 126).
[160] F. Bigoni et al. «Design of airport infrastructures in support of the transition to a hybrid-electric fleet». In: *Advanced Aircraft Efficiency in a Global Air Transport*

System Conference (AEGATS 2018). Toulouse, France, October 23–25, 2018 (cit. on p. 126).

[161] A. Schroeder and T. Traber. «The economics of fast charging infrastructure for electric vehicles». In: *Energy Policy* 43 (2012), pp. 136–144 (cit. on pp. 129, 139).

[162] *Gurobi Optimizer*. URL: `http://www.gurobi.com` (visited on 11/12/2020) (cit. on p. 136).

[163] D. F. Finger, F. Götten, C. Braun, C. Bil, et al. «Cost estimation methods for hybrid-electric general aviation aircraft». In: *2019 Asia-Pacific International Symposium on Aerospace Technology (APISAT 2019)*. 2019, pp. 265–277 (cit. on p. 139).

[164] C. E. D. Riboldi, L. Trainelli, L. Mariani, A. Rolando, and F. Salucci. «Predicting the effect of electric and hybrid-electric aviation on acoustic pollution». en. In: *Noise Mapping* 7.1 (Apr. 2020). Publisher: De Gruyter Section: Noise Mapping, pp. 35–56. DOI: `10.1515/noise-2020-0004` (cit. on pp. 160–163, 169).

[165] F. Salucci, C. E. D. Riboldi, L. Trainelli, A. Rolando, and L. Mariani. «A Noise Estimation Procedure for Electric and Hybrid-Electric Aircraft». In: *AIAA SciTech 2021 Forum*. January 11–15, 2021, p. 0258 (cit. on p. 160).

[166] C. E. Riboldi, L. Mariani, L. Trainelli, A. Rolando, and F. Salucci. «Assessing the Effect of Hybrid-Electric Power-Trains on Chemical and Acoustic Pollution». In: *1st Aerospace Europe Conference (AEC 2020)*. Bordeaux, France, February 25–28, 2020, pp. 1–11 (cit. on p. 160).

[167] ECAC. *Report on standard method for computing noise contours around civil airports - Volume 2: Technical Guide*. Neuilly-sur-Seine, France, 2016 (cit. on pp. 160, 163).

[168] EUROCONTROL. *The Aircraft Noise and Performance (ANP) database: an internationl data resource for noise modellers*. 2006 (cit. on p. 160).

[169] J. B. Ollerhead, D. P. Rhodes, M. S. Viinikainen, D. J. Monkman, and A. C. Woodley. *The UK Civil Aircraft Noise Contour model ANCON: Improvements in Version 2*. Tech. rep. 9842. NATS, 1999 (cit. on p. 160).

[170] S. Pietrzko and R. Bütikofer. «FLULA - Swiss Aircraft Noise Prediction Program». In: *Acoustics 2002 Innovation in Acoustic and Vibration*. Adelaide, Australia, November 13–15, 2002 (cit. on p. 160).

[171] U. Isermann, K. Matschat, and E. A. Müller. «Prediction of Aircraft Noise Around Airports by a Simulation Procedure». In: *Inter-Noise 86*. Cambridge, MA, July 21–23, 1986, pp. 717–722 (cit. on p. 160).

[172] Deutsche Umweltbundesamt. *Anleitung zur Berechnung von Larmschutzbereichen (AzB)*. 2007 (cit. on p. 160).

[173] R. D. Bruce, C. T. Moritz, and A. S. Bommer. «Handbook of noise and vibration control». In: Hoboken: John Wiley & Sons, Inc., 2007. Chap. Sound power level predictions for industrial machinery, pp. 1001–1009 (cit. on p. 161).

[174] ECAC. *Report on standard method for computing noise contours around civil airports - Volume 3: Reference Cases and Verification Framework*. Neuilly-sur-Seine, France, 2016 (cit. on p. 164).

[175] L. Bertsch, W. Dobrzynski, and S. Guerin. «Tool development for low-noise aircraft design». In: *Journal of Aircraft* 47.2 (2010), pp. 694–699 (cit. on p. 171).

[176] E. EEA. «EEA air pollutant emission inventory guidebook—2009». In: *European Environment Agency (EEA), Copenhagen* (2009) (cit. on p. 172).

[177] T. I. Yacovitch et al. *Exhaust Emissions from In-use General Aviation Aircraft*. Transportation Research Board, 2016 (cit. on p. 173).

[178] F. O. of Civil Aviation. *Appendix 5: Calculation of emission factors in Aircraft piston engine emissions*. Bern, Switzerland, 2007 (cit. on p. 173).

[179] L. Trainelli, M. Bruglieri, F Salucci, and D Gabrielli. «Optimal Definition of a Short-Haul Air Transportation Network for Door-to-Door Mobility». In: *1st Aerospace Europe Conference (AEC 2020)*. Bordeaux, France, February 25–28, 2020, pp. 1–8 (cit. on p. 187).

[180] *HereMaps - Routing API*. HERE Developer. URL: `https://developer.here.com/documentation/routing/dev_guide/topics/what-is.html` (visited on 11/12/2020) (cit. on p. 192).

[181] G. Ruijgrok. *Elements of airplane performance*. VSSD, 2009 (cit. on pp. 210, 211).

[182] O. Gur, J. A. Schetz, and W. H. Mason. «Aerodynamic considerations in the design of truss-braced-wing aircraft». In: *Journal of Aircraft* 48.3 (2011), pp. 919–939 (cit. on p. 235).

[183] V. Cipolla et al. «Conceptual design of a box-wing aircraft for the air transport of the future». In: *2018 Aviation Technology, Integration, and Operations Conference*. 2018, p. 3660 (cit. on p. 235).

[184] F. Faggiano, R. Vos, M. Baan, and R. Van Dijk. «Aerodynamic design of a flying V aircraft». In: *17th AIAA Aviation Technology, Integration, and Operations Conference*. 2017, p. 3589 (cit. on p. 235).

[185] R. H. Liebeck. «Design of the blended wing body subsonic transport». In: *Journal of aircraft* 41.1 (2004), pp. 10–25 (cit. on p. 235).

[186] A. Gong and D. Verstraete. «Fuel cell propulsion in small fixed-wing unmanned aerial vehicles: Current status and research needs». In: *International Journal of Hydrogen Energy* 42.33 (2017), pp. 21311 –21333. DOI: `https://doi.org/10.1016/j.ijhydene.2017.06.148` (cit. on p. 250).